EFFECT OF PAVEMENT STRUCTURAL RESPONSE ON ROLLING RESISTANCE AND FUEL ECONOMY

By

Danilo Balzarini

A DISSERTATION

Submitted to
Michigan State University
in partial fulfillment of the requirements
for the degree of

Civil Engineering—Doctor of Philosophy

2019

ABSTRACT

EFFECT OF PAVEMENT STRUCTURAL RESPONSE ON ROLLING RESISTANCE AND FUEL ECONOMY

By

Danilo Balzarini

The massive use of fuel required by road transportation is accountable for the exploitation of non-renewable energy sources, is a major source of pollutants emission, and implies high economic costs. Rolling resistance is a factor affecting vehicles energy consumption; the structural rolling resistance (SRR) is the component of rolling resistance that occurs due to the deformation of the pavement structure. The present research presents an investigation on the SRR in order to identify its causes, characterize it and develop the instruments to predict its impact on fuel consumption for different road and traffic conditions.

First the methods to calculate the SRR on asphalt and concrete pavements were developed. The structural rolling resistance is calculated as the resistance to motion caused by the uphill slope seen by the tires due to the pavement deformation. The SRR can be converted into fuel consumption using the calorific value of the fuel and the engine efficiency, and the greenhouse gas emissions associated with it can be calculated.

Purely mechanistic models were used to determine the structural rolling resistance, and the fuel consumption associated with it, on 17 California pavement sections under different loading and environmental conditions. The results were used to develop simple and rapid-to-use mechanistic empirical heuristic models to predict the energy dissipation associated with the structural rolling resistance on any asphalt or concrete pavement.

The difference in terms of fuel consumption and pollutants emissions between different pavement structures can be significant and could be included in economic evaluations and life cycle assessment studies. For this purpose, a practical tool was created, based on the heuristic models, that allows the calculation of the fuel consumption associated with the SRR for any given traffic and pavement section. Example of applications of such a tool are presented and discussed.

Dedicato a Mamma, Babbo e Mari.
Vi sono grato per il sostegno e l'affetto ricevuto in questi anni.

ACKNOWLEDGMENTS

I would like to express my sincere gratitude to my advisor, Prof. Karim Chatti, for his teaching and for what he meant for my scientific training. I am honored to have been his student. He guided me in my research with his high-level knowledge, patience and motivation. His advice has been a valued encouragement to continue improving, in such way that made my Ph.D. experience productive and stimulating.

Also, I would like to thank every member of my scientific committee: Prof. Neeraj Buch, prof. Alejandro Diaz, prof. John T. Harvey and prof. M. Emin Kutay, for their time, interest, and help.

A special mention goes to Dr. Imen Zaabar who has supported me along the way, both from the academic and the human point of view, with her remarkable scientific skills, willingness, insightful comments and encouragement.

I gratefully acknowledge the funding sources that made my Ph.D. work possible: Caltrans and the University of California Pavement Research Center, as well as the Center for Highway Pavement Preservation.

Finally, special thanks go to my family: my mother, father and aunt Alba for being always by my side, despite the distance, and my partner Maritza for her tireless support.

TABLE OF CONTENTS

LIST OF TABLES

LIST OF FIGURES

1 INTRODUCTION

One of the challenges of science today is to provide tools to pursue a sustainable development that preserves the resources and the environmental balance of our planet. The transportation sector, which is at the core of modern societal development, plays an important part in this matter. The strong demand for energy required by the transportation sector is fulfilled by a massive use of fossil fuels that are a non-renewable energy resource and a source of emissions, which, if not kept under control, can be harmful to the environment. Specifically, this study deals with the road transportation infrastructure: It is aimed at investigating how pavement structure can affect the energy consumption, and therefore the emissions, of the vehicles traveling on it.

The rate at which fossil fuels are used is much higher than the rate at which they are replaced, reason for which they should be utilized wisely in order not to exhaust them. Furthermore, when fossil fuels are burned, a large amount of pollutant gases is produced and is discharged into the surrounding atmosphere. Two of them are particularly harmful: NOx and CO_2. In atmospheric chemistry, NOx indicates a family of nitrogen oxides that are relevant to air pollution, namely nitric oxide (NO) and nitrogen dioxide (NO_2). They derive from nitrogen and oxygen combustion under high pressure and temperatures as it occurs in car engines. NO_2 is not only an important air pollutant by itself, but also reacts in the atmosphere to form ozone (O_3) and acid rain. Breathing air with a high concentration of ozone can have serious effects on the respiratory and cardiovascular systems, especially on hot sunny days, when the ozone concentration reaches higher levels. In addition, NOx and sulfur oxides (SOx) in the atmosphere react with water and form a solution of sulfuric acid and nitric acid. Rainwater, snow, fog, and other forms of precipitation containing such solutions fall to earth as acid rain that, along with dry deposition, severely affects our ecosystems and some segments of our economy (*Organization for Economic Cooperation and Development, 2016*).

Carbon dioxide (CO_2) is a colorless gas which consists of a carbon atom covalently double bonded to two oxygen atoms. It is essential to the survival of plants and animals, aerobic fungi and bacteria, being a product of cellular respiration in organisms that obtain energy by breaking down sugars, fats and amino acids with oxygen as part of their metabolism. Together with other gases, it traps the infrared radiation of sunlight, resulting in the so-called "greenhouse effect", which prevents the earth's surface from large temperature variations in the day-night cycle. However, since the industrial revolution, levels of atmospheric carbon dioxide have dramatically increased, affecting the global climate and causing global warming, whose consequences imply high societal and economic costs: Hurricanes and other storms are likely to become stronger, floods and droughts will become more common; less fresh water will be available, and some diseases will spread (*Crimmins et al., 2016*).

Although governments, over the last decades, have implemented policies to contain pollution (and a lot of pollutant emissions have decreased, as shown below), according to National Oceanic and Atmospheric Administration's Global Monitoring Division (GMD), unprecedented levels of CO2 have been recorded in 2016 (*NOAA, 2017*). Carbon dioxide grew by 2.87 parts per million (ppm) during 2018, jumping from an average of 407.05 ppm on Jan. 1, 2018, to 409.92 on Jan. 1, 2019), registering the fourth-highest annual growth in the concentration of atmospheric carbon dioxide (CO2) in 60 years of record-keeping. Figure 1.1 shows that CO2 is by far the main contributor to Greenhouse gas emissions (*EPA, 2017*).

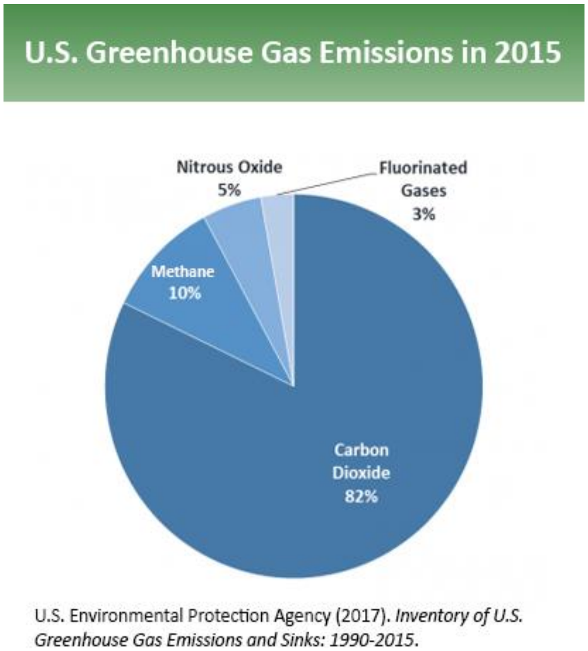

Figure 1.1 U.S. greenhouse gas emissions in 2015 (Source: EPA, 2017)

Figure 1.2(a) shows that in 2015, transportation in the US accounted for about 32% of the total CO2 emissions. Figure 1.2(b), which is related to the generality of greenhouse gases emissions and not specifically to CO2 ones, emphasizes how road transport plays a key role, as it holds 84% of all the transportation sector.

Figure 1.3 shows that, also with respect to NOx emissions in US, road transportation is a major source of emissions, accountable for about 38% of it, and that is about the same percentage estimated in Europe.

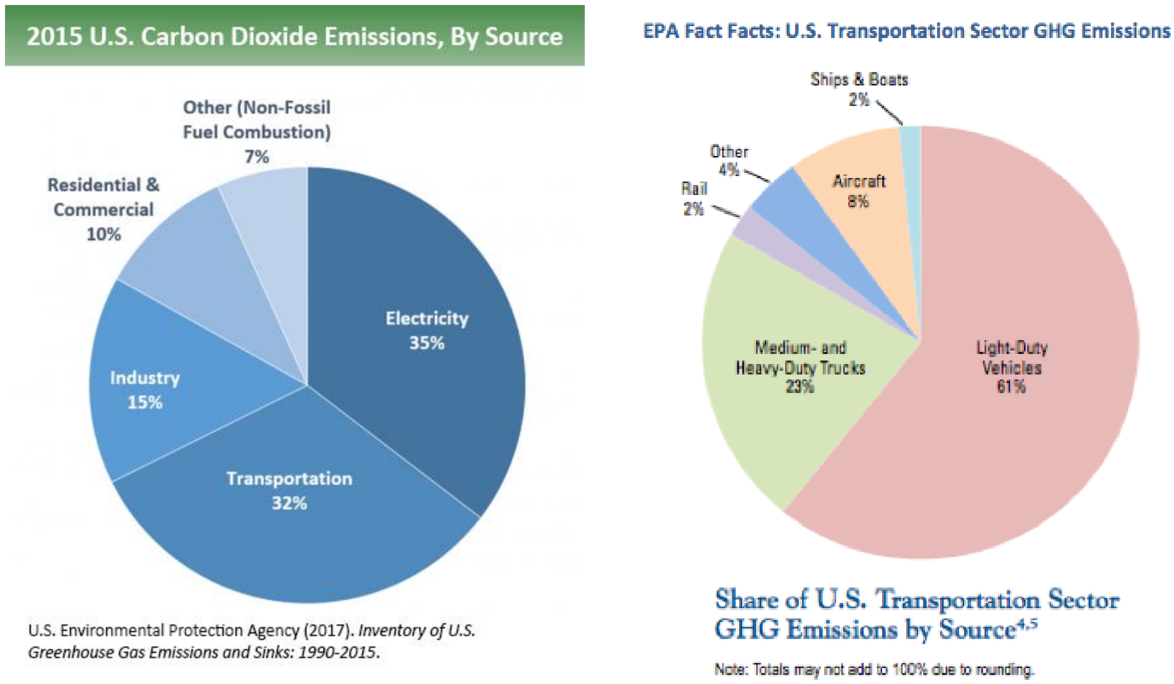

(a) (b)

Figure 1.2 (a) U.S. CO_2 emission in 2015; (b) Share of U.S. Transportation Sector GHG Emissions (Source: EPA, 2017)

It is evident that, although air pollutants are emitted from a range of sources, a large part of harmful emissions come from road transport.

The efforts carried out jointly by scientific research, governmental policies and supranational organizations to address the issue, together with an increased public awareness about environmental issues, have already produced significant results in order to improve the quality of the air we breathe. A positive trend has been detected both in US and in Europe. Figure 1.4 shows how NOx emissions in the US have been strongly reduced from 1990 to 2016 despite the large increase in the number of road vehicles circulating during this period: About 256 million vehicles were registered in 2016 compared to 193 million in 1990. This means that it is possible to preserve the environment while meeting modern societies' needs and indicates that this corrective path should be continued and improved.

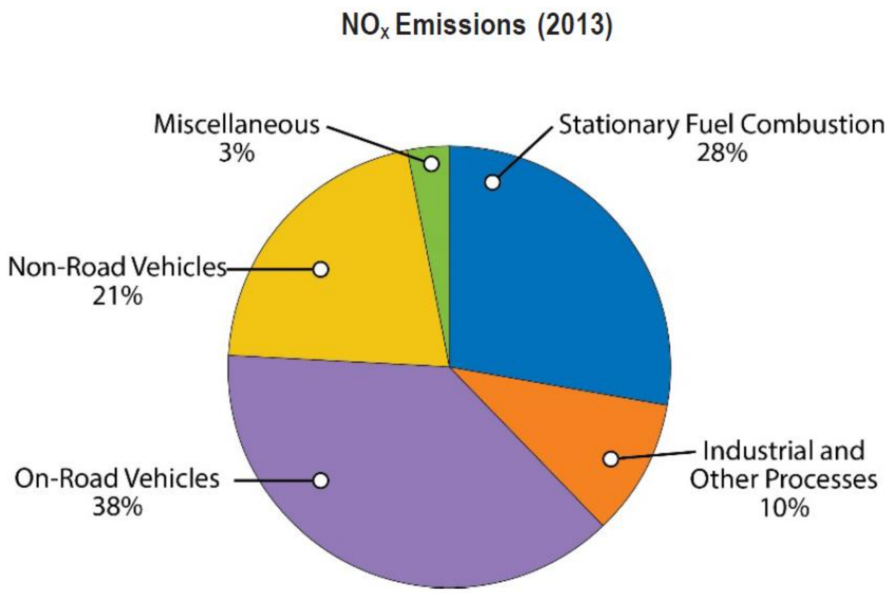

Figure 1.3 U.S. NOx emissions in 2013 (Source: FHWA, 2016)

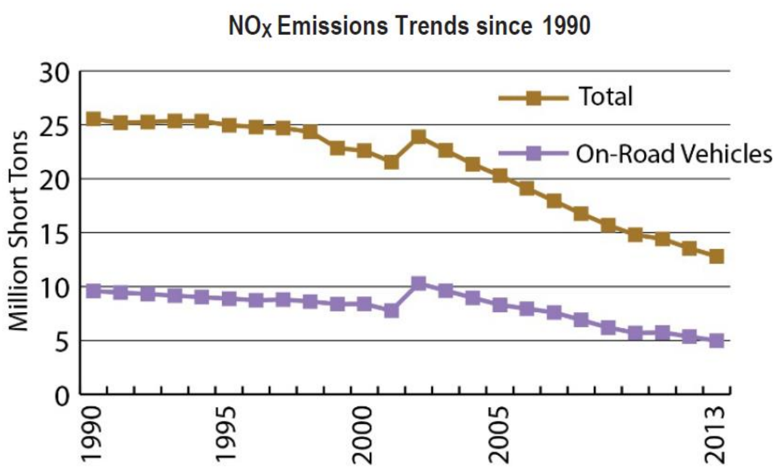

Figure 1.4 U.S. NOx emissions trends. (Source: FHWA, 2016)

But, as of today, the big picture indicates that traffic-related pollution is still a problem to be addressed.

The European Environment Agency (EEA) report on air quality in Europe (*2018*) indicates that air pollution continues to exceed the European Union and World Health Organization limits and guidelines; it outlines that road transport is one of Europe's main sources of air pollution, being the largest contributor to total nitrogen dioxide emissions in the EU. Even if a decrease in population's exposure to pollutants as NO_2, particulate matter, O_3, can be recorded, still a dramatic picture comes out, particularly in urban areas, where the air pollution is responsible for premature deaths, cancer and a wide range of diseases (*EEA*, *2018*). Apart from the impact on the health, air pollution also has a negative impact on European economies and ecosystems.

Also, the American Lung Cancer Association's annual "State of the Air" report (*2018*), through detailed information about how much of each type of pollution is detectable in the air in US cities, reaches the conclusion that, despite improvements in many areas, more than 4 in 10 people (41 per cent) in the US still live in counties with unhealthy levels of air pollution (either ozone or particle pollution).

Because there is a really large number of vehicles circulating, even very small fuel savings for each vehicle will result in a really significant reduction in exhaust emissions into the air, providing also an economic advantage, as fuel consumption can be converted into monetary terms and included in cost/benefit analysis. The vehicle fuel economy depends on the vehicle itself and the infrastructure, and more specifically on three main factors, as shown in Figure 1.5: Engine efficiency, air drag and rolling resistance. As far as the engine efficiency is concerned, all major automobile manufacturers compete with massive investments in technological development and innovation in the search for higher performance engines with lower fuel consumption, in order to reduce emissions throughout the life cycle of the vehicle. The governments, for their part, are imposing stricter regulations, and higher taxes to improve and speed up this process.

The rolling resistance is relevant as cause of energy consumption at lower speeds, while, as the velocity of the vehicle increases, the air resistance becomes predominant. Aerodynamic drag increases with the square of speed; therefore, it becomes critically important at higher speeds. Drag coefficient is used to quantify the resistance of an object to movement through air. The lower the coefficient, the more aerodynamic the vehicle is; hence, reducing the drag coefficient in an automobile improves the performance of the vehicle as it pertains to speed and fuel efficiency.

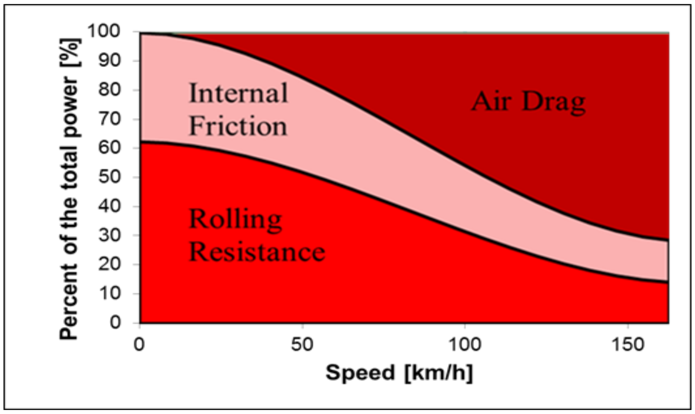

Figure 1.5 Motion Resistances as function of speed (Source: Beuving et al., 2004)

Rolling resistance represents the energy dissipated by the tires per unit of distance travelled, and it is mainly due to the viscoelastic properties of the rubber compounds used to make tires. Due to the weight of the vehicle, the tire deforms at the point of contact with the road surface. This deformation involves energy loss. Laclair, in the essay "*The Pneumatic Tire*," defines the concept of rolling resistance in these terms: “When a tire rolls on the road, mechanical energy is converted to heat as a result of the phenomenon referred to as rolling resistance. Effectively, the tire consumes a portion of the power transmitted to the wheels, thus leaving less energy available for moving the vehicle forward. Rolling resistance therefore plays an important part in increasing vehicle fuel consumption. Rolling resistance includes mechanical energy losses due to aerodynamic drag associated with rolling, energy losses taking place within the structure of the tire, and due to the tire-road interaction.” In this essay, Laclair conceptually defines the physical nature of rolling resistance, quoting the studies of Schuring (*1977*), who gave an important theoretical basis to the study on rolling resistance, and highlights that rolling resistance cannot be considered a force, despite the prevalence of this concept. “Although rolling resistance - defined as energy per unit distance - has the same units as force (J/m = N), it is a scalar quantity with no direction associated with it… Even though the normal symbol used to denote rolling resistance is F_R, it is emphasized that, in many instances, the value of F_R is calculated from operating and geometrical parameters – it does not correspond to an actual physical force”.

The amount of energy loss due to rolling resistance is a variable depending both on the tire and the pavement. Tire manufacturers invest significant resources in scientific research to reduce rolling resistance; however, it has been proven that the rolling resistance in the tire-pavement interaction is significantly affected by the surface of the pavement. A report published by the Joint European Asphalt Pavement Association (EAPA) and Eurobitume Task Group on Fuel Efficiency states that the energy used by the traffic during the lifetime of the road highly surpasses the energy use for construction, maintenance and operating the road, which only accounts for 2-5% (depending on the traffic volume) of the total. Hence, it is justified to focus on how different road pavement surfaces and structures affect the fuel consumption of vehicles (*EAPA, 2004*).

Different textures of road surfaces influence fuel consumption by up to 10%. Surface roughness has a significant influence on the fuel consumption and on noise development.

An exhaustive study of the effect of pavement surface characteristics on fuel consumption and other vehicle operating costs was conducted by Chatti and Zaabar (*2012*), which concluded that: “An increase in IRI of 1 m/km (63.4 in./mi) will increase the fuel consumption of passenger cars by 2% to 3%, irrespective of speed. For heavy trucks, this increase is 1% to 2% at highway speed (112 km/h or 70 mph) and 2% to 3% at a lower speed (56 km/h or 35 mph). Surface texture (MPD) and pavement type have no statistically significant effect on fuel consumption for all vehicle classes with the exception of heavy trucks. An increase in MPD of 1 mm (0.039 in) will increase fuel consumption by about 1.5% at 88 km/h (55 mph) and about 2% at 56 km/h (35 mph).” Zaabar and Chatti (2014) also concluded that “heavy trucks driven over asphalt concrete pavements will consume about 4% more fuel than heavy trucks driven over Portland cement concrete pavements at 56 km/h (35 mph) in summer conditions. The effect of pavement type was statistically not significant at higher speeds.”

Studies to investigate how the structure of the pavement affects the rolling resistance (namely Structural Rolling Resistance or SRR) are still relatively recent and more research is now under way. The present study is among these; it aims at having a better understanding of the SRR and vehicle fuel economy. The following gives a brief outline of the proposed dissertation.

Chapter 2 contains a literature review on these SRR studies. In chapter 3 and 4 the mechanistic models used to simulate the pavement response to a moving load, and the methods to calculate the structural rolling resistance are presented, and an investigation is conducted on how modeling assumptions can affect the results for the calculation of the SRR. In chapter 5 the results of simulations conducted on various rigid and flexible pavements are analyzed and compared. In chapter 6 and 7 simple parametric models to estimate the structural rolling resistance are presented for rigid and flexible pavements, respectively. Finally, chapter 8 shows a practical application of these models in a simple economic analysis and chapter 9 presents the main conclusions of the study.

2 LITERATURE REVIEW

Several researchers have studied the effects of the viscoelastic properties of the materials composing the pavement on the dissipation of energy. One of the first in this field to deal with the topic was William Flugge, who, in his book (*"Viscoelasticity", 1975*), analyzed the viscoelastic response to a moving load on a beam resting on a Kelvin-Winkler foundation. He showed that the viscoelastic deformation caused the vehicle load to move on an upward slope, and, thus, to do work. The force necessary to overcome the slope adds to the rolling resistance.

The effect of the pavement structure on fuel consumption has become the object of renewed research recently, after the National Research Council of Canada's Centre for Surface Transportation conducted a series of studies on the effects of pavement structure on vehicle fuel consumption (*Taylor et al. 2000, 2002 and 2006*). The first study was conducted by measuring the fuel consumption of a tractor semi-trailer moving along different (asphalt, concrete, and composite) pavement sections in-situ. The results showed great differences between flexible and rigid pavements, with a fuel consumption on asphalt pavements up to 11% greater than on concrete pavement (*Taylor et al., 2000*). However, the different surface conditions had not been considered, and there were inconsistencies in the trend of the results. This led to an additional analysis of the data (*Taylor et al., 2002*); the results were corrected to consider the effect of different weather conditions during the field tests. After corrections the differences between asphalt and concrete were reduced to 4.3 – 9.2%; however, the characterization of the section in terms of the pavement roughness was poor, and insufficient to correct the results for the different surface conditions. The tests were repeated in 2006 (*Taylor and Patten, 2006*), choosing sections with similar good surface characteristics, and repeating the tests in different seasons. The new results were used to develop models to estimate the fuel consumption rate (L/100km) as a function of pavement structure, vehicle load and speed, pavement temperature, wind speed, International Roughness Index (IRI) and grade, and the models were then used to compare the consumptions on different pavement structures. According to the authors: "The comparison showed statistically significant fuel savings when operating on concrete pavements compared to asphalt pavements ranging from 0.5 L/100 km to 0.8 L/100 km (1.1% to 5.2%), depending on the model used, IRI range, vehicle speed and weight. The differences between composite and concrete pavements on rougher roads were not statistically different." A limitation of the study is that the pavement structures are not described; there is no information about the thickness and stiffness of the layers, and the pavement texture was not measured. It should be noted that the models developed by the NRC researchers for the fuel consumption estimation are simply a tool to compare different pavement types and have no application outside the study framework.

Another set of studies to investigate the difference in terms of fuel consumption between asphalt and concrete pavement sections was conducted by the Swedish National Road and Transport Institute (*Jonsson and Hultqvist, 2008*). The tests were conducted using a car and a heavy truck. The results showed less fuel consumption for concrete pavements, with higher differences for the heavier vehicle, but the results do not differentiate the effect of pavement structure and pavement surface. The values of mean profile depth (MPD), IRI and rut depth were higher for the asphalt sections, which therefore showed higher rolling resistance.

In 2010, Sumitsawan et al. published another similar study to determine the effect of pavement structure on fuel consumption. A series of field tests was conducted in Texas where two pairs of pavement sections (asphalt and concrete) of similar roughness and grade were selected. It should be pointed out that, as shown in Table 2.1, for the first pair of sections the grade is higher and the

IRI is slightly higher for the asphalt pavement; for the second pair the grade is lower and the IRI is higher for the rigid pavement, while the grade is slightly higher for the asphalt pavement.

Table 2.1 Pavement sections for the Texas study (Sumitsawan et al., 2010)

	Road Section	Pavement Type	Details	Average IRI (in/mi)	Longitudinal Slope in Data Collection Direction (%)
First Test Sites	Abram Street	CRCP	8" continuously reinforced concrete over 2" HMAC type D on 8" lime stabilized subgrade	174.6	+1.2
	Pecandale Drive	HMA	7" HMAC (1.5" Type D, 5.5" Type B) on 6" lime stabilized subgrade	180.6	+1.2
Second Test Sites	Road to Six Flags Street	JPCP	7" reinforced concrete on 6" lime stabilized subgrade 20' transverse joint spacing	323.3	+0.4
	Randol Mill Road	HMA	8" HMAC (2" Type D, 6" Type A) on 6" lime stabilized subgrade	276.7	+0.6

During the fuel consumption measurements tests, the authors kept constant the vehicle mass, the tire pressure and the fuel type, and measured the ambient temperature, humidity, and wind speed. Only one vehicle was used. The authors observed fuel consumption savings of 3% to 17% on PCC pavements depending on the driving mode (accelerating vs constant speed) and surface conditions (dry vs wet). The observed differences were found to be statistically significant at 10% level of significance.

The main limitation of this study is that the authors did not correct their results to account for the different IRI and grade for the two pairs of sections, which means that the effect of structure was not isolated, and the savings associated to the rigid pavements cannot be completely attributed to the pavement structure. The reported percentage differences between the pavement types appear to be too high, especially considering that the tests were run using a vehicle with a relatively low weight (3000lbs), which is lighter than the vehicles used for the previous studies, and for which the pavement structure should not give such a large contribution to fuel consumption.

Zaabar and Chatti (*2014*) also observed from field test measurements that different types of pavement, with similar surface characteristics, can lead to different fuel consumption. Heavy trucks driven over asphalt concrete pavements consume about 4% more fuel than heavy trucks driven over portland cement concrete pavements at 56 km/h (35 mph) in summer conditions. The effect of pavement type was statistically not significant for lighter vehicles (car, van, light trucks) and for the heavy truck at higher speeds (45 mph and 55 mph).

All the mentioned studies used results from field tests to observe and quantify the effect of pavement structure on fuel consumption, without investigating the causes behind these differences from a mechanistic modeling point of view. Chupin et al. (*2013*) further developed the concept introduced by Flugge in 1975 and presented a theoretical approach for the calculation of the structural rolling resistance (SRR). They asserted that the SRR is caused by non-elastic deformations of the pavement under a load. The deflection basin for a wheel moving along an asphalt section is not symmetric due to the delay of the response caused by the viscous behavior, and the wheel moves facing an uphill slope (Figure 2.1); the structural rolling resistance is the resistance that the wheel has to overcome during its motion and is proportional to the slope and the vehicle load ("slope method").

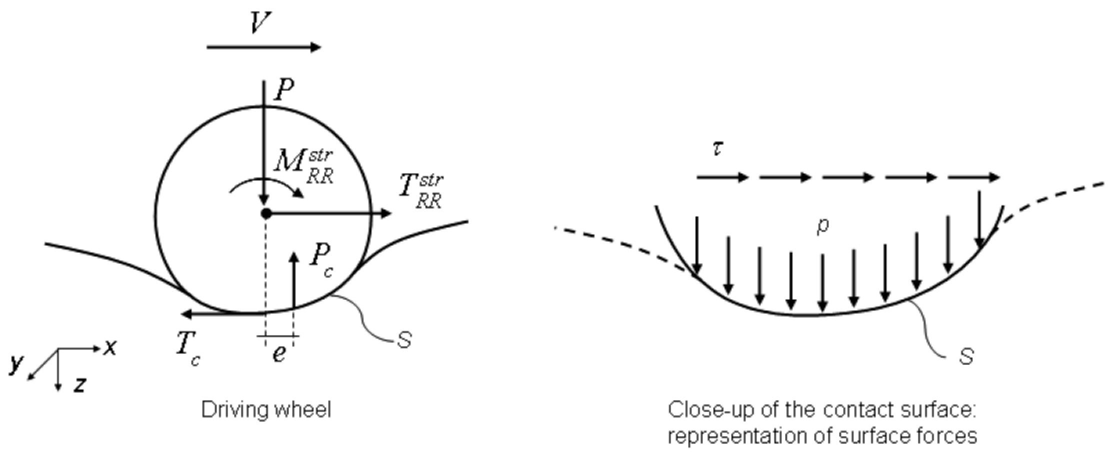

Figure 2.1 Tire pavement contact forces (Chupin et al., 2013)

It is necessary to clarify that all the studies that are dealing with the theoretical calculation of the SRR are entirely focused on the effect of the pavement structure only, and are not dealing with any energy loss associated with the vehicle tires, which are assumed to be non-dissipative; also, the pavement surface is assumed to be perfectly smooth, which will lead to no vibrations of the suspension systems and therefore no additional energy loss. This way the structural rolling resistance is decoupled from all the other rolling resistance components to simplify the models and the calculations.

The method used by Chupin to calculate the energy dissipated due to the SRR requires the calculation of the deflection basin for a moving load, which was done using a software named ViscoRoute (*Chabot, 2010*); the deflection basin is used to obtain the slope as seen by the moving vehicle (Figure 2.2), which can be considered as a gradient resistance force that sums up with the forces opposing the motion of the vehicle. The authors showed how such gradient force is null for a completely elastic structure, which means that there is no structural rolling resistance, while, when the asphalt layer is considered a viscoelastic material, the SRR depends on the material properties. The authors simulated a truck moving along a typical French pavement section; they observed that the structural rolling resistance is about 1.1% of the total fuel consumption of the vehicle for a speed of 65 km/h at about 20° C, and increases as the temperature increases, due to the more viscous behavior of asphalt at higher temperatures. Vehicle speed also affects the SRR, making it lower at higher velocities, due to the time-temperature superposition principle (*Christensen, 1971*).

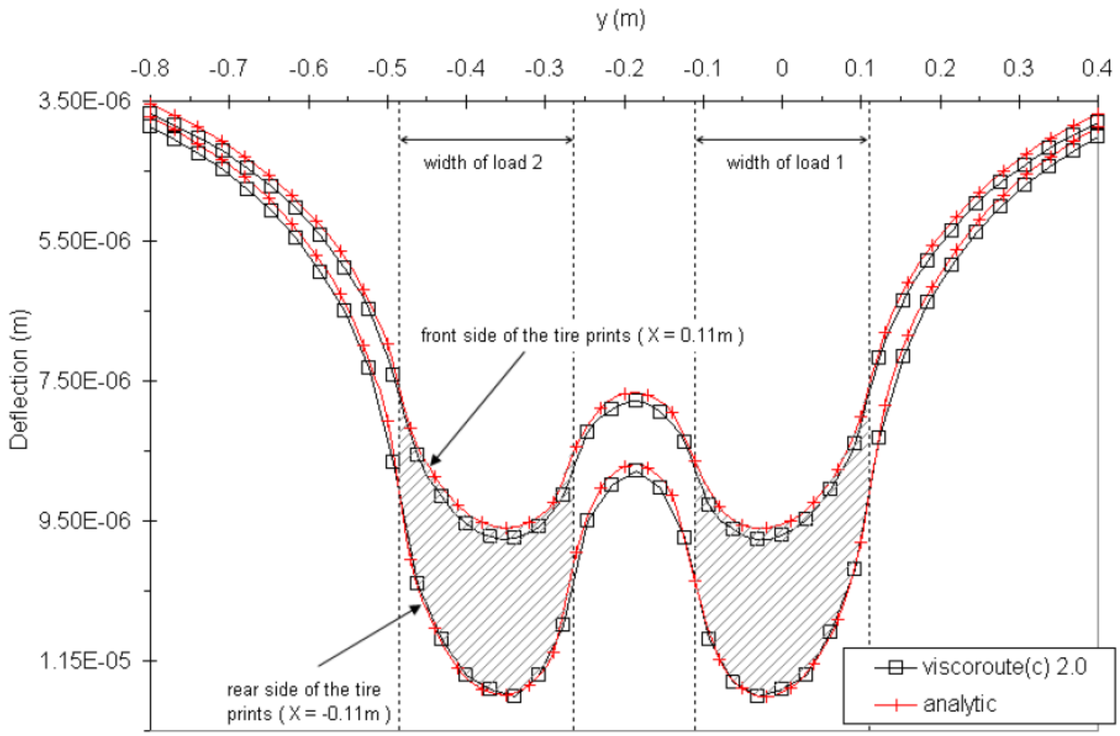

Figure 2.2 Deflection basin as seen by the front and the rear of the tires (Chupin et al., 2013)

At the same time, Pouget et al. (*2012*) published another paper where the structural rolling resistance is calculated as the energy dissipated internally by the pavement ("internal energy method"). The load applied from the tire transmits energy to the pavement while moving. This energy is divided into an elastic part, that is entirely recovered by the wheel (the energy dissipation within the tire is excluded from this analysis), and an inelastic part, that is dissipated by the pavement as the area of the hysteresis loop in the pavement response. The dissipation of the energy is due to the viscous properties of the asphalt layer materials, considering all the other layers as perfectly elastic. The dissipated energy produces small changes in the structure of the pavement. In the long term it results in a decay in the structural performance of pavements, that progressively leads to crack growth.

The energy dissipated by a moving load in a pavement volume *V* can be calculated as:

$$W_{diss} = \iiint \left(\int_{-\infty}^{+\infty} \sigma_{xx} \cdot \dot{\varepsilon}_{xx} + \cdot\sigma_{yy} \cdot \dot{\varepsilon}_{yy} + \cdot\sigma_{zz} \cdot \dot{\varepsilon}_{zz} + \cdot\sigma_{xy} \cdot \dot{\varepsilon}_{xy} + \cdot\sigma_{xz} \cdot \dot{\varepsilon}_{xz} + \cdot\sigma_{yz} \cdot \dot{\varepsilon}_{yz} \;\; dt \right) dV \qquad (2.1)$$

The authors used the internal energy method to calculate the energy dissipated caused by a truck moving along a French highway section (asphalt pavement), using the finite element software ABAQUS for the simulation. For heavy vehicles moving on asphalt pavements at high temperature and low vehicle speed, the authors showed that the SRR can be responsible for up to 5.5% of the vehicle fuel consumption (Figure 2.3). At very low or very high temperatures the material can be considered elastic. This is confirmed by the results, which show that the energy dissipated at those temperatures is close to zero.

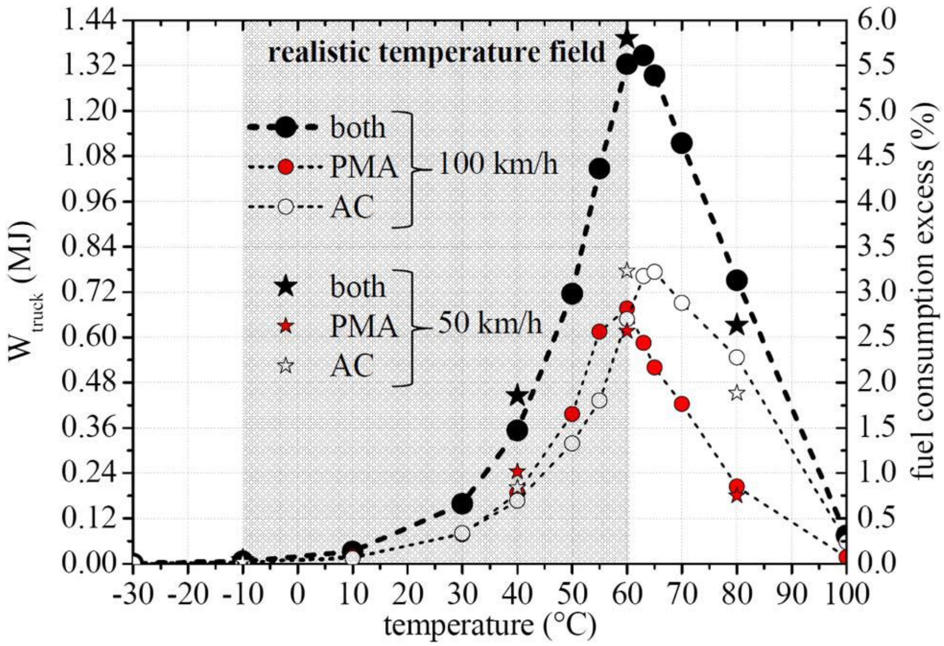

Figure 2.3 Dissipated energy with temperature for a 40-ton truck (Pouget et al., 2012)

Louhghalam et al. (*2014*) showed that, according to the first principle of thermodynamics applied to a closed system, the "internal energy method" and the "slope method" are equivalent, and the structural rolling resistance can be calculated with either of the two methods. The same authors also published another paper (*Louhghalam et al., 2013*) where they describe their own model, which consists of a viscoelastic beam on a Winkler foundation (Figure 2.4); the model was used to calculate the SRR using the "slope method". Their model leads to simple and fast calculations, but it does not realistically describe the behavior of a pavement structure, which is a more complex layered system. Also, the model cannot consider the tire pressure or the tire imprint dimension; rather the only loading input is the weight of the axle.

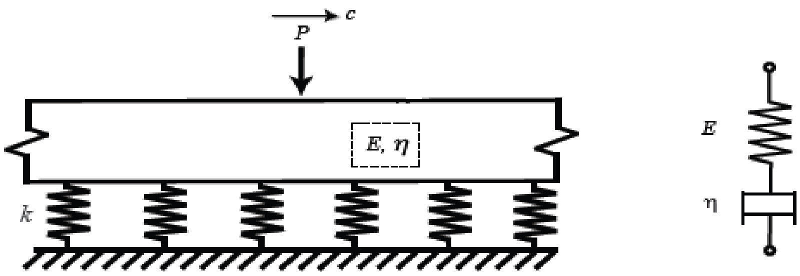

Figure 2.4 Viscoelastic Beam on Winkler foundation (Louhghalam et al. 2013)

Shakiba et al. (*2016*) conducted another study to predict the structural rolling resistance. The authors show a different approach to calculate the SRR using the finite element software ABAQUS by using the rate of external work (which is a direct output of the program) to calculate the power dissipation associated with the SRR. The results from the simulations of a truck moving on pavement sections designed for heavy traffic volume in the U.S. interstate system (different from the French pavement used by the previous studies) are shown in Figure 2.5. For the described case study, the SRR accounts for 0.18 - 1.9% of the total vehicle consumption; the effects of speed and temperature confirm the findings of the French researchers. The authors' new contribution to the state of the art was investigating the effect of damping in the base and subgrade layers, and the tire pressure distribution on the results. The choice of the Rayleigh damping coefficients can affect the results by up to 20%, which means that they must be chosen with particular care. The authors varied the α and β values and showed how the SRR changes accordingly. Since the pavement structure was not meant to represent an existing pavement, the values used for those coefficients were taken from other studies; however, their findings imply that it is necessary to choose very carefully those values if a real pavement section is modeled using ABAQUS. Regarding the effect of the tire contact stress distribution, the authors showed how transverse and longitudinal tire contact stresses do not contribute to the external work rate, but the results change up to 25% when using a non-uniform tire pressure distribution, instead of a uniform pressure.

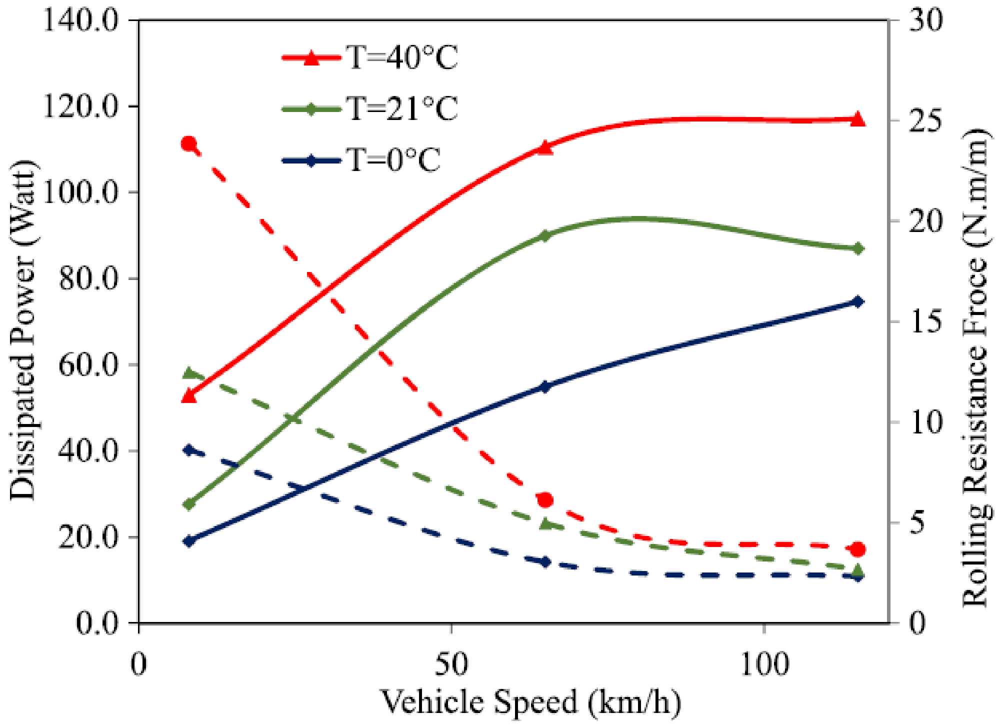

Figure 2.5 Dissipated power and force associated with the SRR (Shakiba et al. 2016)

Bazi et al. (*2018*) used the finite element software ABAQUS to conduct another study on the effect of pavement structure on SRR. The energy dissipation is calculated using the method proposed by Lu et al. (*2010*), which is identical to the “slope method” discussed by Chupin et al. (*2013*). As shown in Figure 2.6, the deflection under the front of the tire is higher than the deflection under the rear of the tire, meaning that the wheel “sees” an uphill slope. The SRR is equal to the gradient force associated with such slope.

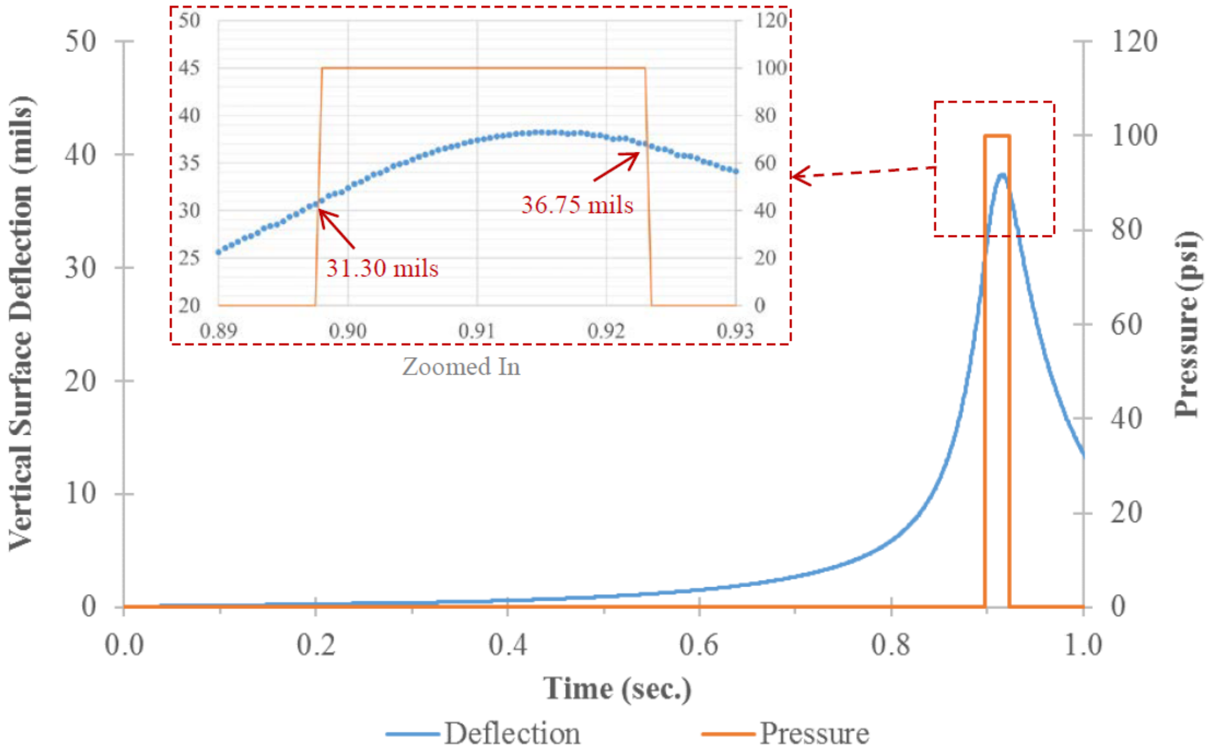

Figure 2.6 Deflection under the tire print (Bazi et al. 2018)

The authors calculated the SRR for asphalt and concrete pavements, concluding that "the rolling resistance, expressed as a percentage of the vehicle weight, was shown to range from 0.01% to 0.09% for the flexible pavements, and from 0.0008% to 0.004% for the rigid pavement". They also proposed a model to predict the rolling resistance from FWD testing using the energy loss from the hysteresis loop, the plate diameter, the plate diameter multiplier and the FWD load. A limitation of this study is that the rigid pavements were modeled as a single slab, of dimensions 250 x 250 ft^2, which may be acceptable to represent a continuously reinforced concrete pavement (CRCP - no transverse joints), but not a jointed concrete pavement (JPCP - has transverse joints), the most common concrete pavement type in use. This point is discussed in more detail in the present study in section 4.1. Also, no indications were provided about the choice of the Rayleigh damping coefficients for the base and subgrade layers.

From the literature review, what stands out the most is the difference between the results obtained from the field tests and the theoretical calculations of the structural rolling resistance using mechanistic models. The experimental field tests studies (with all the limitations discussed for each of them) showed differences between asphalt and concrete pavements in terms of vehicle fuel consumption to be on average about 4% or more of the total vehicle consumption; such differences were attributed to the pavement structure. The theoretical predictions instead showed that the pavement structure should not play such a big role as part of the rolling resistance.

The California Department of Transportation, in collaboration with the University of California - Davis has decided to invest in a project, which also includes the present study, to clarify the inconsistencies in the current state of the art and determine more accurately how much the pavement structure can affect the vehicle fuel consumption. The findings of such study may be used for life cycle assessment (LCA) and life cycle cost analysis (LCCA) and in the general decision-making process of road design.

Phase I of the Caltrans project has been completed, and Phase II is still ongoing. The goal of Phase I was to compare three different modeling approaches and provide first-level estimates of the theoretical calculation of the fuel consumption associated with the SRR ($Fuel_{SRR}$), in preparation for simulations of annual $Fuel_{SRR}$ for different traffic and climate scenarios, as well as different types of pavement structures on the California state highway network. Coleri et al. (*2016*) stated that the comparison of the predicted $Fuel_{SRR}$ for test sections showed that all three models produced different results, which can be attributed to the differences in the three modeling approaches and assumptions.

The main contribution of this Ph.D. research work to the state of knowledge of the structural rolling resistance is to fill the gap between theoretical predictions and field measurements by developing mechanistical models to predict the energy dissipation associated with the SRR based on the pavement, loading and environmental conditions.

3 ASPHALT PAVEMENT MODELING

For the present study the asphalt pavement response is calculated using ViscoWave II – M. The original solution and associated computer program (ViscoWave) was developed by Lee (*2013*) to calculate the deflection at the pavement surface under a Falling Weight Deflectometer (FWD), which applies a stationary transient pulse disk load to the pavement. A parallel solution was developed by Zaabar et al. (*2014*) and the algorithm has been later coded in MATLAB and updated to its second version ViscoWave II in C++ language. Its computational efficiency has been highly improved by using parallel computing and new features were added; the program can now calculate deflections, stresses and strains due to moving loads at any point in the pavement. The accuracy of the results has been shown by Balzarini (*2015*).

Viscowave II - M employs the so-called spectral element method, where each element is defined as one layer of the pavement, to solve the wave propagation problem in the pavement structure and calculate the pavement response to an arbitrary loading. A limitation of the model is the hypothesis of axisymmetric conditions: the condition of radial symmetry must be verified, as shown in Figure 3.1.

The inputs required by the program are the characteristics of the pavement, the loading conditions and the coordinates of the points where the response of the pavement is evaluated. ViscoWave II - M provides the solution for both elastic and viscoelastic materials. To define the structure of the pavement it is necessary to input:

1) the number of layers
2) the thickness of the layers
3) the mechanical characteristics of the layers:
    - Poisson’s ratio

- Density
- Elastic or relaxation modulus
- Material damping

To define the loading conditions, it is necessary to input:

1) the tire pressure
2) the radius of the tire imprint.

It is also required to specify the coordinates of the points where the pavement response to a stationary load is to be calculated. Part of this study was focused on improving and implementing the moving load solution in ViscoWave II - M and verifying the stability and accuracy of the results.

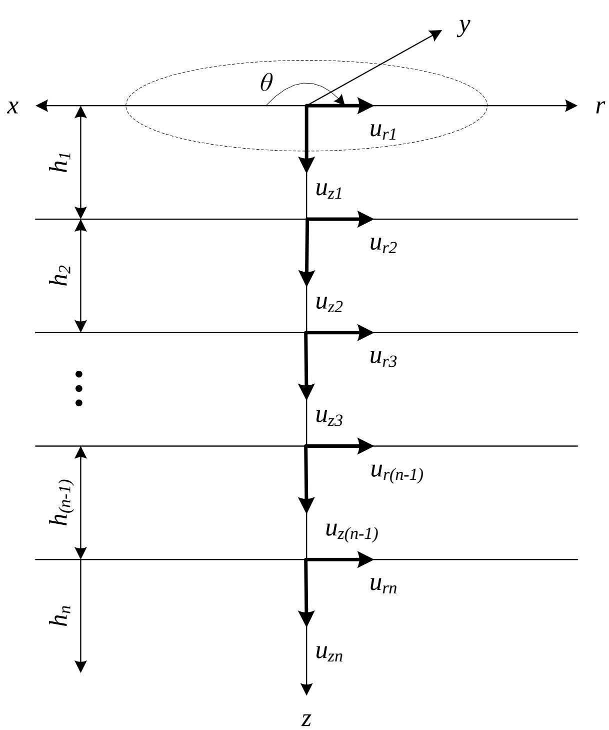

Figure 3.1 Coordinate System for Axisymmetric Layers on a Halfspace (Zaabar et al., 2014)

3.1 Moving load simulation

Viscowave II - M uses a normalized unit impulse load as function of time, as shown in Figure 3.2.

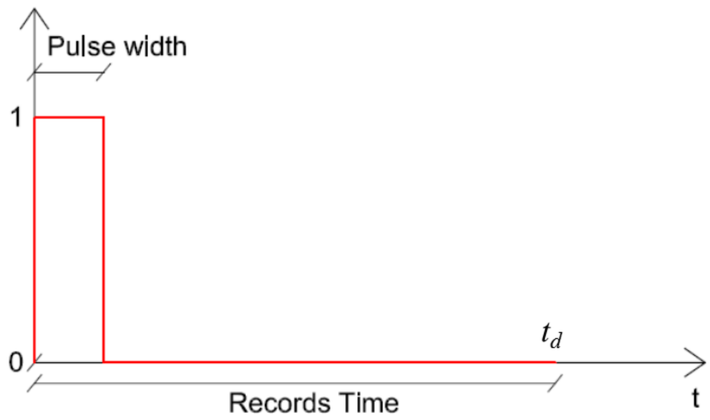

Figure 3.2 Loading function

The pulse width is the time interval Δt used in the analysis, and it has to be small enough to be comparable to a true impulse.

As described above, the loading function is a unit impulse load distributed over a circular area. As such, the vertical displacement, U_z, obtained using ViscoWave II - M represents the unit impulse response of the layered system in time domain. The primary advantage of the time-domain unit impulse response is that the system response to any arbitrary loading can be obtained through the convolution integral. Theoretically, this convolution integral for a continuous function is given as:

$$y_z(t) = U_z(t) * T(t) = \int_0^t U_z(t-\tau) * T(\tau) \tag{3.1}$$

where $T(t)$ is the loading function and $y_z(t)$ is the corresponding vertical displacement.

For a discrete signal,

$$y_z(t_n) = \sum_{i=1}^{n} U_{zi}(t_n - i\Delta t) T(i\Delta t)\Delta t \tag{3.2}$$

where Δt is time interval of the discrete signal, and $t_n = n\Delta t$ for an integer n.

For the calculation of the moving load solution, $T(t)$ is a series of unit impulses at each evaluation point as shown in Figure 3.3 and U_{zi} is the stationary pavement response at evaluation point i. The distance between two consecutive evaluation points, Δx, is imposed to be

$$\Delta x = pulse\ width \cdot v \tag{3.3}$$

where

$pulse\ width = \Delta t$

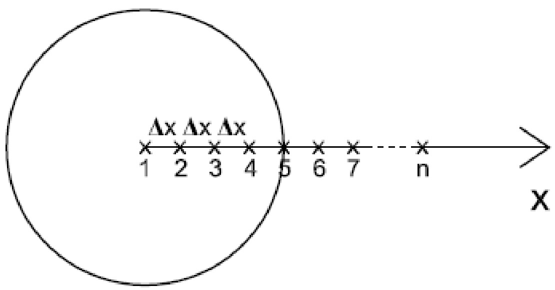

Figure 3.3 Loading area and evaluation point locations

By doing so, the pulse width is the time it takes the moving load to move from one evaluation point to the next one. The accuracy of the results (discussed in section 3.2) depends on the number of evaluation points: The higher the number, the more accurate the numerical method will be. Good accuracy is achieved by having a small pulse width and considering evaluation points up to a distance from the stationary load where the pavement response is almost null.

As shown in Figure 3.2, a quiet zone where the function assumes a value of zero is added, so that the total duration of the loading function (t_d) is significantly longer than the pulse width. The duration t_d has to be long enough to allow the pavement response to return to zero (for a viscoelastic material it takes some time for the deformation caused by a constant step stress to return to zero, as shown in Figure 3.4. A short duration t_d would also lead to a reduced accuracy of the numerical methods used in ViscoWave II - M to perform the inverse Laplace and Hankel transform (*Zaabar et al., 2014*), and a less accurate pavement response with "noise" problems.

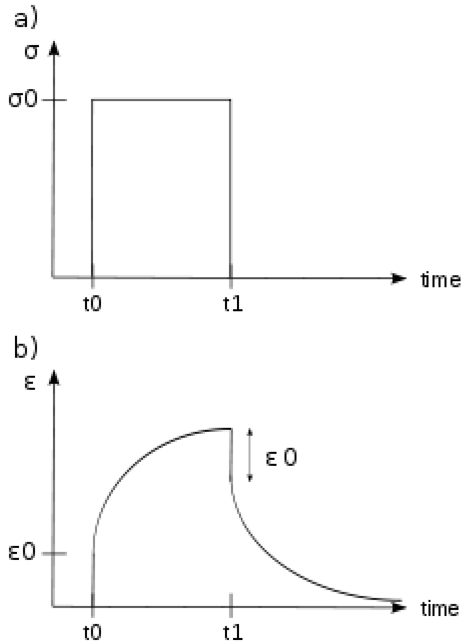

Figure 3.4 Viscoelastic material response to constant step stress (Lakes et al., 2009).

Based on the above formulation, in order to calculate the response to a moving load, first the stationary responses to the load of Figure 3.2 are calculated for each of the *n* evaluation points. Each stationary response is a vector of dimension *m*, which is equals to $t_d/\Delta t$. The vectors are indicated as y_{z_n} in Figure 3.5. The moving load is then calculated by summing up all the evaluation points responses to the stationary load shifted by the time it would take the load to move over consecutive points. This corresponds to the pulse width, or one element of the vectors (Figure 3.6). The moving load is a vector of dimension m+(2n-1). The number of evaluation points, the duration of the pulse width, and the total duration t_d play a major role in the accuracy of the moving load solution.

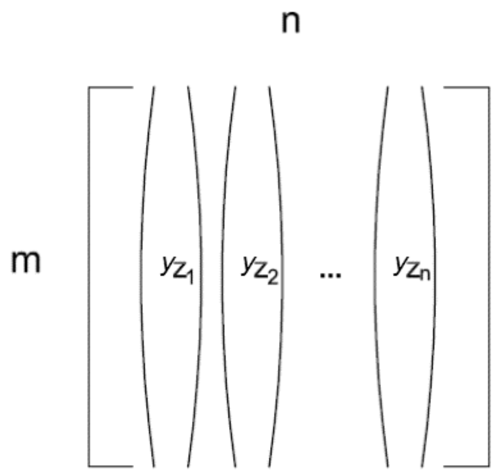

Figure 3.5 Matrix of the stationary responses

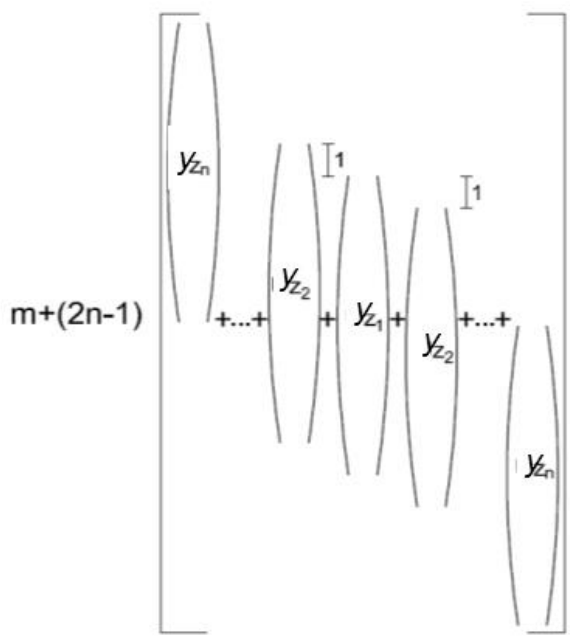

Figure 3.6 Response to moving load vector

3.2 Accuracy of the moving load solution

A sensitivity analysis has been conducted to establish the values of pulse width, duration and the distance of farthest evaluation point from the center of the stationary load to be used in ViscoWave

II - M. Using too small of a pulse width, an excessively long duration, or an unnecessarily large number of evaluation points would reduce the efficiency of the program by increasing the computational time. Figure 3.7 to Figure 3.9 show the sensitivity analysis conducted to observe the effect of these variables on the maximum deflection. Figure 3.7 shows that, for the solution to be stable, the pulse width should be smaller than 0.4 ms. Figure 3.8 shows that the response should be included in the simulations for evaluation points up to a distance of 100 times the loading radius. Figure 3.9 shows that, for the solution to be stable, the duration should be higher than 60 ms. In Figure 3.10 the results for the same simulation conducted using ViscoWave II - M and ViscoRoute (*Chabot, 2010*) are compared.

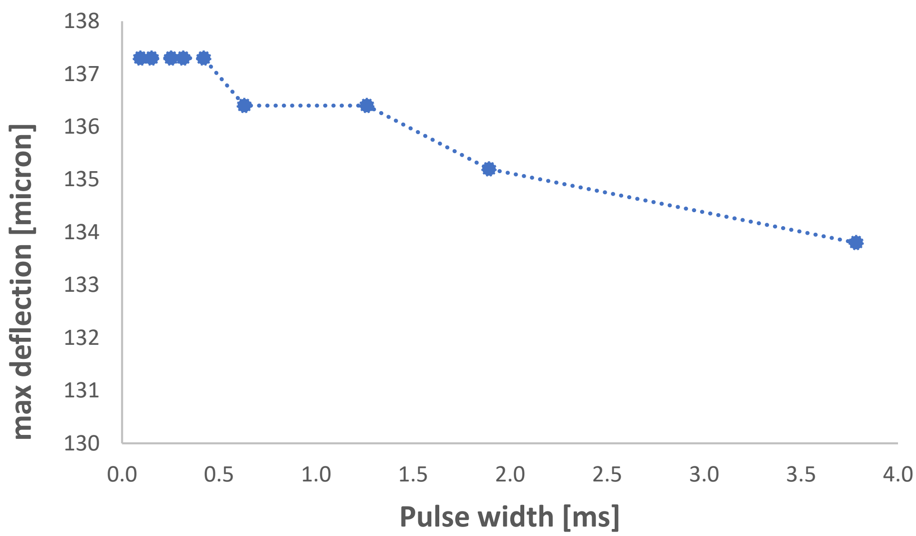

Figure 3.7 Dependency of peak deflection on pulse width

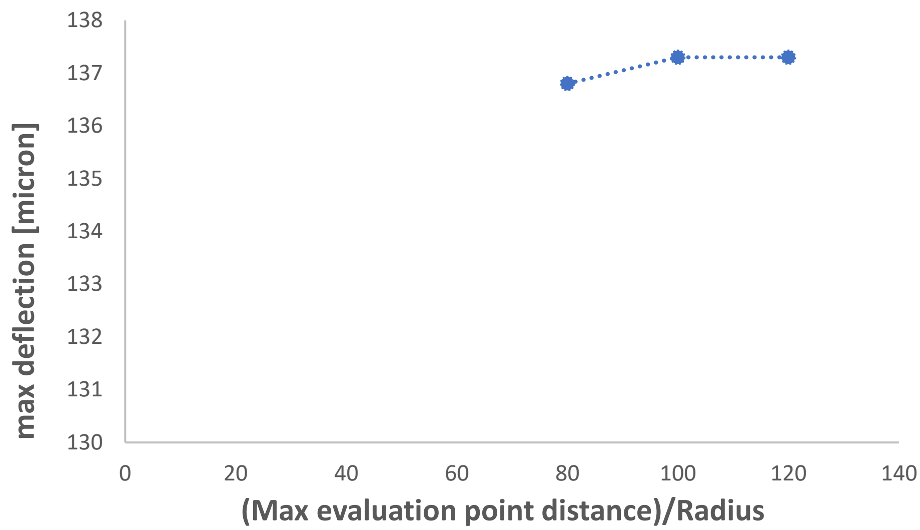

Figure 3.8 Dependency of peak deflection on the maximum distance from the load

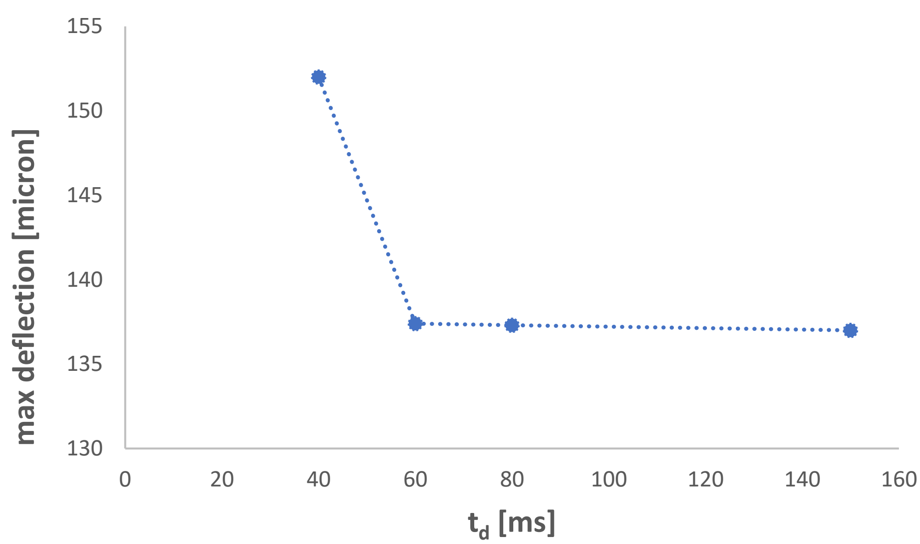

Figure 3.9 Dependency of peak deflection on load duration

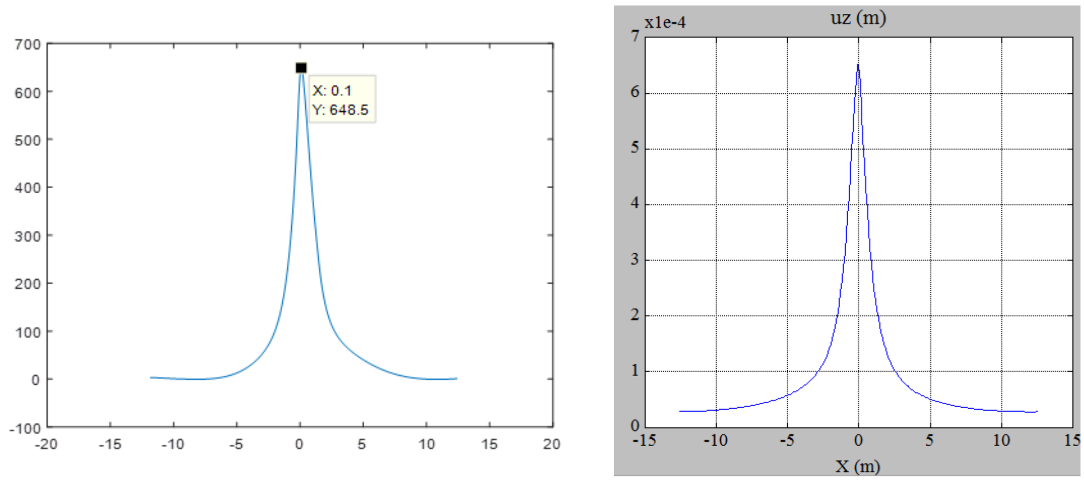

(a)ViscoWave II-M ***(b) ViscoRoute***

Figure 3.10 Comparison of Results using (a) ViscoWave II - M and (b) ViscoRoute

3.3 Calculation of the energy dissipation due to the structural rolling resistance

The pavement response to a moving load is used to calculate the energy dissipated by a vehicle due to the structural rolling resistance. Figure 3.11 shows the vertical deflection of the pavement, where the zero X coordinate corresponds to the middle of the tire imprint. Because of the viscoelasticity of the asphalt layer, the maximum deflection is delayed and located behind the tire midpoint. The slope seen by the moving wheel is indicated with the red line; the deflection under the rear of the tire (right point) is higher than the deflection under the front of the tire, which means that the wheel 'sees' an uphill slope. For an asphalt pavement the slope does not change throughout the travel.

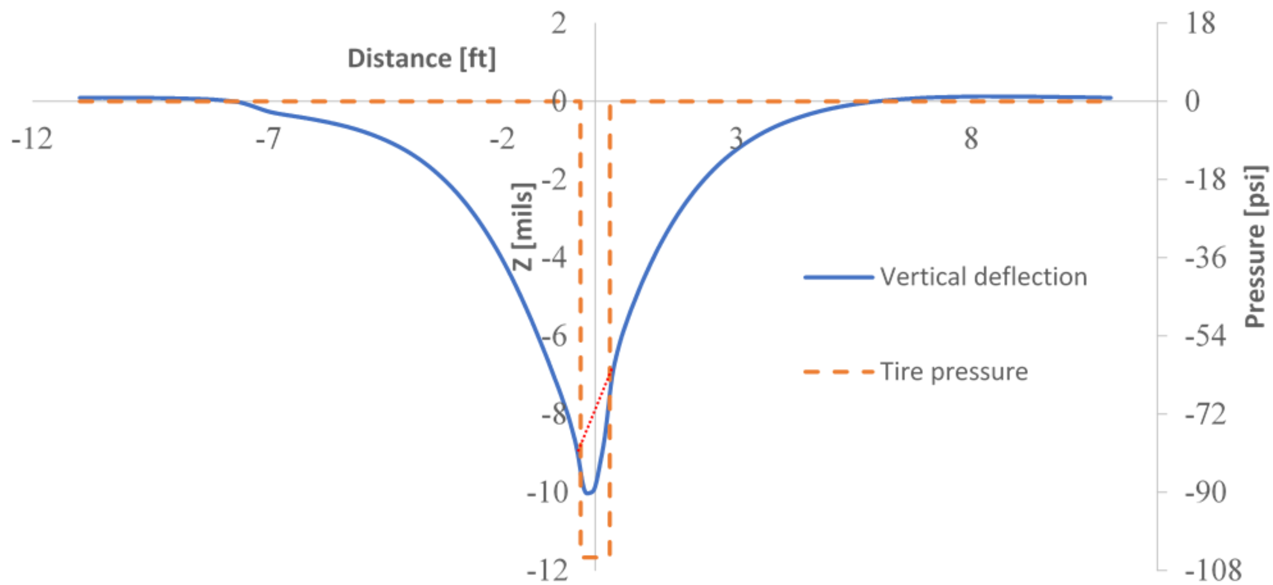

Figure 3.11 Deflection and slope as seen by the moving vehicle (traveling from left to right)

It has been shown by (*Chupin et al. 2013*) that, assuming non-dissipative vehicle tires, the power dissipation of a wheel due to the SRR can be evaluated as

$$P_{RR}^{str} = \int_A p \frac{dw(x,y,z,t)}{dt} dA \quad (3.4)$$

where

p is the pressure applied on the pavement,

A is the area of the tire print,

$w(x,y,z,t)$ is the deflection of the pavement.

The energy dissipation associated with the SRR, for a vehicle moving at constant speed is

$$W_{diss} = \sum_{i=1}^{n} p_i \int_{S_i} \frac{dw(x,y,z,t)}{dx} dS \quad (3.4b)$$

where *n* is the number of wheels.

Equation (3.3) can be simplified into

$$W_{diss} = \sum_{i=1}^{m} p_i A_i \frac{\Delta w_i}{\Delta x_i} \quad (3.4c)$$

where

p_i is the pressure of each vehicle tire,

A_i is the surface area of each vehicle tire,

$\Delta w_i / x_i$ is the moving slope as seen by each vehicle tire.

3.4 Equivalent damping coefficient in the Laplace domain

A damped elastic behavior is assumed for all the other pavement layers, except for the asphalt layer, which is modeled as a viscoelastic material (with the relaxation modulus as input). The addition of damping provides a more realistic characterization of the layers, which are not purely elastic, and is also advantageous from a mathematical point of view, giving more stability to the domain’s transformations of the spectral element method used by ViscoWave II-M. In this section an investigation is conducted to see how a Laplace domain solution can address material damping in the elastic layers. First the complex stiffness method, proposed by Lysmer and Richarts (*1966*) is shown, then a similar procedure, valid for the Laplace domain, is developed.

3.4.1 Complex Stiffness Method

A simple damped oscillator can be used as the one dimensional model to represent a load applied on a footing foundation resting on a halfspace representing the soil system (Figure 3.12). The foundation is characterized by a mass m, and the soil system is represented by a damping coefficient *c* and stiffness k. The equation of motion for a simple damped oscillator can be written as

$$m\ddot{x} + c\dot{x} + kx = P(t) \tag{3.5}$$

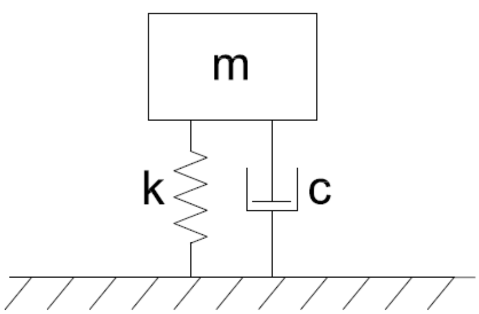

Figure 3.12 Simple damped oscillator

Lysmer (*1966*) proposed a convenient way to simplify the modeling of soil in regards to dynamics by introducing the concept of complex stiffness. A simple harmonic oscillator (Figure 3.13) can be used to model soil by assuming that the stiffness coefficient k* is a complex number (complex stiffness). The equation of motion for a simple harmonic oscillator can be written as

$$m\ddot{x} + k * x = P(t) \tag{3.6}$$

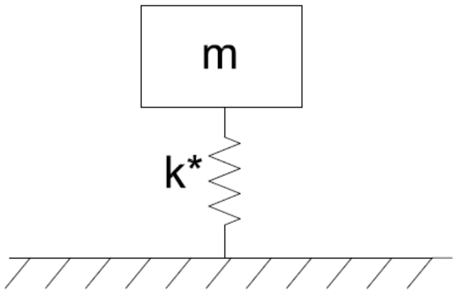

Figure 3.13 Simple harmonic oscillator

Imposing that equations (3.5) and (3.6) give the same solution to a harmonic load in the time domain leads to

$$k^* = k\left(1 - 2\beta^2 + 2i\beta\sqrt{1-\beta^2}\right) \tag{3.7}$$

which, for values of $\beta < 0.1$, reduces to

$$k^* = k\left(1 + 2i\beta\right) \tag{3.8}$$

where

$$\beta = \frac{c}{2\sqrt{k \cdot m}} \tag{3.9}$$

3.4.2 Complex Stiffness Method in the Laplace domain

The algorithm of ViscoWave II – M transforms the variables in the Laplace domain and then uses a numerical procedure to calculate the inverse Laplace transform. In order to have the same time domain solution for equations (3.5) and (3.6), the equality of the solution in the Laplace domain can be imposed. Equation (3.6) can be rewritten as

$$\ddot{x} + \omega_0^2 x = \frac{1}{m} P(t) \tag{3.10}$$

where

$$\omega_0^2 = \frac{k*}{m}.$$

Applying the Laplace transform of eq. (3.10) leads to

$$s^2\tilde{x}(s) - s \cdot x_0 - \dot{x}_0 + \omega_0^2\tilde{x}(s) = \mathcal{L}\left\{\frac{1}{m}P(t)\right\} \tag{3.11}$$

$$\tilde{x}(s) = \frac{\mathcal{L}\left\{\frac{1}{m}P(t)\right\} + s \cdot x_0 + \dot{x}_0}{s^2 + \omega_0^2} \tag{3.12}$$

Equation (3.5) can be rewritten as

$$\ddot{x} + 2\beta\omega_1\dot{x} + \omega_1^2 x = \frac{1}{m}P(t) \tag{3.13}$$

where

$$\omega_1^2 = \frac{k}{m}, \quad \beta = \frac{c}{2\sqrt{k \cdot m}}.$$

Applying the Laplace transform of eq. (3.10) leads to

$$s^2\tilde{x}(s) - s \cdot x_0 - \dot{x}_0 + 2\beta\omega_1(s \cdot \tilde{x}(s) - x_0) + \omega_1^2\tilde{x}(s) = \mathcal{L}\left\{\frac{1}{m}P(t)\right\} \tag{3.14}$$

$$\tilde{x}(s) = \frac{\mathcal{L}\left\{\frac{1}{m}P(t)\right\} + s \cdot x_0 + x_0 + 2\beta\omega_1 x_0}{s^2 + 2\beta\omega_1 s + \omega_1^2} \tag{3.15}$$

Since $x_0 = 0$ is a boundary condition for ViscoWave, the numerators of (3.12) and (3.15) are equal, and imposing the equality of those two equations results in

$$2\beta\omega_1 s + \omega_1^2 = \omega_0^2 \tag{3.16}$$

which can be simplified to

$$k* = k\left(\xi s + 1\right) \tag{3.17}$$

where

$$\xi = \frac{c}{k}.$$

It is worth conducting a simple dimensional analysis on ξ:

The primary dimension of the damping coefficient c is $\left[\frac{Force}{Length^3} \cdot time\right]$.

The primary dimension of the stiffness coefficient k is $\left[\frac{Force}{Length^3}\right]$, so the dimension of ξ is [*time*].

$(\xi s + 1)$ is therefore dimensionless.

ξ Can be expressed as a function of the damping coefficient β,

$$\xi = \frac{c}{k} = 2\beta\sqrt{\frac{m}{k}} = \frac{2\beta}{\omega_1} = \frac{\beta}{\pi f_n} \tag{3.18}$$

where f_n is the natural frequency of the soil system of the corresponding mode number n, which depends not only on the characteristics of the materials but also on the site disposition. It can be calculated as (*Kramer*, *1996*):

$$f_n = \frac{(2n-1) \cdot \bar{v}_s}{4 \cdot H} \tag{3.19}$$

where

n is the mode number,

H is the depth of the soil column to bedrock

v_s is the average shear wave velocity on the site, which can be calculated as

$$\bar{v}_s = \frac{H}{\sum_{i=1}^{n} \frac{h_i}{\bar{v}_{s_i}}} \tag{3.20}$$

where n is the sublayer number over the bedrock, and $H = \sum_{i=1}^{n} h_i$.

One way to obtain the shear wave velocity for a single layer is to use a relation from the results of a standard penetration test, as shown for example in Wair et al. (*2012*).

Alternatively, v_s can be calculated as a function of the elastic shear modulus of the soil material, G, and its density, ρ:

$$\overline{v}_s = \sqrt{\frac{G}{\rho}} \tag{3.21}$$

A simple analysis has been conducted to determine a realistic range of values for ξ. According to Wair, the shear wave velocity for soils ranges between 100 and 400 m/s. Figure 3.14 shows how the natural frequency of the site, assumed for simplicity to be one layer, depends on the shear wave velocity and on the depth to the stiff layer (H). The natural frequency of the site is less than 50 Hz for bedrock depth more than two meters.

Figure 3.15 shows the dependency of ξ on the natural frequency of the site for different values of the material damping; ξ is proportional to β and reduces at higher frequencies (lower bedrock depth). An important consideration has to be made at this point: The mechanical characteristics of all the asphalt pavement sections described in chapter 5 were backcalculated assuming a value of $\xi = 0.001$; prior to the backcalculation the elastic shear moduli of the layers were not known, therefore the value of ξ had to be estimated. The backcalculation procedure is used to find the mechanical characteristics of the layers that provide the best fit between the simulations conducted using ViscoWave II-M and the results of field tests under a Falling Weight Deflectometer, which applies a haversine pulse with a duration of about 30ms. The optimal procedure, since ξ cannot be known before the backcalculation would be to compare the estimated value of ξ used for the backcalculation (0.001) with the actual value calculated using equation (3.18), and iteratively repeat the backcalculation process if the percentage difference between the two values is not within a certain threshold. The backcalculation is computationally expensive and time consuming. An iteration of this type is not recommended; as long as the same algorithm is used for the forward analysis (ViscoWave II-M), the fitting procedure ensures that there is no error associated with ξ. However, such statement may not hold true if the backcalculation results are from a different program, for which case it would be worth checking if the iteration process would lead to significant differences in the mechanical properties of the layers.

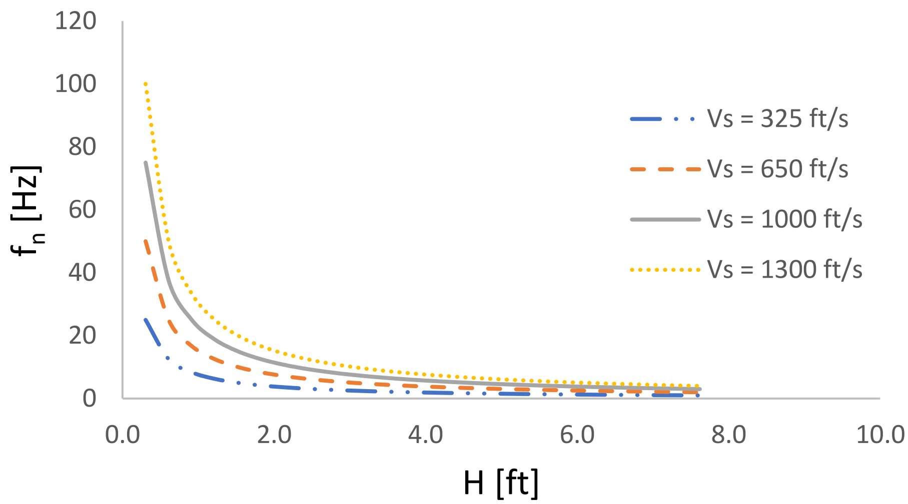

Figure 3.14 Natural frequency of the site as function of the bedrock depth for different materials

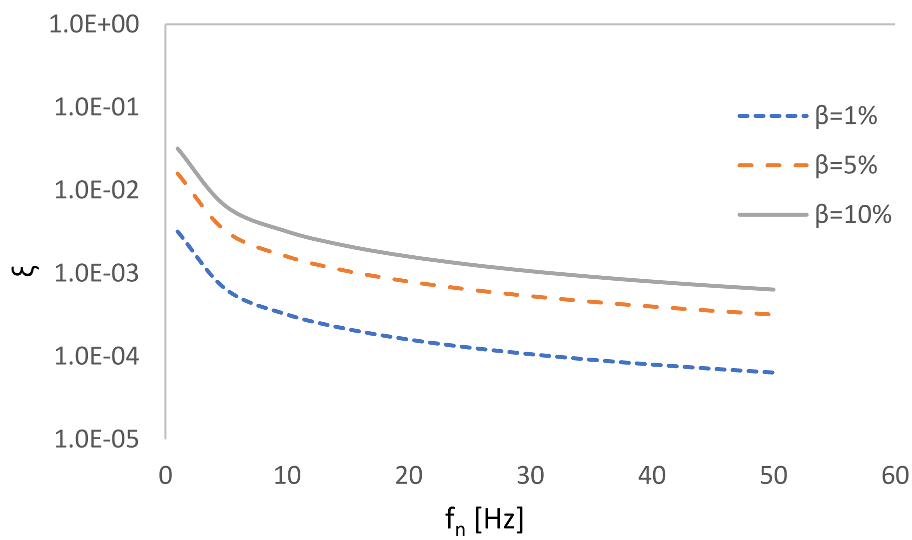

Figure 3.15 Relation between ξ and f_n for different values of the material damping β

3.4.3 Effect of the damping coefficient on the results

Simulations were conducted in order to check the effect of ξ on the pavement response to a moving load. Figure 3.16 through Figure 3.21 show the comparison between the results for the value of the maximum deflection obtained using different dynamic viscoelstic computer programs: ViscoWave II – M, ViscoRoute (*Chabot, 2010*) and 3D-Move (*Nasimifar et al., 2016*).

The pavement section chosen for the simulations is described in Table 3.1. It has a hot mix asphalt (HMA) layer with the same characteristics as the one described by Bazi et al. (*2018*). The linear viscoelastic top layer is characterized by a Prony Series, whose coefficients are reported in Table 3.1. The storage and loss moduli can be calculated using the following equations:

$$E'(w) = E_0 + \sum_{i=1}^{m} E_i \cdot \frac{w^2 \cdot \tau_i^2}{1 + w^2 \cdot \tau_i^2} \tag{3.22}$$

$$E''(w) = \sum_{i=1}^{m} E_i \cdot \frac{w \cdot \tau_i}{1 + w^2 \cdot \tau_i^2} \tag{3.23}$$

Table 3.1 Pavement layers and characteristics

	Thickness	**Elastic modulus**
HMA layer	6 - 10 in	linear viscoelastic
Aggregate base	8 in	E = 30 ksi
Subgrade layer	≈ 80 ft to bedrock	E = 7.5 - 22.5 ksi

Table 3.2 Prony Series Coefficients (Source: Bazi et al., 2018)

i	τ_i	E_i (ksi)	
		68°F	**104°F**
1	0.00000001	131.6113	385.7155
2	0.0000001	96.8276	243.4379
3	0.000001	215.453	489.8896
4	0.00001	319.2816	545.6854
5	0.0001	462.9048	533.5133
6	0.001	558.0011	356.5063
7	0.01	527.0915	170.2489
8	0.1	354.8553	62.72937
9	1	166.9948	22.43296
10	10	61.92215	8.372989
11	100	21.94464	3.573217
12	1,000	8.288531	1.638641
13	10,000	3.507939	0.823457
14	100,000	1.625574	0.42556
15	1,000,000	0.81159	0.229011
16	10,000,000	0.422106	0.124004
17	100,000,000	0.226327	0.068259
18	1,000,000,000	0.119861	0.036619
19	10,000,000,000	0.153706	0.047301
20	100,000,000,000	0.000164	0.000259
Sum E_i		**2,932**	**2,825**
Long term equilibrium modulus E_0		**5**	**5**
Instantaneous modulus		**2,937** (2,932 + 5)	**2,830** (2,825 + 5)

Two different values of ξ are used: 0.001, which is the value used for the backcalculation procedure used to obtain the characteristics of the sections reported in chapter 5, and 0.008, which is approximately the value calculated using equation (3.18) for the pavement described in Table 3.1. (It has been assumed the same for all the cases). The cases simulated are described in Table 3.3.

Table 3.3 Pavement characteristics for the simulation cases

	HMA Layer thickness [in]	[°F]	Subgrade elastic modulus [ksi]
Case 1	6	68	7.5
Case 2	6	68	22.5
Case 3	6	104	7.5
Case 4	6	104	22.5
Case 5	10	68	7.5
Case 6	10	68	22.5

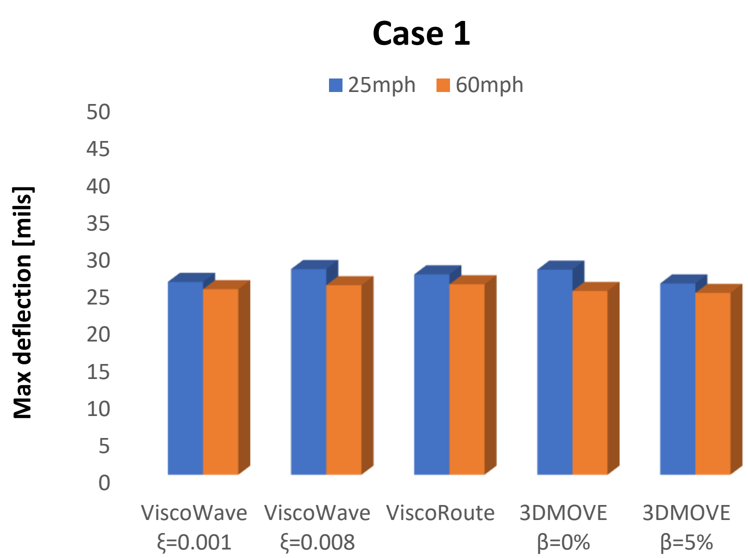

Figure 3.16 Comparison of maximum deflection results from different programs for case 1

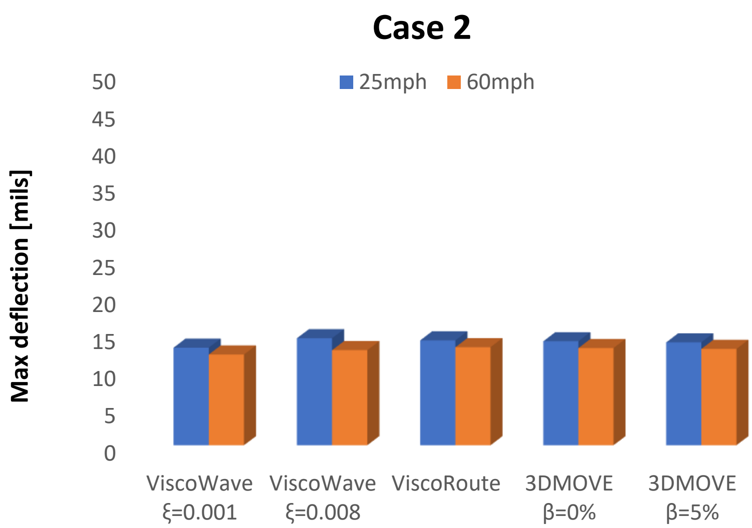

Figure 3.17 Comparison of maximum deflection results from different programs for case 2

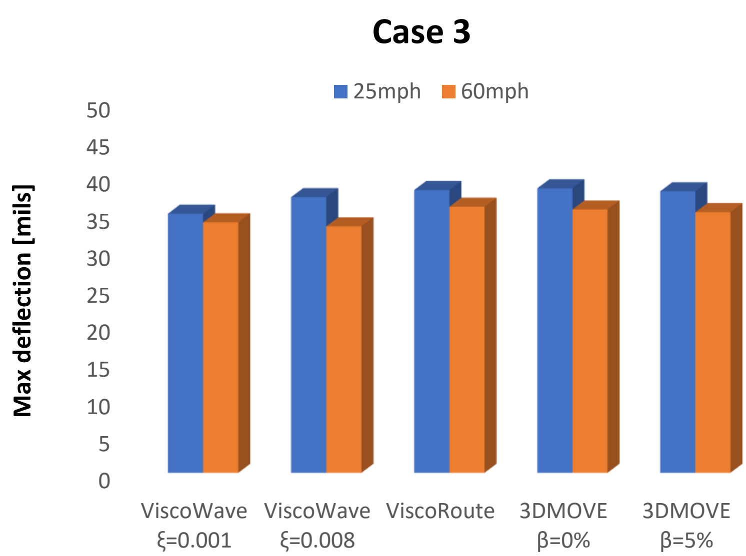

Figure 3.18 Comparison of maximum deflection results from different programs for case 3

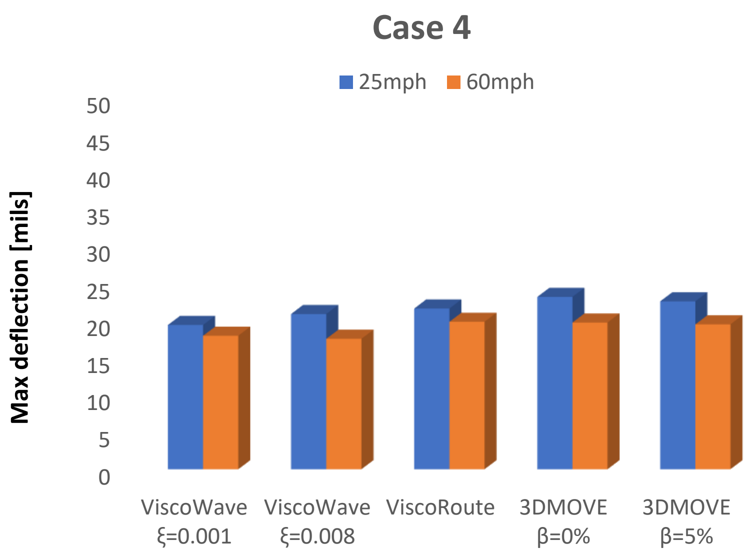

Figure 3.19 Comparison of maximum deflection results from different programs for case 4

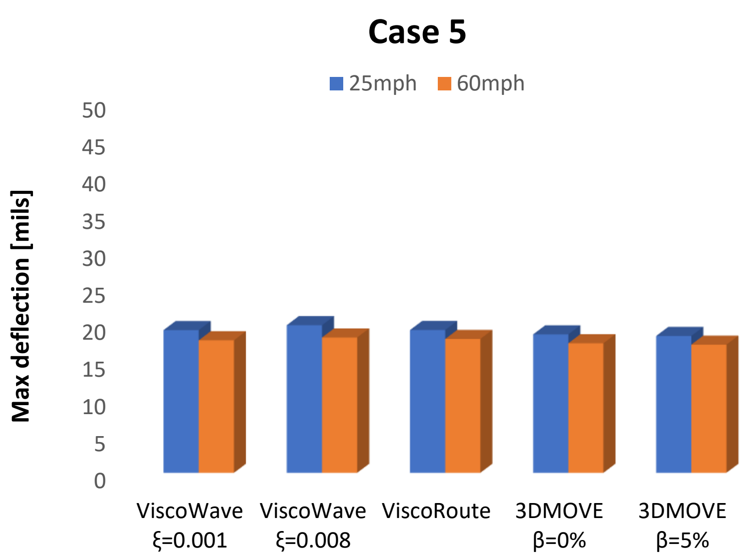

Figure 3.20 Comparison of maximum deflection results from different programs for case 5

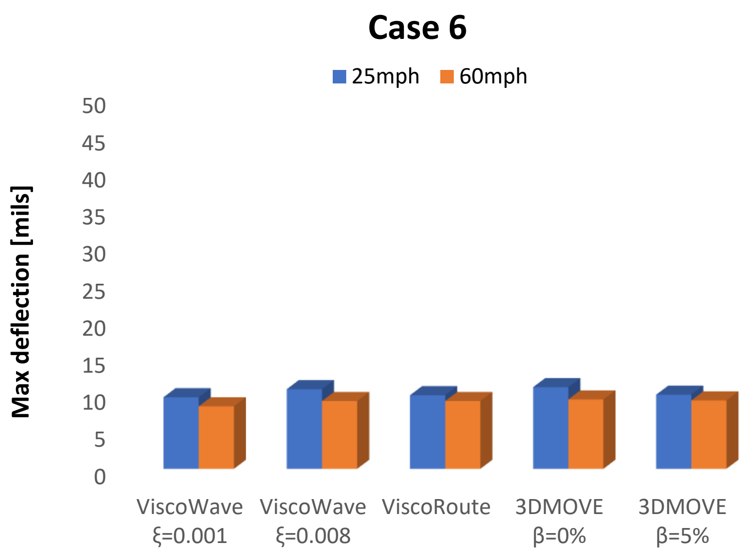

Figure 3.21 Comparison of maximum deflection results from different programs for case 6

The results show that while the choice of the values of ξ used in ViscoWave II – M can lead to differences in terms of maximum deflection, these are in the same range as the differences of the results obtained using different programs (e.g., ViscoRoute and 3D-Move). Nonetheless, these should not be overlooked. However, for this study it is more important to use the same value of ξ for the forward modeling as the one used in the backcalculation process, to ensure consistency of the results.

4 CONCRETE PAVEMENT MODELING

The calculation of the pavement response is performed using the 2D finite element software DYNASLAB *(Chatti, 1992, Chatti et al., 1994)*. The program is computationally efficient and can divide the pavement into slabs (standard dimensions are 15 x 12 ft^2) connected by joints with specific load transfer efficiency (LTE). The structural model for the concrete slab and load transfer mechanisms used in DYNASLAB is a modification of the model used in ILLISLAB *(Tabatabaie and Barenberg, 1978)*. The concrete slab is modeled by rectangular medium-thick plate elements. Each node contains three degrees of freedom: a vertical translation in the z-direction and two rotations about the x and y axes, respectively. In the original version of DYNASLAB, load transfer across joints is modeled either by a vertical spring element (to represent aggregate interlock), or by a bar element (to represent dowel bars). The subgrade is modeled by a damped Winkler foundation with constant or frequency-dependent springs (k) and dashpots (c), uniformly distributed underneath the slabs (Figure 4.1), representing the modulus of subgrade reaction and the damping coefficient of the subgrade. load $P(t)$ moves at a constant speed v. A limitation of DYNASLAB is that the model cannot consider the effects of temperature or moisture, which means that it is not able to address curling and warping in slabs. The pavement is assumed to be in ideal conditions: No distresses are present. The contribution of faulting to the rolling resistance should be included in the framework of the roughness contribution to rolling resistance and therefore excluded from the structural rolling resistance. Instead, cracking might affect the SRR; for example, the effect of a full depth transversal crack on pavement deflection is similar to the effect of a joint. An analysis of the effect of pavement distresses on the SRR is included in the recommendations for future studies in chapter 9.

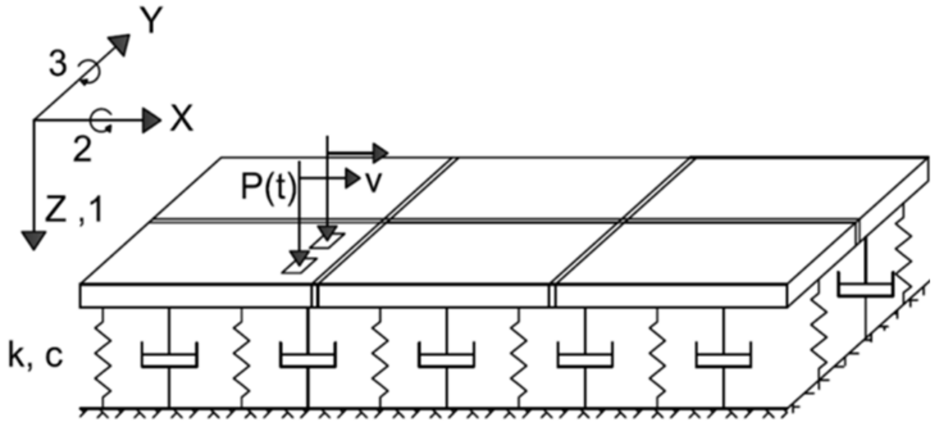

Figure 4.1 DYNASLAB Pavement model (Chatti et al., 1994)

4.1 Effects of the joints on pavement deflection

In jointed concrete pavements, joints transfer the bending and shear stresses between the slabs. The LTE is defined as

$$LTE(\%) = \frac{\Delta_{i+1}}{\Delta_i} \cdot 100 \tag{4.1}$$

where

Δ_i is the deflection on the edge of the loaded slab,

Δ_{i+1} is the deflection on the edge of the adjacent slab.

In the current version of DYNASLAB, the aggregate interlock of the joints is modeled by a spring and dashpot in parallel. A sensitivity analysis has been conducted to establish the relationship between the spring and dashpot coefficients K_{AGG}, C_{AGG} and LTE. FWD tests have been simulated in DYNASLAB using different values of K_{AGG} and C_{AGG}, and the LTE associated with each of those values were calculated. The sensitivity analysis showed that LTE is highly sensitive to the stiffness but not sensitive to the damping coefficient (Figure 4.2).

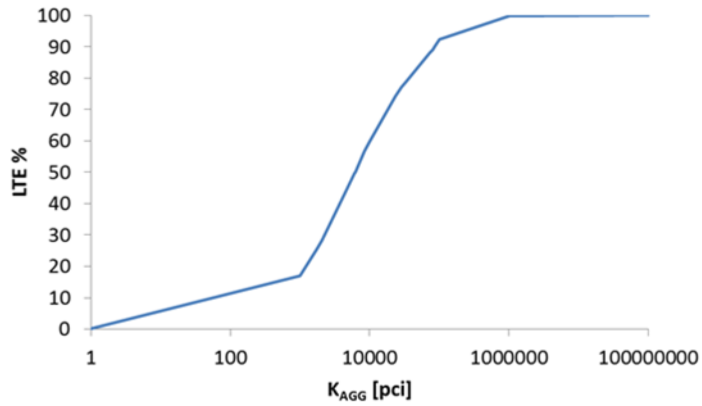

Figure 4.2 Relation between LTE and joint aggregate interlock stiffness

Unlike for asphalt pavements, a concrete pavement cannot be considered as an infinite medium in the longitudinal direction. Joints have a significant impact on the pavement response, and even more on the energy dissipation, since, even when the deflection is continuous along the pavement (LTE=100%), relative rotation between two consecutive slabs is allowed. Therefore, at any different position of the load on the slab, its rotation would change, thus affecting the deflection basin. From the point of view of a wheel moving along an infinite slab, the deflection basin would be the same for the entire duration of travel; the maximum deflection would be constant and located behind the load by a small distance. Instead, considering a slab of finite length, the deflection basin would depend on the position on the slab; the maximum deflection and its position would be different at any point. Figure 4.3 shows the deflection of both a jointed and an infinite PCC pavement under the front wheels of a 33.4 kip tandem axle of a truck. From the point of view of the wheel, the deflection increases as it gets closer to the joints (x=0 in, x=180 in).

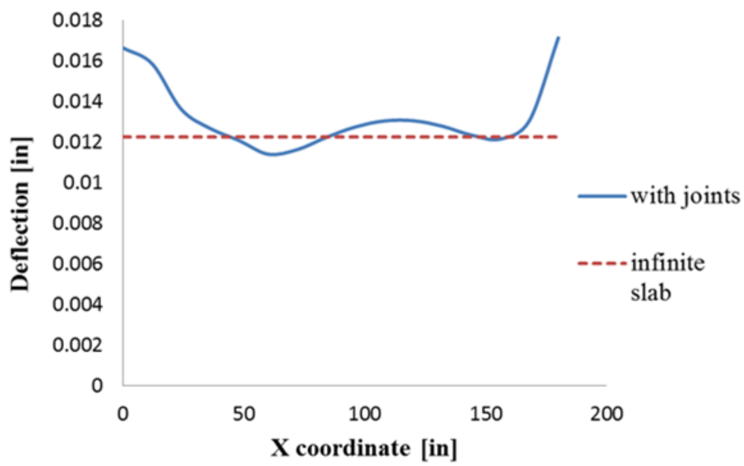

__Figure 4.3 Effects of the joints on the value of the deflection under the tire__

4.2 Calculation of the energy dissipation due to the structural rolling resistance

Similar to asphalt pavements, the energy dissipation associated with the structural rolling resistance can be calculated as

$$W_{diss} = \sum_{i=1}^{n} p_i S_i \left\langle \frac{dw(x,t)}{dx} \right\rangle \tag{4.2}$$

where $\left\langle \frac{dw(x,t)}{dx} \right\rangle$ is the average slope along the loading area.

The difference with asphalt pavements lies in the fact that for jointed plain concrete pavements (JPCP), the deflection basin depends on the position on the slab; at any different instant of time, the average slope under the tire would change. On the other hand, continuously reinforced concrete pavements (CRCP) can be modeled as an infinite slab, and similarly to asphalt pavements, the slope seen by the tires is constant throughout the travel. In Figure 4.4(a) the slope as seen by the front wheels of a trailed tandem axle moving at 62 mph (100 km/h) is shown. The slope has a peak at x=12 in, i.e. after the entire tire print is on the slab, then decreases as the axle gets farther from the joint. At x=60 in, the rear axle of the tandem reaches the joint. Figure 4.4(b) shows that the slope as seen by the rear axle is negative for most of the time. That is because the maximum deflection of the slab is generally located between the two axles. There is no gain of energy, since the effects of the two axles cannot be decoupled, but there is a reduction in the energy dissipated. To take into account the dependency of the slope on time and the position on the slab, the slab (of length L) is divided into m intervals of length $\Delta x = L/m$. The energy dissipated during the travel along the entire slab is calculated as

$$W_{RR} = \sum_{i=1}^{n} p_i S_i \sum_{j=1}^{m} \left\langle \frac{dw(x_j, t_j)}{dx} \right\rangle \cdot \Delta x \tag{4.3}$$

The total energy dissipated by the vehicle per mile can be calculated as

$$W_{diss}[MJ/\text{mile}] = W_{RR} \cdot \frac{63360}{L} \tag{4.4}$$

where L is the length of the slab measured in inches.

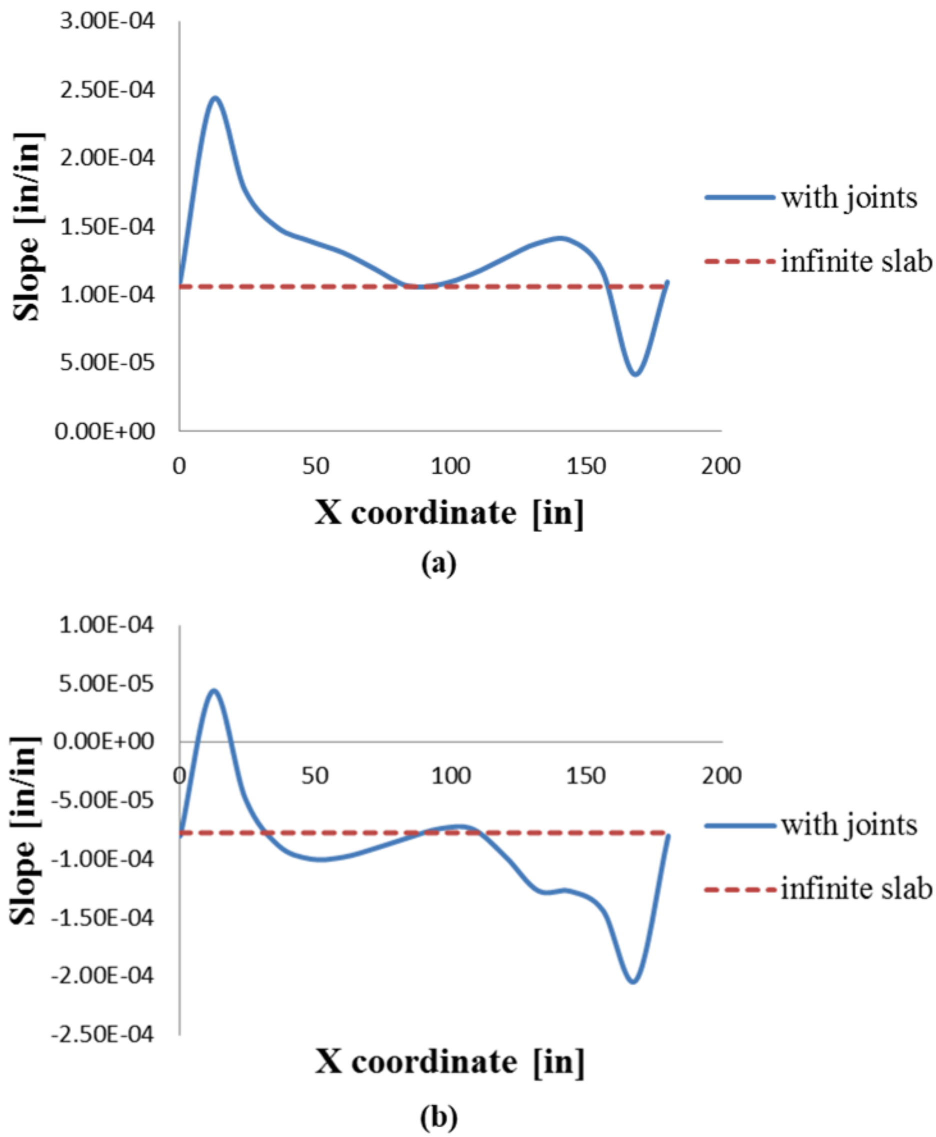

Figure 4.4 Slope as seen by (a) the front wheels of a trailed tandem axle and (b) the rear wheels of the trailed tandem axle of a loaded truck at 62 mph

4.3 Effects of shoulder and adjacent slabs

This section describes the investigation conducted on the effect of the shoulder and adjacent lane on concrete pavement response and structural rolling resistance. When modeling concrete pavements it is necessary to effectively represent the boundary conditions by including not only the slab on which the load is moving, but also the adjacent ones in the simulations. Unlike asphalt pavements, the PCC pavement cannot be considered as a semi-infinite medium. Joints have a significant impact on the response of the pavement and have to be accurately represented both transversally and longitudinally.

In the simulations described in chapter 5 the pavement sections were modeled as shown in Figure 4.5 (left), where no shoulder or adjacent lanes were included, since the pavements considered have asphalt shoulders, which are not bonded to the lanes, and do not have tie bars. However, that is not generally the case. Therefore, this study investigated how the presence of a shoulder, an adjacent lane connected by tie bars, or both can affect the results.

The energy dissipated due to the structural rolling resistance has been calculated for different vehicle positions, values of longitudinal load tranfer efficiency, shoulder/adjacent slab dimension and elastic modulus, and compared to the values calculated for the case without shoulder/adjacent lane.

4.3.1 Effects of shoulder and adjacent slabs on pavement deflection

First the effect of the shoulder on the pavement deflection is analyzed for the four cases shown in Figure 4.5 through Figure 4.8. The analyses are conducted by simulating a tandem axle of a truck weighing 33,382 lb and moving along a continously reinforced concrete pavement. The position of the wheels is indicated below the figures; the load transfer efficiency (LTE) between the main slab and the shoulder is 100% in this case, and all the slabs have the same stiffness, E_{pcc}=5.85 10^6 psi (40,200 MPa). The Winkler foundation parameters are k = 135 pci (36.6 N/cm^3), c = 0.962 pci*s (0.027 N s/cm^3). The pavement is a continuously reinforced concrete section, simulated by a 120 feet long slab. The vehicle is moving at 62 mph (100 km/h).

The proximity of the wheels to the edge of the slab determines how much the pavement response is affected by the adjacent slab/shoulder. Figure 4.5 through Figure 4.7 show how much the deflection of the points located under the wheel path (dashed line) on a CRCP changes when including in the simulation the adjacent lane and the pavement shoulder.

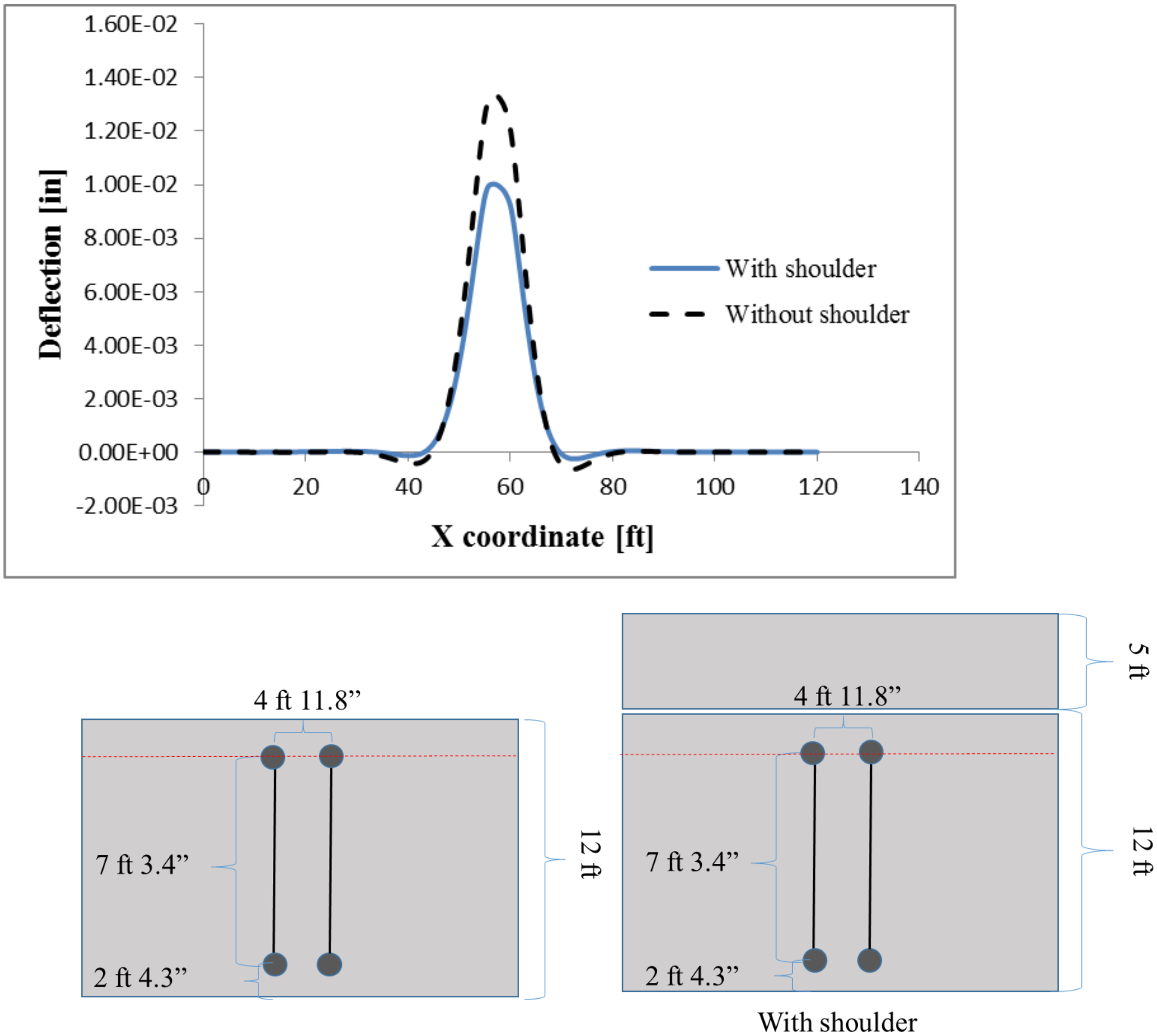

Figure 4.5 Comparison of the offset shoulder deflection (points along the marked wheel path) with and without shoulder

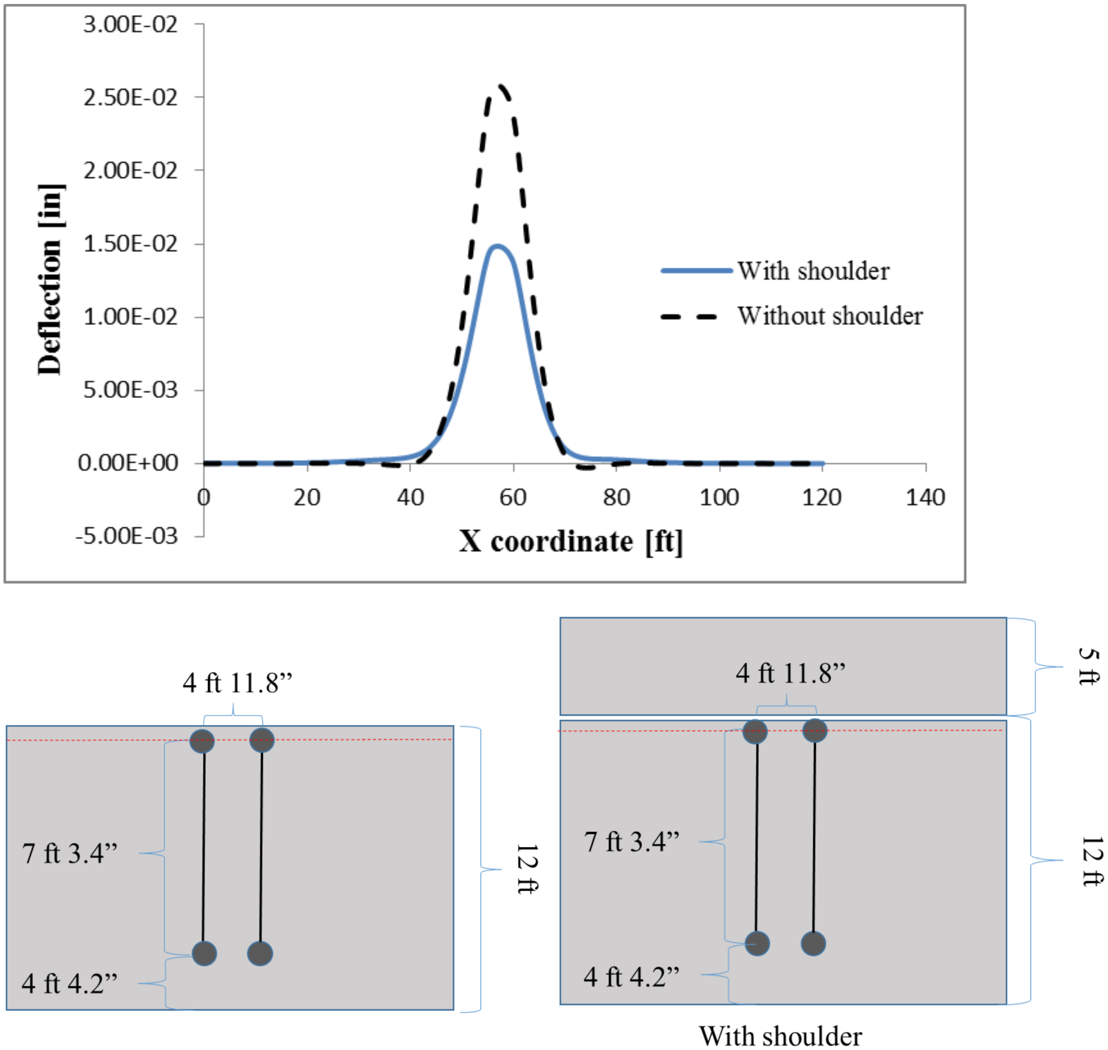

Figure 4.6 Comparison of the edge deflection (points along the marked wheel path) with and without shoulder

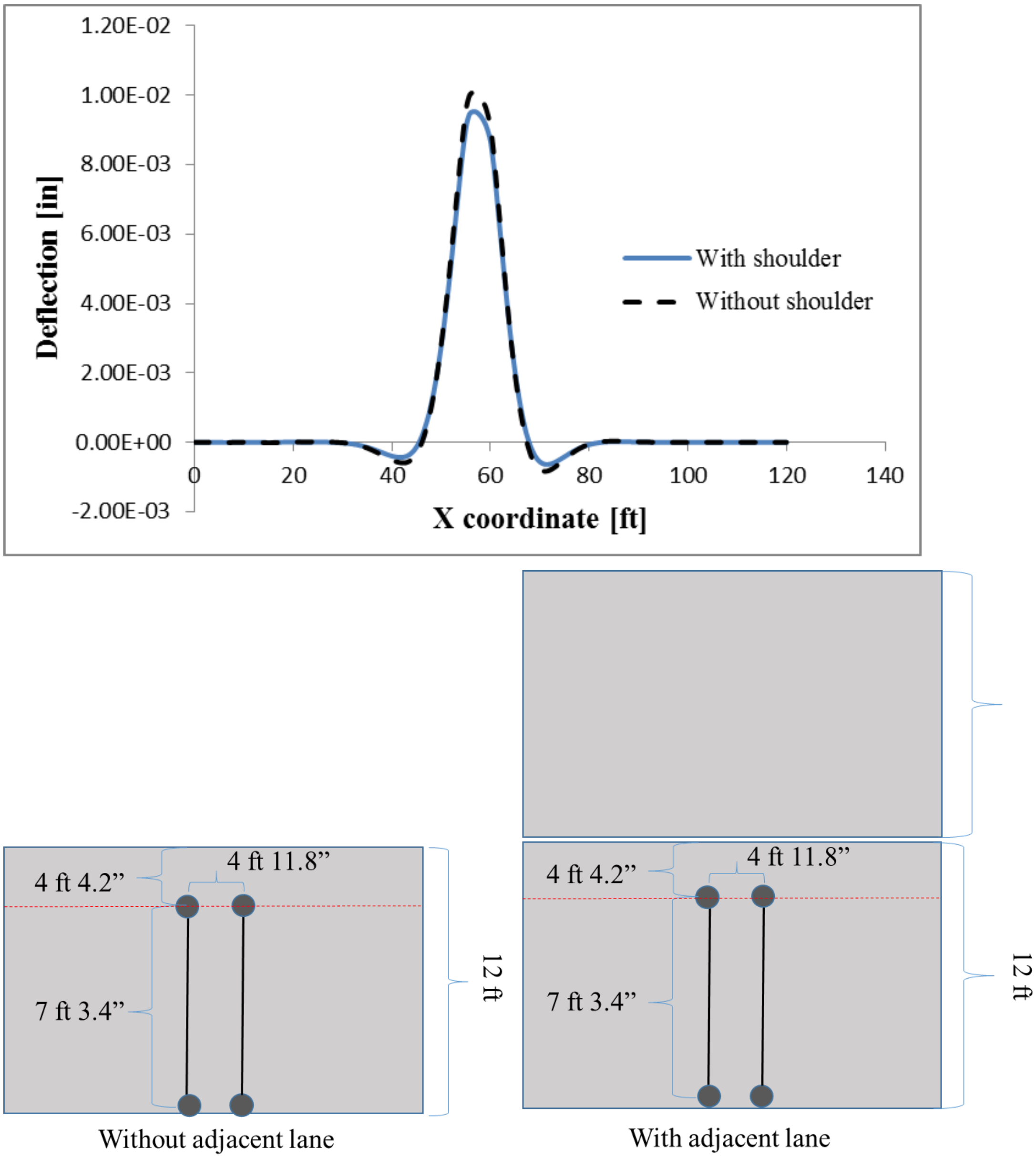

Figure 4.7 Comparison of the offset lane deflection (points along the marked wheel path) with and without adjacent lane

DYNASLAB can only simulate two slabs in the transversal direction, which means that the shoulder and the adjacent lane cannot be included in the same simulation. However, the effect of the shoulder on the wheels that are far away from it is very small, as shown in Figure 4.8, which is the case where such effect is maximum. In light of this, in order to account for both the shoulder and the adjacent lane, it is acceptable to obtain the energy dissipated by the wheels from two different simulations; the first being done considering the shoulder and calculating the energy dissipated by two wheels near it, and the second being done considering the adjacent lane and calculating the energy dissipated by two wheels near it. Then the energy dissipated by the vehicle is obtained by summing up the two results.

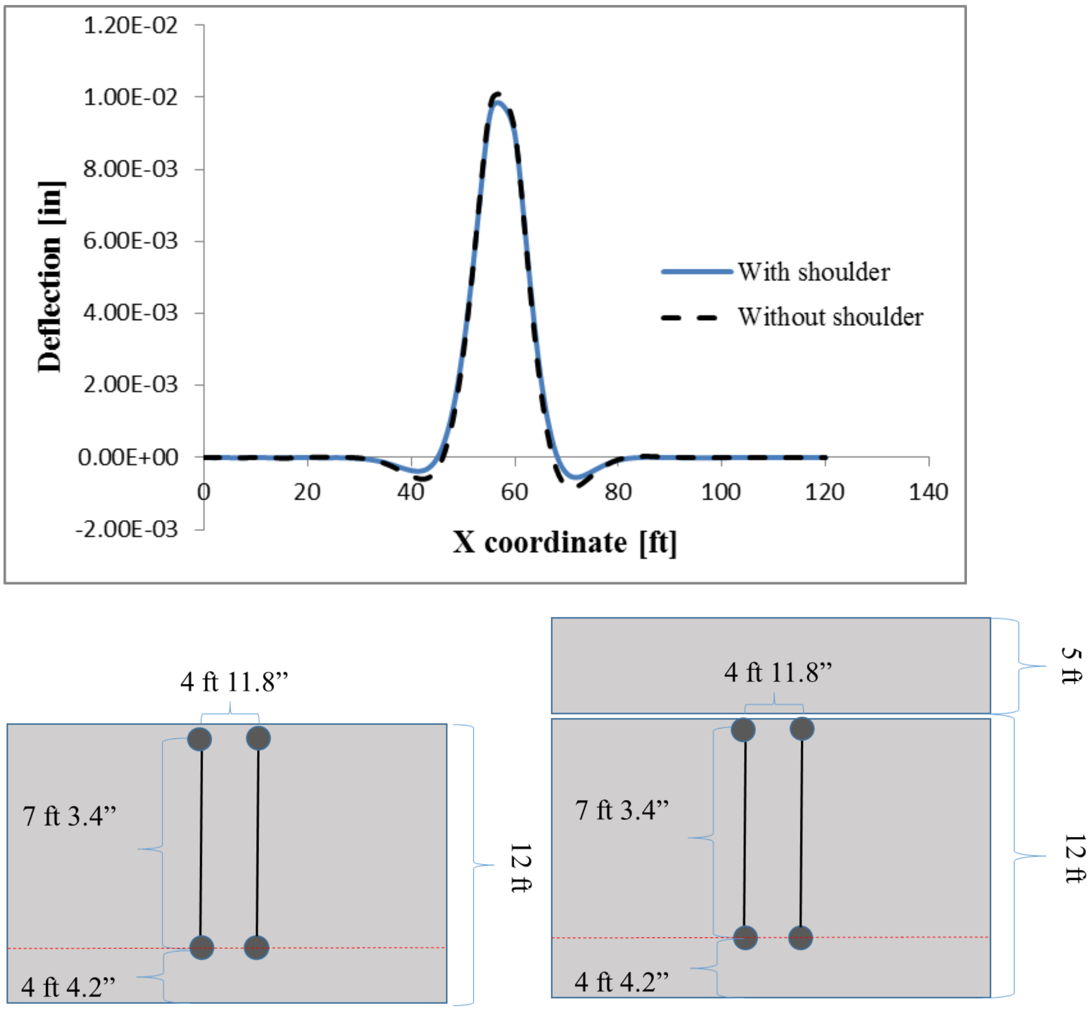

Figure 4.8 Comparison of the far deflection (points along the marked wheel path) with and without adjacent shoulder

4.3.2 Effects of shoulder and adjacent slabs on energy dissipation associated with the structural rolling resistance

A sensitivity analysis has been conducted to quantify the reduction of the calculated energy dissipation (W_{diss}), varying the shoulder/adjacent lane characteristics. Figure 4.9 through Figure 4.11 show the effect of shoulder/lane width, elastic modulus and load transfer efficiency (LTE) of the longitudinal joint, respectively. W_{diss} has been calculated using the method described in section 4.2. The normalized energy dissipation is calculated as the energy dissipated in each case divided by the energy dissipated in the case without shoulder/adjacent lane. Offset shoulder refers to Figure 4.5; edge refers to Figure 4.6 and offset lane refers to Figure 4.7.

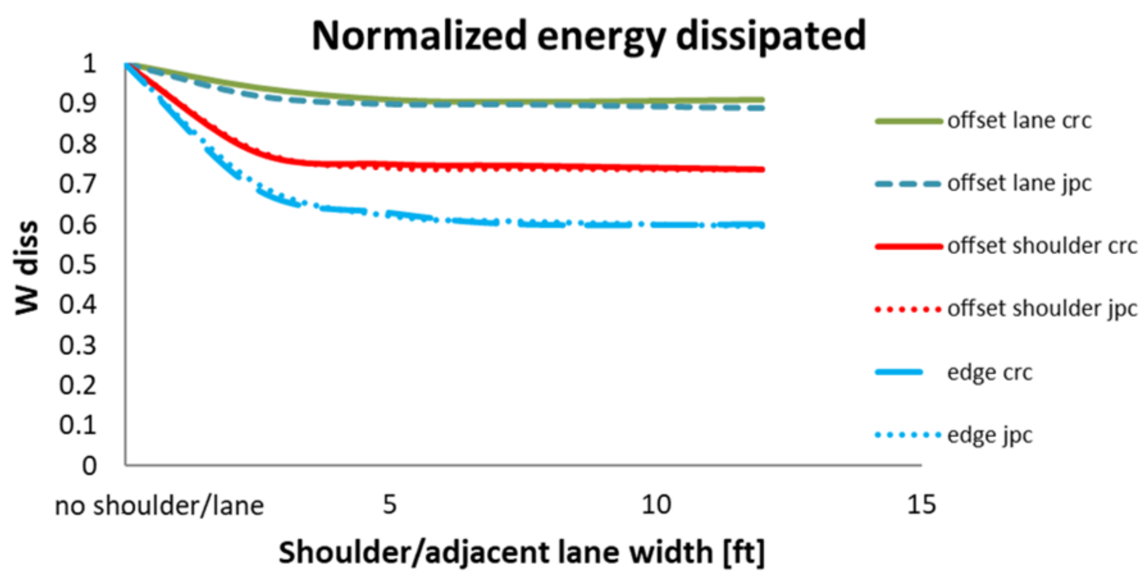

Figure 4.9 Normalized energy dissipated versus shoulder width for different vehicle positions. The graph has been obtained using LTE=50% and E_{pcc}=5.85 10^6 psi (40,200 MPa)

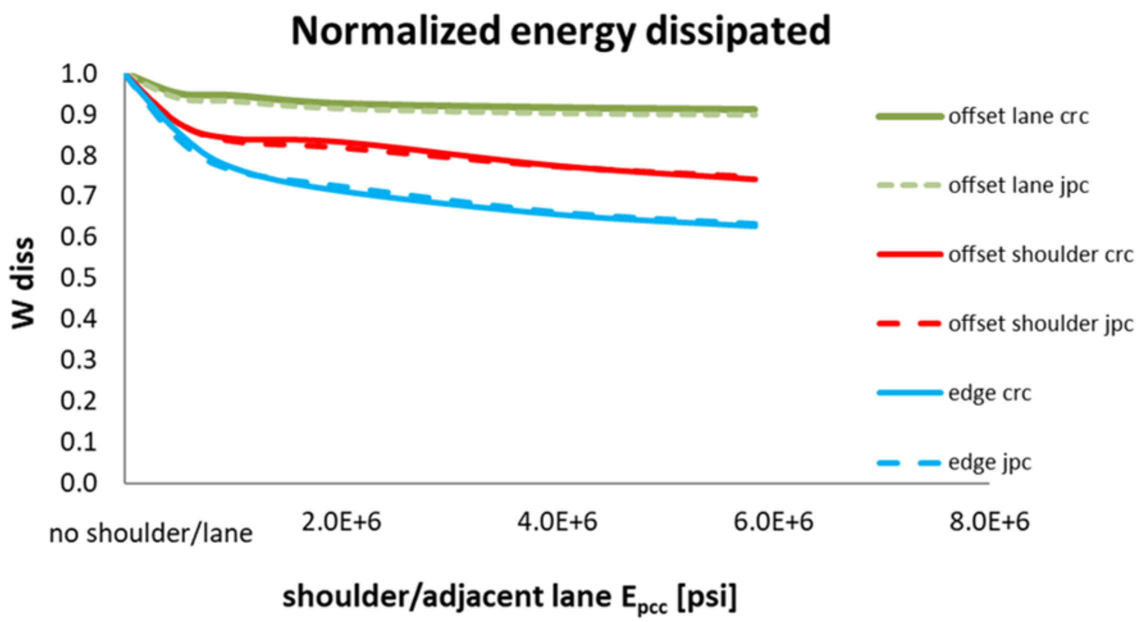

Figure 4.10 Normalized energy dissipated versus modulus of the concrete shoulder/adjacent lane for different vehicle positions. The graph has been obtained using LTE=50% and the slab dimensions respectively indicated in figures 4.5 - 4.7

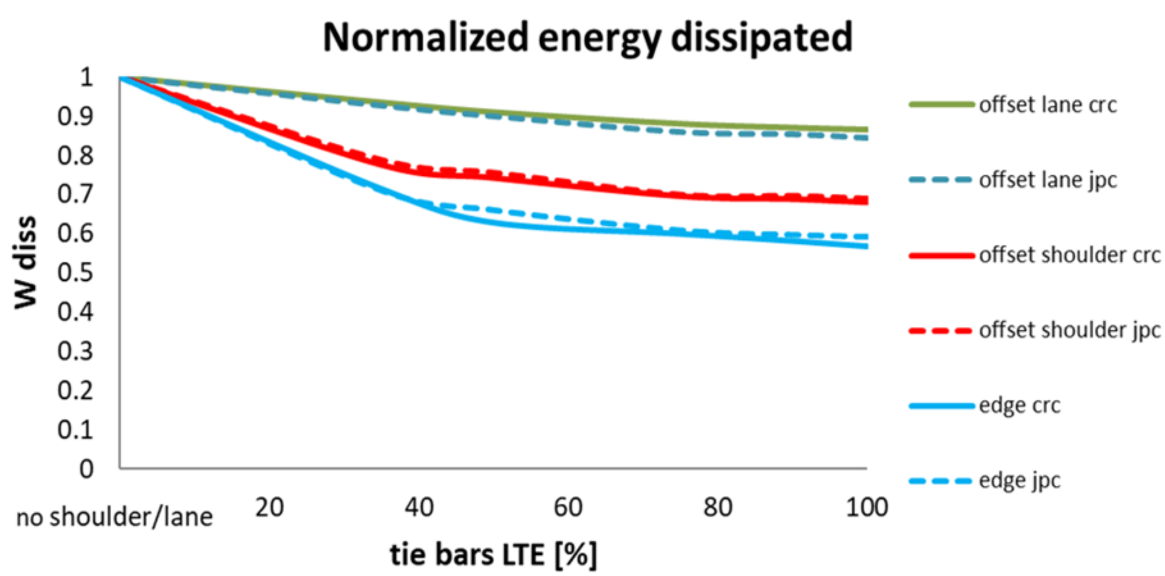

Figure 4.11 Normalized energy dissipated versus longitudinal joint load transfer efficiency of the concrete shoulder/adjacent lane for different vehicle positions. The graph has been obtained using E_{pcc}=5.85 10^6 psi (40,200 MPa) and the slab dimensions respectively indicated in figures 4.5 - 4.7

The case of a widened lane has also been analyzed. The positions of the wheels considered are shown in Figure 4.12 and the results are presented in Table 4.1. The widened lane reduces the energy dissipation of approximately 15% mainly because the wheels are located farther from the longitudinal joints.

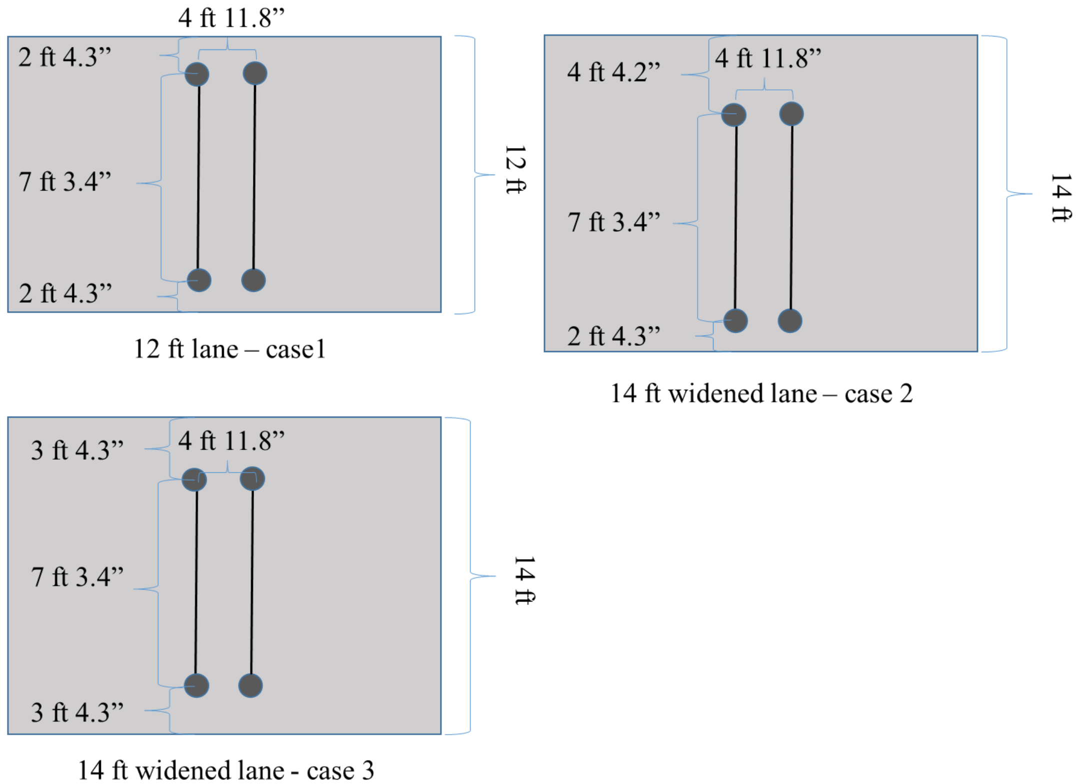

Figure 4.12 Cases of study for the widened lane

Table 4.1 Reduction of energy dissipation with a widened lane

Case considered	**W_{diss} [MJ]**	**Decrease of W_{diss} [%]**
12 feet lane (case 1)	2.06E-03	0.0
Widened lane (case 2)	1.76E-03	14.6
Widened lane (case 3)	1.75E-03	15.4

5 CALTRANS CASE STUDY

The models described in chapters 3 and 4 are purely mechanistic, and, to guarantee that the calculation of the energy dissipated, and therefore fuel consumption, due to the structural rolling resistance is realistic, their results should be compared with results obtained from field measurements. The California Department of Transportation, in collaboration with the University of California Pavement Research Center (UCPRC) at UC Davis, has conducted a series of field tests aimed at observing the effect of the structural rolling resistance on vehicle fuel economy. The field results will be compared with the results from the simulations conducted using ViscoWave II and DYNASLAB to check the quality of the models. In this chapter the results from the mechanistic models simulating the same loading conditions and pavement sections as the California field test are presented and discussed.

5.1 Backcalculation of the mechanical characteristics of the asphalt pavement sections

The mechanical characteristics of the pavement sections were backcalculated from Falling Weight Deflectometer (FWD) tests. For each pavement, three FWD tests were conducted using three load levels – 5, 8 and 12 kips – on multiple stations. The mechanical properties were backcalculated for those stations where both FWD and GPR test information were available.

DYNABACK-VE was used to backcalculate pavement layer properties with field data. DYNABACK-VE uses a time domain viscoelastic dynamic solution (ViscoWave II) as a forward routine and a genetic algorithm for backcalculation analysis (*Zaabar et al., 2014*). The genetic algorithm search method has a high potential for converging efficiently to a global solution. The advantage of this solution is that it can analyze the response of pavement systems in the time domain and can therefore accommodate time-dependent layer properties and incorporate wave propagation.

The GA is an evolutionary optimization method. In general terms, the GA performs the following operations: (a) initialization, (b) selection, (c) generation of offspring, and (d) termination. In initialization, the GA generates a pool of solutions by using a subset of the feasible search space, the so-called population. Each solution is a vector of feasible variable values. In the selection process, each solution is evaluated with an objective function, and the best-fitted solutions are selected. The selected solutions are then used to generate the next-generation population (offspring). This process involves two operators: crossover and mutation. In crossover, a new solution is formed through exchange of information between two parent solutions, which is done by swapping a portion of parent vectors. In mutation, a new solution is formed by randomly changing a portion of the parent solution vector. The newly generated population is evaluated with the objective function. This process is repeated until a termination criterion is reached. Through guided random search from one generation to another, the GA minimizes the desired objective function. The key advantage of GAs and direct search methods is that they can find a global optimum.

The backcalculation algorithm was used to backcalculate six unknowns for the master curve: four $E(t)$ master curve sigmoidal coefficients and two time–temperature shift factors; the resilient moduli for the unbound base or subbase and subgrade materials and the elastic modulus of the stiff layer and the depth to stiff layer, if present. Equation 5.1 gives the formulation of the optimization problem. The bound constraints were applied to the sum of c_1 and c_2 coefficients of the master curve. The $E(t)$ curves obtained through consideration of the upper and lower limits of the parameters individually represent curves well beyond the actual database domain. Therefore, putting a limit on the sum of the first two sigmoid coefficients (c_1 and c_2) instead of constraining the two coefficients will reduce the search domain.

The objective function is

$$Er = \sum_{k=1}^{m} 100 \sum_{i,o=1}^{n} \frac{\left| d^{k}{}_{i} - d^{k}{}_{0} \right|}{\left\{ d^{k} \right\}} \tag{5.1}$$

and the bound constraints are

$$\begin{cases} c_1^l \le c_1 \le c_1^u \\ C^l \le C = c_1 + c_2 \le C^u \\ c_3^l \le c_3 \le c_3^u \\ c_4^l \le c_4 \le c_4^u \end{cases} \quad \begin{cases} a_1^l \le a_1 \le a_1^u \\ a_2^l \le a_2 \le a_2^u \end{cases} \quad E_i^l \le E_i \le E_i^u$$

where

m is the number of sensors,

d_{ki} is the input deflection information obtained from field at sensor k,

d_{ko} is the output deflection information obtained from forward analysis at sensor k,

n is the total number of deflection data points recorded by a sensor,

c_i are the sigmoid coefficients,

E_i are the Elastic modulus of the i-layer,

a_i are the shift factor polynomial coefficients,

l, u are the lower and upper limits.

In order to have a wider range of temperature, and thus a more precise backcalculation of the mastercurve, the backcalculation itself was performed for each station by combining the data of the summer and the winter testing. Each layer was divided into smaller sublayers where the temperature was assumed to be constant. Figure 5.1 shows the good match between the FWD measurements and the simulations using the backcalculated parameters for PH09, station 37.

The values of the mechanical properties calculated for the different stations were averaged and fitted to a sigmoidal function to get the mechanical properties of the sections (Figure 5.2). Since the differences between stations were small there was no need to divide into subsections.

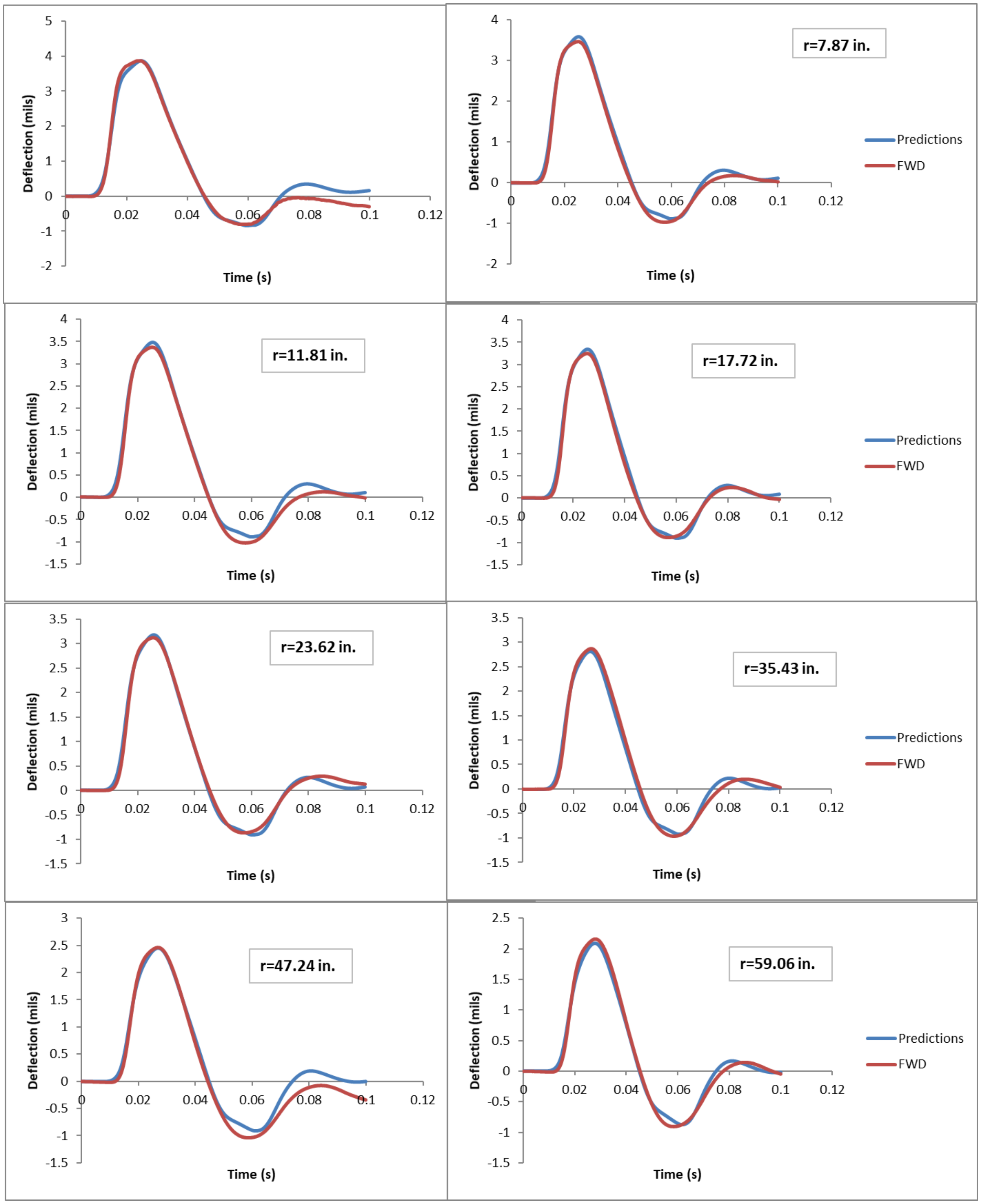

Figure 5.1 Predicted versus measured time histories by sensor, PH09, station 37

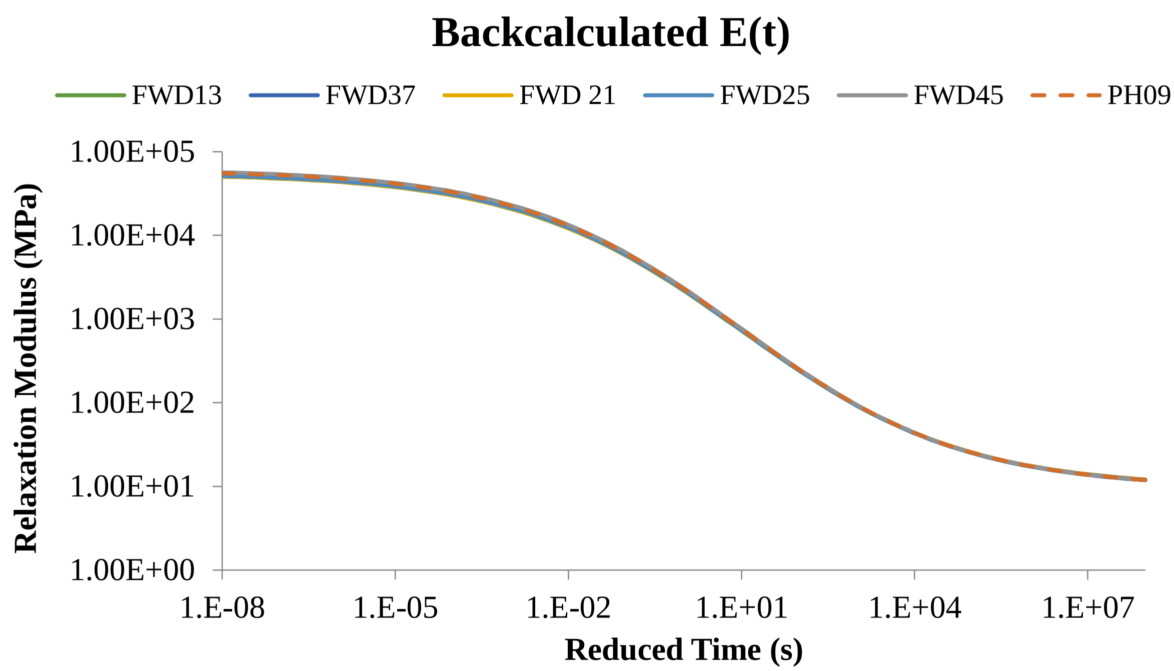

(a)

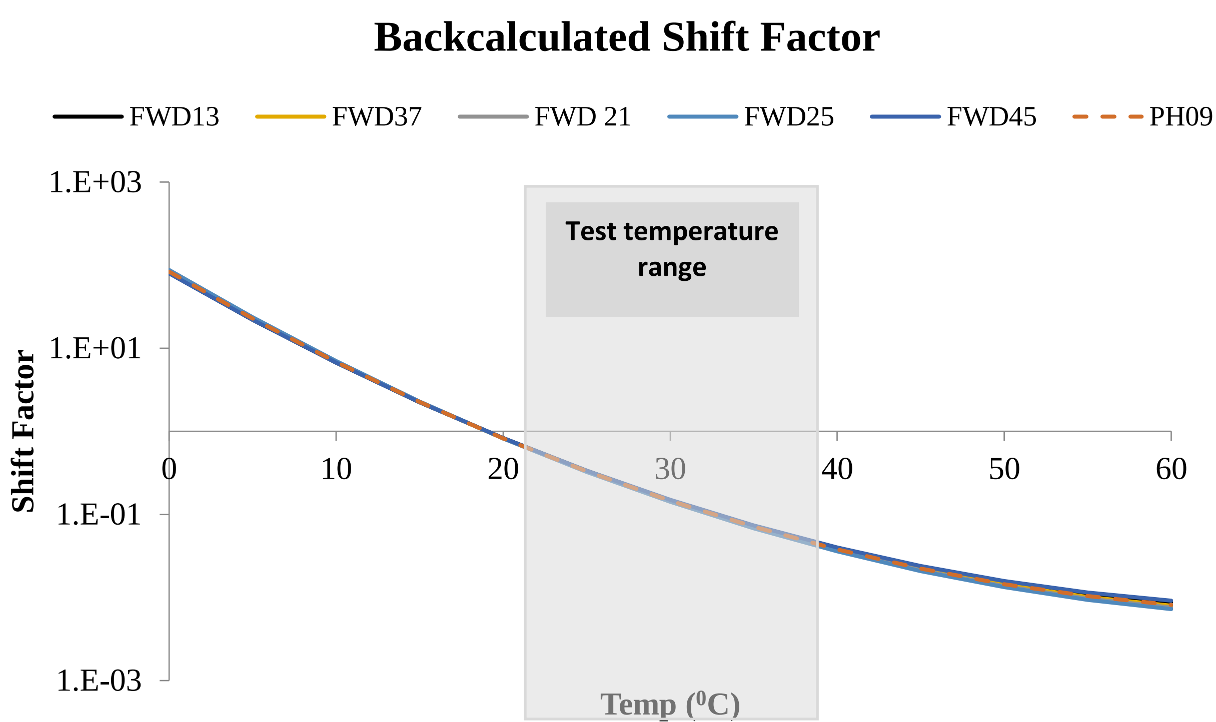

(b)

Figure 5.2 Backcalculated relaxation modulus (a) and shift factor (b) for each station and the average for PH09

5.2 Backcalculation of the mechanical characteristics of the rigid pavement sections

5.2.1 General Approach

The approach is a simple and direct method for backcalculating the dynamic subgrade stiffness and damping coefficients from FWD deflection basins. The method consists of first decomposing the transient deflection signal of each sensor into a series of harmonic motions using the Fast Fourier Transform (FFT) algorithm. Then, for each frequency, the real and imaginary components of the displaced volume underneath the slab are calculated from the complex deflection basin. The dynamic force-displacement relationship is decomposed into real and imaginary parts, leading to a simple system of equations that can be easily solved for k and c. A simple dynamic backcalculation program, called DYNABACK-R, for rigid pavements was developed based on the closed-form solution described below (*Chatti et al., 1994*). The input data for the program are slab size and thickness, and time-histories of FWD load and sensor deflections. The obtained k values were then compared to the static k values obtained using the best fit method (*Khazanovic et al., 2001*). Since there was a good agreement between both values, the elastic modulus of concrete obtained from the static backcalculation is used.

5.2.2 Dynamic Backcalculation Method

The method presented in this section was developed by Chatti (*1992*) and Chatti and Kim (*2001*). The theoretical backcalculation of the dynamic stiffness and radiation damping coefficients of the subgrade soils requires writing the dynamic force-displacement relationship of a slab resting on a viscoelastic foundation consisting of distributed springs and dashpots. The internal forces in the system are the elastic, viscous and inertial forces, represented by the springs, k, the dashpots, c, and the slab density, ρ, respectively. The only external force for this system is the FWD load (Figure 5.3).

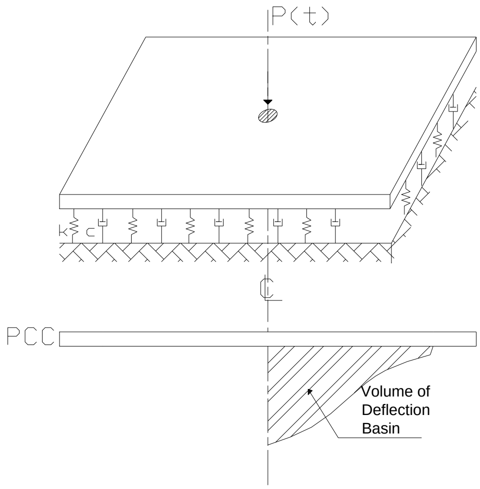

Figure 5.3 Determination of subgrade parameters (Chatti and Kim, 2001).

Then, k and c are obtained using the following system of equations:

$$k = \frac{\mathrm{Re}(P_0)\int_A \mathrm{Re}UdA + \mathrm{Im}(P_0)\int_A \mathrm{Im}UdA}{\left(\int_A \mathrm{Re}UdA\right)^2 + \left(\int_A \mathrm{Im}UdA\right)^2} + \omega^2 \rho \tag{5.2}$$

$$c = -\frac{1}{\omega}\frac{\mathrm{Re}(P_0)\int_A \mathrm{Im}UdA - \mathrm{Im}(P_0)\int_A \mathrm{Re}UdA}{\left(\int_A \mathrm{Re}UdA\right)^2 + \left(\int_A \mathrm{Im}UdA\right)^2} \tag{5.3}$$

The radius of the deflection basin for calculating k and c in Equations (5.2) and (5.3) can be taken as the equivalent radius for the slab area (A):

$$r_{eq} = \sqrt{\frac{A}{\pi}} \tag{5.4}$$

The volume of the deflection basin at each frequency is calculated as:

$$Volume = 2 \cdot \pi \sum_{i=1}^{7} A_i \cdot r_i^c \tag{5.5}$$

where A_i are calculated using the trapezoidal rule:

$$\begin{aligned}
A_1 &= 4\cdot(d_0 + d_8)\\
A_2 &= 2\cdot(d_8 + d_{12})\\
A_3 &= 3\cdot(d_{12} + d_{18})\\
A_4 &= 3\cdot(d_{18} + d_{24})\\
A_5 &= 6\cdot(d_{24} + d_{36})\\
A_6 &= 12\cdot(d_{36} + d_{60})\\
A_7 &= \frac{r_{eq} - 60}{2}\cdot(d_{60} + d_{r_{eq}})
\end{aligned} \tag{5.6}$$

The variables d_0, d_8, d_{12}, d_{24}, d_{36}, d_{60}, and $d_{r_{eq}}$ are the real or imaginary parts of the deflection at different sensors, and r_{eq} is the equivalent radius from Equation (5.4). The variables $r^c{}_1$ through $r^c{}_7$ are the centroidal distances in the radial direction of areas A_1 through A_7, respectively:

$$r_i^c = \begin{cases} \dfrac{d_{i+1}\cdot(r_i + r_{i+1}) + d_i\cdot(2\cdot r_i + r_{i+1})}{3\cdot(d_i + d_{i+1})} & for \quad |d_i| \ge |d_{i+1}| \\ \dfrac{d_{i+1}\cdot(4\cdot r_i + 5\cdot r_{i+1}) - d_i\cdot(r_i + 2\cdot r_{i+1})}{3\cdot(d_i + d_{i+1})} & for \quad |d_i| \le |d_{i+1}| \end{cases} \tag{5.7}$$

The deflection, $d_{r_{eq}}$, beyond the outermost sensor is calculated from the (static) solution of an infinite plate on an elastic foundation given by

$$d(r_{eq}) = d_0 \cdot \frac{4}{\pi}\cdot kei(\lambda\cdot r_{eq}) \tag{5.8}$$

where $kei(\lambda\cdot r_{eq})$ is the so-called Thomson function of zeroth order (*Lysmer, 1965*), λ is the inverse of the radius of relative stiffness as determined by*:*

$$l_k = \left[\frac{\ln\left[\dfrac{60 - AREA}{289.708}\right]}{-0.698}\right]^{2.566} \tag{5.9}$$

with $AREA = 4 + 6*\dfrac{d_8}{d_0} + 5*\dfrac{d_{12}}{d_0} + 6*\dfrac{d_{18}}{d_0} + 9*\dfrac{d_{24}}{d_0} + 18*\dfrac{d_{36}}{d_0} + 12*\dfrac{d_{60}}{d_0}$

Finally, the *k*-value at 0 Hz and a constant (average) *c*-value were used in the dynamic analysis since it was shown (*Chatti and Kim, 2001*) that accurate prediction of the dynamic response of rigid footings can be obtained using these values. The corresponding damping ratio is $\beta = c/(2 \cdot \sqrt{k \cdot \rho})$.

Figure 5.4 presents typical FWD Data. As highlighted in the figure, the time histories include errors in the post peak zone that will affect the results when transforming in the frequency domain. To overcome such problem, the time histories were first smoothed by fitting a haversine to both the load and deflection time histories, as shown in Figure 5.5, before using the FFT algorithm.

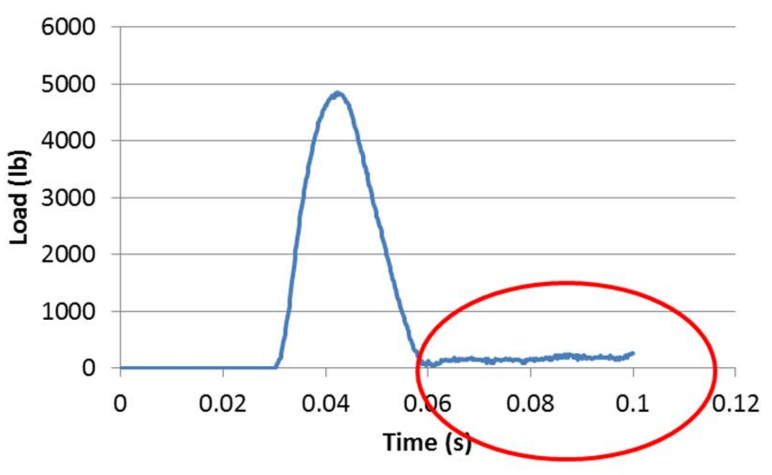

(a) Load Pulse

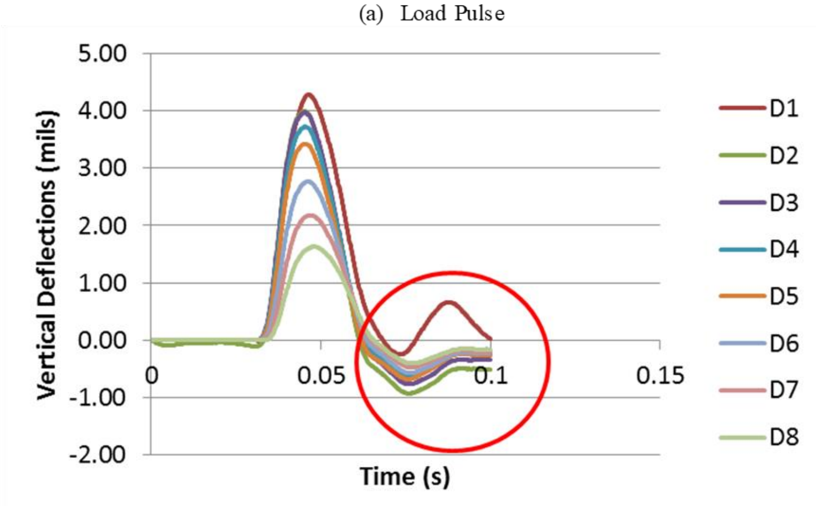

(b) Deflection Time Histories

Figure 5.4 Typical FWD load pulse and deflection time histories

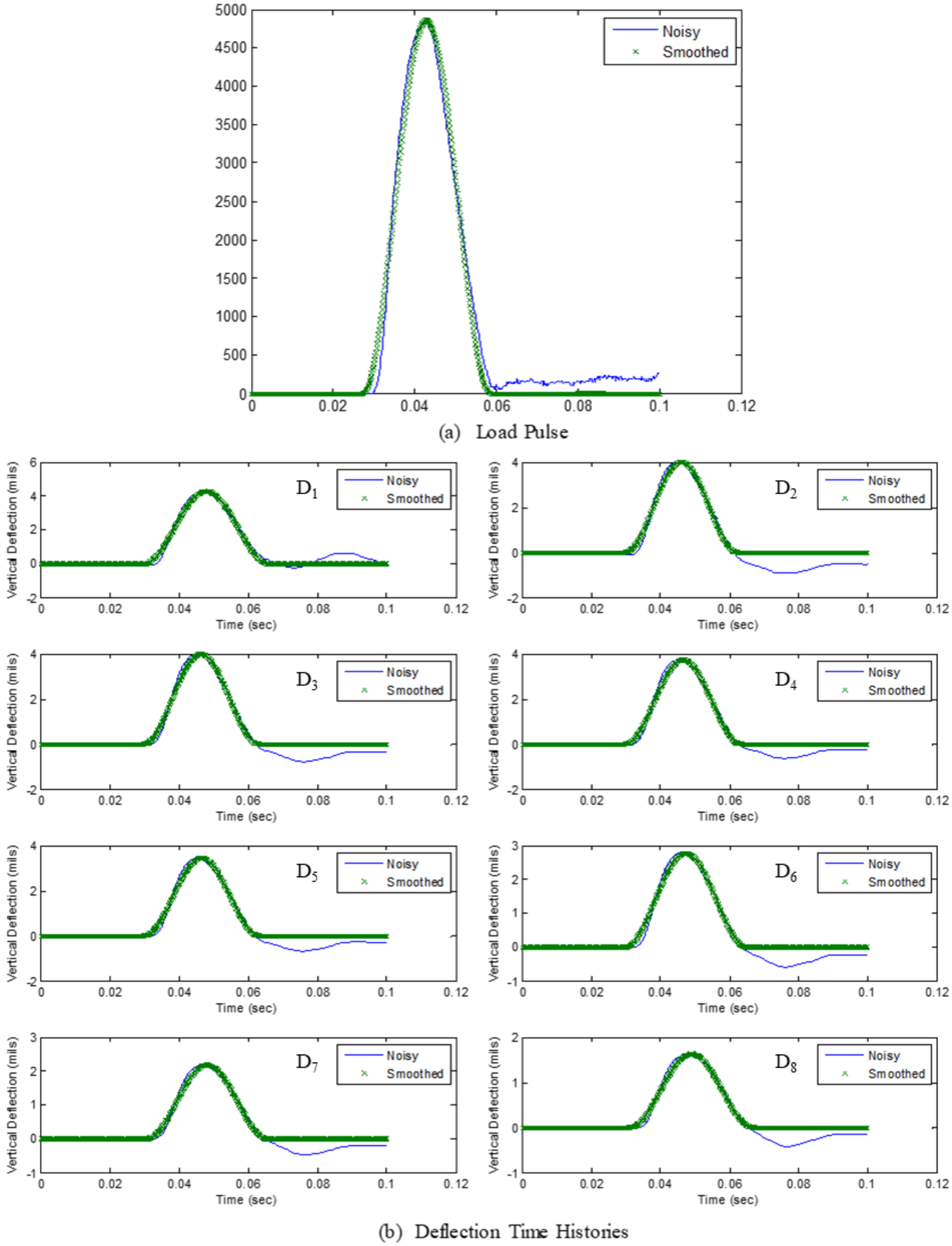

Figure 5.5 Measured vs smoothed FWD data.

5.2.3 Static Backcalculation Method for Dense Liquid Foundation

The method presented in this section was developed by Khazanovich (*2010*). The backcalculation procedure is based on the plate theory. The Best Fit method solves for a combination of the radius of relative stiffness, *l*, and the modulus of subgrade reaction, *k*, which produces the best possible agreement between the predicted and measured deflections at each sensor.

The forward method is based on Westergaard's solution for the interior loading of a plate consisting of a linear elastic, homogeneous, and isotropic material resting on a dense-liquid foundation. Under a load uniformly distributed over a circular area of radius *a*, the distribution of deflections, *w*(*r*), may be written as

$$\begin{cases} w(r) = \dfrac{p}{k} f\left(r, l\right) & (5.10) \\ f\left(r\right) = 1 - C_1\left(a_l\right)\mathrm{ber}\left(s\right) - C_2\left(a_l\right)\mathrm{bei}\left(s\right) \quad \mathit{for}\; 0 < r < a & (5.11) \\ f\left(r\right) = C_3\left(a_l\right)\mathrm{ker}\left(s\right) + C_4\left(a_l\right)\mathrm{kei}\left(s\right) \quad \mathit{for}\; r > a & (5.12) \end{cases}$$

where

a_l is the dimensionless radius of the applied load (*a/l*),

r is the radial distance measured from the center of the load

s is the normalized radial distance (*r/l*),

l is the radius of relative stiffness of plate-subgrade system for the dense-liquid foundation, $l = \left(D / k\right)^{1/4}$

D is the flextural rigidity of the plate, $D = \left(Eh^3 / 12\left(1 - \mu^2\right)\right)$

E is the plate elastic modulus

μ is the plate Poisson's ratio

h is the plate thickness

k is the modulus of subgrade reaction

p is the applied load pressure

ber, *bei*, *ker*, and *kei* are Kelvin Bessel functions. These constants have the following form for any value of the radius of the applied load:

$$\begin{cases} C_1 = -a_l \operatorname{ker}'(a_l) \\ C_2 = a_l \operatorname{kei}'(a_l) \\ C_3 = -a_l \operatorname{ber}'(a_l) \\ C_4 = -a_l \operatorname{bei}'(a_l) \end{cases} \tag{5.13}$$

where *ker'*, *kei'*, *ber'*, and *bei'* are the first derivatives of the functions *ker*, *kei*, *ber*, and *bei*, respectively.

The algorithm finds a combination of concrete elastic modulus and subgrade *k*-value for which the calculated deflection closely matches the measured one. The problem is formulated as the minimization of the error function, *F*, defined as follows:

$$F(E,k) = \sum_{i=0}^{n} \alpha_i \left(w(r_i) - W_i \right)^2 \tag{5.14}$$

where α_i is the weighting factor, $w(r_i)$ is the calculated deflection, and W_i is the measured deflection. Using equation 5.14, the error function, *F*, can be presented in the following form:

$$F(E,k) \equiv F(l,k) = \sum_{i=0}^{n} \alpha_i \left(\frac{p}{k} f_i(l) - W_i \right)^2 \tag{5.15}$$

Equations (5.16) for the *k*-value and (5.17) for the radius of relative stiffness represent the solution of the error function:

$$k = p \frac{\sum_{i=0}^{n} \alpha_i \left(f_i(l) \right)^2}{\sum_{i=0}^{n} \alpha_i W_i f_i(l)} \tag{5.16}$$

$$\frac{\sum_{i=0}^{n}\alpha_i f_i(l)\, f_i^{'}(l)}{\sum_{i=0}^{n}\alpha_i\left(f_i(l)\right)^2} = \frac{\sum_{i=0}^{n}\alpha_i W_i f_i^{'}(l)}{\sum_{i=0}^{n}\alpha_i W_i f_i(l)} \tag{5.17}$$

In this study, the following procedures were used:

1) Assign weighting factors for equation (5.14), equal to 0 or 1, depending on whether the sensor is being used for backcalculation.
2) Determine the radius of relative stiffness that satisfies equation (5.17).
3) Use equation (5.16) to determine the modulus of subgrade reaction.

Knowing the calculated values of *l* and *k*, the elastic modulus for the plate, E_{PL}, may be determined from the following relationship:

$$E_{PL} = \frac{12\left(1-\mu_{PL}^2\right)l^4 k}{h_{PL}^3} \tag{5.18}$$

where

h_{PL} is the plate slab thickness,

μ_{PL} is the PCC Poisson's ratio.

5.3 Pavement test sections

The field tests were conducted on the sections reported in Figure 5.7(b).

Sections PH04, PH18 and PH19 are composite sections: A hot mixed asphalt overlay was placed over a concrete slab over a cement treated base. Sections PH18 and PH19 are the opposite lanes of the same road, however the thickness of the layer changes, hence those sections were studied independently.

Sections PH15 and PH16 are semirigid sections: the asphalt layer lays over a cement treated base.

Sections PH7 - PH13 consist of an asphalt layer over an aggregate base or an asphalt layer over the subgrade. The viscoelastic layer properties of asphalt layers are described by the Relaxation modulus, fitted to a sigmoidal function

$$E(t) = \delta + \frac{\alpha}{1 + e^{(-\beta - \gamma \log(t_R))}} \tag{5.19}$$

where δ, α, β, γ are the sigmoidal coefficients, and t_R is the reduced time, defined as

$$t_R = \frac{t}{a_T} \tag{5.20}$$

where t is the time, and a_T is the shift factor,

$$Log_{10}(a_T) = c_1 \cdot (T - T_{ref}) + c_2 \cdot (T - T_{ref})^2 \tag{5.21}$$

where c_1, c_2 are the shift factor coefficients, T is the temperature, T_{ref} is the reference temperature, set to 19 °C. The behavior of all the other layers is considered to be damped elastic, as described in section 3.4. The relaxation moduli of the HMA layers are shown in Figure 5.7(a); the asphalt layers are different for each section, varying from soft to very stiff.

Sections PH01, PH02, PH03, PH21, PH22 and PH23 are jointed plain concrete pavement (JPCP) sections, section PH20 is a continuously reinforced concrete section (CRCP). All the JPCP sections are undoweled and were modeled assuming a spacing of 12ft between joints.

For each section, different characteristics were backcalculated from tests conducted during summer and during winter, so that the backcalculated parameters, which depend on temperature and soil saturation, effectively represent the pavement conditions during the field tests. To simplify the modeling, overlaying layers of the same materials have been combined into a single layer of thickness equal to the sum of the thickness of the two layers. For this reason, some of the top layers reported in Figure 5.7(b) are very thick.

The vehicles used for the testing are showed in Figure 5.6. The pressure distribution is assumed to be uniform. A detailed description of the sections and the vehicles used is in Appendices A-C.

Figure 5.6 Vehicles used for the field tests. Load per axle indicated in lbs. Source: UC Davis

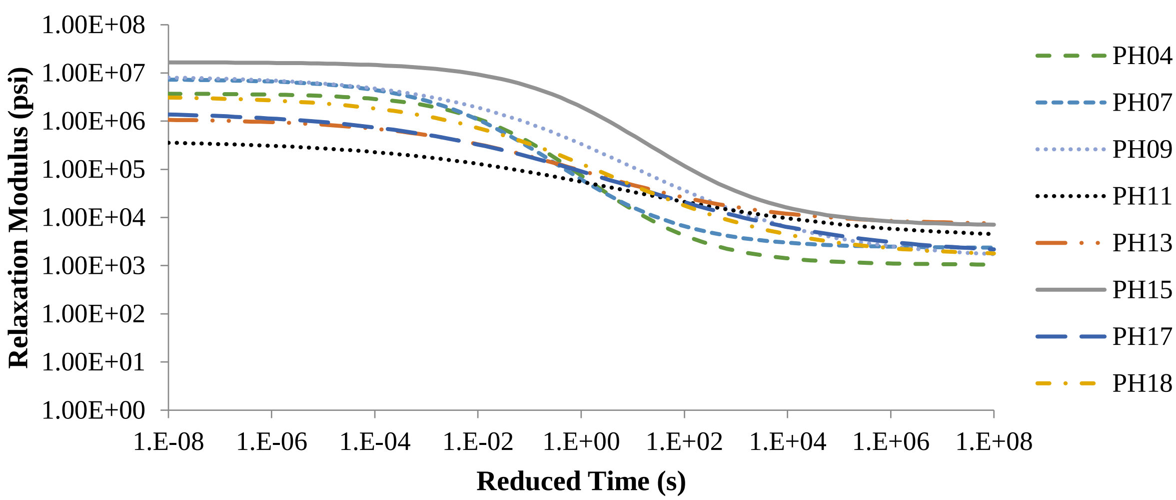

(a)

Figure 5.7 Relaxation moduli of the HMA layers (a) and field testing pavement sections (b)

Figure 5.7 (cont'd) Relaxation moduli of the HMA layers (a) and field testing pavement sections (b)

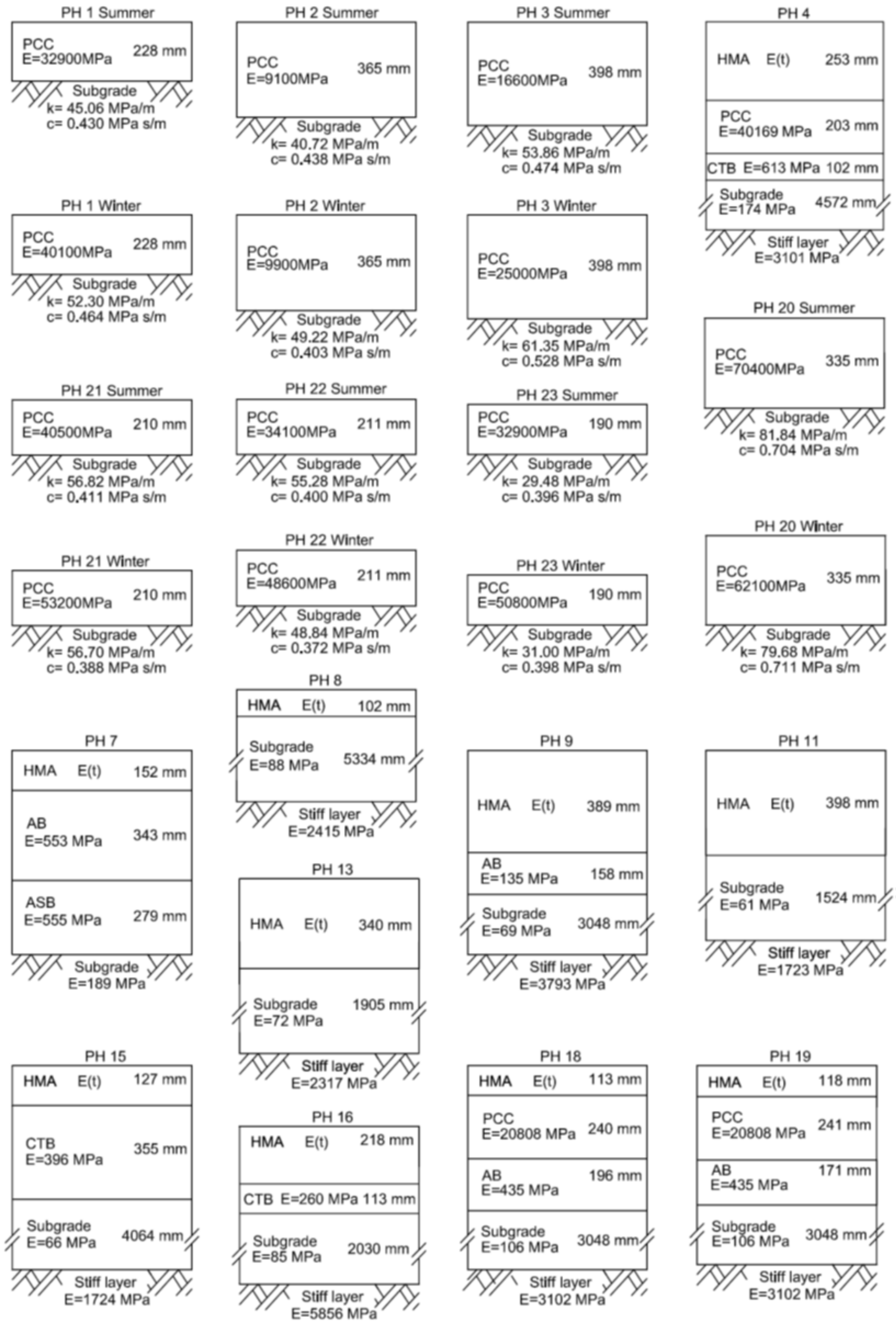

(b)

5.4 Simulation results

5.4.1 Asphalt pavement sections

For each of the asphalt pavement sections all the vehicles were simulated moving at four different speeds: 25, 35, 45 and 55 mph, at three different pavement surface temperatures: 68, 95 and 122°F, representing winter, spring/fall and summer. The simulations were run using a constant temperature for the HMA layer, calculated at one third depth using the BELLS3 equation (eq. 7.1b).

For asphalt pavements at high temperatures the asphalt materials behavior is more viscous; for this reason, the energy dissipated is higher in summer conditions than in winter. Similarly, because of the time temperature superposition principle for viscoelastic materials, the energy dissipated is higher at low speeds. This can be observed in Figure 5.8. The results for all the asphalt sections for a heavy truck are shown in Figure 5.9, which shows that different pavement structures show significantly different results. The energy dissipated by the other vehicles is much lower than that by the heavy truck, as shown in Figure 5.10; an average car only dissipates 1-3% of the energy dissipated by a truck.

It can be noted in Figure 5.9 that the effect of temperature depends on the pavement section; comparing PH04 and PH07, the energy dissipation is similar during winter and fall, but much higher for PH04 during the summer. The same concept applies to the effect of speed and loading.

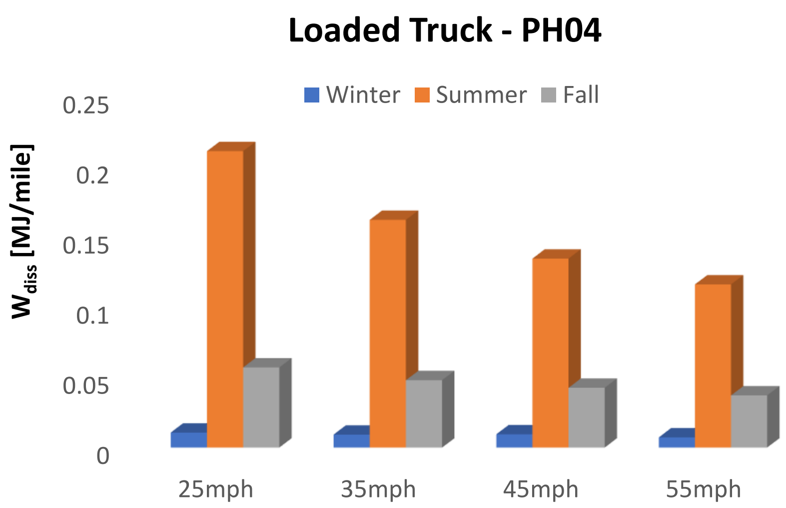

Figure 5.8 Effect of speed and temperature for asphalt pavements

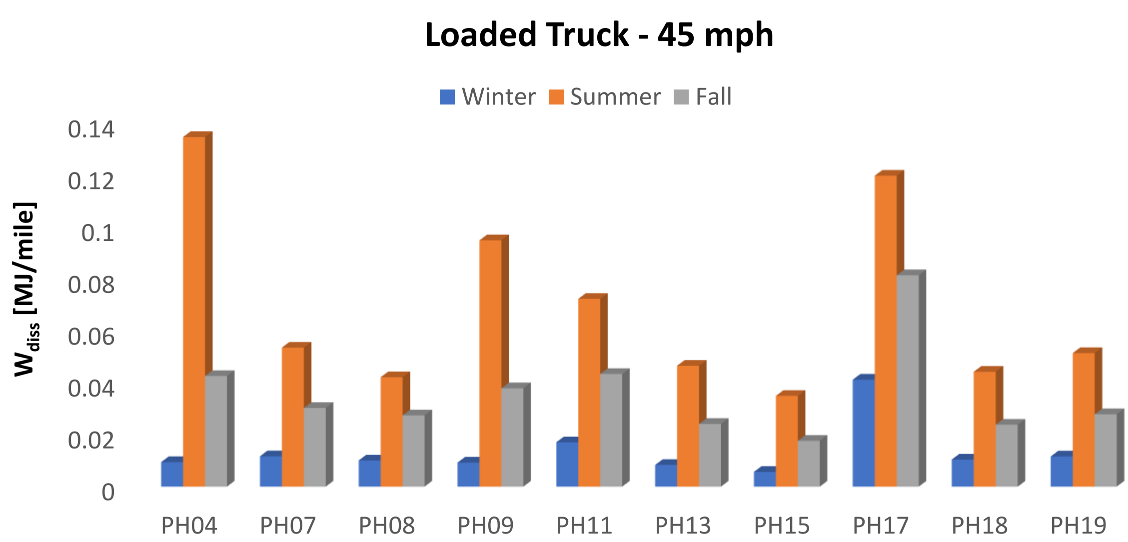

Figure 5.9 Energy dissipated for all asphalt pavement sections

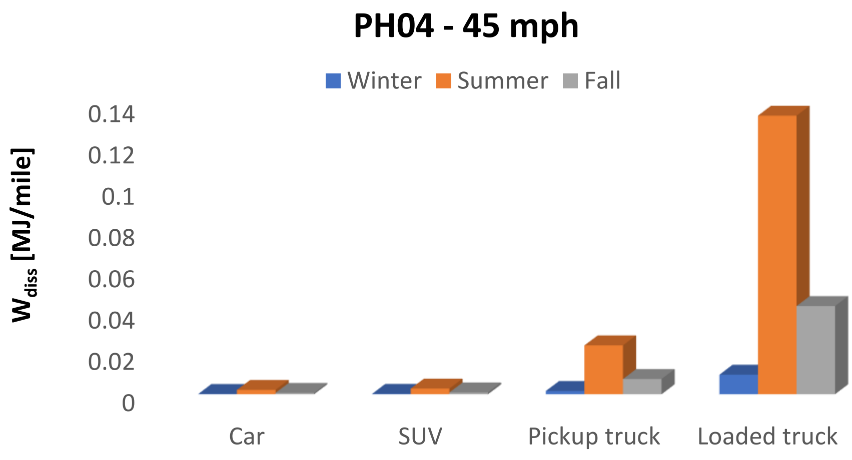

Figure 5.10 Energy dissipated by different vehicles

5.4.2 Jointed concrete pavement sections

For each of the JPC pavement sections all the vehicles were simulated moving at two different speeds: 45 and 55 mph, in two different seasons, summer and winter, using two values of LTE between two consecutive slabs for the JPCP: 40 and 90%. The JPCP sections for the field tests have an asphalt shoulder and do not have tie bars; therefore, no shoulders or adjacent lanes were included in the simulation. For concrete pavements the effects of temperature and speed are small, as shown in Figure 5.11.

Similar to the asphalt sections, the energy dissipation is higher in summer conditions; however, the effect of speed has a reversed trend: at higher speed the energy dissipation increases (the same effect was observed also by Bazi et al., 2018). This is due to the different way asphalt and concrete sections are modeled: On concrete pavements the damping in the subgrade causes the peak deflection to be more delayed with respect of the center of the tire print when the speed increases, increasing the slope seen by the moving vehicle. On asphalt pavements such effect is masked by the fact that at higher velocity the asphalt layer behavior becomes more elastic, reducing the viscous dissipation of energy. The load transfer efficiency between two consecutive slabs has a significant effect on energy dissipation, as shown in Figure 5.12.

Similar to asphalt pavements, on the concrete sections heavy trucks dissipate much more energy than lighter vehicles, as shown in Figure 5.13.

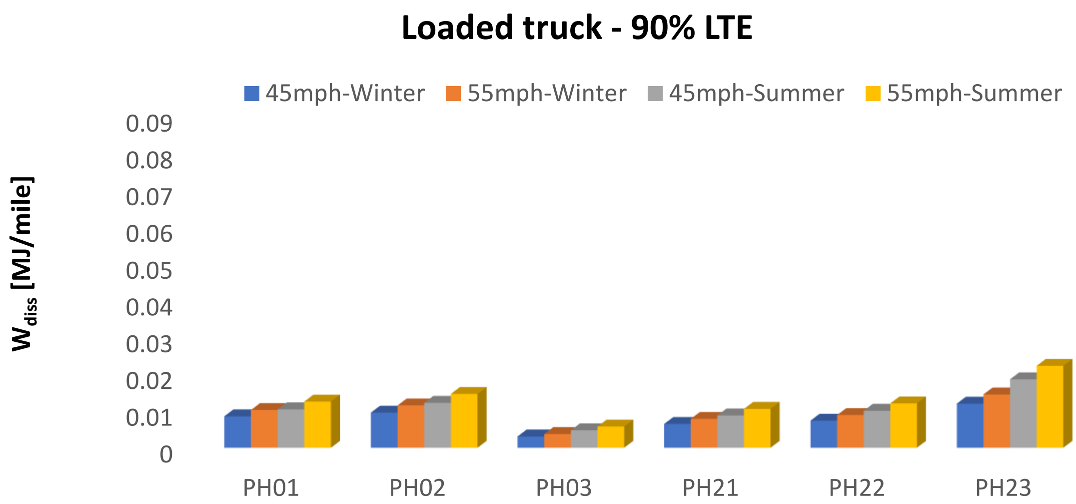

Figure 5.11 Effect of speed and temperature for JPCP sections

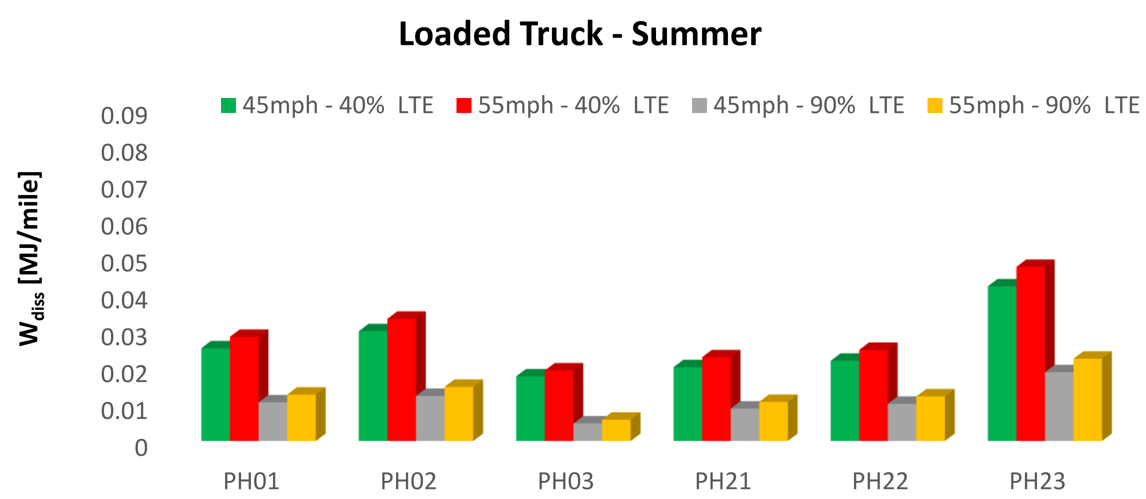

Figure 5.12 Effect of speed and LTE for JPCP sections

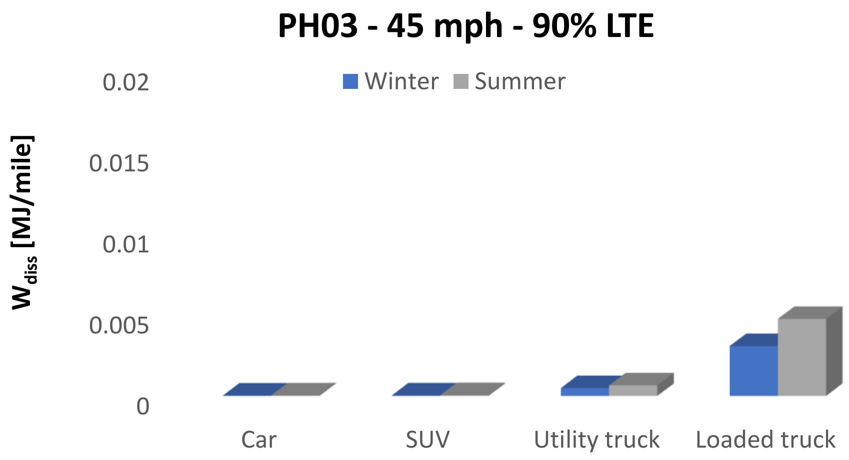

Figure 5.13 Energy dissipated by different vehicles. Note: different scale from the other figures

5.4.3 Relation between energy dissipation and fuel consumption

The energy dissipated due to the structural rolling resistance can be expressed as fuel consumption excess, which can be evaluated as follows:

$$Fuel_{SRR} = \frac{W_{diss}}{\xi_b} \tag{5.22}$$

The factor ξ_b is the effective calorific value of the combustible and is a function of the engine technology. According to Baglione (*2007*), the maximum efficiency of gasoline engines is about 25-30% while it is about 40% for diesel engines. Those percentages represent the energy released by the engines that will be available to move the vehicle. Since the calorific value of diesel is about 151.4 MJ/gal (40 MJ/L) and the one of gasoline is about 128.7 MJ/gal (34 MJ/L), the value used for ξ_b is 60.6 MJ/gal (16 MJ/L) for a diesel engine and 39.7 MJ/gal (10.5 MJ/L) for a gasoline engine, in accordance with the values reported in (*Chatti and Zaabar, 2012*).

The fuel consumption can also be expressed as a percentage of the total fuel consumption of the vehicle, as shown in Equation 5.23

$$Fuel_{SRR\%} = \frac{Fuel_{SRR}}{F_c} \tag{5.23}$$

where F_c is the total fuel consumption of the vehicle, calculated using the calibrated HDM4, i.e. NCHRP720 model (*Chatti and Zaabar, 2012*), assuming no grade, no curvature, and a smooth surface condition, with IRI of 60 in/mile.

5.4.4 Comparison of results from asphalt and concrete sections

Comparing the two types of pavement, Figure 5.15 through Figure 5.22 show that the percentage of fuel consumption due to the SRR is higher in flexible pavements than in rigid pavements in summer conditions for a heavy truck; the difference is smaller for cars, SUVs and the utility truck. As the load transfer efficiency of the JPCP slabs reduces, the energy dissipated increases; hence the difference in SRR between flexible and rigid pavements reduces. The CRCP section has the lowest energy dissipation, for two reasons: First, it has an asphalt shoulder and two lanes connected by tie bars, so an adjacent lane with full bonding (100% LTE) has been included in the simulation; this, as shown in chapter 4, reduces the SRR energy dissipation. Second, the backcalculated values of the pavement mechanical characteristics are different from the JPCP sections (Figure 5.7), with a much higher value of the elastic modulus of the slab and modulus of subgrade reaction.

While the energy dissipated increases at higher speeds on rigid pavements, also the total vehicle fuel consumption increases, causing the percentage of the total fuel consumption due to the SRR to decrease (Figure 5.14).

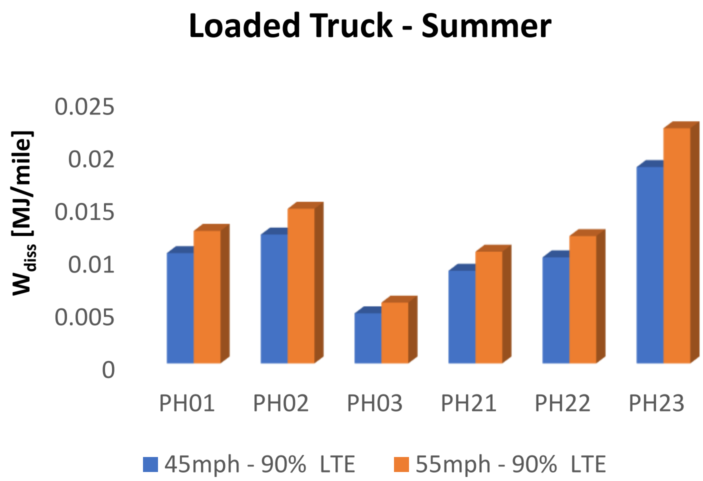

(a)

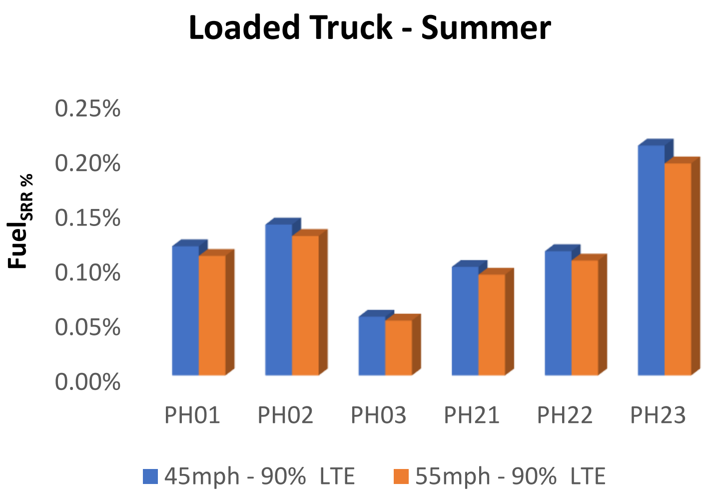

(b)

Figure 5.14 Reversed trends for (a) energy dissipation as function of speed, and (b) percentage fuel consumption as function of speed for a rigid pavement

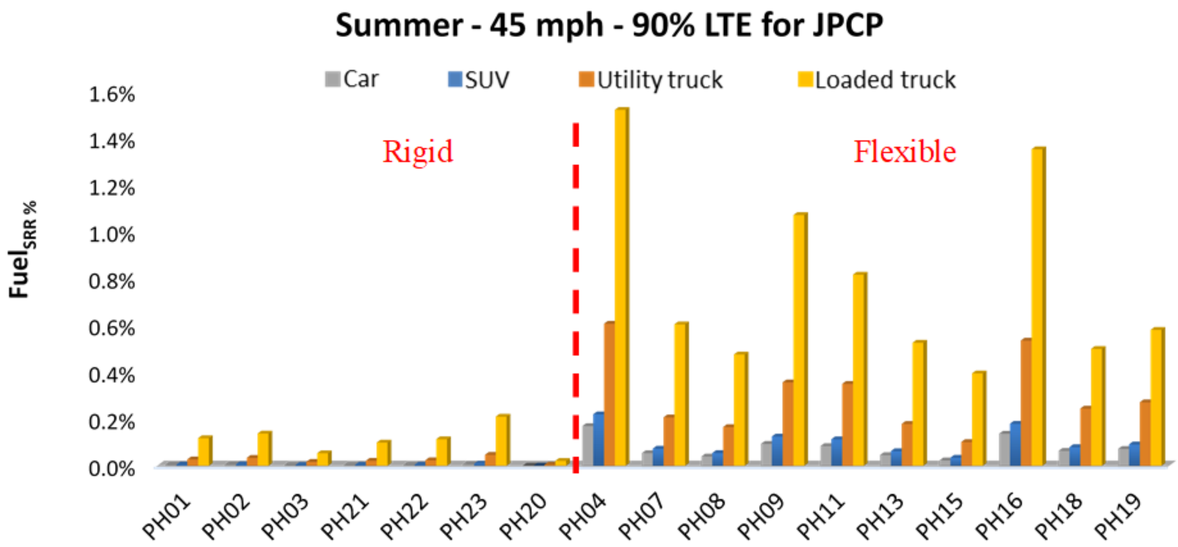

Figure 5.15 Percentage of total fuel consumption caused by the structural rolling resistance for all the pavement sections, during summer, for all vehicles at 45 mph, 90% LTE in the JPCP sections

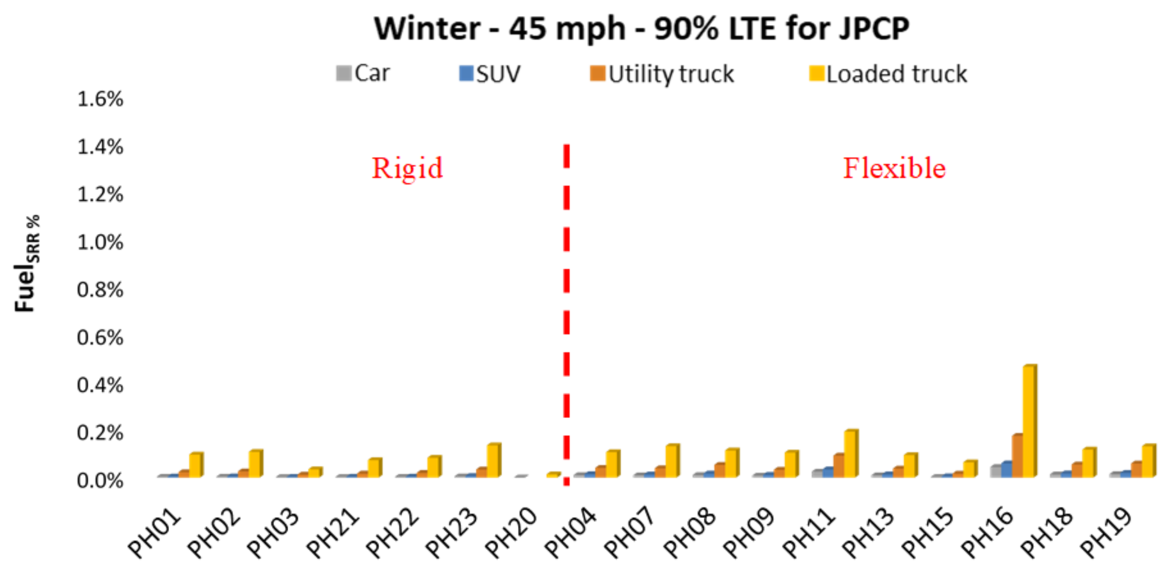

Figure 5.16 Percentage of total fuel consumption caused by the structural rolling resistance for all the pavement sections, during winter, for all vehicles at 45 mph, 90% LTE in the JPCP sections

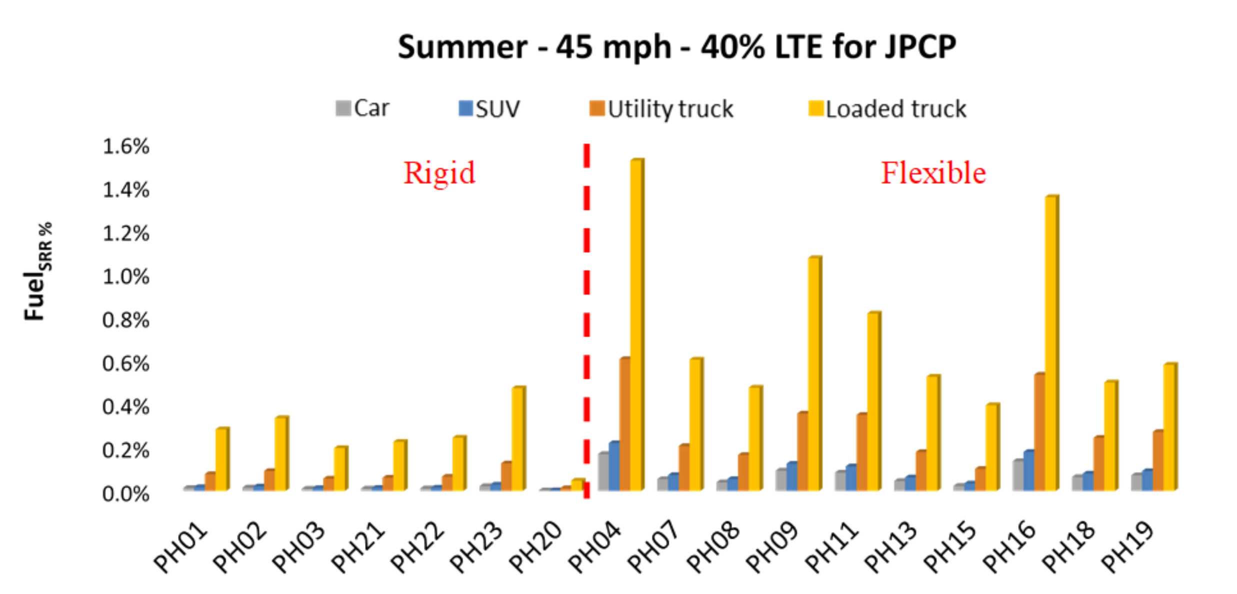

Figure 5.17 Percentage of total fuel consumption caused by the structural rolling resistance for all the pavement sections, during summer, for all vehicles at 45 mph, 40% LTE in the JPCP sections

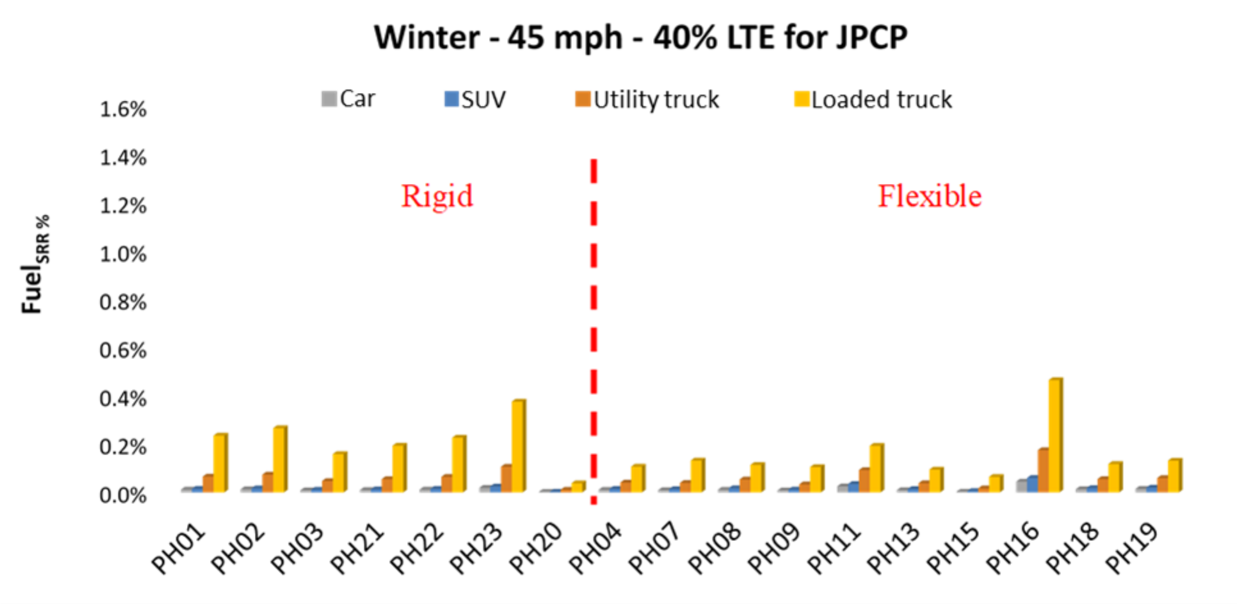

Figure 5.18 Percentage of total fuel consumption caused by the structural rolling resistance for all the pavement sections, during winter, for all vehicles at 45 mph, 40% LTE in the JPCP sections

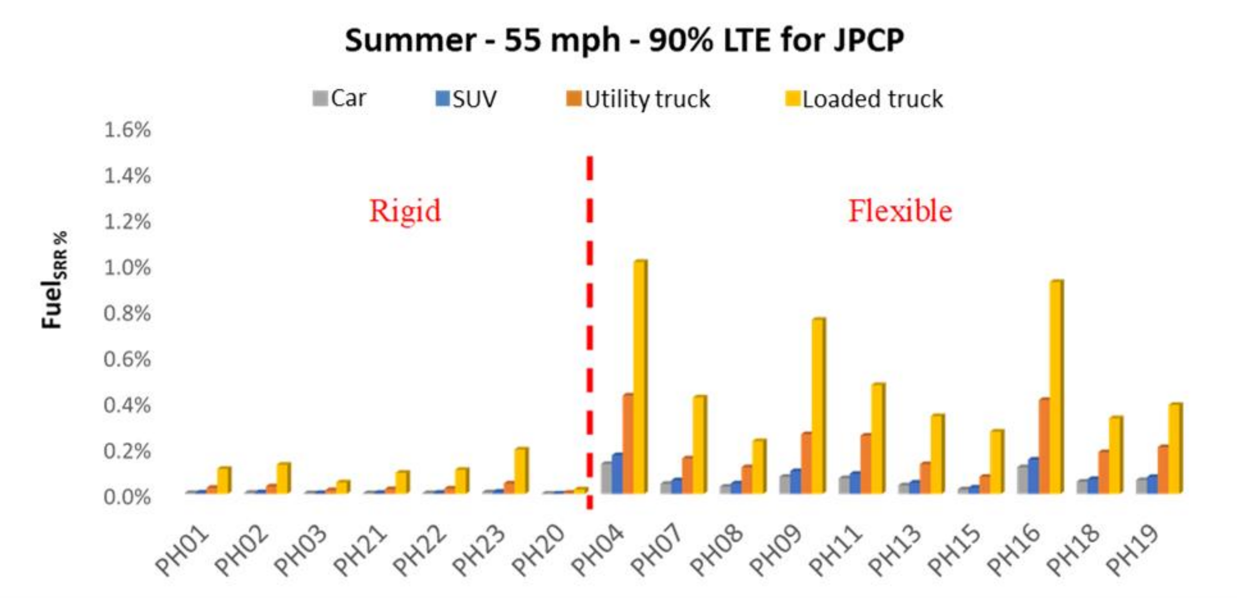

Figure 5.19 Percentage of total fuel consumption caused by the structural rolling resistance for all the pavement sections, during summer, for all vehicles at 55 mph, 90% LTE in the JPCP sections

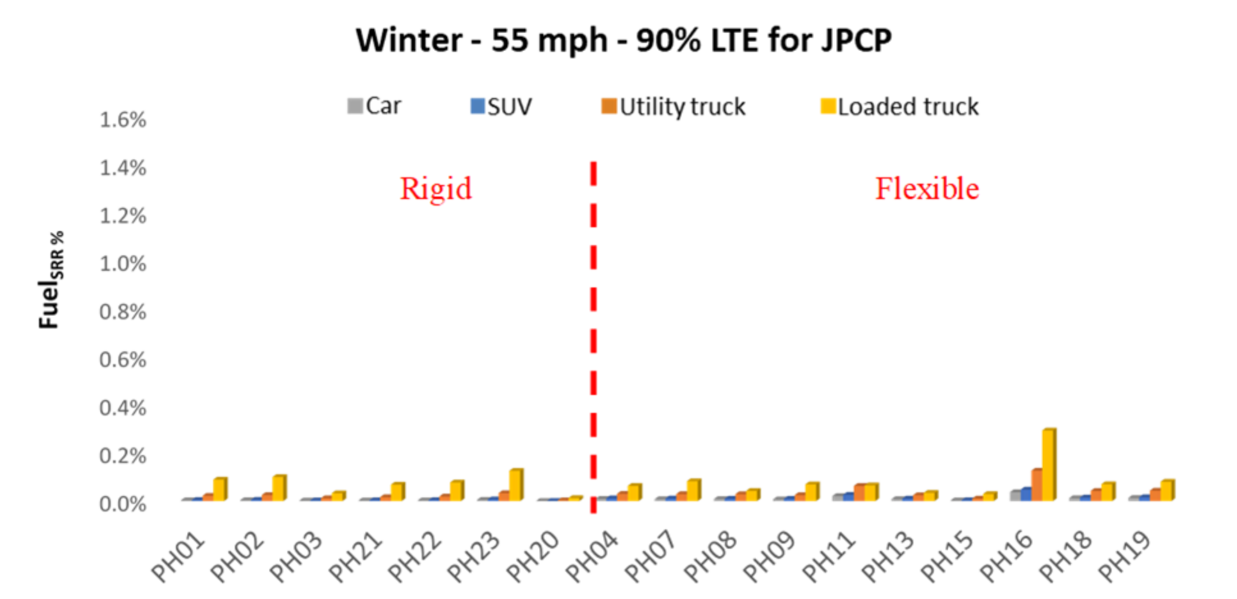

Figure 5.20 Percentage of total fuel consumption caused by the structural rolling resistance for all the pavement sections, during winter, for all vehicles at 55 mph, 90% LTE in the JPCP sections

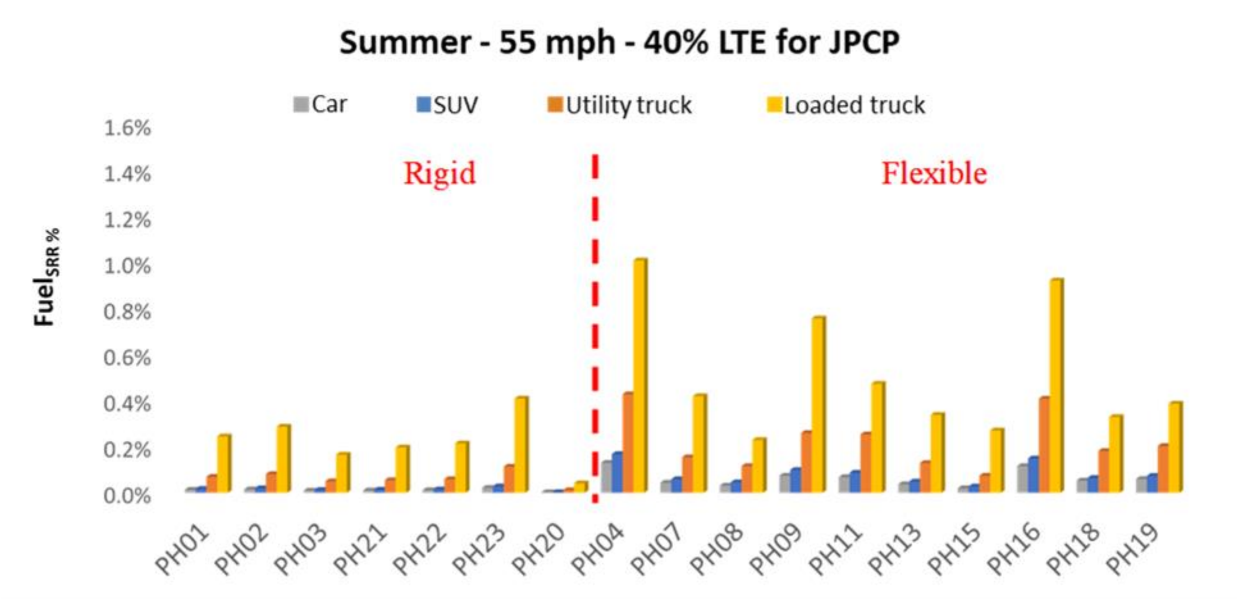

Figure 5.21 Percentage of total fuel consumption caused by the structural rolling resistance for all the pavement sections, during summer, for all vehicles at 55 mph, 40% LTE in the JPCP sections

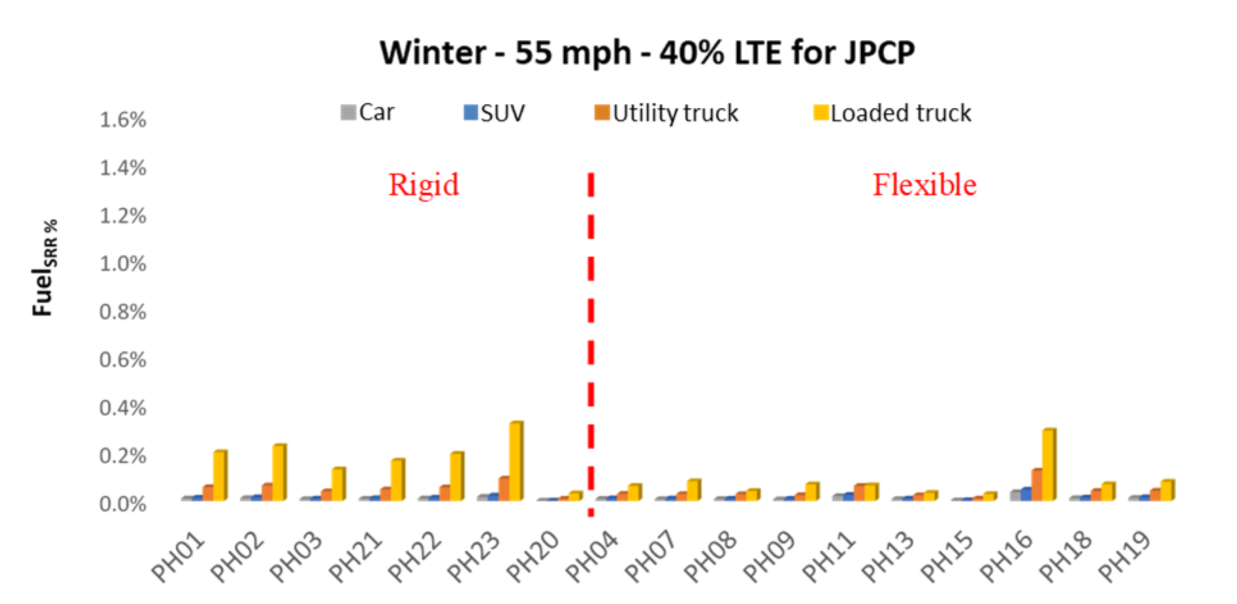

Figure 5.22 Percentage of total fuel consumption caused by the structural rolling resistance for all the pavement sections, during winter, for all vehicles at 55 mph, 40% LTE in the JPCP sections

5.5 Conclusions

The simulations have shown differences in terms of structural rolling resistance (SRR) between rigid and flexible pavements; these differences mainly depend on:

1) Temperature: On flexible pavements at high temperatures the viscous properties of the asphalt layer (which can be considered a linear viscoelastic material) are enhanced, the area of the hysteresis loop is larger, and the energy dissipated within the pavement is greater. At higher temperatures the pavement deflects more under a moving load, the slope seen by the tire becomes steeper, and, as a direct consequence, the structural rolling resistance increases. The model used for the rigid pavements cannot consider the effects of temperature or moisture, however curling and warping will affect rolling resistance as part of roughness, more than in terms of SRR. The interaction between roughness and structural rolling resistance is investigated in section 7.5, where the differences in terms of SRR between a static and a dynamic vehicle axle load caused by pavement roughness will be compared. In the simulations, for the same section, different mechanical characteristics, backcalculated from FWD tests conducted in summer and winter, were used to simulate different seasons. The results show a small effect of temperature on rigid pavement.
2) Velocity: For any viscoelastic material the time-temperature superposition principle can be applied. The pavement response to a vehicle moving at a low speed (which has a long loading time, or low frequency), is equivalent to the vehicle moving at higher speed (shorter loading time, or higher frequency) at a higher temperature. Therefore, for the reasons presented in point 1), the structural rolling resistance on flexible pavements decreases at higher speeds. On the other hand, the damping effects of the subgrade are more

relevant for rigid pavements at higher speeds, causing an increase in the structural rolling resistance.

3) Load: The weight of the vehicle plays a major role in determining the SRR effects. For light vehicles such as cars and SUVs the contribution of SRR to the total fuel consumption is very small, and different pavement structures would probably not bring significant changes in terms of rolling resistance. However, for heavy trucks the differences between flexible and rigid pavements appear to be not negligible, especially at higher temperatures and lower speeds.

6 DEVELOPMENT OF A PREDICTIVE FUNCTION FOR CALCULATING THE SRR ON A RIGID PAVEMENT

The results presented in chapter 5 can be used to develop a simple model that provides an estimate of the energy dissipated due to the structural rolling resistance to be used in a life cycle assessment (LCA) and life cycle cost (LCCA) analysis. The predictive function should allow network and project level calculations without having to conduct any simulations of moving vehicles.

6.1 Parametric analysis

The effect of pavement characteristics (k, c, E, h and LTE), and the loading conditions on the energy consumption due to the SRR have been investigated to have a clear idea of what should be the form of the function. The results are shown in Figure 6.1 through Figure 6.6.

The effect of h, E, k and the LTE can be fit to a negative exponential function; the energy dissipated decreases as the modulus of subgrade reaction, the slab stiffness or its thickness increase. The effect of c is very close to linear; as expected, when the system becomes completely elastic the energy dissipation tends to zero. The effect of the load is a second order polynomial function; the slope seen by the wheels increases linearly with the load, and therefore the energy dissipation increases as the quadratic of the load.

All the discussed variables influence the SRR energy consumption and are to be included in the predictive function. The effect of tire pressure is negligible; Figure 6.7 shows that the energy dissipated depends on the total load, and not on the tire contact area or pressure distribution.

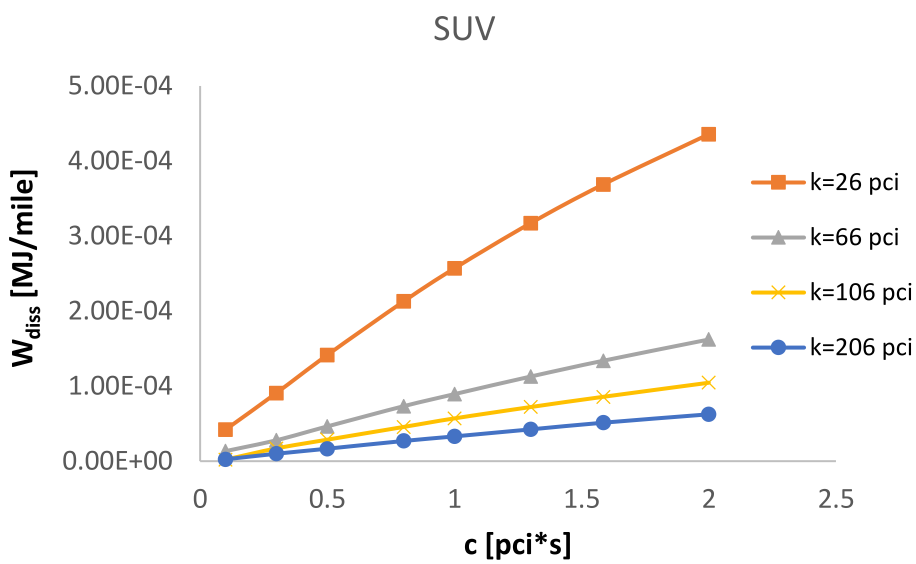

Figure 6.1 Energy dissipated due to SRR as a function of the damping coefficient

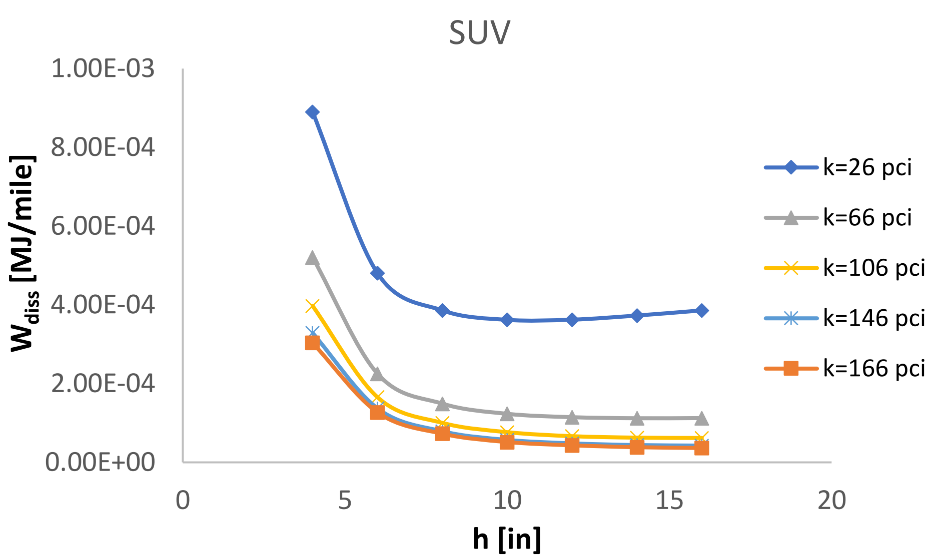

Figure 6.2 Energy dissipated due to SRR as a function of the slab thickness

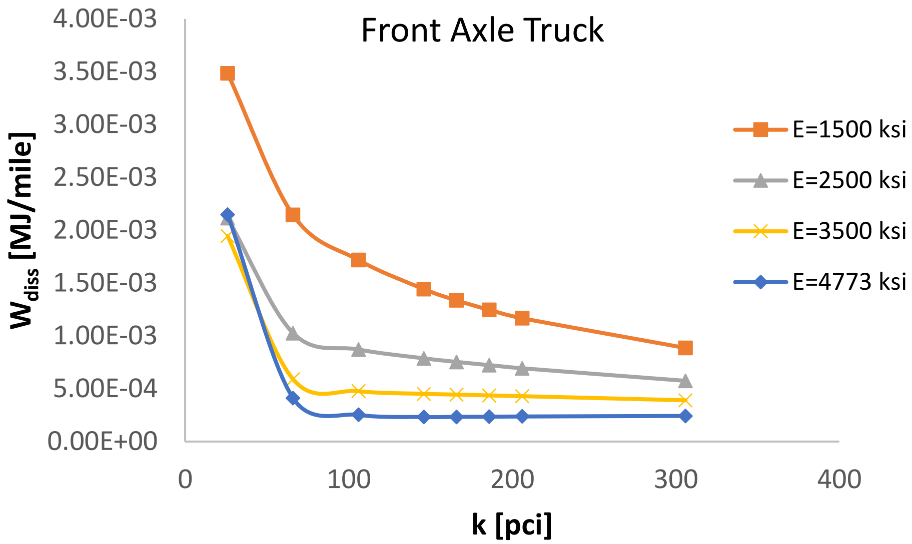

Figure 6.3 Energy dissipated due to SRR as a function of the modulus of subgrade reaction

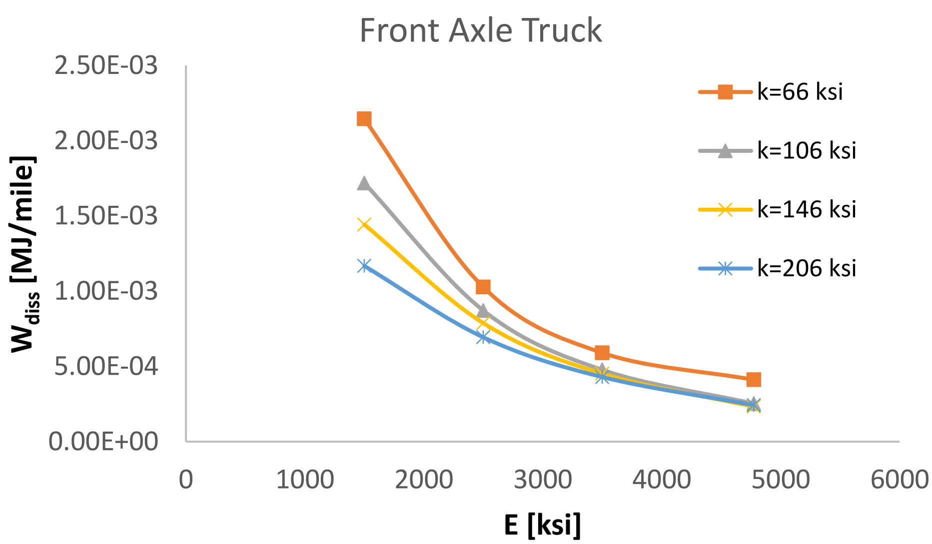

Figure 6.4 Energy dissipated due to SRR as a function of the elastic modulus of the slab

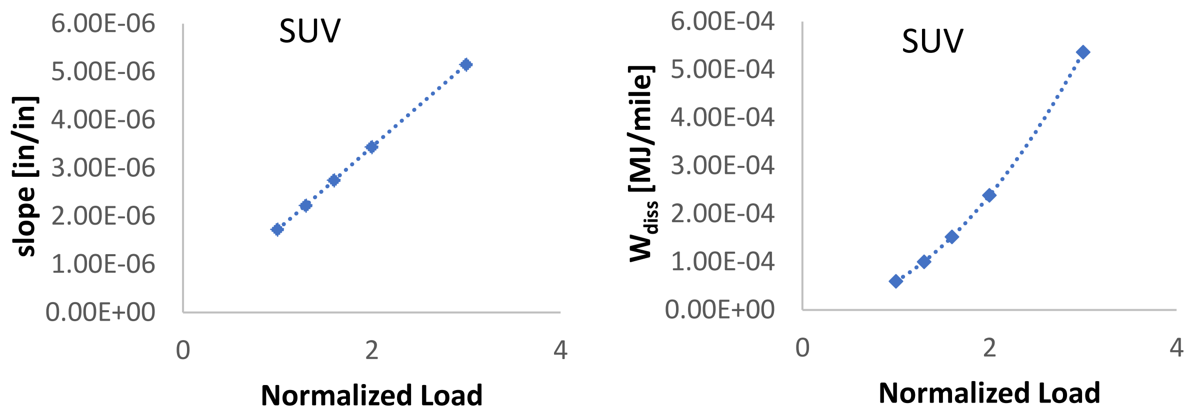

(a) *(b)*

Figure 6.5 (a) Slope and (b) W_{diss} seen by the wheels due to SRR as a function of the normalized load

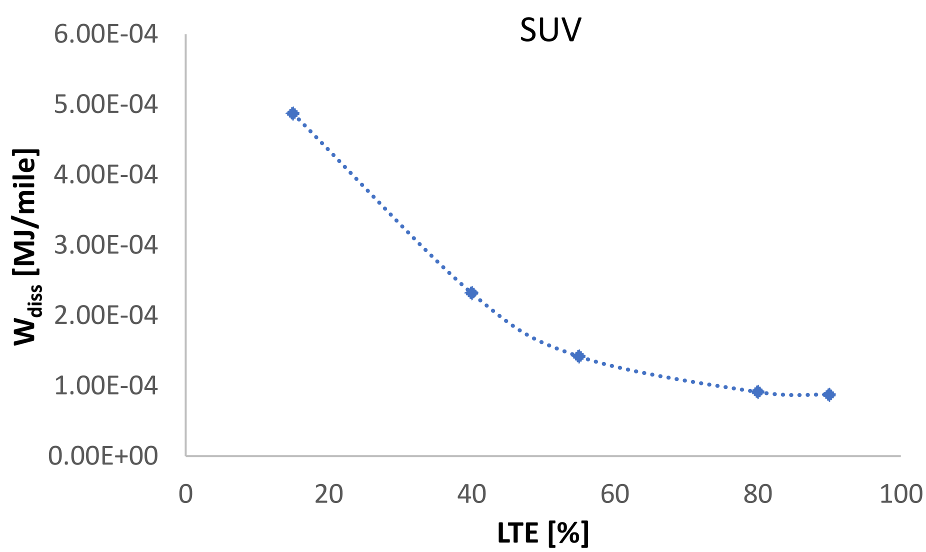

Figure 6.6 Energy dissipated due to SRR as a function of LTE between slabs

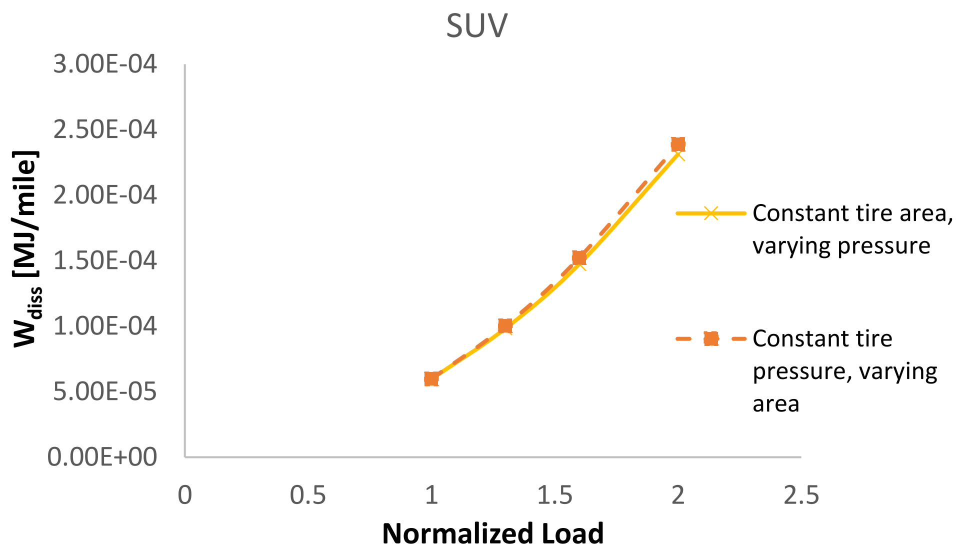

Figure 6.7 Energy dissipated due to SRR as a function of the normalized load for different tire pressures and areas

6.2 Fitting of the predictive function

Based on the simulation results and the parametric analysis the form of the function to predict the energy dissipation due to the SRR should be

$$W_{diss} = a_1 \cdot c \cdot L^2 \cdot e^{\left(a_2 + a_3 \cdot v + a_4 \cdot \frac{LTE}{100} + a_5 \cdot E + a_6 \cdot k + a_7 \cdot c + a_8 \cdot l\right)} \tag{6.1}$$

where

a_1-a_8 are the coefficients reported in Table 6.1, which depend on the vehicle type,

c is the damping coefficient [pci*s],

L is the total vehicle load [kip],

v is the vehicle speed [mph],

E is the elastic modulus of the concrete slab [ksi],

k is the modulus of subgrade reaction [pci],

l is the radius of relative stiffness [in].

The coefficients a_1-a_9 have been obtained by minimizing the function

$$f = \sum_{i=1}^{n} \left(\frac{2}{Log_{10}(y_i)} - \frac{2}{Log_{10}(f_i)} \right)^2 \tag{6.2}$$

where y_i are the values of energy dissipated obtained from the mechanistic simulations showed in chapter 5, and f_i are the values of energy dissipated predicted by equation 6.1.

The function of equation 6.2 was chosen to be logarithmic since the energy dissipated values (W_{diss}) are in the order of 10^{-2} – 10^{-5} [MJ/mile], and the logarithm was chosen to be in the denominators so that larger values of energy dissipation are weighted more, avoiding to have the larger errors for larger values of energy dissipation. Referring to Table 6.2, the form of function 6.2 is such that it is given more importance to minimizing the mean absolute error at the expense of a larger value of the mean absolute percentage error.

Table 6.1 Coefficients for concrete pavement predictive function

	CAR	**SUV**	**F450**	**TRUCK**
a_1	2.45E-04	1.87E-04	5.98E-05	1.53E-04
a_2	-0.6261	-0.6866	-0.2250	-0.7618
a_3	1.07E-02	1.28E-02	1.30E-02	1.32E-02
a_4	-2.5747	-2.3772	-2.0917	-1.9447
a_5	-2.06E-05	-2.07E-05	-2.25E-05	-2.38E-05
a_6	-7.47E-03	-7.47E-03	-7.69E-03	-7.82E-03
a_7	-0.3182	-0.3038	-0.3189	-0.3051
a_8	-0.0272	-0.0276	-0.0311	-0.0460

Figure 6.8 through Figure 6.15 show the quality of the fit for the different vehicles types (which are described in Figure 5.6 and Figure C.1). The number of points used for model fitting represents 80% of the total, while the remaining 20% is used for testing. Table 6.2 reports the values of the coefficient of determination (R^2), the mean absolute error (MAE) and the mean absolute percentage error (MAPE) of each model.

$$R^2 = 1 - \frac{RSS}{TSS} \tag{6.3}$$

$$RSS = \sum_{i=1}^{n} \left(y_i - f_i \right)^2 \tag{6.4}$$

$$TSS = \sum_{i=1}^{n} \left(y_i - \bar{y} \right)^2 \tag{6.5}$$

$$\bar{y} = \frac{1}{n} \sum_{i=1}^{n} y_i \tag{6.6}$$

$$MAE = \frac{1}{n} \sum_{i=1}^{n} \left| y_i - f_i \right| \tag{6.7}$$

$$MAPE = \frac{100\%}{n} \sum_{i=1}^{n} \frac{\left| y_i - f_i \right|}{y_i} \tag{6.8}$$

Table 6.2 Parameters showing quality of the fit

	R^2	MAE [MJ/mile]	MAPE [%]
Car model	0.99	3.88E-06	4
SUV model	0.99	5.20E-06	4
F450 model	0.99	7.68E-05	5
Truck model	0.99	7.68E-04	8

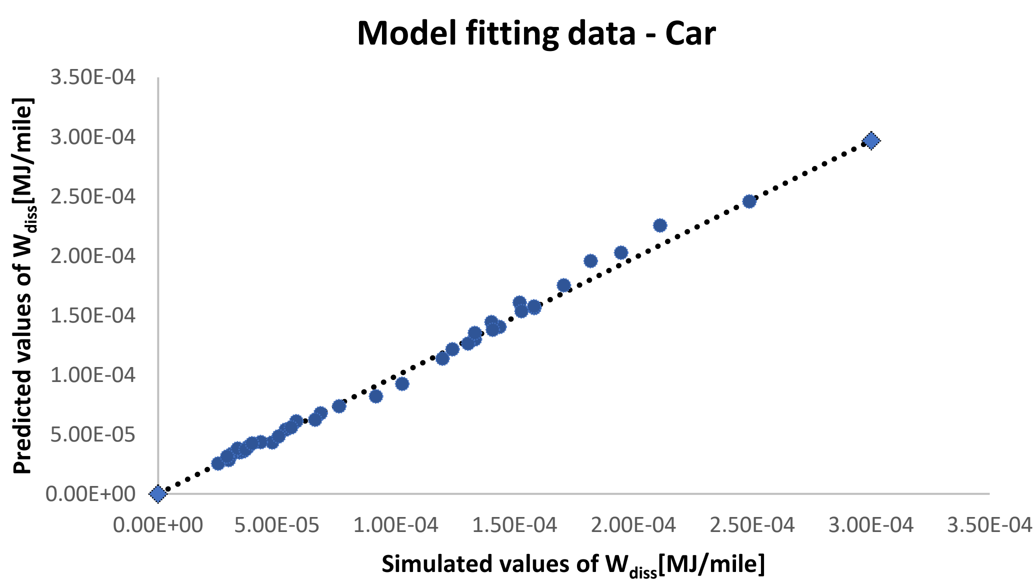

Figure 6.8 Model fitting for a passenger car

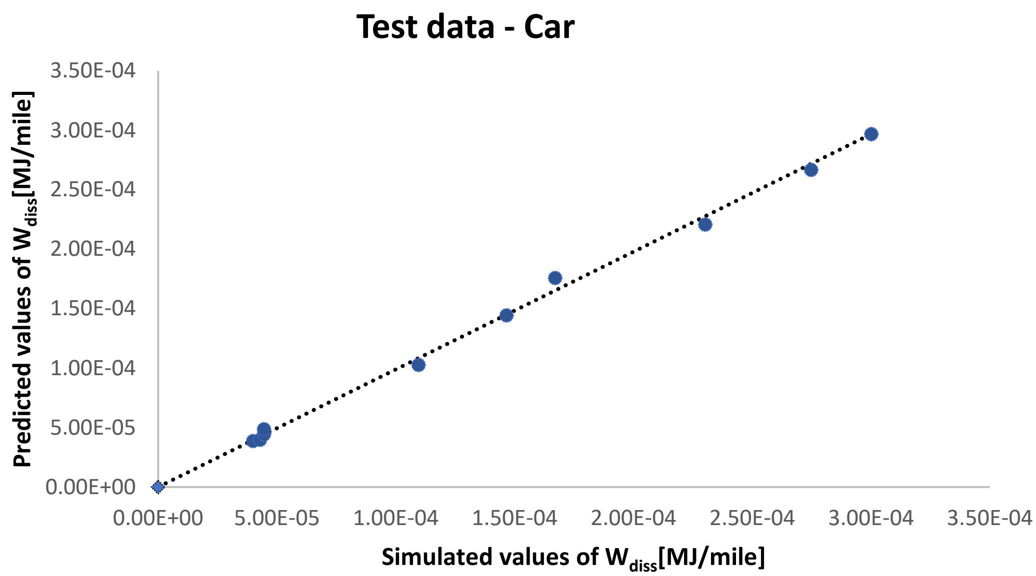

Figure 6.9 Model testing for a passenger car

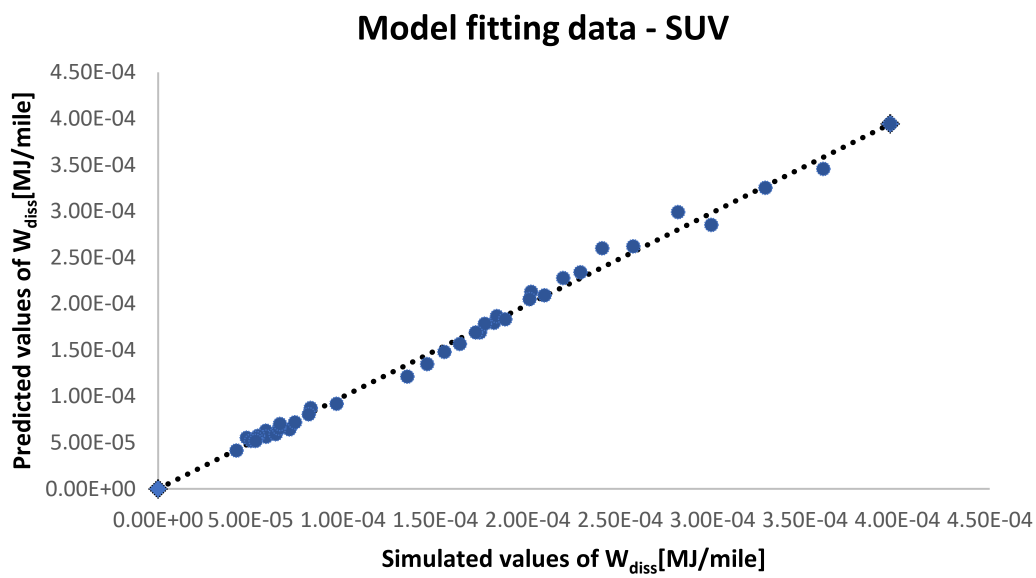

Figure 6.10 Model fitting for a SUV

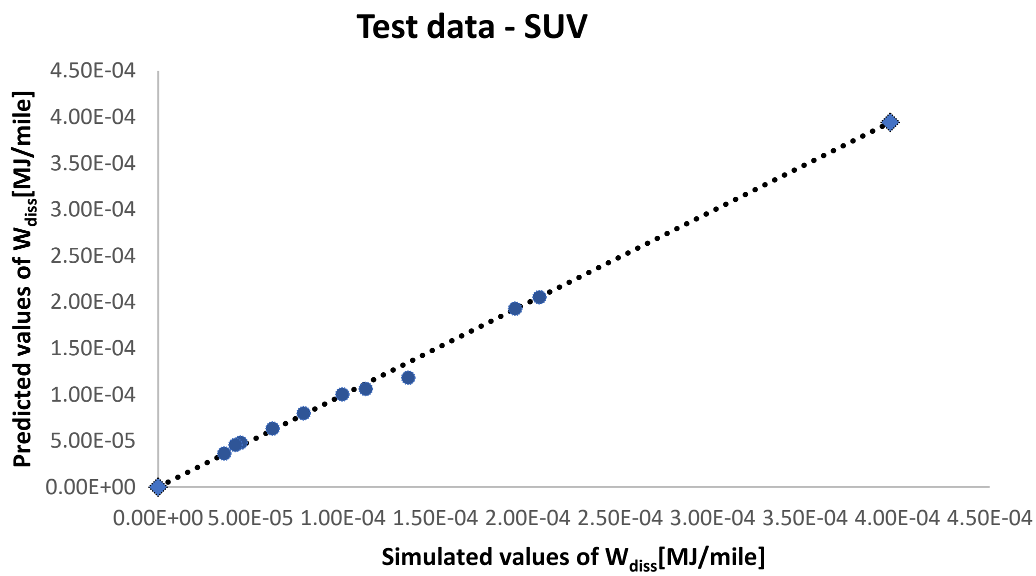

Figure 6.11 Model testing for a SUV

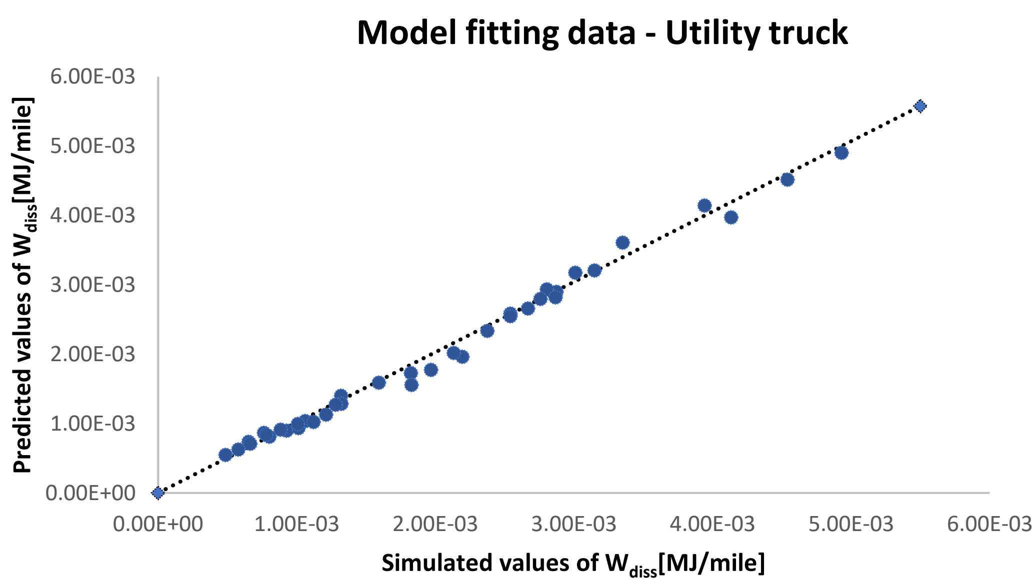

Figure 6.12 Model fitting for a F450 utility truck

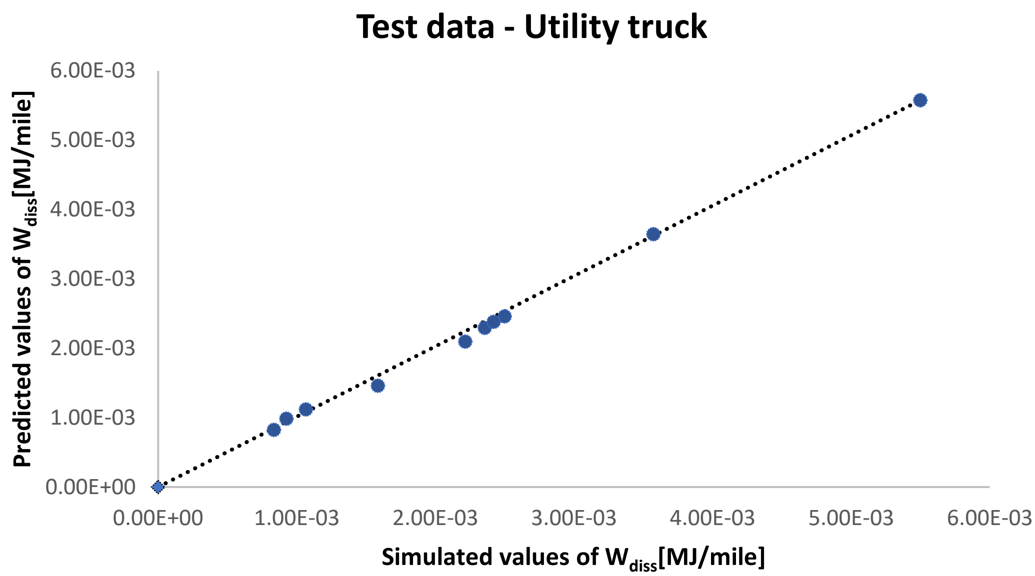

Figure 6.13 Model testing for a F450 utility truck

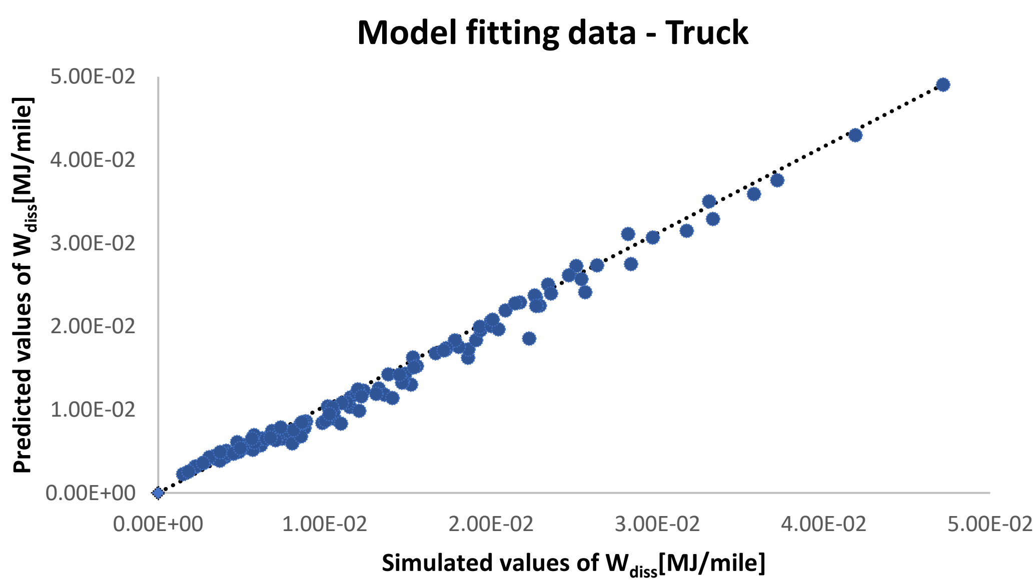

Figure 6.14 Model fitting for a heavy truck

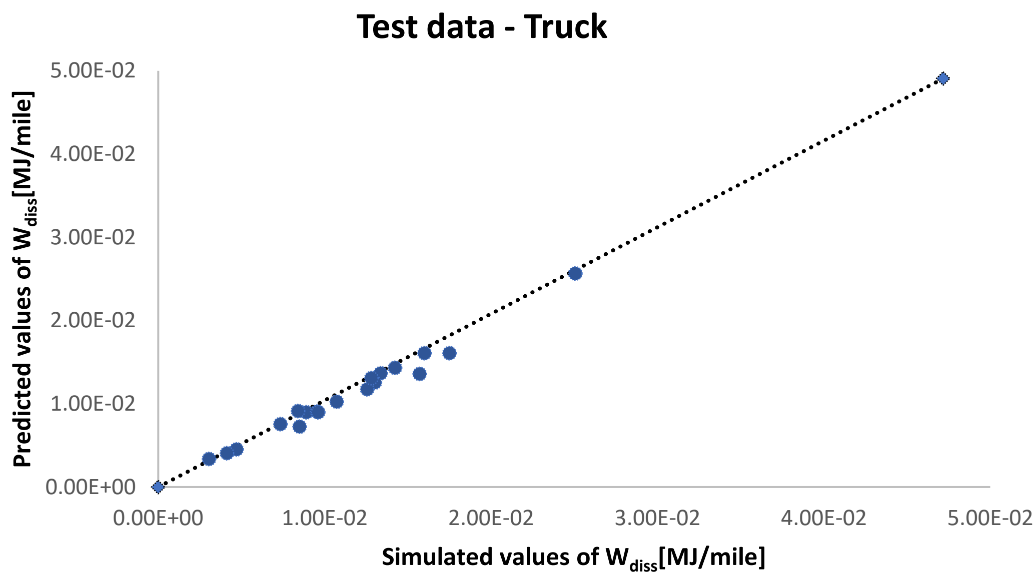

Figure 6.15 Model testing for a heavy truck

6.2.1 Use of penalized-likelihood criteria to choose the model form

The objective of this analysis is to check whether adding another variable to equation 6.1 could improve the results. The criteria used are the Akaike's Information Criteria (AIC) and the Bayesian Information Criteria (BIC). The AIC can be calculated as

$$AIC = -2\ln(likelihood) + 2K + 2K\frac{(K+1)}{(n-K-1)} \tag{6.9}$$

Or, in terms of the residual sum of square

$$AIC = n\ln\left(\frac{SRR}{n}\right) + 2K + 2K\frac{(K+1)}{(n-K-1)} \tag{6.10}$$

where

n is the number of data points,

K is the number of parameters used in the model.

In the present case study, the ratio *n/K* is smaller than 40. For this reason, the small sample bias adjustment $2K\frac{(K+1)}{(n-K-1)}$ has been added to the equation (Royall, 1997).

The best model can be chosen by comparing the Aikake weights (w_i) for the models, equation 6.11. The Aikake weight represents the probability for a model to be the best among the set of candidate models.

$$w_i = \frac{e^{-0.5\Delta_i}}{\sum_{i=1}^{m} e^{-0.5\Delta_i}} \qquad \Delta_i = AIC_i - AIC_{\min} \tag{6.11}$$

The BIC can be calculated as

$$BIC = n \cdot \ln\left(\frac{RSS}{n}\right) + K \cdot \ln(n) \tag{6.12}$$

The best model has a lower *BIC* value. The difference between the *BIC* of two models indicates the strength of the evidence against the model with a higher *BIC*.

$$\Delta BIC = n \cdot \ln\left(\frac{RSS_1}{RSS_2}\right) + (K_1 - K_2) \cdot \ln(n) \tag{6.13}$$

If $\Delta BIC < 2$ it is a weak evidence; if $2 < \Delta BIC < 6$ it is a moderate evidence; if $6 < \Delta BIC < 10$ it is a strong evidence; and if $\Delta BIC > 10$ it is a very strong evidence.

For the present case study, the value of the data points, namely the value of the energy dissipation due to the structural rolling resistance, are very small. Consequently, the values of the RSS are also very small, and the likelihood values are extremely high, which would make the use of the described criteria inaccurate. Therefore, it was decided to compare the logarithms of the results from the models, calculating RSS as

$$RSS = \sum_{i=1}^{n}\left(Log(y_i) - Log(f_i)\right)^2 \qquad (6.14)$$

The model shown in equation 6.1 was determined to be the best according to the *AIC* and *BIC* criteria after comparing it with several other models where more parameters were added.

An example is reported in Table 6.3, showing the results of the two criteria when comparing the model of equation 6.1, with the model shown in equation 6.15, where the variable *h* (slab thickness) and the parameter a_9 were added. The model with 8 parameters is preferable to the model with 9 parameters.

$$W_{diss} = a_1 \cdot c \cdot L^2 \cdot e^{\left(a_2 + a_3 \cdot v + a_4 \cdot \frac{LTE}{100} + a_5 \cdot E + a_6 \cdot k + a_7 \cdot c + a_8 \cdot R + a_9 \cdot h\right)} \qquad (6.15)$$

It should be noted that the radius of relative stiffness (*l*) is already proportional to $h^{3/4}$.

Table 6.3 Best model selection criteria summary – addition of parameter h

		Model with 8 param.	**Model with 9 param.**	**Best model using *AIC***	**Best model using *BIC***
CAR	*AIC*	-174.44	-171.11	Model with 8 param.	Model with 8 param.
	w	0.84	0.16		
	BIC	-163.16	-159.01		
	Δ*BIC*	4.2			
SUV	*AIC*	-173.03	-170.64	Model with 8 param.	Model with 8 param.
	w	0.77	0.23		
	BIC	-161.75	-158.54		
	Δ*BIC*	3.2			
F450	*AIC*	-167.50	-164.47	Model with 8 param.	Model with 8 param.
	w	0.82	0.18		
	BIC	-156.22	-152.36		
	Δ*BIC*	3.9			
TRUCK	*AIC*	-835.00	-833.27	Model with 8 param.	Model with 8 param.
	w	0.70	0.30		
	BIC	-812.31	-807.88		
	Δ*BIC*	4.4			

6.3 Truck class correction factor

For vehicles moving on concrete pavements the slope as seen by each tire depends on the axle configuration, and the tires of two axles with the same load can see a very different slope, as shown in Figure 4.4. For this reason, equation 6.1 requires as input the total load of the vehicle. The predictive function coefficients reported in Table 6.1 were developed from simulations conducted in chapter 5 (car, SUV, class 5 truck and class 11 truck), and, since the axle configuration plays an effect on the results, different coefficients were reported for the different vehicles. While for different types of cars and SUVs the axle configuration remains the same, for trucks the axle configurations vary depending on the truck class. Classes 6 to 13 trucks (Figure 6.16, Table 6.4) were simulated moving along the same sections to observe the dependency of the energy dissipation on the axle configuration.

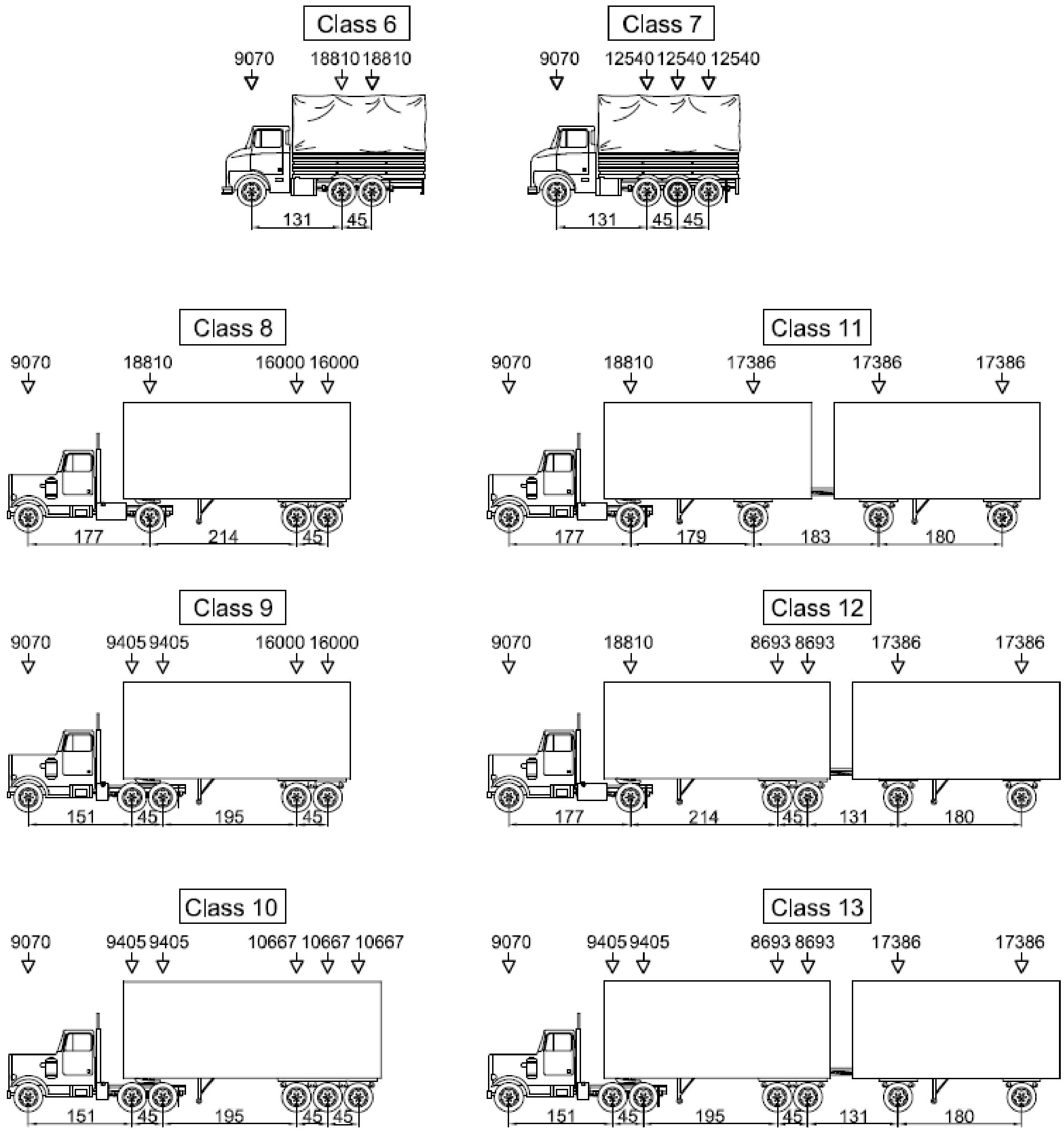

Figure 6.16 Truck classes – loads in [lbs], distances in [in]

Table 6.4 Truck classes total load

Class	Axles	Total load [kips]
6	single - tandem	46.69
7	single - tridem	46.69
8	single - single - tandem	59.88
9	single - tandem - tandem	59.88
10	single - tandem - tridem	59.88
11	single - single - single - single - single	80.04
12	single - single - tandem - single - single	80.04
13	single - single - tandem - single - single	80.04

It should be noted that the simulations have been conducted assuming the same total load for classes 6 and 7, 8-10 and 11-13, respectively. The actual total load is not relevant, since the purpose of these simulations is to determine a correction factor that allows the use of equation 6.1 (for which the total load is a variable) for different truck classes with different axle configurations.

The total energy dissipated by each truck class moving along sections PH01 and PH02 is shown in Figure 6.17.

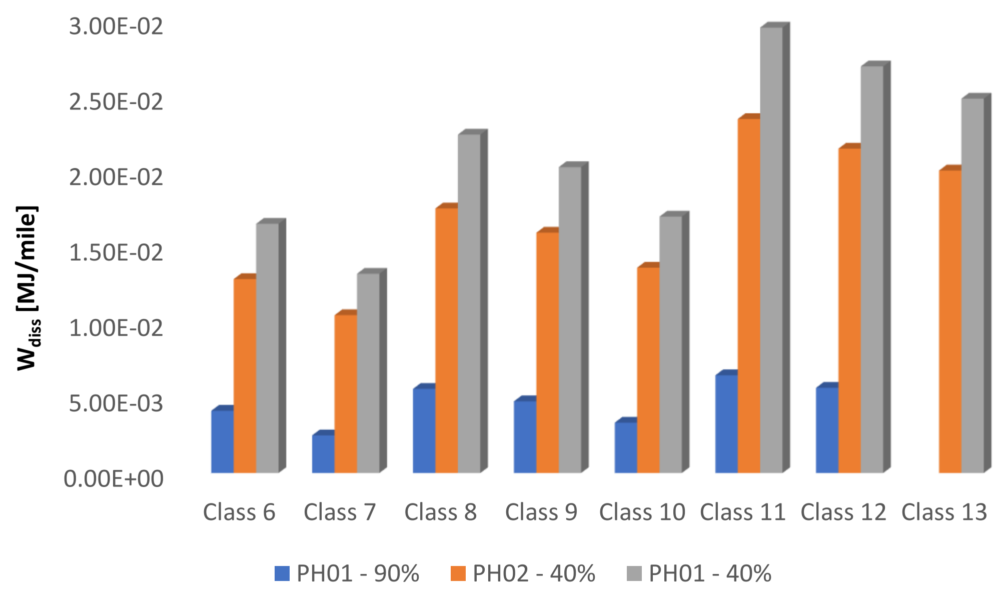

Figure 6.17 Energy dissipated by different truck classes

To compare the results for different truck classes with different loadings, the energy dissipated for a class N truck is weighted relative to the class 11 truck. According to Figure 6.5 and equation 6.1, the energy dissipated increases as the square power of the load; therefore the energy dissipated by a class N truck weighted to a class 11 truck is calculated as

$$W_{Diss}^{N}(Load^{11}) = W_{Diss}^{N}\left(Load^{N}\right)\cdot\left(\frac{Load^{N}}{Load^{11}}\right)^{2} \tag{6.16}$$

where

$Load^N$ is the load of a class N truck,

W^N_{diss} $(Load^{11})$ is the energy dissipated by a class N truck weighted as a class 11 truck,

W^N_{diss} $(Load^N)$ is the energy dissipated by a class N truck.

The correction factor for the class N truck is obtained as the ratio of the energy dissipated by the class N truck weighted as a class 11 truck to the energy dissipated by the class 11 truck.

$$C_f^N = \frac{W_{Diss}^{N}\left(Load^{11}\right)}{W_{Diss}^{11}\left(Load^{11}\right)} \tag{6.17}$$

Figure 6.18 shows the value of the correction factor based on simulations conducted on sections PH01 and PH02 (40% LTE). The correction factor can be assumed to be independent of the section's mechanical characteristics, except for the load transfer efficiency, which has an effect on C_f, as shown in Figure 6.19. The correction factors for each class have been fitted to equation 6.18 to account for different LTE values.

$$C_f^N = b_1^N \cdot LTE^2 + b_2^N \cdot LTE + b_3^N \tag{6.18}$$

The values of the b_i^N coefficients for the class N truck and the quality of the fit are reported in Table 6.5.

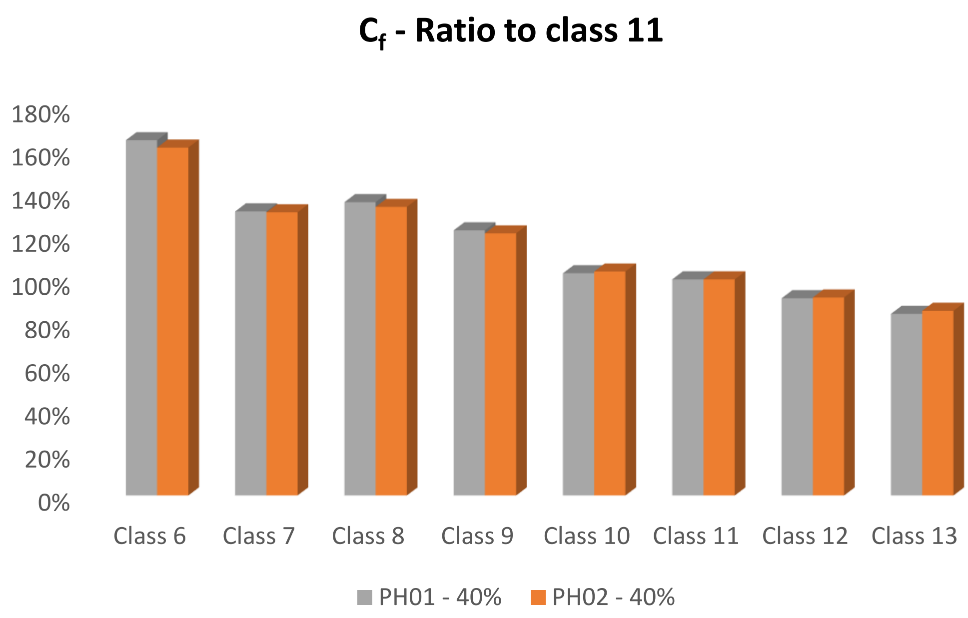

Figure 6.18 Truck class correction factor – PH01 and PH02

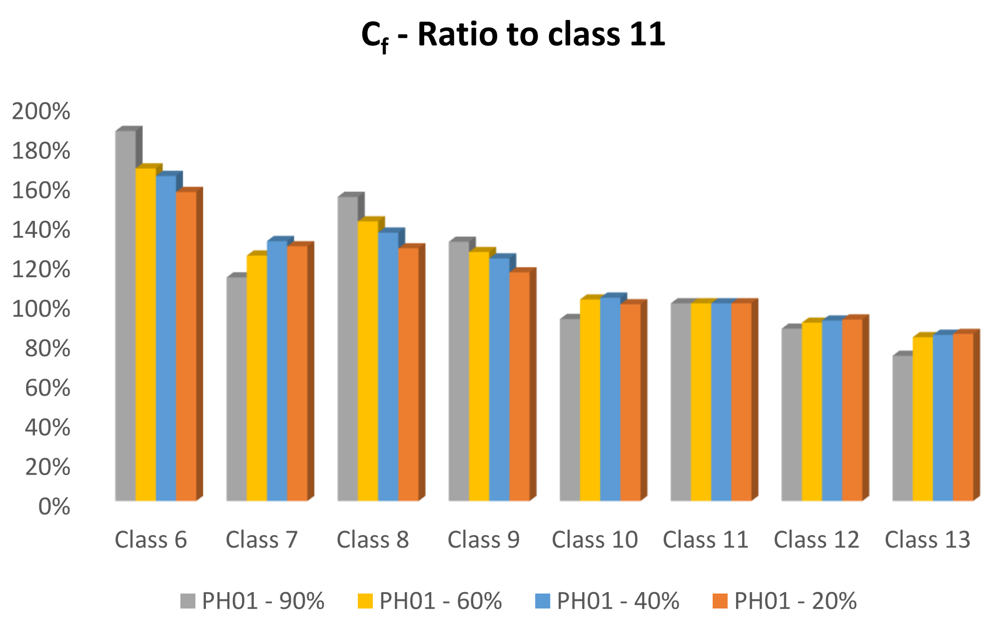

Figure 6.19 Truck class correction factor for different LTE values

Table 6.5 Parameters showing quality of the fit for C_f^N

	b_1	b_2	b_3	R^2	MAPE [%]
Class 6	3.33E-05	5.73E-04	1.546	0.98	0.8
Class 7	-4.84E-05	2.93E-03	1.256	0.97	0.9
Class 8	4.97E-06	3.11E-03	1.217	1	0.4
Class 9	-1.70E-05	4.02E-03	1.086	0.99	0.4
Class 10	-5.54E-05	5.03E-03	0.916	1	0.0
Class 12	-8.34E-06	2.58E-04	0.916	1	0.0
Class 13	-3.46E-05	2.27E-03	0.811	0.99	0.5

6.4 Shoulder effect

The concrete sections described in chapter 5 have asphalt shoulders and the load transfer efficiency between slabs in the transversal direction is very low, as tie bars are not present. For these reasons the simulations - on which the proposed model of equation 6.1 was based - were conducted without including any shoulder or adjacent slabs. Additional simulations have been conducted to observe the effect of transversal bonding between slabs on the SRR energy dissipation, and the results are shown in section 4.3.2 (Figure 4.9 through Figure 4.11). A correction factor to account for the presence of shoulder or adjacent lane can be calculated using equation 6.19. The correction factor should not be applied in case of asphalt shoulders or if LTE=0. Also, the factor can never exceed the value of 1.

$$C_{f2} = C_1 \cdot C_2 \cdot C_3 = \frac{W_{diss\_with\ shoulder}}{W_{diss\_without\ shoulder}} < 1 \qquad (6.19)$$

where C_1, C_2 and C_3 account respectively for the longitudinal load transfer efficiency, the shoulder/adjacent slab width and the ratio of the Young modulus of the shoulder and the concrete slab. Equations 6.20 to 6.23 have been obtained by fitting logarithmic functions to the results showed in Figure 4.9 through Figure 4.11. C_1 is effectively the ratio of the energy dissipated due to the SRR when including a shoulder in the simulations to the energy dissipated without a shoulder. C_1 was calculated assuming that the elastic moduli of the slab and the shoulder are equal, and a width of the shoulder equal to 60 inches. C_2 and C_3 were obtained similarly, as the ratio of the energy dissipated due to the SRR with the baseline conditions used to determine C_1 to the energy dissipated when varying the shoulder/adjacent lane width and the Young modulus ratio.

$$C_1 = 0.87 - 0.046 \cdot Log_{10}(LTE + 0.131) - 0.104 \cdot \frac{LTE}{100} + \frac{0.892}{LTE + 10} \tag{6.20}$$

where LTE is the load transfer efficiency value expressed as a percentage.

$$C_2 = 1.182 - 0.094 Log_{10}(W + 0.017) \tag{6.21}$$

where W is the slab width in inches.

$$C_3 = 1.09 - 0.097 \cdot Log_{10}\left(\frac{E_{shoulder}}{E_{slab}} + 0.002\right) - 0.089 \frac{E_{shoulder}}{E_{slab}} \tag{6.22}$$

where E is the young modulus.

Figure 6.20 through Figure 6.22 show the fitting of C_1, C_2 and C_3, respectively. The quality of the fit is reported in Table 6.6.

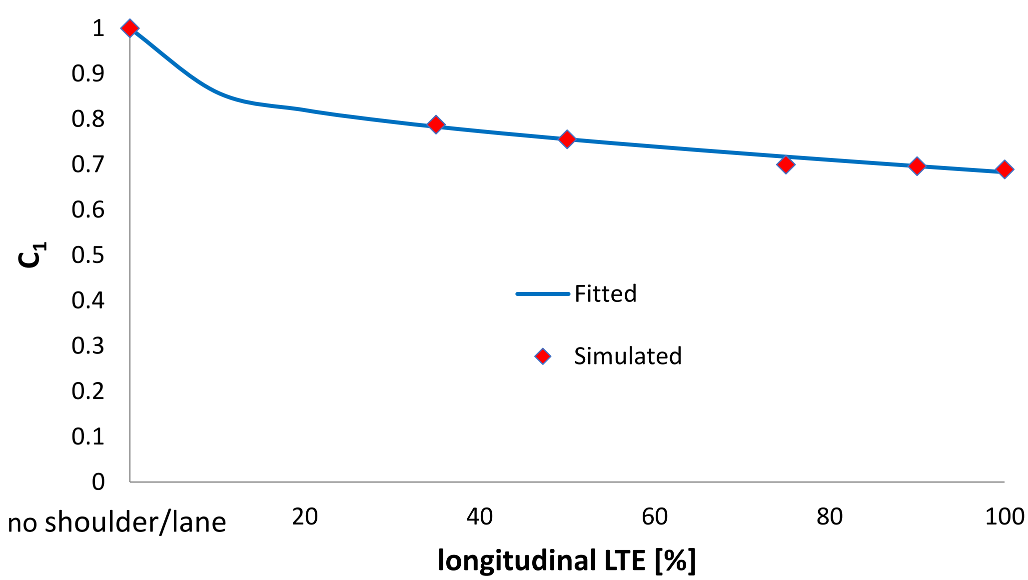

Figure 6.20 Fitting of C_1

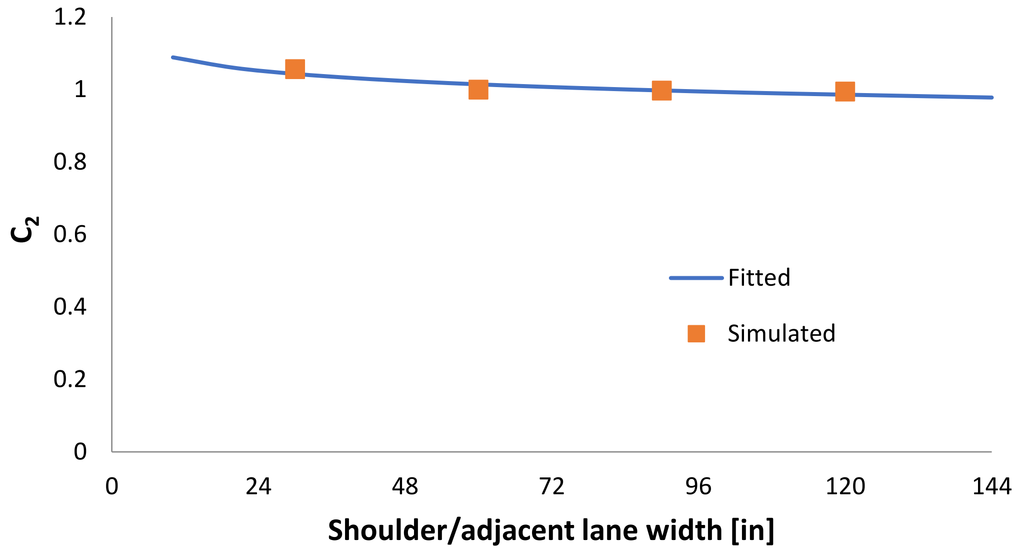

Figure 6.21 Fitting of C_2

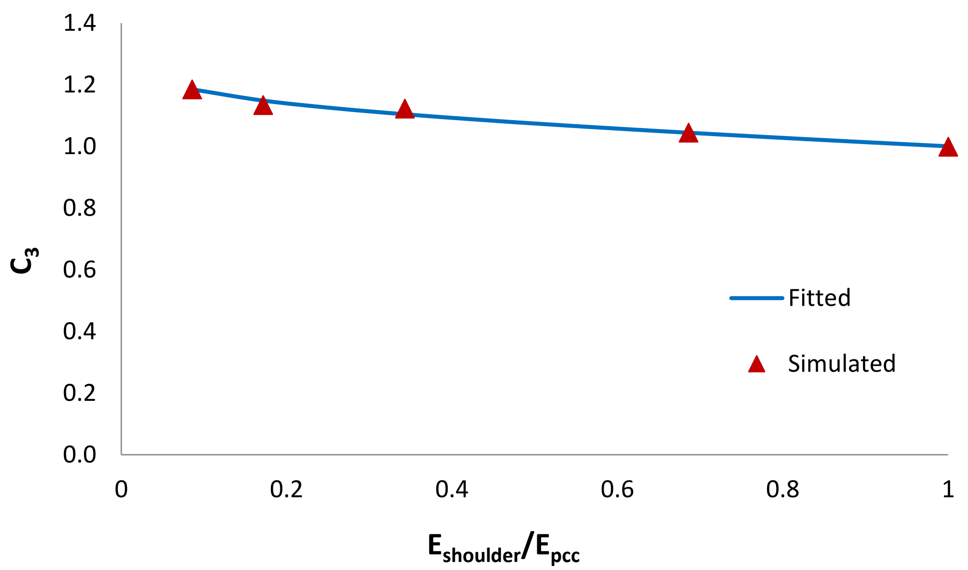

Figure 6.22 Fitting of C_3

Table 6.6 Parameters showing quality of the fit for C_1, C_2 and C_3

	R^2	MAPE [%]
C_1	1.00	0.67
C_2	1.00	0.72
C_3	0.99	0.51

7 DEVELOPMENT OF A PREDICTIVE FUNCTION FOR CALCULATING THE SRR ON ASPHALT PAVEMENT

In this chapter, a model that provides an estimate of the energy dissipated due to the structural rolling resistance on flexible, semi-rigid and composite pavements is presented. It can be used in a life cycle assessment (LCA) and life cycle cost (LCCA) analysis. The predictive function should allow network and project level calculations without having to conduct any simulations of moving vehicles.

7.1 Fitting of the predictive function for each section

The effect of the pavement characteristics and the loading conditions on the energy consumption due to the SRR have been investigated to determine the functional form of the predictive model. Unlike for rigid pavements, where the entire pavement could be defined using only 5 variables (E, h and LTE to characterize the slabs, k and c for the subgrade), for flexible pavements each layer is described by 4 parameters: elastic modulus (E) for the unbound layers or relaxation modulus ($E(t)$) for the HMA layer , thickness (h), Poisson ratio (v) and density (ρ) (assuming the same small damping coefficient in each unbound layer).

Another difference from concrete pavements is the effect of tire pressure. Jointed concrete pavements are not continuous, and the way the loads are located on the slabs affects the pavement response, which means that different load configurations (vehicle types) are better described by different model coefficients. Asphalt pavements are modeled as continuous, and a single model can be used for any vehicle. The tire pressure of a car and a truck is significantly different, and, as shown in Figure 7.1, the same force does not produce the same SRR energy dissipation on asphalt pavements for different pressure/loading areas. For this reason, tire pressure is to be included in the model.

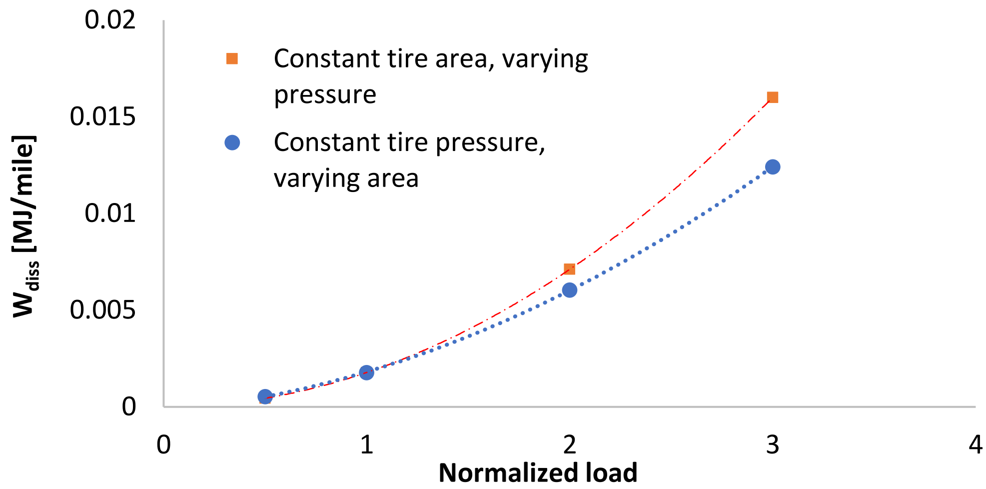

Figure 7.1 Energy dissipated due to the SRR as a function of the normalized load for different tire pressures and contact areas

While each pavement section can be easily fit to a model like the one developed for concrete pavements, it becomes a very hard task to develop a single model which includes all the layer parameters. The characteristics of each layer have a different impact on the structural rolling resistance (Figure 7.18 -Figure 7.21), and different pavement structures can have different number or type of layers. Considering this, a different approach will be used to develop the general predictive function for asphalt pavements.

In the first place, each individual section is fitted to a predictive function that is based only on the temperature and loading condition (eq. 7.1). The form of the function to predict the energy dissipation due to the SRR for each individual section is:

$$W_{diss} = L^2 \cdot (1+\delta) \cdot \exp\left(a_1 + a_2 \cdot (30+T) + a_3 \cdot v + a_4 \cdot \frac{L \cdot (1+\delta)}{p}\right) \tag{7.1}$$

where:

a_1-a_4 are the model coefficients which depend on the pavement section,

L is the tire load [kip],

v is the vehicle speed [mph],

T is the pavement temperature, assumed to be constant and equal to the temperature at 1/3 depth of the HMA layer [°C],

p is the tire pressure [psi],

δ is a coefficient equal to 0 for a single tire, and to (T+30) · a_5 for dual tires.

The temperature at 1/3 depth of the HMA layer is calculated using the Bells 3 equation:

$$\begin{aligned} T_d &= 0.95+0.892IR+\left(Log(d)-1.25\right)\left[-0.448IR+0.621(1day)+1.83\sin(h_{r18}-15.5)\right] \\ &+0.042IR\sin(h_{r18}-13.5) \end{aligned} \qquad (7.1b)$$

where:

T_d is the pavement temperature at depth d [°C],

IR is the pavement surface temperature [°C],

d is the depth at which the material temperature is to be predicted [mm],

1day is the average air temperature the day before testing [°C],

h_{r18} is the time of day, in a 24-hr clock system, but calculated using an 18-hr asphalt concrete (AC) temperature rise-and-fall time cycle.

The coefficients a_1-a_5 have been obtained by minimizing the function

$$f=\sum_{i=1}^{n}\left(\frac{1}{Log_{10}(y_i)}-\frac{1}{Log_{10}(f_i)}\right)^2 \qquad (7.2)$$

where y_i are the values of energy dissipated obtained from the mechanistic simulations showed in chapter 5, and f_i are the values of energy dissipated predicted by equation 7.1.

The predictive function of equation 7.1 has a similar form to equation 6.1, and can predict very well the energy dissipated for a specific pavement structure, as reported in Figure 7.2 - Figure 7.17. As already discussed, for JPCP the axle configuration is important for the calculation of the W_{diss}, as it affects the slab deflection, and therefore the predictive function of eq. 6.1 calculates the energy dissipated by the entire vehicle. For asphalt pavements, the effect of the proximity of the wheels is discussed in section 7.4. The model proposed for asphalt pavements provides the energy dissipated by a single tire. The energy dissipated by a vehicle can be calculated by summing up the energy dissipated by each tire.

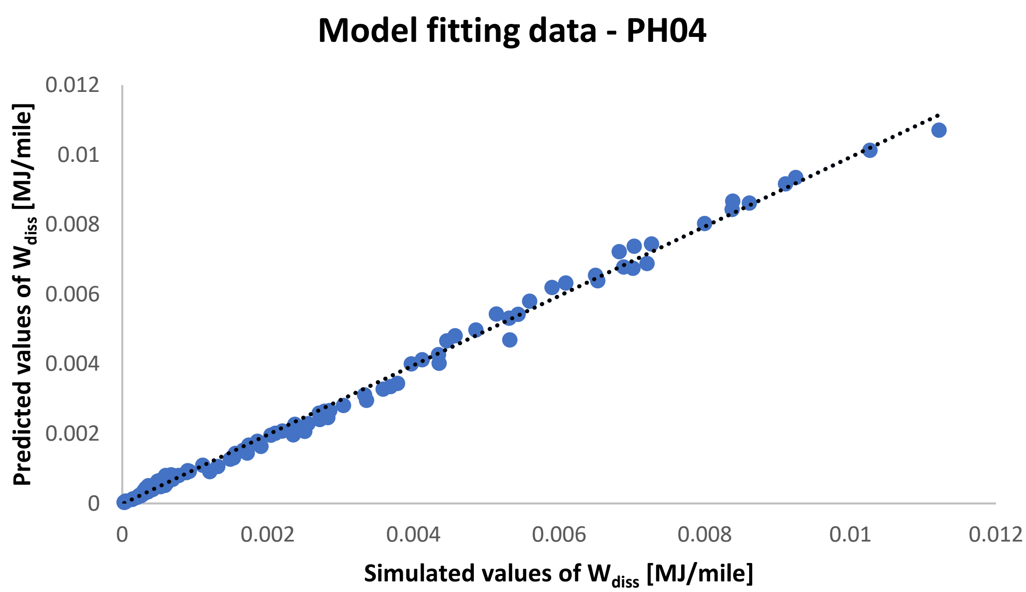

Figure 7.2 PH04 model fitting

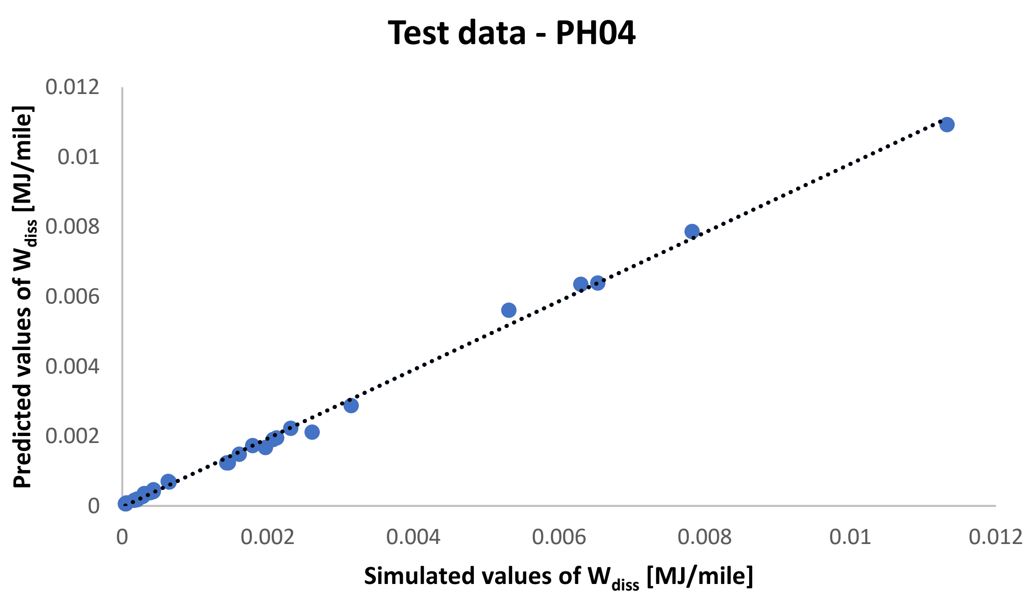

Figure 7.3 PH04 model testing

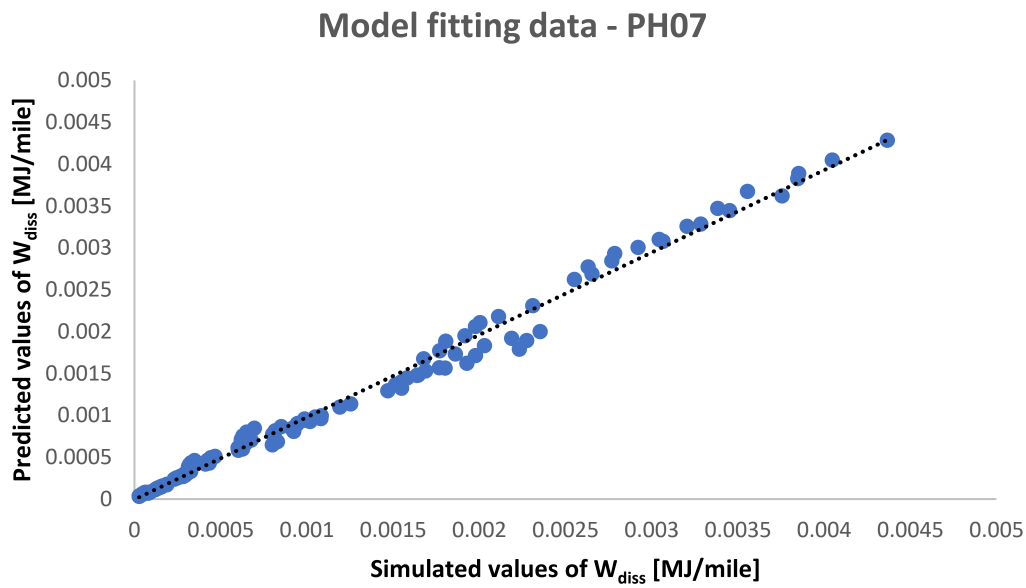

Figure 7.4 PH07 model fitting

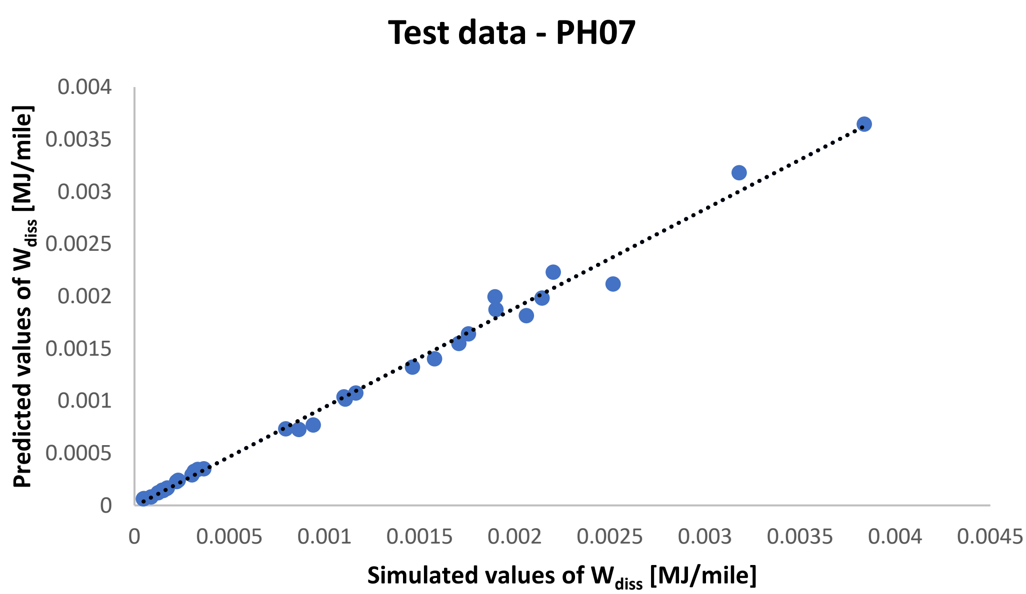

Figure 7.5 PH07 model testing

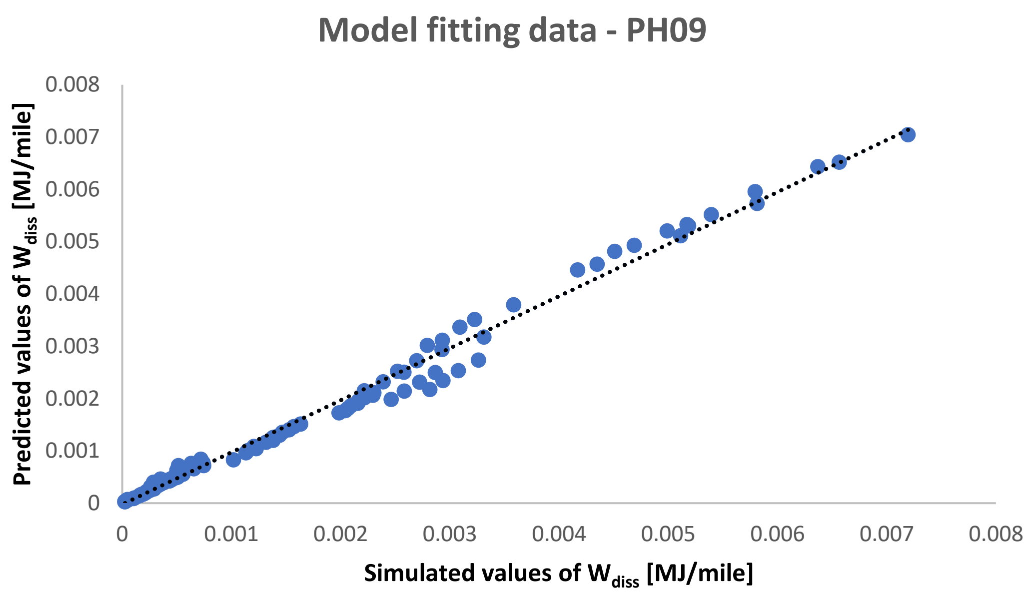

Figure 7.6 PH09 model fitting

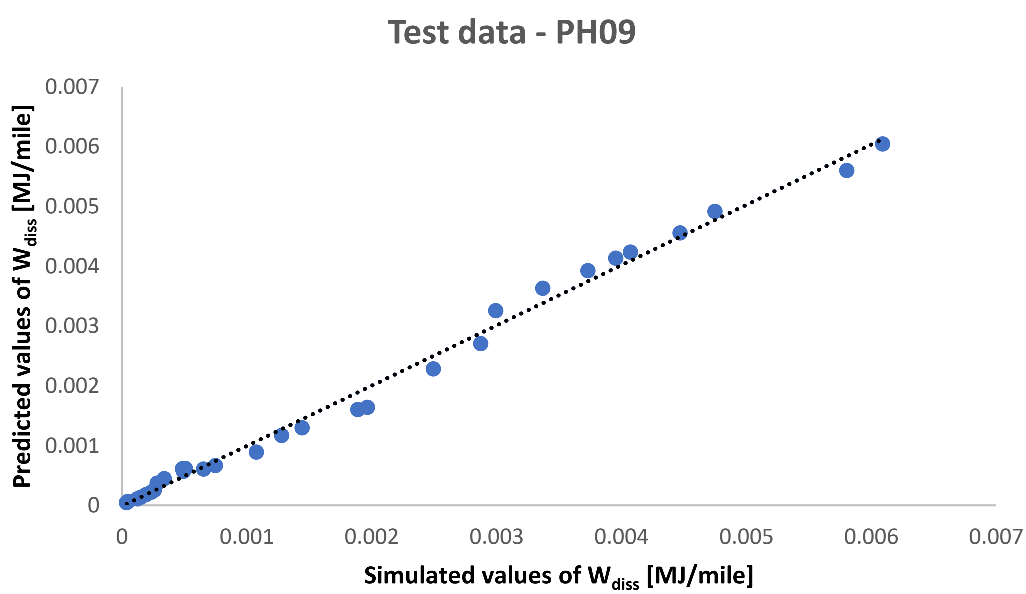

Figure 7.7 PH09 model testing

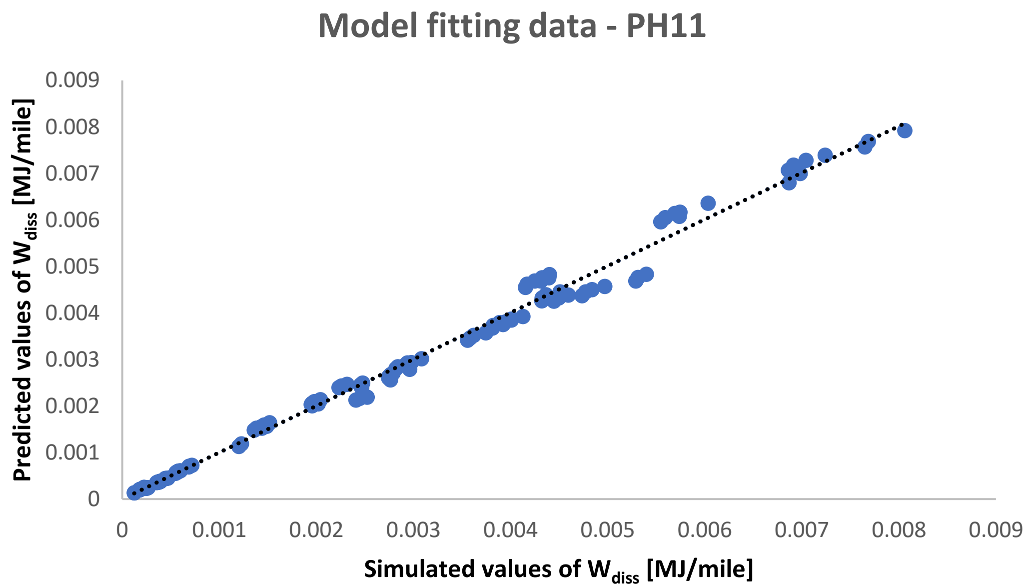

Figure 7.8 PH11 model fitting

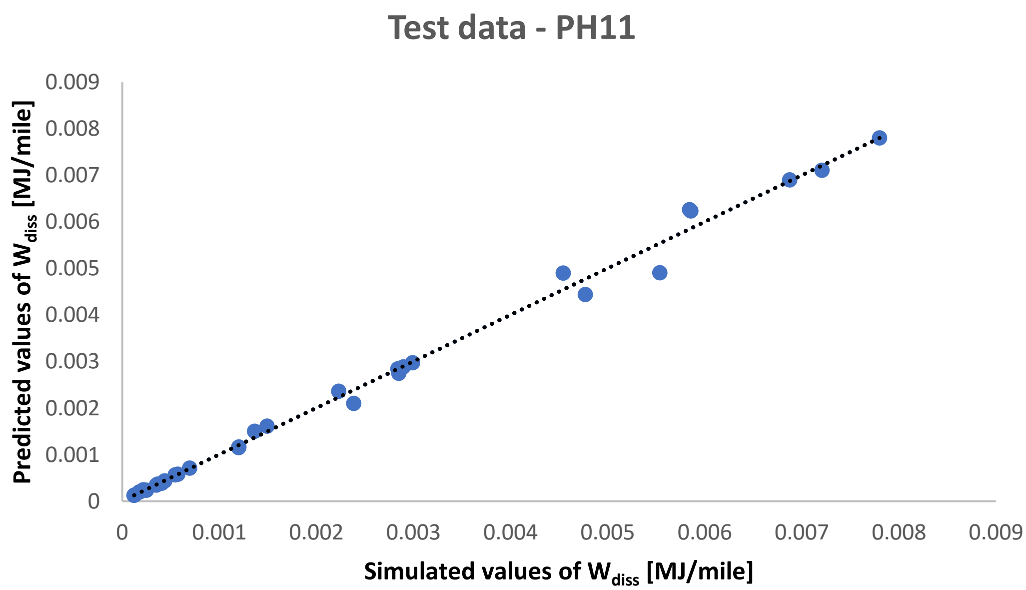

Figure 7.9 PH11 model testing

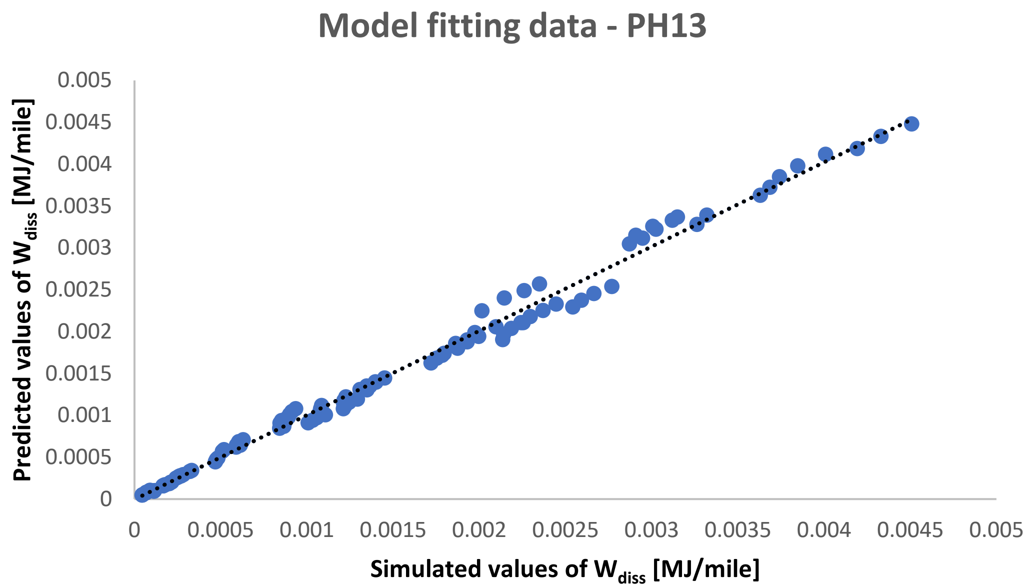

Figure 7.10 PH13 model fitting

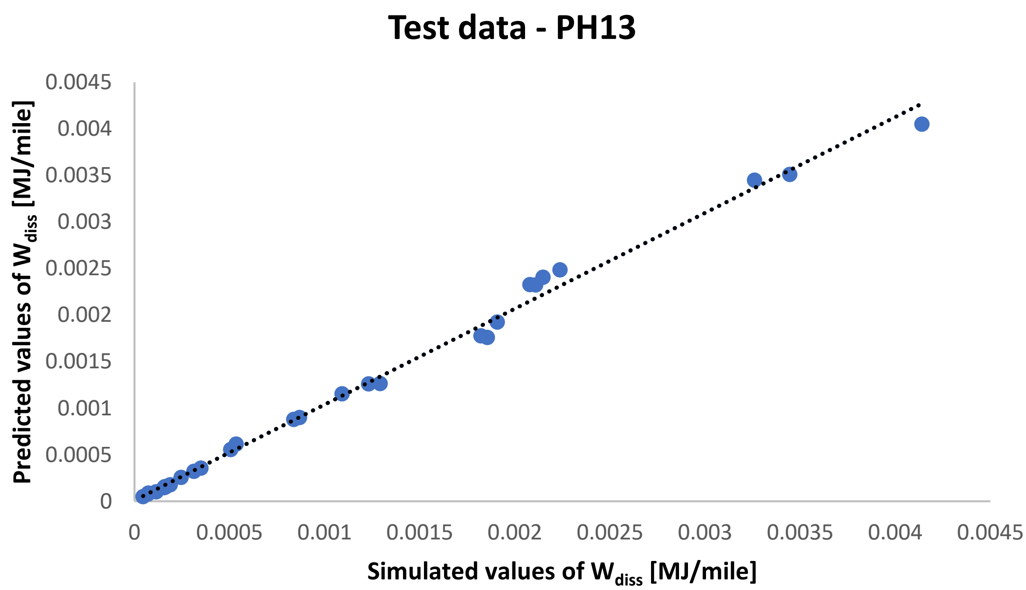

Figure 7.11 PH13 model testing

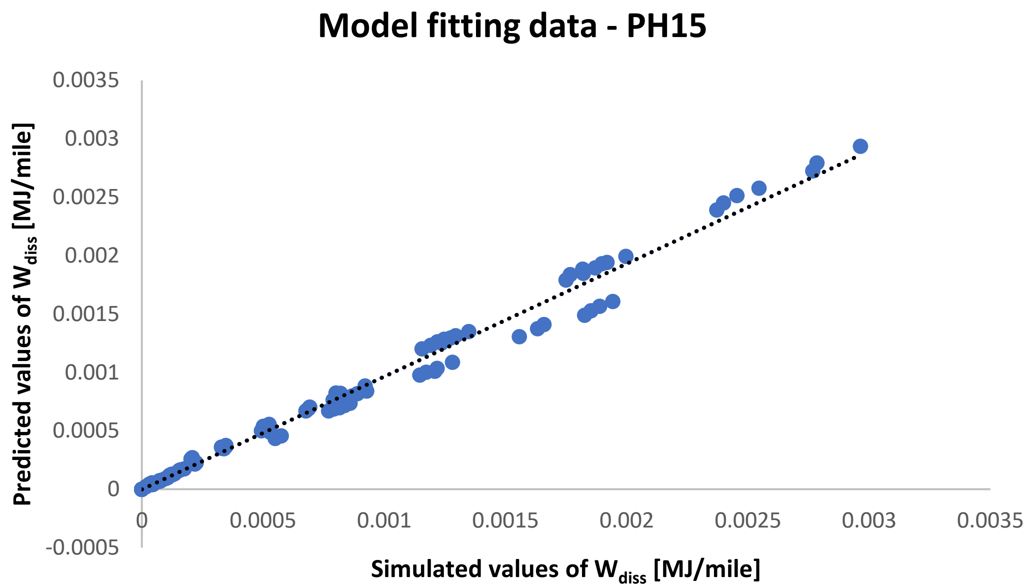

Figure 7.12 PH15 model fitting

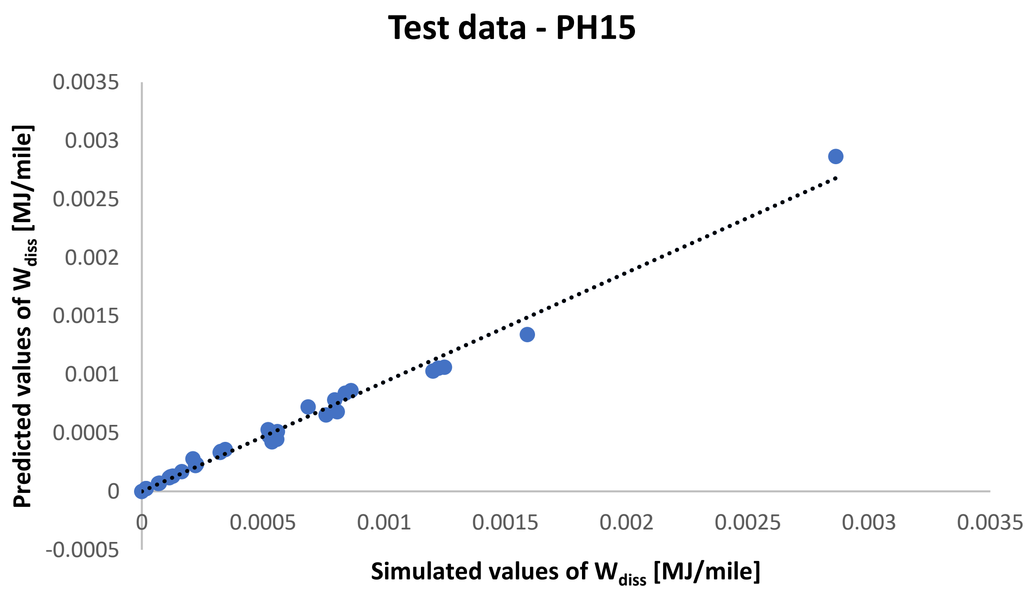

Figure 7.13 PH15 model testing

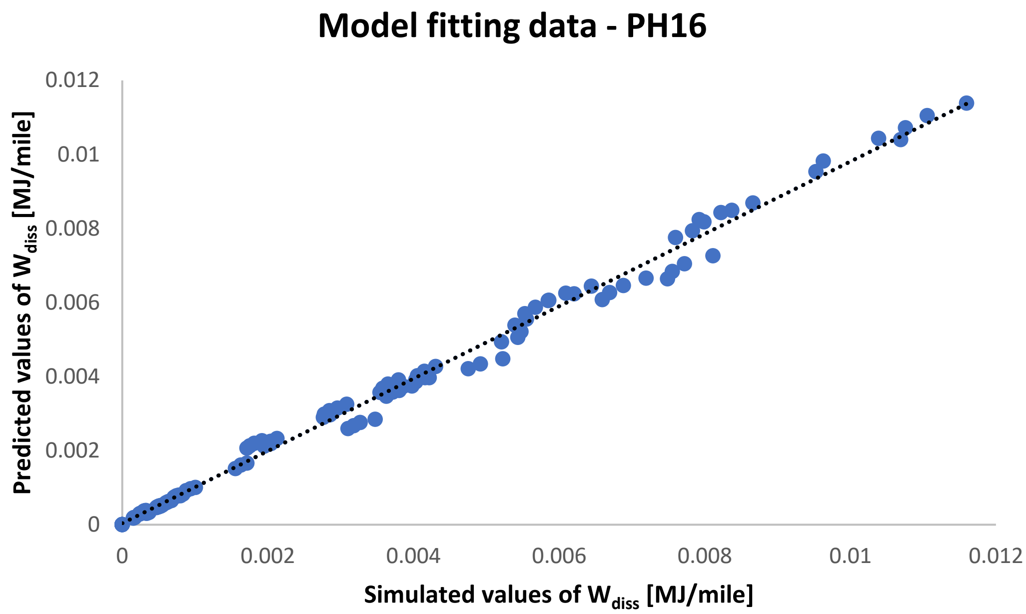

Figure 7.14 PH16 model fitting

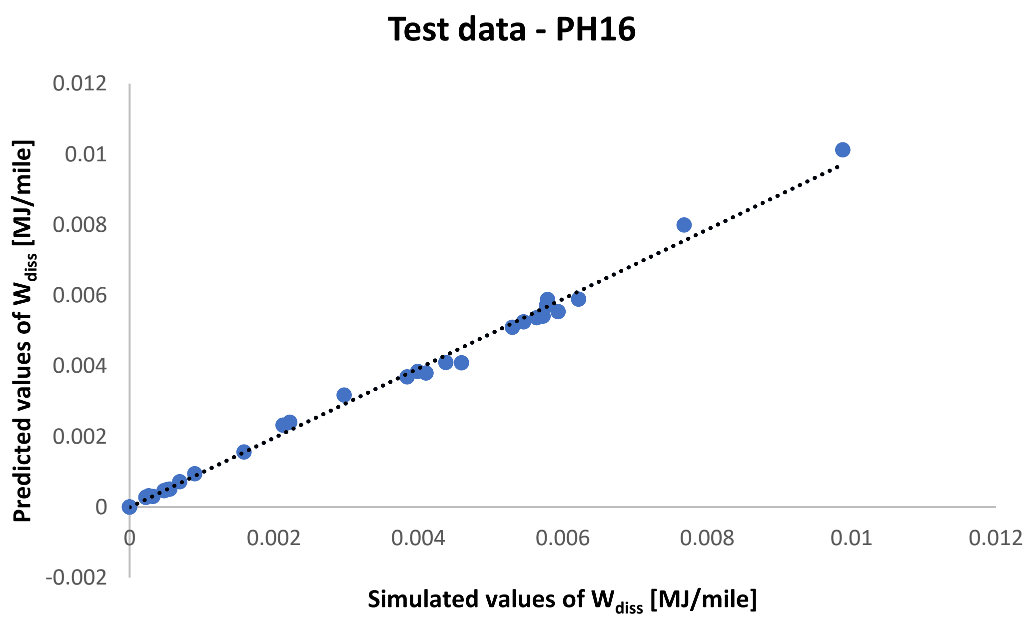

Figure 7.15 PH16 model testing

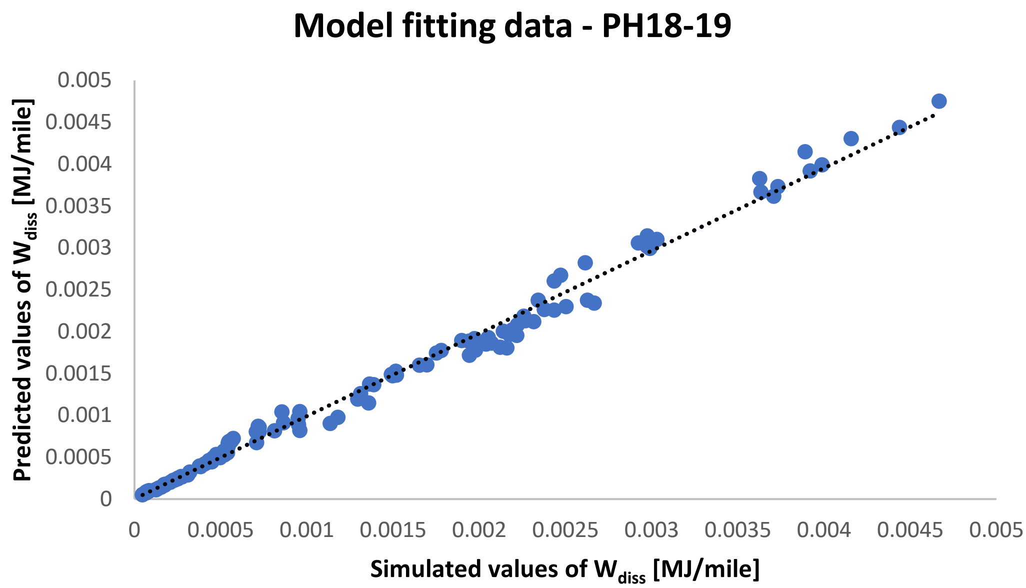

Figure 7.16 PH18 and 19 model fitting

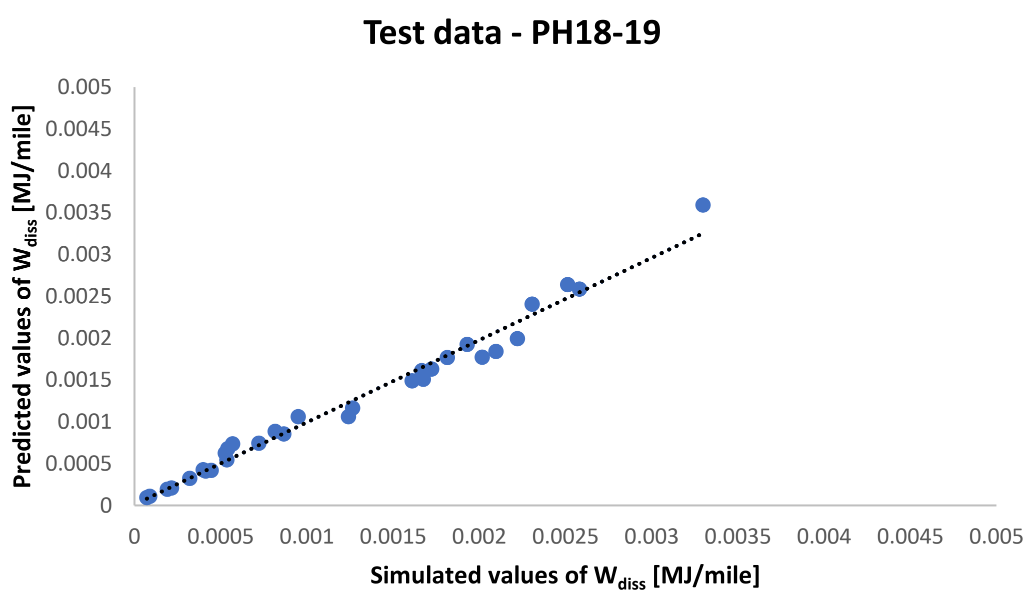

Figure 7.17 PH18 and PH19 model testing

7.2 Parametric analysis

A parametric analysis has been conducted to observe the effect of the characteristics of each layer on W_{diss}; Figure 7.18 - Figure 7.21 show the results for section PH15. The Poisson's ratio and the density of the layers have negligible effects on the value of W_{diss}; however, the thickness and stiffness of each layer are important. The effect of layer thickness and elastic modulus depend on the layer. In general, the closer to the surface, the more the parameter affects the calculation of W_{diss}. For example, Figure 7.18a shows an exponential relation between the thickness of the top layer and energy consumption, while Figure 7.18b shows a linear relation between the base layer thickness and energy consumption. This makes it harder to develop a model that depends directly on the layers characteristics, as for different pavement structures the results will change significantly. Moreover, the stiffness of the top layer depends on temperature and loading conditions.

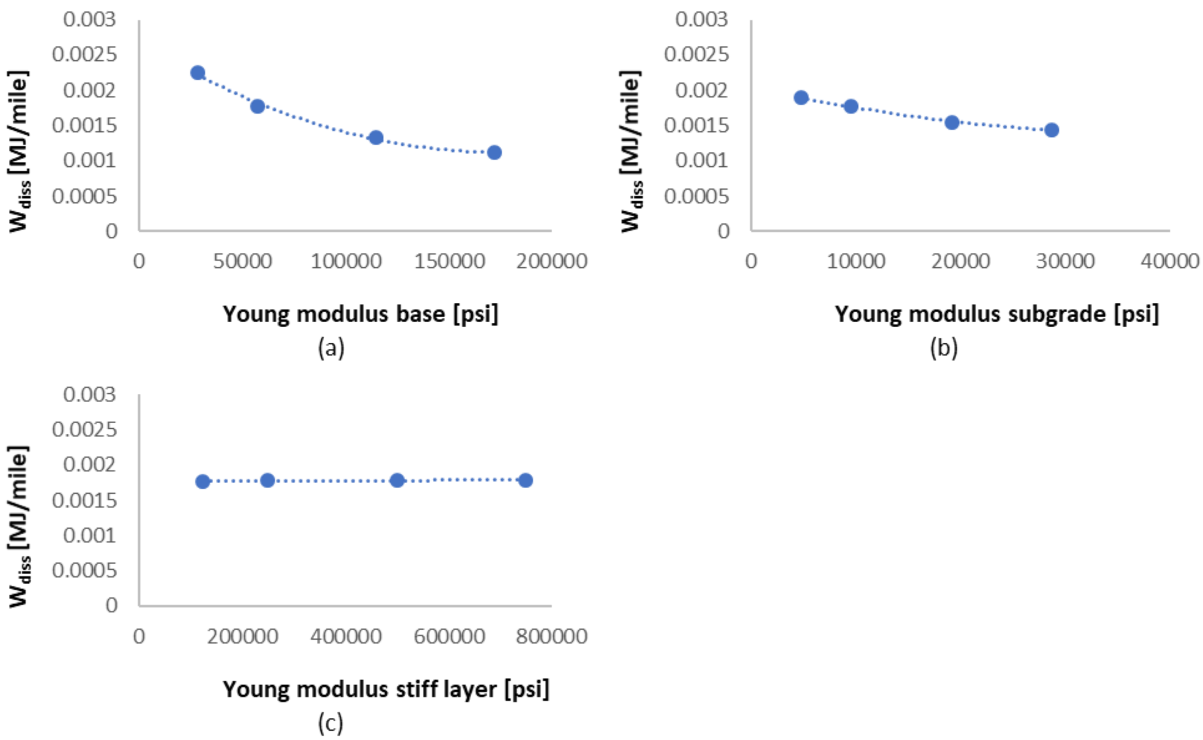

Figure 7.18 Energy dissipated due to the SRR as a function of the modulus of (a) base, (b) subgrade, (c) stiff layer

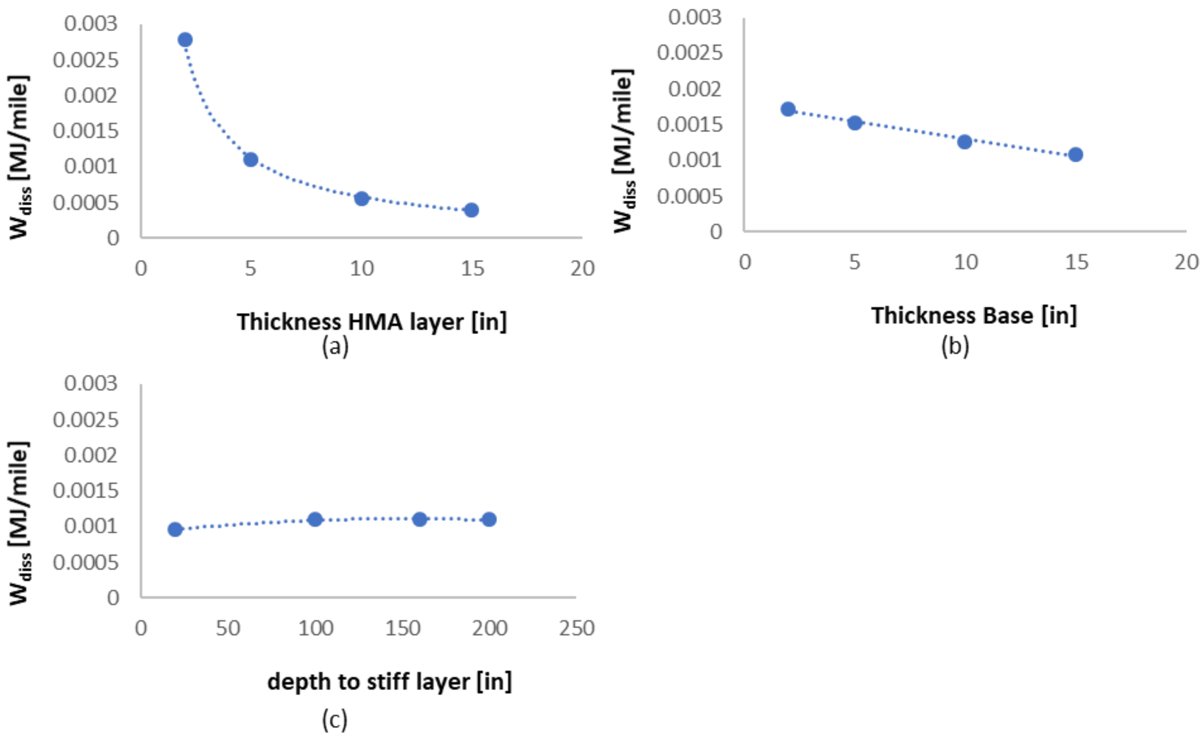

Figure 7.19 Energy dissipated due to the SRR as a function of (a) HMA layer thickness, (b) base thickness, (c) depth to the stiff layer

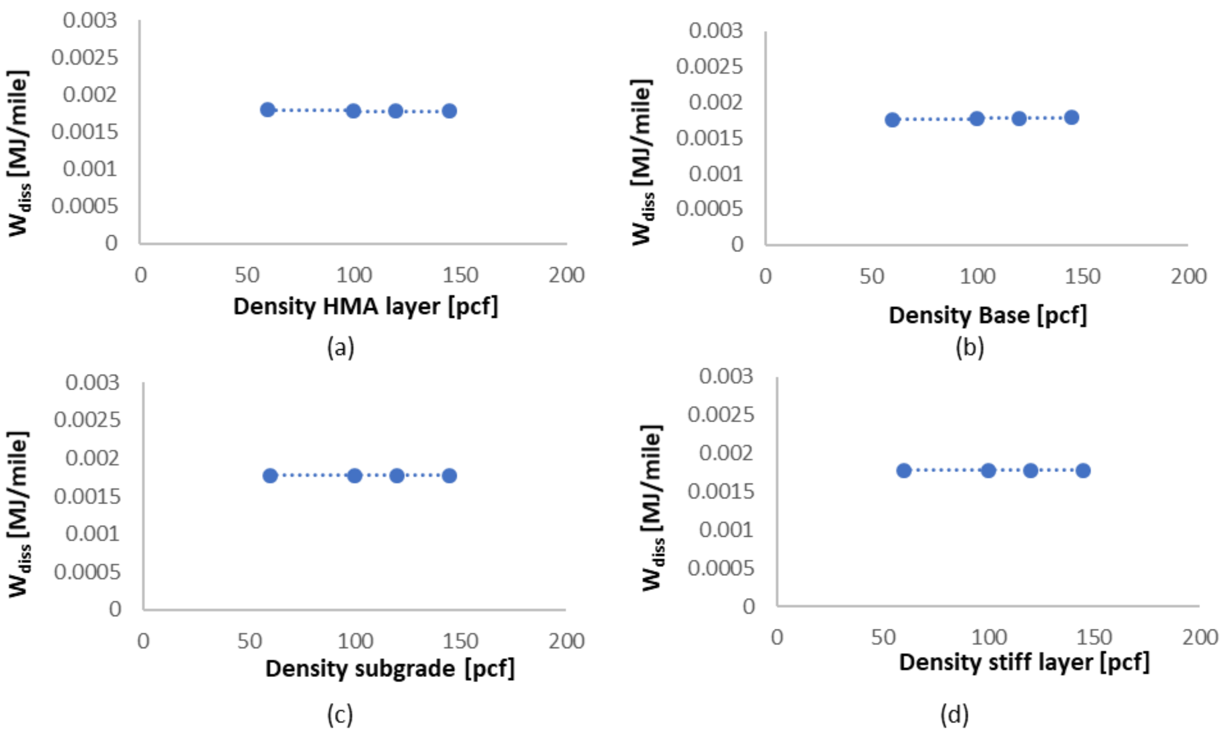

Figure 7.20 Energy dissipated due to the SRR as a function of density of (a) HMA layer, (b) base, (c) subgrade, (d) stiff layer

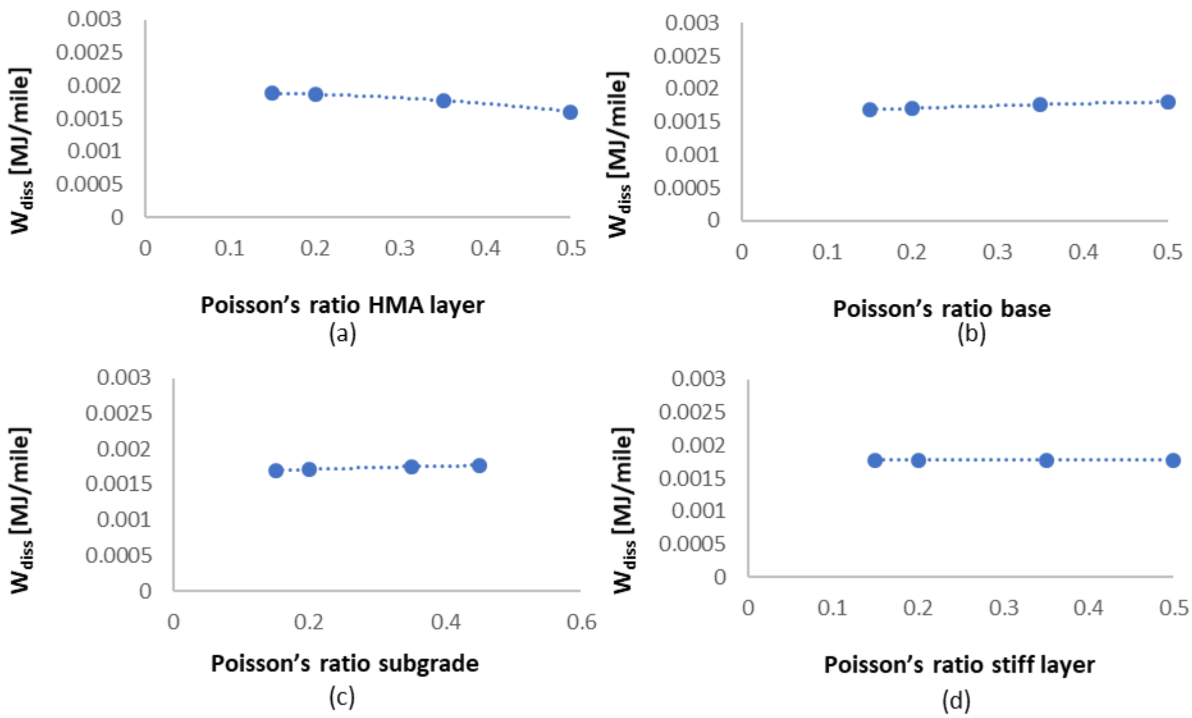

Figure 7.21 Energy dissipated due to the SRR as a function of Poisson's ratio of (a) HMA layer, (b) base, (c) subgrade, (d) stiff layer

It could be noted that the effect of temperature, load etc. on the energy dissipated would not be the same for two pavements with the same structure and layer properties, but different HMA Relaxation modulus. So, for the model to be realistic, the coefficients (a_1-a_5) of equation 7.1. should depend on the pavement characteristics. The viscoelasticity of the HMA layer is what mostly causes the SRR. Also, as shown in Figure 7.18 and Figure 7.19, pavements with stiffer/thicker layers dissipate less energy; if a pavement deflects more, the slope will be higher. Therefore, it has been decided to characterize the pavement using the phase angle of the HMA layer at three specific temperatures and the pavement deflection under a specific load at the same temperatures. The phase angle gives information about the viscous properties of the AC layer and the pavement deflection about the stiffness of the entire structure.

7.3 Fitting a general predictive function for any asphalt section

Each model coefficient a_1-a_5 is then fit to an equation that depends on the pavement deflection under a static load and the sine of the phase angle at specific temperatures. Eight sections were used to calculate the coefficients, and two were used as control. These equations are reported in equations 7.3 - 7.7, and their fitting is shown in Figure 7.22. By fitting the model coefficients a_1-a_5, instead of the predicted values of energy dissipation (which was done for each individual section), a condition to limit the error for larger values of W_{diss} cannot be imposed.

$$a_1 = -16.818 + 2.526 \cdot D_{40} + 0.090 \cdot \frac{D_{40}}{D_{15}} - 7.800 \cdot (\sin\theta_{40} - \sin\theta_{15}) + 9.576 \cdot D_{40} \cdot \sin\theta_{40} \quad (7.3)$$

$$a_2 = \exp(-2.97 - 1.90 \cdot \sin\theta_{40} - 27.44 \cdot (\sin\theta_{40} - \sin\theta_{30}) + 13.30 \cdot (\sin\theta_{40} - \sin\theta_{15})) \quad (7.4)$$

$$a_3 = 0.00143 \cdot \exp(0.00102 \cdot (\sin\theta_{40}) + 0.00101 \cdot (\sin\theta_{15}) + 0.001 \cdot (\sin\theta_{40} - \sin\theta_{15}) + 0.33187 \cdot (D_{40} - D_{15}) + 0.09383/D_{15}) \quad (7.5)$$

$$a_4 = -0.0438 - 0.9280 \cdot D_{40} - 0.9699 \cdot \frac{D_{40}}{h_{HMA}} \quad (7.6)$$

$$a_5 = \exp(-4.51 + 134.83 \cdot D_{40} \cdot \sin\theta_{40} - 144.12 \cdot D_{30} \cdot \sin\theta_{30} - 10.82 \cdot (\sin\theta_{40} - \sin\theta_{15}) - 39.94 \cdot (D_{40} - D_{15})) \quad (7.7)$$

D_{40}, D_{30}, D_{15}, θ_{40}, θ_{30}, θ_{15} are the pavement deflection and the phase angle at 40, 30 and 15^o C, respectively, and should be calculated as follows:

- Assume that the loading frequency is 10.73 Hz at 15 °C, 19.46 Hz at 30°C and 25.30 Hz at 40°C. These frequencies are representative of a moving truck, and are chosen arbitrarily, based on on the equations from Losa and Di Natale (*2012*) - equations 7.8 and 7.9 - to calculate the equivalent loading frequency of a moving vehicle.

$$f_z = 0.043\,\frac{V}{2a}e^{-2.65z + \beta(T)} \tag{7.8}$$

where:

f_z is frequency in z direction [Hz],

V is the speed [m/s],

a is half-length of the rectangular footprint in the direction of motion [m],

z is the depth in asphalt concrete layer [m], $0.037 < z \leq 0.30$ m for f_z,

$\beta(T)$ is the effect of asphalt concrete temperature in the z-direction.

$$\beta(T) = 1.25 \cdot 10^{-5}\mathrm{T}^3 - 1.6 \cdot 10^{-3}\mathrm{T}^2 + 9.2 \cdot 10^{-2}\mathrm{T} \tag{7.9}$$

From Table C.3, the area of the tire print for the front axle of the loaded truck is 42.16in^2 = 0.0272 m^2, a = ½ (0.0272 m^2)$^{0.5}$ = 0.0824 m. Assuming V = 35 mph = 15.65 m/s, f_z = 10.73 Hz at 15°C, 19.46 Hz at 30°C and 25.30 Hz at 40°C.

These frequencies are only meant to be used to determine D_{40}, D_{30}, D_{15}, θ_{40}, θ_{30}, θ_{15}, parameters that represent the pavement behavior at different temperatures and a given loading condition.

- Using the shift factor and the loading frequencies given in step 1, calculate the reduced frequency, then use it to determine the equivalent elastic modulus from the HMA mastercurve and the phase angle at 40, 30 and 15 °C. The mastercurve and the relation between reduced frequency and phase angle can be obtained from the relaxation modulus if not known.
- Calculate the pavement deflection under a static circular load (9000lbs, 12in plate diameter – chosen arbitrarily) assuming an elastic behavior of the HMA layer, and using the three equivalent elastic moduli from step 2 to get D_{40}, D_{30} and D_{15}.

The calculation of the pavement deflection under a static load is simple and can be done using tools such as OpenPave (*Lea, undated*).

The parameters a_1-a_5 are only used to describe the pavement structure, and are chosen to be independent of the loading conditions, which only come into play in equation 7.1.

The fitting of equations 7.3 - 7.7 is shown in Figure 7.22. Seven sections were used for the fitting (full dots), and 2 sections for control (empty dots).

Figure 7.23 and Figure 7.24 show the results of substituting equations 7.3 - 7.7 in equation 7.1. It can be observed that the error grows for larger values of energy dissipation.

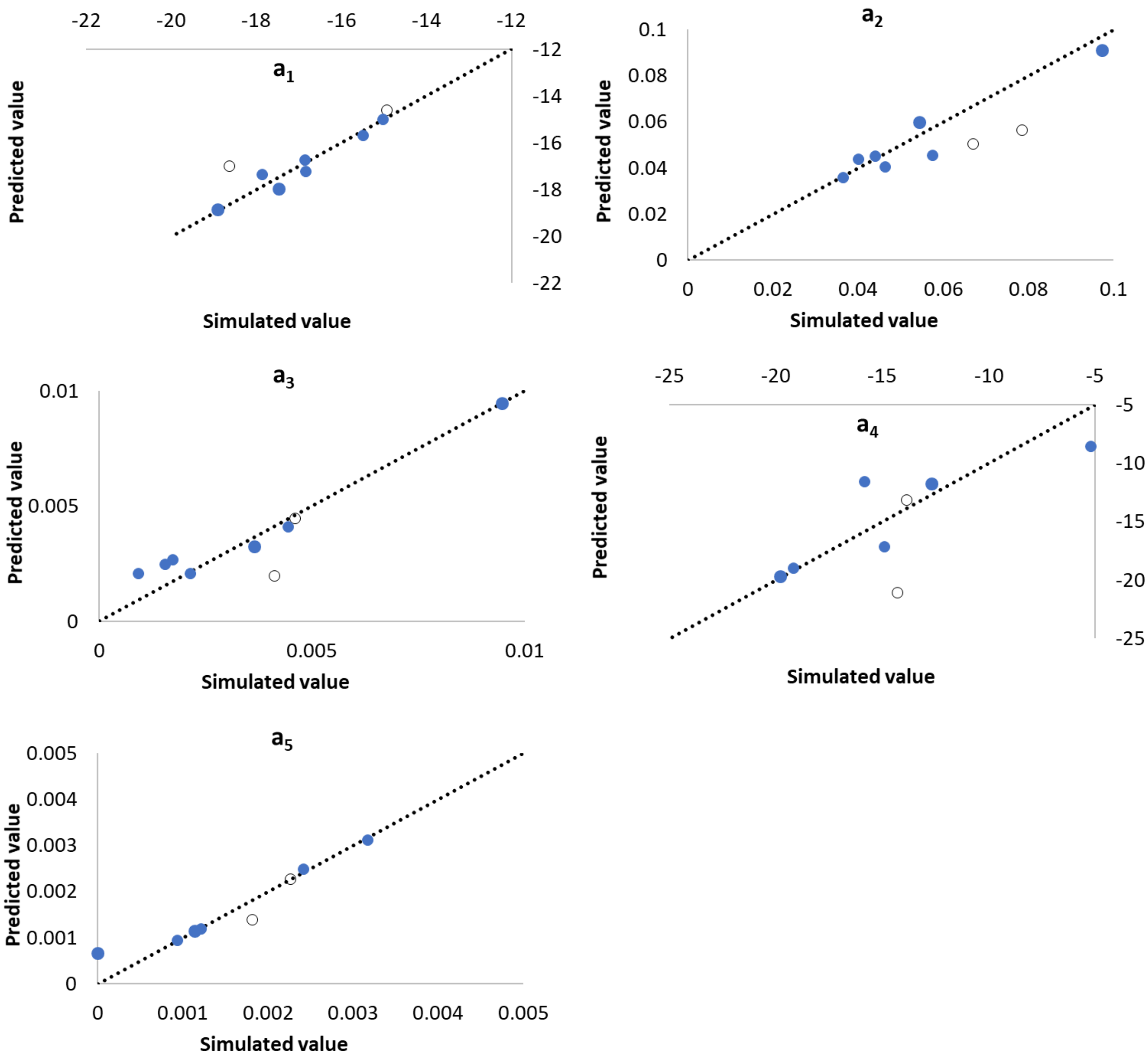

Figure 7.22 Fitting of model coefficients. Empty dots indicate model testing

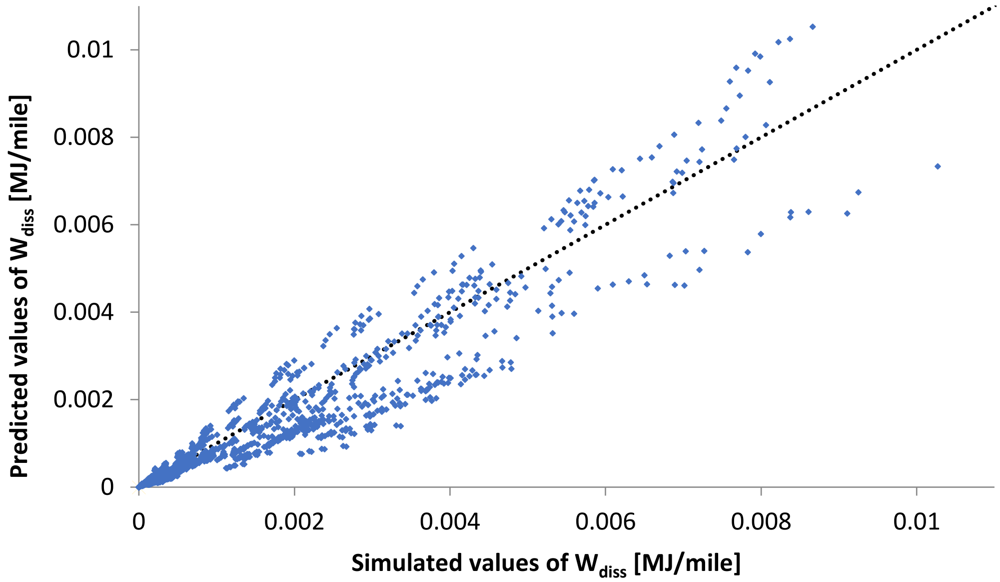

Figure 7.23 General model using equations 7.3-7.7

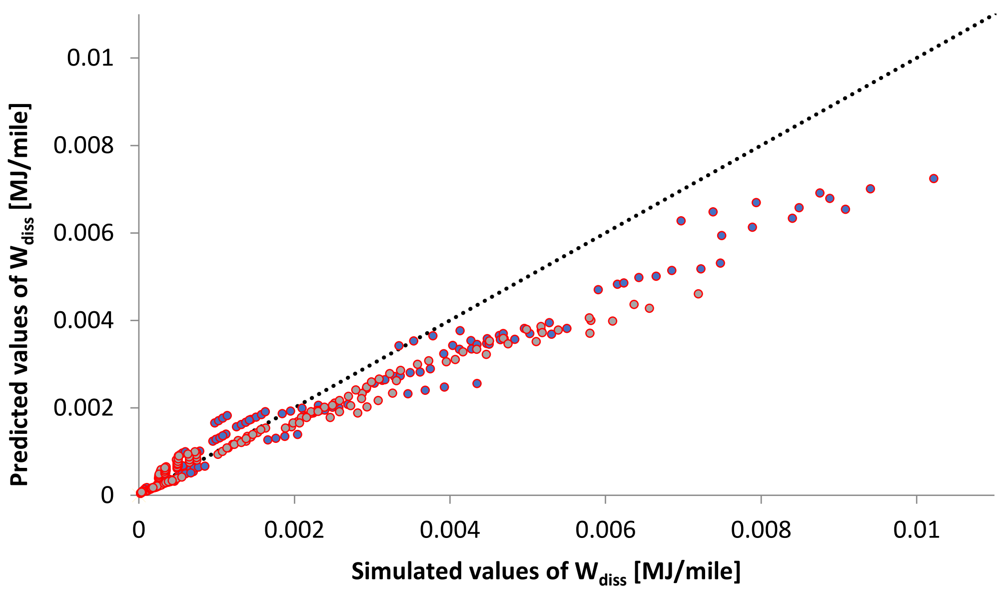

Figure 7.24 General model testing using equations 7.3-7.7

Finally, having now established the functional form of a_1-a_5, the function of eq. 7.2 can be minimized again to determine new coefficients of equations 7.3-7.7, that are reported below.

$$a_1 = -14.983 - 0.092 \cdot D_{40} - 0.290 \cdot \frac{D_{40}}{D_{15}} - 11.178 \cdot (sin\,\theta_{40} - sin\,\theta_{15}) \\ + 6.826 \cdot D_{40} \cdot sin\,\theta_{40} \tag{7.10}$$

$$a_2 = \exp(-3.19 - 0.71 \cdot sin\,\theta_{40} - 17.48 \cdot (sin\,\theta_{40} - sin\,\theta_{30}) + 8.92 \\ \cdot (sin\,\theta_{40} - sin\,\theta_{15})) \tag{7.11}$$

$$a_3 = 0.00170 \cdot \exp(0.00110 \cdot (sin\,\theta_{40}) + 0.00108 \cdot (sin\,\theta_{15}) + 0.00100 \\ \cdot (sin\,\theta_{40} - sin\,\theta_{15}) + 0.40465 \cdot (D_{40} - D_{15}) + 0.06468/D_{15}) \tag{7.12}$$

$$a_4 = -14.254 - 0.001 \cdot D_{40} - 0.888 \cdot \frac{D_{40}}{h_{HMA}} \tag{7.13}$$

$$a_5 = \exp(-4.51 + 134.83 \cdot D_{40} \cdot sin\,\theta_{40} - 144.12 \cdot D_{30} \cdot sin\,\theta_{30} - 10.82 \\ \cdot (sin\,\theta_{40} - sin\,\theta_{15}) - 39.94 \cdot (D_{40} - D_{15})) \tag{7.14}$$

The new model fitting (80% of the data) and testing (20% of the data) are shown in Figure 7.25 and Figure 7.26, respectively. The model has also been validated on a section that was not used for the calibration, and the results are shown in Figure 7.27. Since the model is used to predicted values of W_{diss} of different order of magnitude (10^{-5} to 10^{-2} MJ/mile), the mean absolute error (MAE) and the mean absolute percentage error (MAPE) are not good indicators of the quality of the model. The MAE is low because the error for the smaller order of magnitude values is much lower than the error for the larger values of W_{diss}. Inversely, the MAPE is high because the percentage error for the smaller order of magnitude values is greater than the percentage error for the larger values of W_{diss}. The quality of the fit (Table 7.1) is measured by the maximum error and the coefficient of determination.

Table 7.1 Quality of the fit for the general model

	R^2	Max error [MJ/mile]
General model fitting	0.98	1.40E-03
General model testing	0.98	1.48E-03
General model validation	0.89	1.74E-03

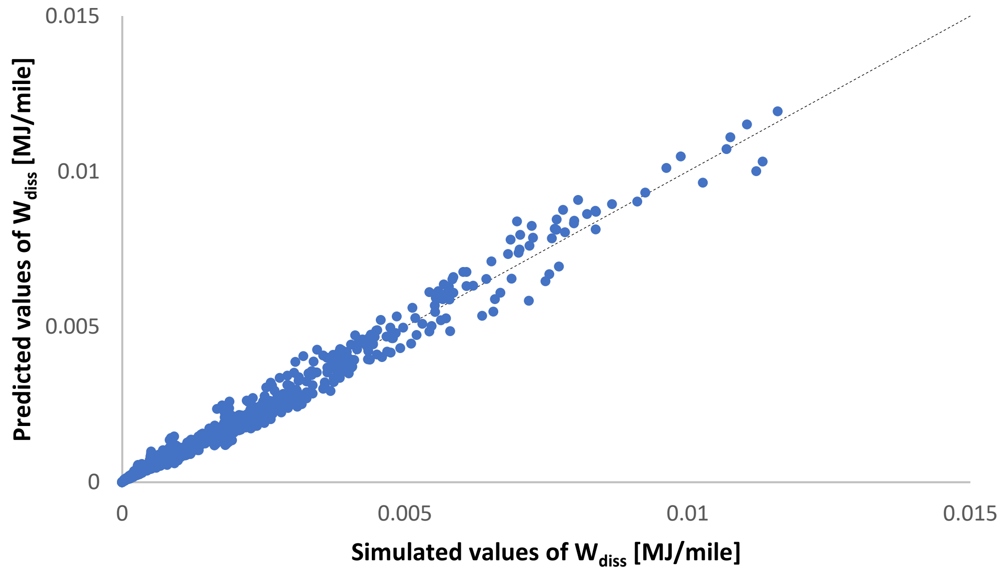

Figure 7.25 General model fitting

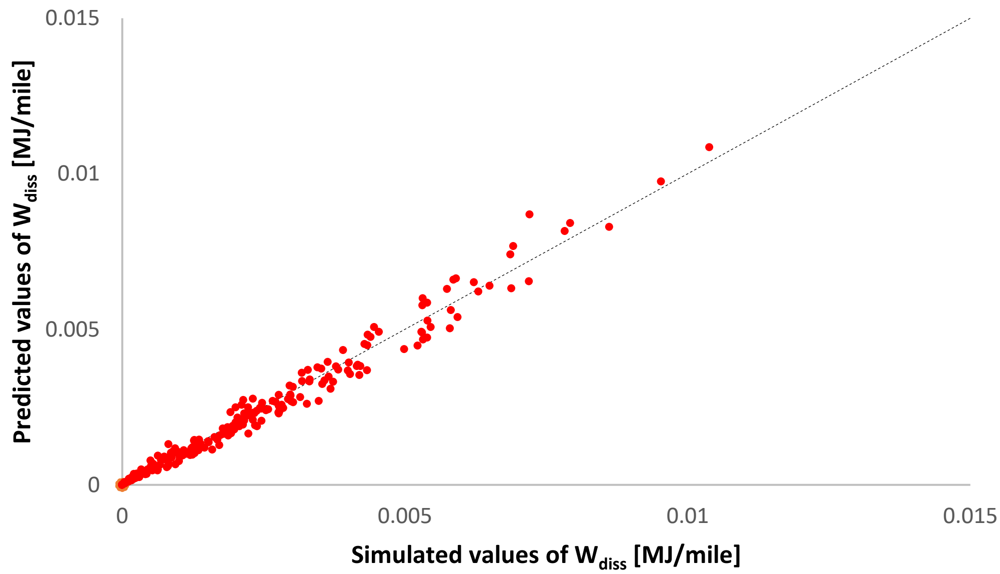

Figure 7.26 General model testing

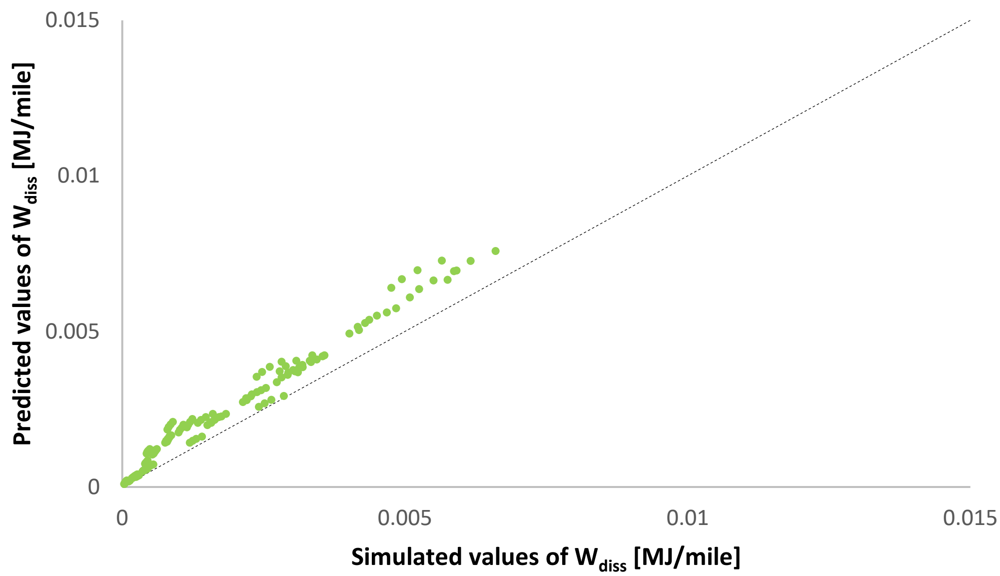

Figure 7.27 General model validation

7.4 Effect of proximity of the wheels

The vehicles used for the field testing and in the simulations (Figure 5.6) do not have tandem axles. In this section the effect of tandem axle spacing on SRR is investigated. First, six tandem axles were simulated moving along different pavement sections (Figure 7.28), calculating the energy dissipation due to the SRR for each.

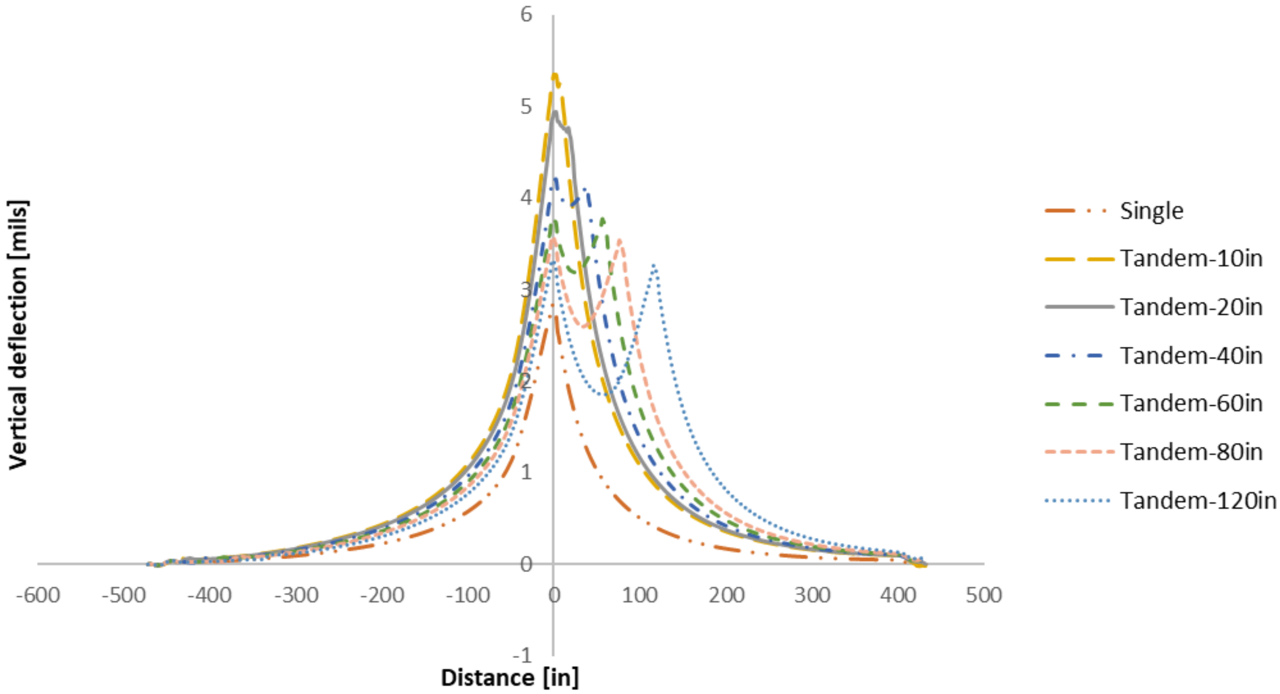

Figure 7.28 Deflection for tandem axles with different spacing – PH07

As the axle spacing increases, the normalized W_{diss} (the ratio of the energy dissipated by two wheels of the tandem axle and the energy dissipated by two single axles) tends to 1, while for short spacing the energy dissipated due to the SRR by a tandem axle is lower than the energy dissipated by two single axles, and the normalized W_{diss} is less than 1; for stiffer top layers this effect is accentuated. Table 7.2 shows the equivalent elastic modulus of the HMA layer calculated as described in section 7.3, and Figure 7.29 shows the energy dissipation normalized with respect to the energy dissipated by two single axles. In Figure 7.29 the tandem axle spacing has been extended up until 20 ft, which is unrealistic, just to show the convergence of the functions for any structure.

Table 7.2 Equivalent elastic modulus of the HMA layer calculated as described in section 7.3

	E [ksi]	
	Summer	**Winter**
PH07	1392	3868
PH09	547	2638
PH11	150	228
PH15	6080	11191
PH18,19	387	1035

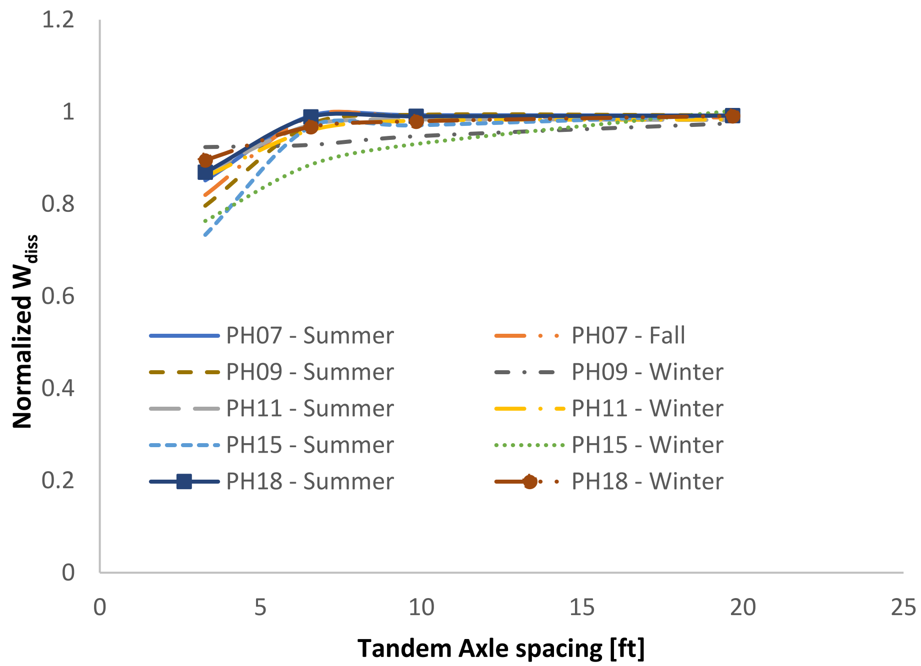

Figure 7.29 Normalized energy dissipated for tandem axles with different spacing

A function to predict the effect of the tandem axle spacing is proposed in equation 7.10. The value of C_{tandem} is imposed to be equal or less than 1. The goodness of the prediction is shown in Figure 7.30, where $R^2 = 0.9$, MAPE = 1.6%

$$C_{tandem} = (0.0202\ln(D) - 0.0058)\cdot\ln(E) - 0.00191\cdot(10^{-8}\cdot E^2) + 0.906 \leq 1 \qquad (7.10)$$

where:

D is the axle spacing [*in*],

E is the equivalent elastic modulus of the HMA layer [*ksi*].

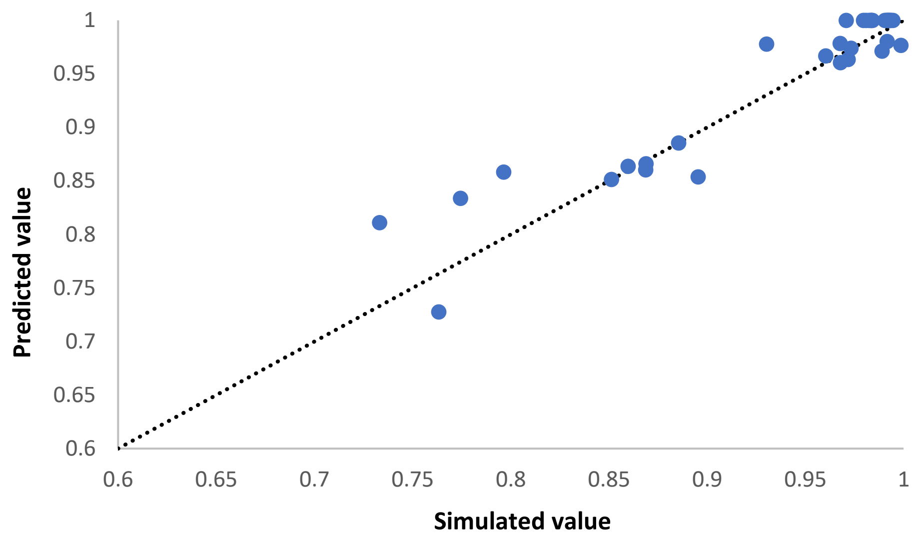

Figure 7.30 Tandem correction factor model fitting

7.5 Effect of dynamic load on SRR

The differences in terms of SRR between a static and a dynamic vehicle axle load caused by pavement roughness have been compared to investigate the interaction between roughness and structural rolling resistance. The dynamic load caused by the pavement roughness has been calculated using the two degrees of freedom quarter car model developed by Zaabar and Chatti (*2011*), shown in Figure 7.31.

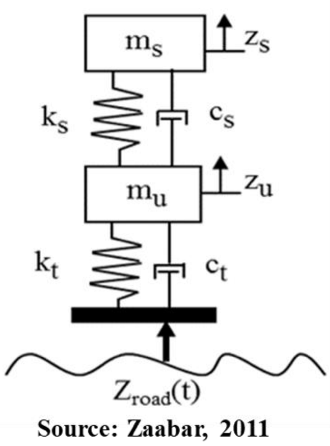

Figure 7.31. Quarter car model

The dynamic load is calculated as

$$F = c_t(\dot{z}_u - \dot{z}_r) + k_t(z_u - z_r) + (m_s + m_u)g \tag{7.11}$$

z_u is obtained solving

$$m_s\ddot{z}_s + c_s(\dot{z}_s - \dot{z}_u) + k_s(z_s - z_u) = 0 \tag{7.12}$$

$$m_u\ddot{z}_u + c_t(\dot{z}_u - \dot{z}_r) + k_t(z_u - z_r) - c_s(\dot{z}_s - \dot{z}_u) - k_s(z_s - z_u) = 0 \tag{7.13}$$

where:

m_s and z_s are the mass and displacement of the sprung mass (vehicle),

$m_u$and z_u are the mass and displacement of the unsprung mass (axle),

c_s and k_s are the damping and stiffness of the suspension,

c_t and k_t are the damping and stiffness of the tire,

z_r is the road profile elevation.

The tire pressure is constant, so the contact area changes due do the dynamic loading. Pavement deflection increases linearly with the pressure, but nonlinearly with the contact area, affecting the structural rolling resistance. The instantaneous value of the structural rolling resistance has been calculated using the dynamic loading of a single and a tandem axle over 500ft of pavement (Figure 7.32). Table 7.3 shows that the error made by using the static instead of the dynamic loading over the 500ft section is negligible. While the instantaneous value of energy dissipation can change by about 10% due to the dynamic loading, for a long enough section the average dynamic load is almost equal to the static load, and so is the energy dissipation. The structural rolling resistance is a very small quantity by itself, and 1% of the SRR is not a significant value. The static load can be used to determine the SRR. It can be observed that the difference in energy dissipation between the average dynamic load and the actual average energy dissipation (caused by the non-linearity of the relation between pavement deflection and tire print) is also negligible.

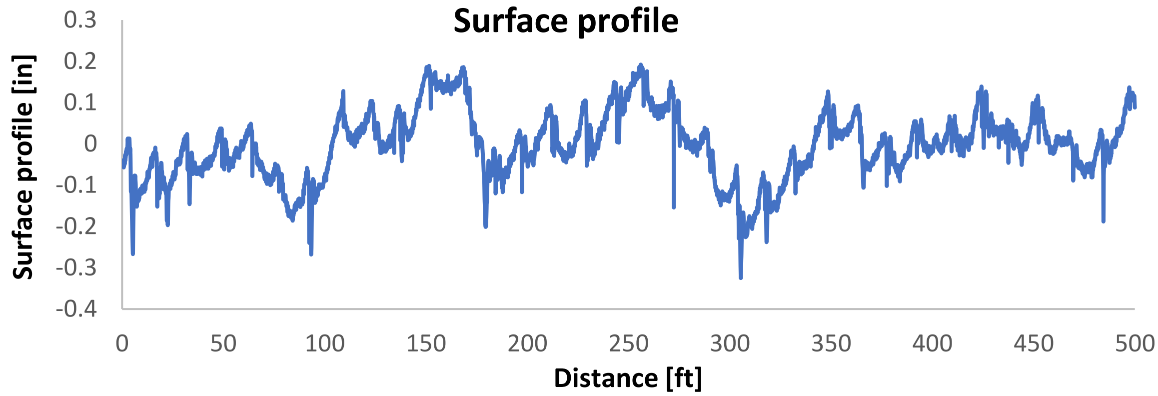

(a)

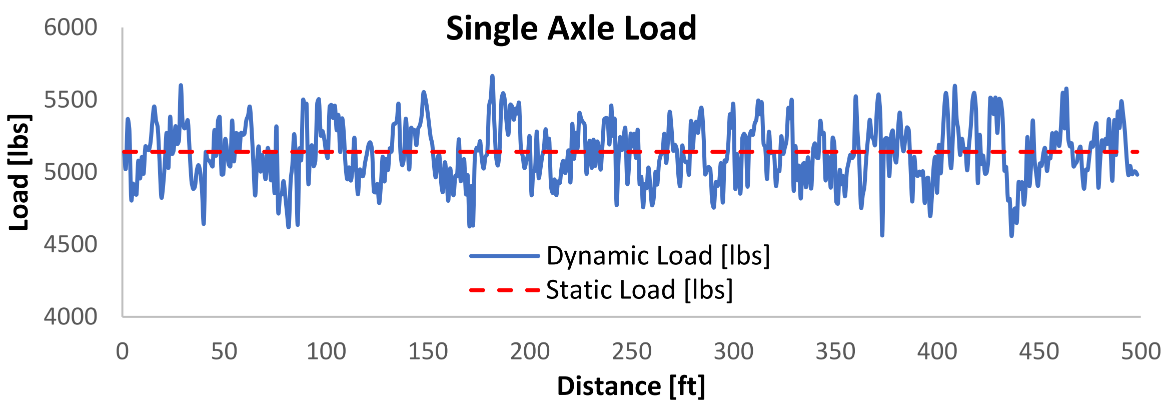

(b)

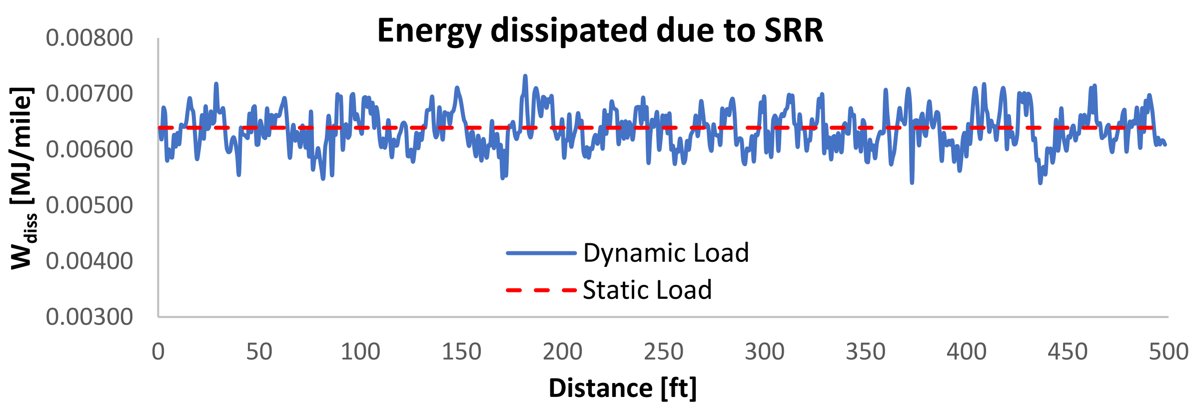

(c)

Figure 7.32 (a) Surface profile, (b) Dynamic loading and (c) energy dissipation due to the structural rolling resistance

Table 7.3 Energy dissipation associated with static and dynamic loading

	Static Load [lbs]	Static W_{diss} [MJ/mile]	Average Dynamic load [lbs]	W_{diss} for the average dynamic Load [MJ/mile]	Average W_{diss} [MJ/mile]	Error using static load
Single	5140.5	0.00639	5131.2	0.00633	0.00636	-0.5%
Tandem	5906.5	0.00773	5934.9	0.00774	0.00781	1.1%

8 DEVELOPMENT AND APPLICATION OF A PRACTICAL TOOL FOR THE CALCULATION OF THE STRUCTURAL ROLLING RESISTANCE

This chapter aims to show an application of the models developed as part of an LCA study, by conducting an analysis to quantify the effects of the structural rolling resistance on a pavement section in terms of fuel consumption and greenhouse gas (GHG) emissions. A potential small reduction in fuel consumption becomes larger when considering the entire fleet of vehicles that travel over a pavement section over a one-year period.

The model coefficients implemented in the tool were determined using the results from chapter 5, where only a limited number of pavement sections within certain ranges of pavement deflection and structural properties were considered. The models might not be accurate for sections with properties outside that range, for example a much higher deflection value. If that is the case, it is recommended to determine the SRR as shown in chapters 3 and 4 and verify the validity of the model before using the tool.

8.1 Tool for the calculation of the SRR on a jointed concrete pavement

A simple Excel tool has been developed for this purpose. The tool is valid for JPC pavements; for CRC pavements the SRR can be assumed to be null, as shown in chapter 5. The tool requires the following input:

- Concrete pavement mechanical characteristics, including information on the LTE and the shoulder dimensions, as shown in Figure 8.1. The load and axle configurations are assumed to be as shown in Figure 6.16.
- Traffic conditions: AADT, traffic distribution, average speed and vehicle loads, as shown in Figure 8.2.

Concrete pavement mechanical characteristics

h	10	Thickness [in]
E	3000	Young modulus of the slab [ksi]
LTE	90	Load transfer efficiency between consecutive slabs [%]
k	135	modulus of subgrade reaction [pci]
c	1.1	subgrade damping coefficient [pci s]
R	37.1	Radius of relative stiffness

Does it have a concrete shoulder ? Yes

Width	60	Shoulder width [in]
LTE	90	Load transfer efficiency between lane and concrete shoulder [%]
$E_{shoulder}/E_{sl}$	0.5	Ratio of the Young modulus of concrete shoulder to Young modulus of concrete slab of the lane [ksi/ksi]

Does it have a single lane ? No

LTE	90	Load transfer efficiency between adjacent lanes [%]

Figure 8.1 Concrete pavement mechanical characteristics input

Traffic conditions

AADT	25000	Average annual daily traffic

	Traffic flow					
	free flow condition		saturated condition		saturated condition 2	
	N hours	Avg speed	N hours	Avg speed [	N hours	Avg speed [mph]
OK	21	55	2	45	1	35

Are the average velocity of light vehicles and trucks different ? Yes

Heavy traffic flow					
free flow condition		saturated condition		saturated condition 2	
N hours	Avg speed	N hours	Avg speed [	N hours	Avg speed [mph]
21	50	2	40	1	30

Traffic spectra

CAR %	SUV %	Truck %	Truck classes %									
			Class 5	Class 6	Class 7	Class 8	Class 9	Class 10	Class 11	Class 12	Class 13	
45	25	30	30	5	1	20	33	2	5	2	2	OK

Vehicle loading

	CAR	SUV	Truck									
			Class 5	Class 6	Class 7	Class 8	Class 9	Class 10	Class 11	Class 12	Class 13	
Load1	2.6	5	16	20	23	26	29	32	35	38	41	Total vehicle 1 load [kip]
% load 1	95	95	90	90	90	90	90	90	90	90	90	% of vehicles within such class with that weight
Load2	3	6	18	21	24	27	30	33	36	39	42	Total vehicle 2 load [kip]
%load 2	8	8	8	8	8	8	8	8	8	8	8	% of vehicles within such class with that weight
Load3	2	7	20	22	25	28	31	34	37	40	43	Total vehicle 3 load [kip]
%load3	0	0	2	2	2	2	2	2	2	2	2	% of vehicles within such class with that weight

Figure 8.2 Traffic spectra and vehicle loading input

The tool calculates the energy dissipation associated with the SRR of every vehicle for each load and speed, applying the correction factors to account for the shoulder, the adjacent lane, and the vehicle class type, using the models from chapter 6. Then it calculates the number of vehicles every day traveling at each speed as:

$$N_{ij} = AADT \cdot P_i \cdot \frac{h_j}{24} \tag{8.1}$$

where

N_{ij} is the number of vehicles i traveling at speed j per day,

$AADT$ is the annual average daily traffic,

P_i is the percentage of vehicles i in the traffic spectra,

h_j is the number of hours that vehicles travel at speed j,

The total energy dissipated every day by the vehicles i due to the SRR is

$$W_{diss\_day\_i} = \sum_j N_{ij} \cdot W_{ij} \tag{8.2}$$

where

W_{ij} is the energy dissipated by the vehicles i traveling at speed j.

The total energy dissipated every year due to the SRR is obtained summing up the energy dissipated by every vehicle.

$$W_{diss\_1year} = 365 \sum_i W_{diss\_day\_i} \tag{8.3}$$

The final output is the total fuel consumption due to the SRR per year per mile, calculated using equation 5.4.

8.2 Tool for the calculation of the SRR on an asphalt pavement

A second Excel tool has been developed for asphalt pavements. It requires the following input:

1. Traffic conditions: AADT, traffic spectra and average speed, as shown in Figure 8.2.
2. Vehicle loads and axle configurations, as shown in Figure 8.3. Differently from JPC pavements, where the model to predict the SRR uses the entire vehicle load and predefined axle configurations, for asphalt pavements the model to predict the SRR uses the tire load, and the user can choose any axle loading and spacing.

		Class 9 Truck
P_9	30	**percentage of trucks with this load**

L_{31}	4.50	**Single tire load [kip]**
p	118	**tire pressure [psi]**
n	2	**Number of tires with this load**
Are these dual tires ?		No
do they belong to a tandem axle?		No
d		**Value not required**
L_{32}	4.70	**Single tire load [kip]**
p	118	**tire pressure [psi]**
n	4	**Number of tires with this load**
Are these dual tires ?		No
do they belong to a tandem axle?		Yes
d	60	**Tandem axle spacing [in]**
L_{32}	8.00	**Single tire load [kip]**
p	118	**tire pressure [psi]**
n	4	**Number of tires with this load**
Are these dual tires ?		No
do they belong to a tandem axle?		Yes
d	60	**Tandem axle spacing [in]**
Total Load (check)	59.8 kip	

Figure 8.3 Example of vehicle loading input for asphalt pavement

3. Asphalt pavement mechanical characteristics of each layer.

For asphalt pavements the tool offers different options (named "Levels") to input the HMA mechanical properties. Level one and two use the mastercurve from laboratory tests or from backcalculation, and are preferable, while level three and four use models or estimates to determine the mastercurve and are less accurate.

<u>Level one</u> requires the input of either:

A. Sigmoidal coefficients of the mastercurve, phase angle and shift factor coefficients, in the forms shown in equation 8.4 - 8.6

$$\log\left(|E^*|\right) = \delta + \frac{\alpha}{1+\exp(-\beta-\gamma\log(f_R))} \tag{8.4}$$

$$\Phi = d_1 \cdot \mathrm{e}^{-\frac{(-d_2+\log(f_R))^2}{2(d_3)^2}} \tag{8.5}$$

$$\log\left(a(\mathrm{T})\right) = \mathrm{a}_1\,\mathrm{T}^2 + \mathrm{a}_2\,\mathrm{T} + \mathrm{a}_3 \tag{8.6}$$

where:

E^* is the dynamic modulus,

Φ is the phase angle,

a(T) is the shift factor,

$\alpha, \beta, \gamma, \delta$ are the sigmoidal coefficients,

d_1, d_2, d_3 are the phase angle coefficients,

a_1, a_2, a_3 are the shift factor coefficients,

f_R is the reduced frequency [1/s], $f_R = f \cdot a(T)$,

B. Or, the results of a dynamic modulus test, as shown in Figure 8.4.

Initial Data			
T (C)	f (Hz)	E*	Phase angle
-10.0	25	21381	6.1
-10.0	10	20144	6.7
-10.0	5	19123	7.2
-10.0	1	16628	8.7
-10.0	0.5	15379	9.4
-10.0	0.1	12300	11.9
10.0	25	10525	14.6
10.0	10	9110	16.2
10.0	5	8095	17.5
10.0	1	5912	20.8
10.0	0.5	5084	22.0
10.0	0.1	3437	25.2
21.0	25	5777	22.3
21.0	10	4637	24.1

Figure 8.4 Example of laboratory determined dynamic modulus test data

The coefficients of equation 8.4, 8.5 and 8.6 are fit by minimizing the following error function.

$$Error = \sum_j \left(Log(E^*_{j\_lab}) - Log(E^*_{j\_fit}) \right)^2 + \sum_j \left(Log(\delta_{j\_lab}) - Log(\delta_{j\_fit}) \right)^2 \quad (8.7)$$

where:

$E^*_{j\_lab}$ is the value of dynamic modulus measured during the test at the frequency *j*,

$E^*_{j\_fit}$ is the value of dynamic modulus given by the fitted equation 8.4,

δ_{j_lab} is the value of phase angle measured during the test at the frequency *j*,

δ_{j_fit} is the value of phase angle given by the fitted equation 8.5.

Level two requires the input of the sigmoidal coefficients of the relaxation modulus and the shift factor coefficients.

$$\log\left(E(t)\right) = c_1 + \frac{c_2}{1 + \exp(-c_3 - c_4 \log(t_R))} \tag{8.8}$$

$$\log(a(\mathrm{T})) = \mathrm{a}_1\,\mathrm{T}^2 + \mathrm{a}_2\,\mathrm{T} + \mathrm{a}_3 \tag{8.9}$$

where:

$E(t)$ is the relaxation modulus,

$a(\mathrm{T})$ is the shift factor,

c_1-c_4 are the sigmoidal coefficients of the relaxation modulus,

a_1, a_2, a_3 are the shift factor coefficients,

t_R is the reduced time [s], $t_R = t \cdot a(T)$.

Equation 8.8 is used to generate values of relaxation modulus for different loading times, which are used for the fitting of the Prony series shown in equation 8.10.

$$E(t) = E_\infty + \sum_{i=1}^{N} E_i \cdot e^{-\frac{t_R}{\rho_i}} \tag{8.10}$$

where:

E_i are the Prony series coefficients,

τ_i are the relaxation time coefficients,

t_R is the reduced time [s], $t_R = t \cdot a(T)$,

N is the number of Prony series coefficients used, chosen arbitrarily to be 33.

The coefficients of equation 8.10 are fit by minimizing the following error function.

$$Error = \sum_j \left| \frac{\left(Log(E(t_j)_{lab}) - Log(E(t_j)_{fit})\right)}{Log(E(t_j)_{lab})} \right| \tag{8.11}$$

where:

$E(t_j)_{lab}$ is the value of relaxation modulus measured for the loading time t_j,

$E(t_j)_{fit}$ is the value of dynamic modulus given by the fitted equation 8.10.

Using the Prony series, the dynamic modulus and the phase angle are calculated using equations 8.12 - 8.15

$$E'(\omega_R) = E_\infty + \sum_{i=1}^{N} E_i \cdot \frac{(\omega_R \cdot \rho_i)^2}{1+(\omega_R \cdot \rho_i)^2} \tag{8.12}$$

$$E''(\omega_R) = \sum_{i=1}^{N} E_i \cdot \frac{\omega_R \cdot \rho_i}{1+(\omega_R \cdot \rho_i)^2} \tag{8.13}$$

$$|E^*| = \sqrt{E'^2 + E''^2} \tag{8.14}$$

$$\Phi = \tan^{-1}\left(\frac{E''}{E'}\right) \tag{8.15}$$

where:

E^* is the dynamic modulus,

Φ is the phase angle,

E' is the storage modulus,

E'' is the loss modulus,

ω_R is the reduced angular frequency[1/s], $\omega_R = 2\pi f_R$.

The dynamic modulus and phase angle are calculated for several frequencies, similar to a lab test, and used to determine the sigmoidal coefficients of the mastercurve, as done in level 1.

Level three requires volumetric input. The Hirsch model (Christensen et al., 2003), shown in equation 8.16 – 8.18 is used to determine the phase angle and the dynamic modulus.

$$|E^*| = P_c\left[4,200,000\left(1-\frac{VMA}{100}\right)+3|G^*|\left(\frac{VFA\cdot VMA}{10,000}\right)\right]+\frac{(1-P_c)}{\frac{\left(1-VMA/100\right)}{4,200,000}+\frac{VMA}{3|G^*|(VFA)}} \tag{8.16}$$

$$\phi = -21\left(\log\left(P_c\right)\right)^2 - 55\log\left(P_c\right) \tag{8.17}$$

$$P_c = \frac{\left(20+3|G^*|\cdot\frac{VFA}{VMA}\right)^{0.58}}{650+\left(3|G^*|\cdot\frac{VFA}{VMA}\right)^{0.58}} \tag{8.18}$$

where:

|E*| is the HMA dynamic modulus [MPa];

G* is the asphalt binder complex modulus at the desired |E*| temperature and frequency [MPa];

F/A is the filler to bitumen ratio.

In case the asphalt layer contains RAP (reclaimed asphalt pavement), the user can choose the model proposed by Lanotte et al. (*2017*) shown in equation 8.19 - 8.22

$$\left|E^*\right| = 10^{0.0965\ln\left[G^{*2}\cdot(F/A)^3\cdot\exp\left(\frac{\#4}{\#200}\right)\right]-0.00225\left[\%RAP+P_b+V_{be}+G^*\right]} \cdot 10^{-0.116\left(\frac{\#4}{\#200}\right)+0.0607\ln G^*+3.77} \tag{8.19}$$

$$\begin{aligned}\delta &= 0.249\phi + 0.499T + 0.836VMA - 14.8\left(F/A\right) + \exp(-f)\left(6.45 - 0.00114\exp(\sqrt{\phi})\right)\\ &\quad - 0.0001T^3\left(\frac{1}{2\left(F/A\right)^3}+1\right) - 1.21\frac{f}{T}\\ &\quad + 0.531\exp\left(\frac{T}{VMA}\right)\exp(-1.45\exp(-f)) - (0.257\phi f)/T^2 + 0.97\end{aligned} \tag{8.20}$$

where:

|E*| is the HMA dynamic modulus [MPa],

G* is the asphalt binder complex modulus at the desired |E*| temperature and frequency [MPa],

F/A is the filler to bitumen ratio,

#4 is the cumulative percentage of aggregate retained in #4 sieve,

#200 is the cumulative percentage of aggregate retained in 3/8-inch sieve,

%RAP is the reclaimed asphalt pavement content [%],

P_b is the asphalt binder content [%],

V_{be} is the percentage of effective asphalt content [%],

δ is the HMA phase angle [°],

ϕ is the asphalt binder phase angle at the desired temperature and frequency [°],

T is the temperature [°C],

f is the frequency [Hz],

VMA is the voids in mineral aggregates [%].

Level four can be used in case no information is available on the dynamic modulus of the asphalt layer or its volumetric properties. A list of mix designs is provided, each associated with its mastercurve. The user can choose the mix design more similar to the case study.

The tool calculates the phase angle and the stiffness modulus at the equivalent frequencies reported in section 7.1, to be used in OpenPave. All the other layer mechanical properties are also input in OpenPave to determine the pavement deflection to be used in the model of eq. 7.2. The energy dissipation associated with the structural rolling resistance is calculated for each vehicle, at the given speed and temperatures.

The total energy dissipated every year due to the SRR is calculated using the same method described in section 8.1, with the difference that the energy dissipation associated with the rolling resistance is calculated for every season, and equation 8.3 becomes

$$W_{diss\_1year} = W_{diss\_summer} + W_{diss\_fall} + W_{diss\_winter} + W_{diss\_spring} \tag{8.21}$$

8.3 Practical application

In this chapter three examples of application of the tools are presented. The first example is the calculation of the fuel consumption associated with the SRR for some existing sections. Two pairs of sections were chosen from the ones described in section 5: (PH03, PH04) and (PH19, PH20). PH03 is located on Interstate 505 near Yolo (CA) between Post Mile (PM) 0.7 and PM 6.3, northbound direction, while PH04 is on the same road but in the southbound direction. PH04 is a semi-rigid section, while PH03 is a JPCP section.

Section PH19 is located on Interstate 5 near Bakersfield (CA) between PM 52.9 and PM 56.3, northbound direction, while PH20 is on the same road but in the southbound direction, between PM 52.9 and PM 54.2. PH19 is a semi-rigid section, while PH20 is a CRCP section (Figure 5.7).

These pairs of sections are ideal to highlight the difference between asphalt and concrete pavements due to the structural rolling resistance, since, being the opposite direction of the same road, the traffic levels and environmental conditions are very similar for each pair.

The traffic conditions have been obtained from Caltrans (Annual Aveage Daily Truck Traffic on the California State Highway System, 2015, and Traffic Volumes on the California State Highway System, 2016), and are summarized in Table 8.1, where the following assumptions have been made: The average vehicle speed is 45mph for two hours and a half (peak hours), and for any other hour of the day the average vehicle speed is 55mph. Since no information was available on the percentages of cars and SUVs, it has been assumed that the percentage of cars is 15% more than the percentage of SUVs. There is no seasonal variation of traffic. These assumptions may not be accurate; however, the purpose of this chapter is to compare the fuel consumption due to the SRR on asphalt and concrete pavements; therefore, the focus is not on the absolute value of fuel consumption, but on the difference between the fuel consumption on two sections of the same road.

Table 8.2 shows the total fuel consumption per mile caused by the structural rolling resistance in one year; it is obtained using the tool described in section 8.1 and 8.2. For the JPCP a value of load transfer efficiency of 60% has been used, which is the average value obtained from the falling weight deflectometer testing on the joints. For the CRCP section the results from section 5 have been used.

Although trucks are a smaller component of traffic than light vehicles, heavy vehicles are the major contributors of the total fuel consumption per year associated with the structural rolling resistance. The SRR is so low for cars and SUVs that, even when looking at the entire fleet of light vehicles traveling along a road, its contribution to fuel consumption is still small.

Table 8.1 Average annual daily traffic (AADT) and traffic spectra distribution

SECTION	Name	AADT	Truck %					Car %	SUV %
			% of the total vehicles	within the trucks					
				2 axles	3 axles	4 axles	5 axles		
PH03	Yolo 505 N	18650	10	8.2	5.1	2.2	84.6	52.5	37.5
PH04	Yolo 505 S	21500	10	8.2	5.1	2.2	84.6	52.5	37.5
PH19	KER 5 N	38750	26	18	3	2	77	44.5	29.5
PH20	KER 5 S	39500	24.2	19	2.7	1.1	77.2	45.4	30.4

Table 8.2 Fuel consumption caused by the SRR

Section	Vehicle	Fuel per mile per year [gal/mile]	Total fuel per year [gal/mile]
PH03	All Cars	6.06	107.7
	All SUVs	6.02	
	All Trucks	97.64	
PH04	All Cars	94.7	688.4
	All SUVs	85.1	
	All Trucks	508.6	
PH19	All Cars	140.3	1953.7
	All SUVs	126.1	
	All Trucks	2334.3	
PH20	All Cars	1.0	10.0
	All SUVs	0.8	
	All Trucks	8.2	

The second example of application of the tool is a comparison of the fuel consumption associated with the SRR for different pavement structures under the same loading conditions, chosen to be the traffic of PH04 from Table 8.1. The results, presented in Figure 8.5, show that the structural rolling resistance varies significantly for different pavement structures. The structural rolling resistance is negligible on CRC pavement (PH20), but it would be inappropriate to state that the SRR is smaller on rigid pavement than on asphalt ones. A JPC pavement with asphalt shoulder, and low load transfer efficiency can have a higher SRR then a flexible pavement; for example, the fuel consumption associated with the SRR is greater in PH23 than in PH15. While in the first example the real traffic was used for each section, in the second example the same traffic has been used for each section, which explains why PH04 has a higher value of fuel consumption than PH19.

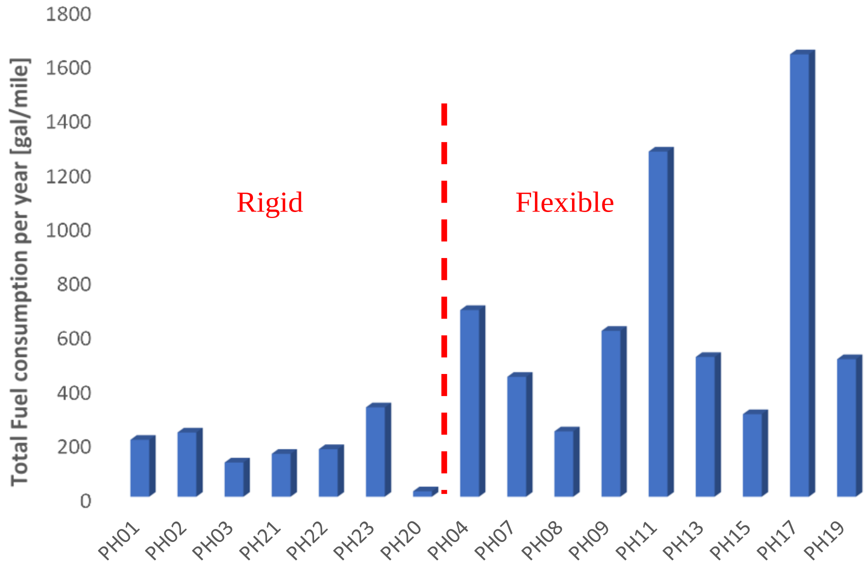

Figure 8.5. Fuel consumption associated with different pavement structures.

The third example is a comparison of the fuel consumption associated with the SRR for different thicknesses of the top layer. Figure 8.6 and Figure 8.7 show the relation between total traffic fuel consumption and layer thickness for PH04 and PH03, respectively.

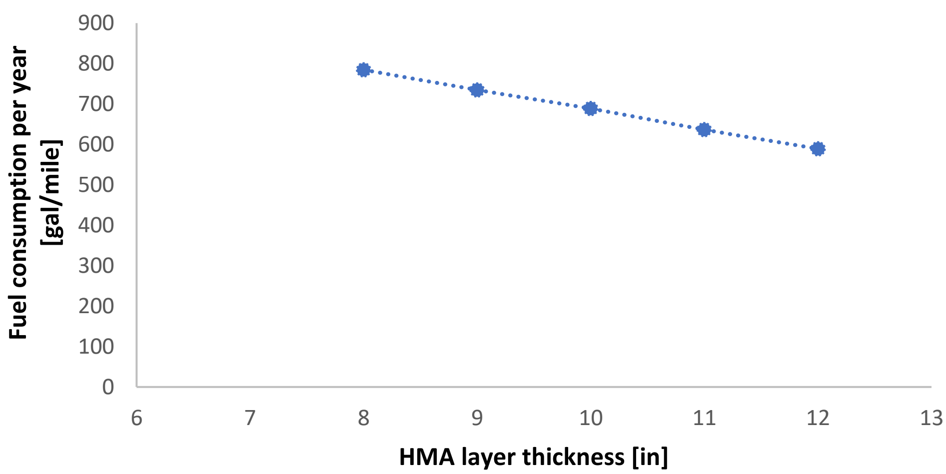

Figure 8.6. Dependency of fuel consumption on HMA layer thickness

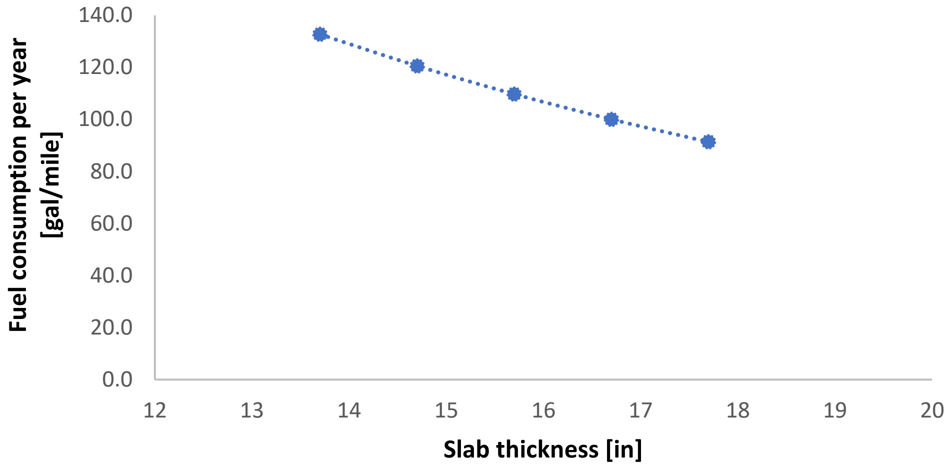

Figure 8.7. Dependency of fuel consumption on PCC slab thickness

Increasing the top layer thickness, the total fuel consumption decreases almost linearly, between 6 and 8% per inch for the asphalt pavement, and between 8.5 and 9.5% for the concrete pavement. The decrease in fuel consumption associated with a thicker top layer is not sufficient to justify design choices but could be taken in consideration as one of the factors in the design process.

The results from Table 8.2 can also be used to estimate the greenhouse gas emissions caused by the structural rolling resistance in those sections. According to EPA (*2014*) diesel engines produce 10.21 kg of CO_2 per gallon of fuel, and gasoline engines produce 8.78 kg of CO_2 per gallon of fuel. To estimate the production of CH_4 and NO_2, EPA (*2014*) provides a factor, which depends on the vehicle production year. According to the IHS Automotive Survey the average vehicle age in the United States is 11.5 years, so the CH_4 and NO_2 emission factors have been calculated as the average of the values for vehicle produced in the last 22 years; for cars and SUVs the CH_4 emission factor is 0.0176 grams per mile, and the NO_2 emission factor is 0.0133 grams per mile. For pickups and trucks the CH_4 emission factor is 0.0463 grams per mile, and the NO_2 emission factor is 0.0659 grams per mile. These factors can be multiplied by the standard fuel consumption of the vehicles, calculated from the NCHRP720 calibrated HDM4 model (*Chatti and Zaabar,* *2012*), to obtain a new factor, whose unit is grams per gallon (Table 8.3). The analysis assumes an IRI of 1 m/km, no grade, and no curvature; these are realistic assumptions for those sections and have also been used in chapter 5. The emission factors of Table 8.3 can be used to convert the results of Table 8.2 to greenhouse gas emissions (Table 8.4).

Table 8.3 CH_4 and NO_2 emission factors in grams/gallon

Vehicle	Standard Fuel Consumption [miles/gallon]	CH_4 emissions factor[grams/gallon]	NO_2 emissions factor [grams/gallon]
CAR	31.9	0.561	0.424
SUV	31.9	0.561	0.424
TRUCK 2 axles	15.7	0.725	1.034
TRUCK 3 axles	14.1	0.651	0.928
TRUCK 4 axles	8.5	0.393	0.560
TRUCK 5 axles	6.7	0.310	0.442

Table 8.4 Total greenhouse gas emissions due to the structural rolling resistance produced by all traffic

Section	Total CO_2 per year [lb/mile]	Total CH_4 emissions per year [lb/mile]	Total NO_2 emissions per year [lb/mile]
PH03	2388.8	0.08	0.11
PH04	14970.96	0.61	0.72
PH19	43451.60	1.64	2.19
PH20	218.13	0.01	0.02

It can be observed that, because of the rolling resistance component caused by the pavement structure, on the I 505 near Yolo every year the vehicles traveling south (PH04) consume 581 gal/mile of fuel more than the vehicles traveling in the north direction (PH03), and produce 12,582 more pounds of CO_2, 0.61 more pounds of NO_2 and 0.52 more pounds of CH_4 per mile. On the I 5 near Bakersfield, every year the vehicles traveling north (PH19) consume 1943 gal of fuel more than the vehicles traveling in the south direction (PH20), and produce 43,233 more pounds of CO_2, 2.17 more pounds of NO_2 and 1.63 more pounds of CH_4. Sections PH19 and PH20 have more traffic, and a higher percentage of heavy vehicles than PH03 and PH04.

Assuming an average cost of gasoline of \$3.5/gallon, which is low for California, without considering any direct or indirect cost related to the GHG emission, the cost associated with the SRR is \$6,802/year per mile. Considering the lifespan of a pavement to be 20 years, for section

PH19, during its lifetime the SRR will cost about \$136,057/mile which is about 3.4% of the total cost of the road (assumed to be \$4,000,000/mile).

9 CONCLUSION

The objective of this study was to investigate the effects of the pavement structural response on rolling resistance, determine its importance in the vehicle fuel economy, and provide a practical tool for applications such as a pavement life cycle cost analysis.

First the methods to calculate the SRR on asphalt and concrete pavements were developed. The structural rolling resistance is calculated as the resistance to motion caused by the uphill slope seen by the tires due to the pavement deformation. Using the calorific value of the fuel, and the engine efficiency, the SRR can be converted into fuel consumption.

The backcalculated mechanical characteristics of 17 California pavement sections were used to conduct a series of simulations to investigate the effect of temperature, load and speed on SRR and fuel consumption, showing that:

- The structural rolling resistance is maximum for heavy vehicles, at low speed and high temperature on asphalt pavements.
- Comparing asphalt and concrete pavements, asphalt pavements show higher SRR in summer conditions. In winter conditions concrete pavements with low load transfer efficiency show higher energy dissipation, although the percentage of fuel consumption due to the SRR is less than 0.5% at low temperatures.
- In term of percentage of fuel consumption, for the case study, the maximum contribution given by the SRR is less than 2% of the total consumption of the vehicle.

Based on the simulation results, heuristic models were developed to predict the structural rolling resistance on asphalt and concrete pavements. For a concrete pavement:

- The SRR is negligible on a continuously reinforced concrete pavement.

- For a jointed concrete pavement, the energy dissipation associated with the SRR is modeled as function of load, speed, load transfer efficiency between consecutive slabs, slab thickness, PCC elastic modulus, and subgrade properties.
- Jointed concrete pavements cannot be treated as continuous elements; different axles spacing lead to different results, and, considering that, different sets of coefficients were determined for each vehicle type. Correction factors were also determined to account for the different truck classes.
- Load transfer efficiency between adjacent slabs, and between slab and shoulder, also plays a role in energy dissipation. A longitudinal load transfer efficiency greater than 90% reduces the energy dissipation by 30%.

For an asphalt pavement:

- The energy dissipation associated with the SRR is modeled as a function of load, speed, pavement temperature, tire pressure, pavement deflection and phase angle of the HMA layer under specified conditions.
- The proximity of the wheels has an effect on the structural rolling resistance. The energy dissipated by a tandem axle is lower than the energy dissipated by two single axles. Increasing the spacing between axles reduces the effect, becoming null for distances greater than 10ft.

It has also been shown that the dynamic loading due to the pavement roughness does not affect the SRR; therefore, roughness induced rolling resistance and structural rolling resistance can be treated independently.

The calibration of the heuristic model coefficients was successful, and the model can accurately match the mechanistic simulations.

The models were implemented in a tool that allows the calculation of the structural rolling resistance, and the fuel consumption associated with it, for any given traffic and pavement section. Applications of the tool showed that:

- The reduction of structural rolling resistance associated with a lower deflection would not justify an increase of thickness of the pavement layers during pavement design. The savings in terms of fuel consumption would be smaller than the cost to build thicker layers.
- Asphalt pavements showed the higher values of structural rolling resistance and fuel consumption associated with it. However, the structural rolling resistance of concrete pavements is not always smaller than that of asphalt pavements; each pavement structure behaves differently and, with the exception of CRCP, it should not be generalized that a pavement type performs better than another in terms of SRR.
- During the entire service life of a roadway, without considering the costs associated with pollutants emissions, the economic impact of the structural rolling has been estimated to be 3.4% of the cost of construction of the road for a case study considering an average annual traffic of 38,750 vehicles, of which 26% is heavy truck traffic.
- The difference in fuel consumption between different pavement structures can be significant and, depending on the traffic levels could be included in a life cycle assessment study.

To further expand the knowledge on structural rolling resistance, the following list of recommendations for future research is provided:

- Study the effect of joint spacing and pavement distresses on the SRR.
- Study the effect of tire types, with different shapes of the tire print and pressure distributions, resuming the work of Shakiba et al. (*2016*)
- Study how pavement overlays affect the SRR by modeling multiple asphalt layers, or concrete slabs over asphalt layers.

APPENDICES

Appendix A. Mechanical characteristics of the asphalt pavement sections

In this appendix, the mechanical characteristics of the asphalt pavement structure described on chapter 5 are reported. Below are reported the abbreviations used in the following tables.

HMA	Hot mixed asphalt
PCC	Plain cement concrete
CTB	Concrete treated base
AB	Aggregate base
ASB	Aggregate subbase
pcf	Pound per cubic feet
psi	pound per square inch
in	inch

Section PH04

Table A.1 Mechanical characteristics section PH04

E(t) sigmoidal coefficients				a_T shift factor coefficients		
δ	α	β	γ	c_1	c_2	T_{ref} [°C]
8.58E-01	3.55E+00	8.55E-02	-8.35E-01	6.07E-04	-9.85E-02	19

HMA	Relaxation modulus	see above
	Poisson's ratio	0.35
	Mass Density (pcf)	145
	average thickness (in)	10.0
PCC	Poisson's ratio	0.2
	Mass Density (pcf)	150
	Average Modulus (psi)	5830000
	average thickness (in)	8.0
CTB	Poisson's ratio	0.4
	Mass Density (pcf)	125
	Average Modulus (psi)	89000
	average thickness (in)	4.0
Subgrade	Poisson's ratio	0.45
	Mass Density (pcf)	100
	Average Modulus (psi)	25200
	Subgrade Thickness (in)	180.0
Stiff layer	Poisson's ratio	0.2
	Mass Density (pcf)	120
	Average Modulus (psi)	450000

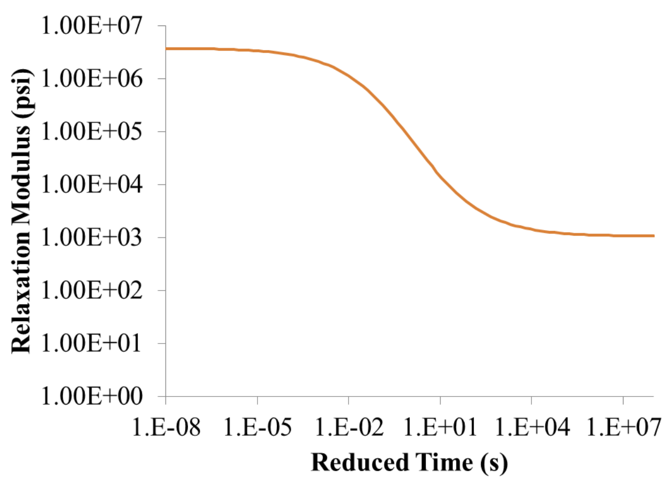

Figure A.1 Relaxation modulus section PH04

Section PH07

Table A.2: Mechanical characteristics section PH07

E(t) sigmoidal coefficients				a_T shift factor coefficients		
δ	α	β	γ	c_1	c_2	T_{ref} [°C]
1.208	3.502	0.43	-0.767	6.13E-04	-8.85E-02	19

HMA	Relaxation modulus	see above
	Poisson's ratio	0.35
	Mass Density (pcf)	145
	average thickness (in)	6.0
AB	Poisson's ratio	0.4
	Mass Density (pcf)	125
	Average Modulus (psi)	80300
	average thickness (in)	13.5
ASB	Poisson's ratio	0.4
	Mass Density (pcf)	125
	Average Modulus (psi)	80500
	average thickness (in)	11.0
Subgrade	Poisson's ratio	0.45
	Mass Density (pcf)	100
	Average Modulus (psi)	27400

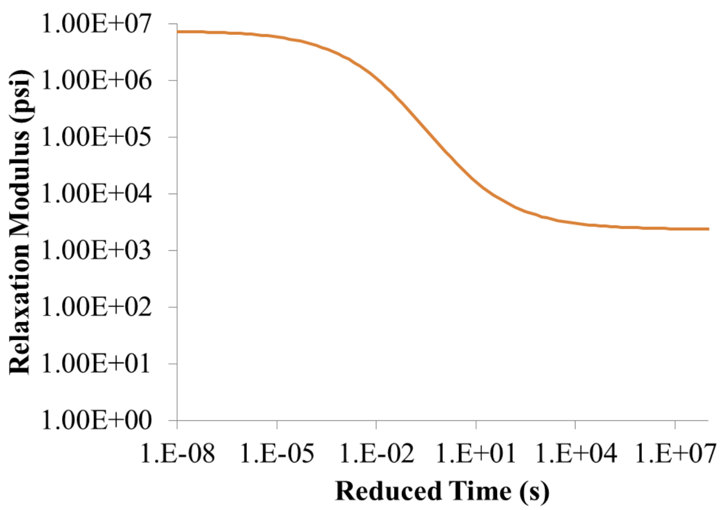

Figure A.2 Relaxation modulus section PH07

Section PH08

Table A.3: Mechanical characteristics section PH08

E(t) sigmoidal coefficients				a_T shift factor coefficients		
δ	α	β	γ	c_1	c_2	T_{ref} [°C]
1.62	2.74	0.944	-0.38	4.58E-04	-6.91E-02	19

HMA	Relaxation modulus	see above
	Poisson's ratio	0.35
	Mass Density (pcf)	145
	average thickness (in)	4.0
Subgrade	Poisson's ratio	0.45
	Mass Density (pcf)	100
	Average Modulus (psi)	12800
	Subgrade Thickness (in)	210.0
Stiff layer	Poisson's ratio	0.2
	Mass Density (pcf)	60
	Average Modulus (psi)	350554

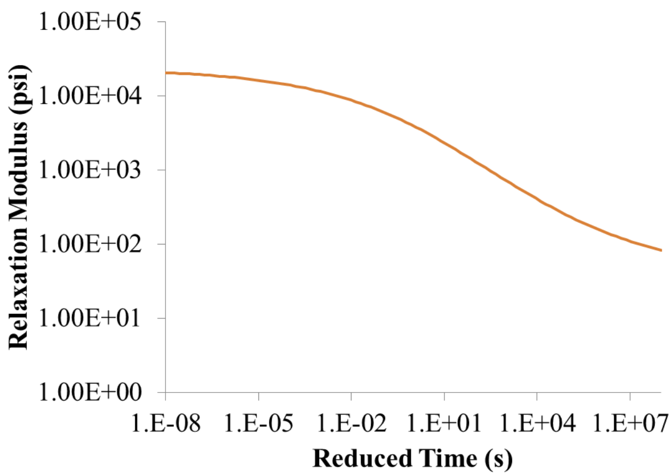

Figure A.3 Relaxation modulus section PH08

Section PH09

Table A.4 Mechanical characteristics section PH09

E(t) sigmoidal coefficients				a_T shift factor coefficients		
δ	α	β	γ	c_1	c_2	T_{ref} [°C]
0.978	3.8	0.521	-0.519	8.39E-04	-1.17E-01	19

HMA	Relaxation modulus	see above
	Poisson's ratio	0.35
	Mass Density (pcf)	145
	average thickness (in)	15.3
AB	Poisson's ratio	0.4
	Mass Density (pcf)	125
	Average Modulus (psi)	19609
	average thickness (in)	6.2
Subgrade	Poisson's ratio	0.45
	Mass Density (pcf)	100
	Average Modulus (psi)	9944
	Subgrade Thickness (in)	120.0
Stiff layer	Poisson's ratio	0.2
	Mass Density (pcf)	120
	Average Modulus (psi)	550554

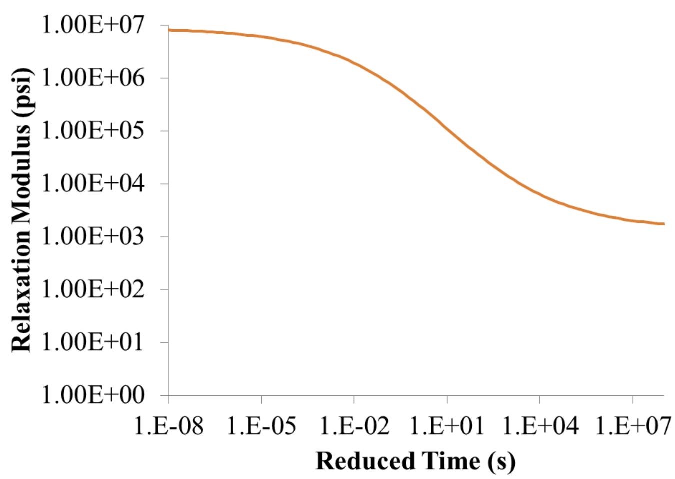

Figure A.4 Relaxation modulus section PH09

Section PH11

Table A.5 Mechanical characteristics section PH11

E(t) sigmoidal coefficients				a_T shift factor coefficients		
δ	α	β	γ	c_1	c_2	T_{ref} [°C]
1.4	2.04	0.944	-0.417	5.02E-04	-8.96E-02	19

HMA	Relaxation modulus	see above
	Poisson's ratio	0.35
	Mass Density (pcf)	145
	average thickness (in)	15.7
Subgrade	Poisson's ratio	0.45
	Mass Density (pcf)	100
	Average Modulus (psi)	8800
	Subgrade Thickness (in)	60.0
Stiff layer	Poisson's ratio	0.2
	Mass Density (pcf)	60
	Average Modulus (psi)	250000

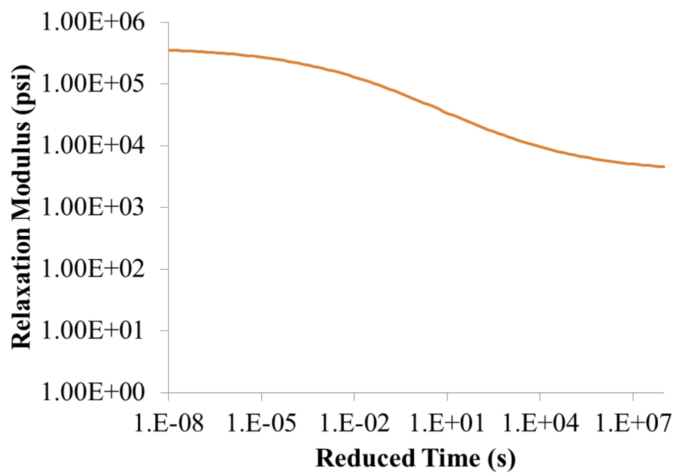

Figure A.5 Relaxation modulus section PH11

Section PH13

Table A.6 Mechanical characteristics section PH13

E(t) sigmoidal coefficients				a_T shift factor coefficients		
δ	α	β	γ	c_1	c_2	T_{ref} [°C]
1.69	2.2	0.99	-0.553	2.55E-04	-8.24E-02	19

HMA	Relaxation modulus	see above
	Poisson's ratio	0.35
	Mass Density (pcf)	145
	average thickness (in)	13.4
Subgrade	Poisson's ratio	0.45
	Mass Density (pcf)	100
	Average Modulus (psi)	10500
	Subgrade Thickness (in)	75.0
Stiff layer	Poisson's ratio	0.2
	Mass Density (pcf)	60
	Average Modulus (psi)	336345

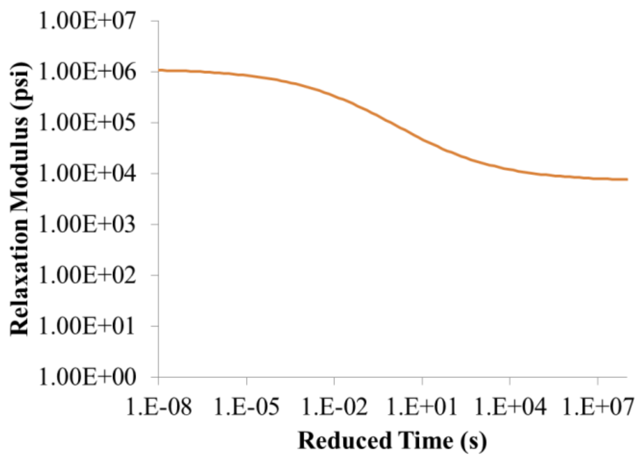

Figure A.6 Relaxation modulus section PH13

Section PH15

Table A.7 Mechanical characteristics section PH15

E(t) sigmoidal coefficients				a_T shift factor coefficients		
δ	α	β	γ	c_1	c_2	T_{ref} [°C]
1.67	3.39	0.981	-0.767	5.10E-04	-8.17E-02	19

HMA	Relaxation modulus	see above
	Poisson's ratio	0.35
	Mass Density (pcf)	145
	average thickness (in)	5.0
CTB	Poisson's ratio	0.4
	Mass Density (pcf)	125
	Average Modulus (psi)	57500
	average thickness (in)	14.0
Subgrade	Poisson's ratio	0.45
	Mass Density (pcf)	100
	Average Modulus (psi)	9600
	Subgrade Thickness (in)	160.0
Stiff layer	Poisson's ratio	0.2
	Mass Density (pcf)	60
	Average Modulus (psi)	250246

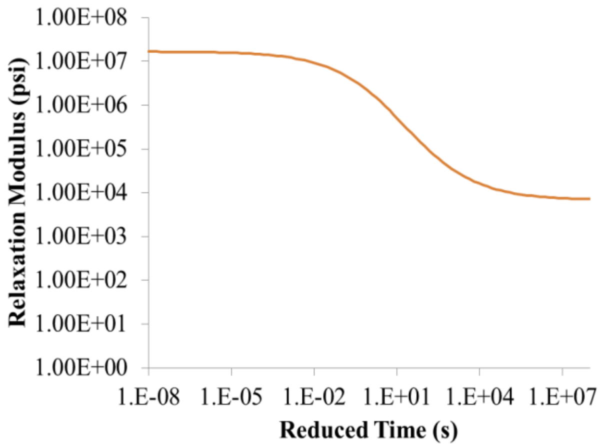

Figure A.7 Relaxation modulus section PH15

Section PH16

Table A.8 Mechanical characteristics section PH16

E(t) sigmoidal coefficients				a_T shift factor coefficients		
δ	α	β	γ	c_1	c_2	T_{ref} [°C]
1.054	2.986	0.335	-0.436	5.12E-04	-7.73E-02	19

HMA	Relaxation modulus	see above
	Poisson's ratio	0.35
	Mass Density (pcf)	145
	average thickness (in)	9.0
CTB	Poisson's ratio	0.4
	Mass Density (pcf)	125
	Average Modulus (psi)	37788
	average thickness (in)	4.4
Subgrade	Poisson's ratio	0.45
	Mass Density (pcf)	100
	Average Modulus (psi)	12433
	Subgrade Thickness (in)	80.0
Stiff layer	Poisson's ratio	0.2
	Mass Density (pcf)	60
	Average Modulus (psi)	850053

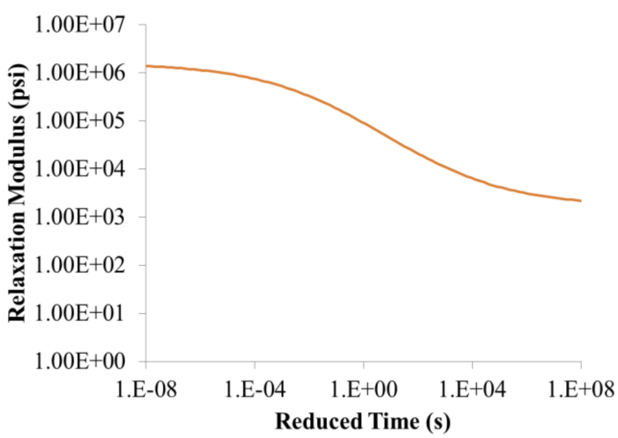

Figure A.8 Relaxation modulus section PH16

Section PH18

Table A.9 Mechanical characteristics section PH18

E(t) sigmoidal coefficients				a_T shift factor coefficients		
δ	α	β	γ	c_1	c_2	T_{ref} [°C]
1.033	3.327	0.311	-0.54	6.38E-04	-8.80E-02	19

HMA	Relaxation modulus	see above
	Poisson's ratio	0.35
	Mass Density (pcf)	145
	average thickness (in)	4.4
PCC	Poisson's ratio	0.2
	Mass Density (pcf)	150
	Average Modulus (psi)	3020000
	average thickness (in)	9.4
CTB	Poisson's ratio	0.4
	Mass Density (pcf)	125
	Average Modulus (psi)	63200
	average thickness (in)	7.7
Subgrade	Poisson's ratio	0.45
	Mass Density (pcf)	100
	Average Modulus (psi)	15400
	Subgrade Thickness (in)	120
Stiff layer	Poisson's ratio	0.2
	Mass Density (pcf)	120
	Average Modulus (psi)	450231.0

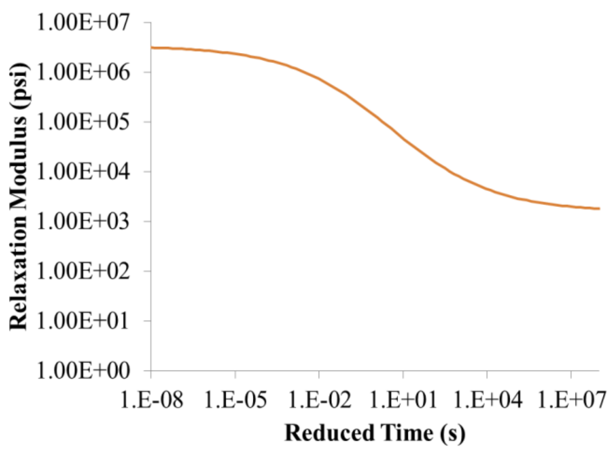

Figure A.9 Relaxation modulus section PH18

Section PH19

Table A.10 Mechanical characteristics section PH19

E(t) sigmoidal coefficients				a_T shift factor coefficients		
δ	α	β	γ	c_1	c_2	T_{ref} [°C]
1.033	3.327	0.311	-0.54	6.38E-04	-8.80E-02	19

HMA	Relaxation modulus	see above
	Poisson's ratio	0.35
	Mass Density (pcf)	145
	average thickness (in)	4.6
PCC	Poisson's ratio	0.2
	Mass Density (pcf)	150
	Average Modulus (psi)	3020000
	average thickness (in)	9.5
CTB	Poisson's ratio	0.4
	Mass Density (pcf)	125
	Average Modulus (psi)	63200
	average thickness (in)	6.7
Subgrade	Poisson's ratio	0.45
	Mass Density (pcf)	100
	Average Modulus (psi)	15400
	Subgrade Thickness (in)	120
Stiff layer	Poisson's ratio	0.2
	Mass Density (pcf)	120
	Average Modulus (psi)	450231.0

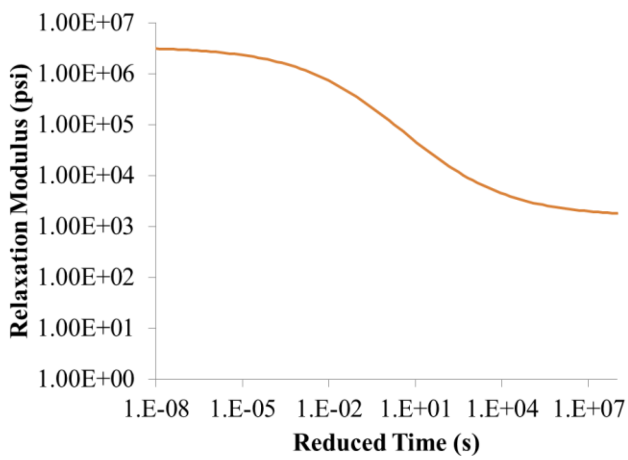

Figure A.10 Relaxation modulus section PH19

Appendix B. mechanical characteristics of the concrete pavement sections

In this appendix, the mechanical characteristics of the rigid pavement structure described on chapter 5 are reported.

<u>Section PH01 – summer</u>

Table B.1 Mechanical characteristics section PH01 – summer

PCC (JPCP)	Poisson's ratio	0.20
	Mass Density (pcf)	150
	average Elastic Modulus (ksi)	4773
	average thickness (inch)	9.0
Subgrade (CTB/ACB+AB +CL)	Average k (pci)	166.0
	Damping Ratio β	1.375
	Average Damping Coefficient *c* (pci*sec)	1.585

<u>Section PH01 – winter</u>

Table B.2 Mechanical characteristics section PH01 – winter

PCC (JPCP)	Poisson's ratio	0.20
	Mass Density (pcf)	150
	average Elastic Modulus (ksi)	5823
	average thickness (inch)	9.0
Subgrade (CTB/ACB+AB +CL)	Average k (pci)	192.6
	Damping Ratio β	1.375
	Average Damping Coefficient *c* (pci*sec)	1.708

Section PH02 – summer

Table B.3 Mechanical characteristics section PH02 – summer

PCC (JPCP)	Poisson's ratio	0.20
	Mass Density (pcf)	150
	average Elastic Modulus (ksi)	1319
	average thickness (inch)	14.4
Subgrade (AB +CL)	Average k (pci)	150.0
	Damping Ratio β	1.163
	Average Damping Coefficient *c* (pci*sec)	1.612

Section PH02 – winter

Table B.4 Mechanical characteristics section PH02 – winter

PCC (JPCP)	Poisson's ratio	0.20
	Mass Density (pcf)	150
	average Elastic Modulus (ksi)	1440
	average thickness (inch)	14.4
Subgrade (AB +CL)	Average k (pci)	181.3
	Damping Ratio β	0.974
	Average Damping Coefficient *c* (pci*sec)	1.484

Section PH03 – summer

Table B.5 Mechanical characteristics section PH03 – summer

PCC (JPCP)	Poisson's ratio	0.20
	Mass Density (pcf)	150
	average Elastic Modulus (ksi)	2412
	average thickness (inch)	15.7
Subgrade (AB +CH)	Average k (pci)	198.4
	Damping Ratio β	1.048
	Average Damping Coefficient *c* (pci*sec)	1.745

Section PH03 – winter

Table B.6 Mechanical characteristics section PH03 – winter

PCC (JPCP)	Poisson's ratio	0.20
	Mass Density (pcf)	150
	average Elastic Modulus (ksi)	3630
	average thickness (inch)	15.7
Subgrade (AB +CH)	Average k (pci)	226.0
	Damping Ratio β	1.095
	Average Damping Coefficient *c* (pci*sec)	1.945

Section PH21 – summer

Table B.7 Mechanical characteristics section PH21 – summer

PCC (JPCP)	Poisson's ratio	0.20
	Mass Density (pcf)	150
	average Elastic Modulus (ksi)	5871
	average thickness (inch)	8.3
Subgrade (CTB +CL)	Average k (pci)	209.3
	Damping Ratio β	1.219
	Average Damping Coefficient *c* (pci*sec)	1.515

Section PH21 – winter

Table B.8 Mechanical characteristics section PH21 – winter

PCC (JPCP)	Poisson's ratio	0.20
	Mass Density (pcf)	150
	average Elastic Modulus (ksi)	7718
	average thickness (inch)	8.3
Subgrade (CTB +CL)	Average k (pci)	208.9
	Damping Ratio β	1.152
	Average Damping Coefficient *c* (pci*sec)	1.429

Section PH22 – summer

Table B.9 Mechanical characteristics section PH22 – summer

PCC (JPCP)	Poisson's ratio	0.20
	Mass Density (pcf)	150
	average Elastic Modulus (ksi)	4952
	average thickness (inch)	8.3
Subgrade (AB +CL)	Average k (pci)	203.6
	Damping Ratio β	1.199
	Average Damping Coefficient *c* (pci*sec)	1.472

Section PH22 – winter

Table B.10 Mechanical characteristics section PH22 – winter

PCC (JPCP)	Poisson's ratio	0.20
	Mass Density (pcf)	150
	average Elastic Modulus (ksi)	7046
	average thickness (inch)	8.3
Subgrade (AB +CL)	Average k (pci)	179.9
	Damping Ratio β	1.188
	Average Damping Coefficient *c* (pci*sec)	1.371

Section PH23 – summer

Table B.11 Mechanical characteristics section PH23 – summer

PCC (JPCP)	Poisson's ratio	0.20
	Mass Density (pcf)	150
	average Elastic Modulus (ksi)	4766
	average thickness (inch)	7.5
Subgrade (AB +CL)	Average k (pci)	108.6
	Damping Ratio β	1.713
	Average Damping Coefficient *c* (pci*sec)	1.458

Section PH23 – winter

Table B.12 Mechanical characteristics section PH23 – winter

PCC (JPCP)	Poisson's ratio	0.20
	Mass Density (pcf)	150
	average Elastic Modulus (ksi)	7370
	average thickness (inch)	7.5
Subgrade (AB +CL)	Average k (pci)	114.2
	Damping Ratio β	1.682
	Average Damping Coefficient *c* (pci*sec)	1.468

Section PH20 – summer

Table B.13 Mechanical characteristics section PH20 – summer

PCC (CRCP)	Poisson's ratio	0.20
	Mass Density (pcf)	150
	average Elastic Modulus (ksi)	10760
	average thickness (inch)	13.2
Subgrade (HMA+AS)	Average k (pci)	301.6
	Damping Ratio β	1.377
	Average Damping Coefficient *c* (pci*sec)	2.594

Section PH20 – winter

Table B.14 Mechanical characteristics section PH20 – winter

PCC (CRCP)	Poisson's ratio	0.20
	Mass Density (pcf)	150
	average Elastic Modulus (ksi)	9000
	average thickness (inch)	13.2
Subgrade (HMA+AS)	Average k (pci)	293.5
	Damping Ratio β	1.409
	Average Damping Coefficient *c* (pci*sec)	2.619

Appendix C. Vehicle characteristics

Four types of vehicles were used for the field test, as showed in Figure 1a. Figure C.1 shows the axle configuration. More information is provided in Tables C.1-C.4.

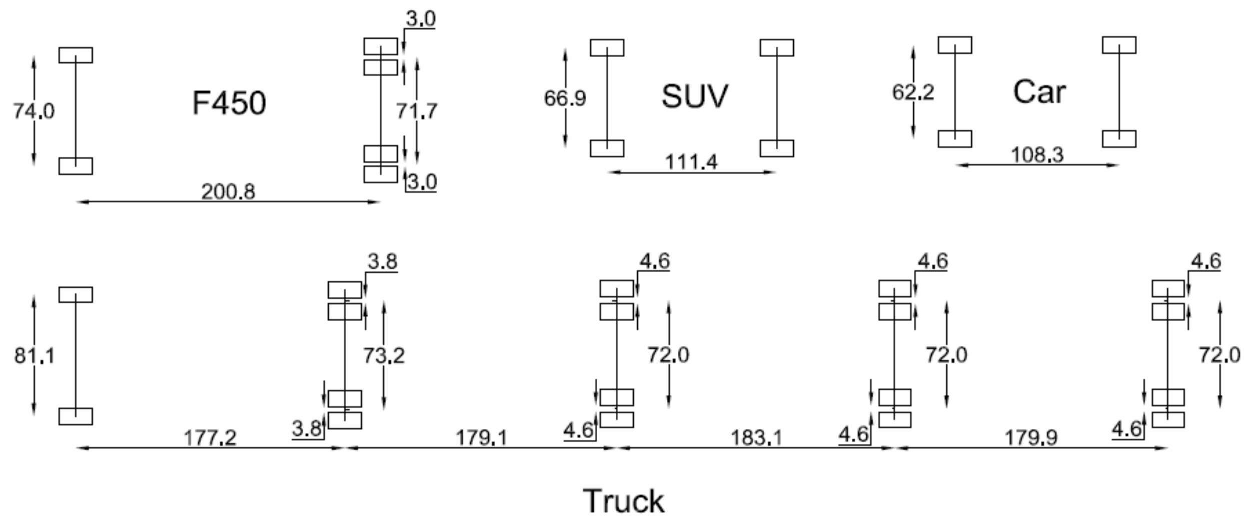

Figure C.1 Axle configuration, measurements in inches

Table C.1 Vehicle and fuel types, number of axles and wheels

				number of wheels				
Vehicle Class	**Fuel type**	**Number of Wheels**	**Number of axles**	**Front axle**	**Rear axle**	**Trailer1 (rear Axle)**	**Trailer2 (front Axle)**	**Trailer2 (rear Axle)**
Medium car (2015 Chevy Impala)	gasoline	4	2	2	2			
SUV (2014 Ford explorer)	gasoline	4	2	2	2			
F450 (2011 Ford)	diesel	6	2	2	4			
Truck (2013 Peterbilt)	diesel	18	5	2	4	4	4	4

Table C.2 Vehicle loads and tire inflated pressures

Vehicle	**Front Axle (lbs)**	**Rear Axle (lbs)**	**Driver weight (lbs)**	**Adjusted Front Axle (lbs)**	**Adjusted Rear Axle (lbs)**	**Trailer1 (rear Axle)**	**Trailer2 (front Axle)**	**Trailer2 (rear Axle)**	**Total weight (lbs)**	**Operating Tire Pressure (psi)**	**Time (mins) to reach operating pressure**
Car	2180	1540	220	2290	1650				3940	38.00	15-35
SUV	2520	2080	250	2645	2205				4850	38.00	22-44
F450	5660	8980	220	5770	9090				14860	118.06	35-50
Truck (fully loaded)	8960	18700	220	9070	18810	17387	17387	17387	80040	107.62	
Truck (partially loaded 1)	9040	17820	220	9150	14930	14660	14660	14660	68060	107.62	
Truck (partially loaded 2)	9040	17820	220	9150	11930	11660	11660	11660	56060	107.62	

Table C.3 Axle loads, tire contact area and tire loads

	Front axle		Rear axle		Trailer1 (rear Axle)		Trailer2 (front Axle)		Trailer2 (rear Axle)	
Vehicle Class	**Load per tire (lb)**	**Contact Area (in^2)**	**Load per tire (lb)**	**Contact Area (in^2)**	**Load per tire (lb)**	**Contact Area (in^2)**	**Load per tire (lb)**	**Contact Area (in^2)**	**Load per tire (lb)**	**Contact Area (in^2)**
Car	1144.3	30.07	825.0	21.70						
SUV	1321.9	34.88	1101.6	28.99						
F450	2884.3	24.49	2272.8	19.22						
Truck (fully loaded)	4534.4	42.16	4703.0	43.71	4345.6	40.46	4345.6	40.46	4345.6	40.46
Truck (partially loaded 1)	4574.9	42.47	3731.8	34.72	3664.4	34.10	3664.4	34.10	3664.4	34.10
Truck (partially loaded 2)	4574.9	42.47	2983.2	27.75	2915.8	27.13	2915.8	27.13	2915.8	27.13

Table C.4 Axle and tire spacing

	UCPRC measurements Axle Length (in)					Axle Spacing (in)				Space between Dual tires (in)	
Vehicle Class	**Front Axle**	**Rear Axle**	**Trailer1 (rear Axle)**	**Trailer2 (front Axle)**	**Trailer2 (rear Axle)**	**Front-rear1**	**Rear1-Rear2**	**Rear2-Rear3**	**Rear3-Rear4**	**Rear Axle**	**Trailer axles**
Car	62.2	62.2				108.3					
SUV	66.9	66.9				111.4					
F450	74.0	71.7				200.8				3.0	
Truck	81.1	73.2	72.0	72.0	72.0	177.2	179.1	183.1	179.9	3.8	4.6

REFERENCES

REFERENCES

American Lung Association (2018), "*State of the Air 2018*".

Baglione, M. (2007), "*Development of System Analysis Methodologies and Tools for Modeling and Optimizing Vehicle System Efficiency"*. Ph.D. Dissertation, University of Michigan.

Balzarini, D. (2015), "*Fuel Consumption Excess Prediction on a Flexible Pavement"*. *MS* Dissertation thesis, University of Pisa.

Bazi, G., Hajj, E. Y., Ulloa-Calderon, A., & Ullidtz, P. (2018). "*Finite element modelling of the rolling resistance due to pavement deformation".* International Journal of Pavement Engineering, 1-11.

Beuving, E., De Jonghe, T., Goos, D., Lindahl, T., and Stawiarski, A. (2004), "*Environmental Impacts and Fuel Efficiency of Road Pavements*". European Roads Review, No. 2.

Burnham, K.P., and Anderson, D.R. (2002), "*Model selection and inference: a practical information-theoretic approach, second edition*". Springer-Verlag, New York.

Caltrans (2015), *Annual Average Daily Truck Traffic on the California State Highway System.*

Caltrans (2016), *Traffic Volumes on the California State Highway System.*

Chabot, A., Chupin, O., Deloffre, L., and Duhamel, D. (2010), "*Viscoroute 2.0: a tool for the simulation of moving load effects on asphalt pavement"*. RMPD Special Issue on Recent Advances in Numerical Simulation of Pavements 11(2):227–250.

Chatti, K. (1992), "*Dynamic Analysis of Jointed Concrete Pavements Subjected to Moving Transient Loads"*. Ph.D. dissertation, University of California-Berkley.

Chatti, K., Lysmer, J. and Monismith, C. L. (1994), *"Dynamic Finite-Element Analysis of Jointed Concrete Pavements*". Journal of Transportation Research Board, Transportation Research Record No. 1449, TRB of the National Academies, Washington, D.C., pp. 79-90.

Chatti, K. and Kim, T.K. (2001) "*Simple Dynamic Backcalculation Procedure for Falling Weight Deflectometer Testing of Rigid Pavements*". Journal of Transportation Research Board, Transportation Research Record No. 1764, National Academies, Washington, D.C., pp. 30-38.

Chatti, K., and Zaabar, I. (2012). "*Estimating the Effects of Pavement Conditions on Vehicle Operation Costs*". TRB's NCHRP Report 720.

Chatti K., and Zaabar I. (2014). "*Effect of Pavement Surface Conditions on Sustainable Transport"*. In: Gopalakrishnan K., Steyn W., Harvey J. (eds) Climate Change, Energy, Sustainability and Pavements. Green Energy and Technology. Springer, Berlin, Heidelberg.

Christensen, R. M. (1971), *"Theory of viscoelasticity: An introduction"*. New York: Academic Press.

Christensen, Jr., D.W., Pellinen, T.K., and Bonaquist, R.F. (2003). *"Hirsch Model for Estimating the Modulus of Asphalt Concrete,"*. Journal of the Association of Asphalt Paving Technologists, 72, 97–121.

Crimmins, A., J. Balbus, J.L. Gamble, C.B. Beard, J.E. Bell, D. Dodgen, R.J. Eisen, N. Fann, M.D. Hawkins, S.C. Herring, L. Jantarasami, D.M. Mills, S. Saha, M.C. Sarofim, J. Trtanj, and L. Ziska, 2016. "*The Impacts of Climate Change on Human Health in the United States: A Scientific Assessment*". U.S. Global Change Research Program, Washington, DC, 312 pp.

Chupin, O.,Chabot, A. and Piau, J.M. (2013) "*Evaluation of the Structure-induced Rolling Resistance (SRR) for pavements including viscoelastic material layers*". Materials & Structures 46: 683.

Coleri, E., Harvey, J. T., Zaabar, I., Louhghalam A., and Chatti, K.; 2016 "*Model Development, Field Section Characterization, and Model Comparison for Excess Vehicle Fuel Use Attributed to Pavement Structural Response*". Journal of Transportation Research Board, Transportation Research Record No. 2589, pp. 40–50.

Eapa/Eurobitume Task Group Fuel Efficiency (2004), "*Environmental Impacts and Fuel Efficiency of Road Pavements*". Industry report.

EPA (2017), "*Inventory of U.S. Greenhouse Gas Emissions and Sinks: 1990–2015"*.

EPA (2009), "*Mandatory Reporting of Greenhouse Gases"*. Final Rule, 30 Oct 09, 261 pp. (Tables C-1 and C-2). Table of Final 2013 Revisions to the Greenhouse Gas.

EPA. (2014). *Inventory of U.S. Greenhouse Gas Emissions and Sinks: 1990-2012*.

European Environment Agency (2018), "*Air quality in Europe 2018*". EEA Report No 13/2017.

Flugge, W. (1967), "*Viscoelasticity*". Springer, Berlin.

FHWA (2016), "*Transportation Air Quality: Selected Facts and Figures"*.

FHWA (2016). "*LTPP Guide to Asphalt Temperature Prediction and Correction".*

Jonsson, P., and Hultqvist, B. (2009). "*Measurement of Fuel Consumption on Asphalt and Concrete Pavements North of Uppsala*". ReportNo. VTI N31-2008. Swedish National Road and Transport Research Institute(VTI), Linköping, Sweden.

Khazanovich, L., Tayabji S.D., and Darter M. I. (2001). "*backcalculation of layer parameters for ltpp test sections, Volume I: Slab on Elastic Solid and Slab on Dense-Liquid Foundation*

Analysis of Rigid Pavements". Federal Highway Administration, Publication No. FHWA-RD-00-086, January 2001.

LaClair, T. J. (2006). "*Rolling Resistance*". in NHTSA, *The Pneumatic Tire*, Chapter 12.

Lakes, R., & Lakes, R. S. (2009). "*Viscoelastic materials"*. Cambridge university press.

Lanotte, M., Soleimani, S., Kutay, M. E. (2018). "*Application of the Multi-Gene Genetic Programming (MGGP) Approach for Estimating Dynamic Modulus and Phase Angle of Asphalt Concrete*". 96th Transportation Research Board Annual Meeting.

Lee, H. (2013). "*Development of a New Solution for Viscoelastic Wave Propagation of Pavement Structures and its Use in Dynamic Backcalculation"*. Ph.D. dissertation, Department if Civil and Environmental Engineering, Michigan State University.

Louhghalam A., Akbarian, M., and Ulm F.J. (2013). "*Scaling Relations Of Dissipation-Induced Pavement-Vehicle Interactions"*. Journal of Transportation Research Board, Transportation Research Record No. 2457, National Academies, Washington, D.C.

Louhghalam, A., Akbarian, M., and F.-J. Ulm (2014). "*Flügge's Conjecture: Dissipation- versus Deflection-Induced Pavement–Vehicle Interactions*". American Society of Civil Engineers, 2013 DOI: 10.1061/(ASCE)EM.1943-7889.0000754.

Losa, M., Di Natale, A. (2012). "*Evaluation of Representative Loading Frequency for Linear Elastic Analysis of Asphalt Pavements"*. Journal of Transportation Research Board, Transportation Research Record No. 2305, National Academies, Washington, D.C.

Lysmer, J. (1965). "*Vertical Motion of Rigid Footings*". Ph.D. Dissertation, University of Michigan.

Lysmer J. and Richart F.E. (1969). "*Dynamic response of footings to vertical loading*". Journal of Engineering Mechanics, ASCE, 95:4, 65-91.

Nasimifar, M., Siddharthan, R. S., Hajj, E. Y., and Motamed, R. (2016). "*Investigation of 3D-Move ResponsesUnder Traffic Speed DeflectionDevices (TSDDs)*". The Roles of Accelerated Pavement Testing in Pavement Sustainability, DOI 10.1007/978-3-319-42797-3_1

National Oceanic and Atmospheric Administration (NOAA), (2017). "*Atlantic Hurricanes, Climate Variability, and Global Warming"*. State of the Science Fact Sheet.

Organization for Economic Cooperation and Development (OECD) (2016). "*The economic consequences of outdoor air pollution*". OECD Publishing, Paris.

Pouget, S., Sauzéat, C., Benedetto, H., and Olard, F. (2012). *"Viscous Energy Dissipation in Asphalt Pavement Structures and Implication for Vehicle Fuel Consumption"*. J. Mater. Civ. Eng., 10.1061/(ASCE), pp. 568-576.

Royall, R.M. (1997). "*Statistical evidence: a likelihood paradigm*". Chapman and Hall, New York.

Shakiba M., Ozer H., Ziyadi M. and Al-Qadi IL. (2016). "*Mechanics based model for predicting structure-induced rolling resistance (SRR) of the tire-pavement system*". Mechanics of Time-Dependent Materials. May 19; pp.1-22.

Schuring, D.J., (1977). "*A New Look at the Definition of Tire Rolling Loss*". in Tire Rolling Losses and Fuel Economy, an R&D Planning Workshop, pp. 31-37.

Thom, N.H., T. Lu and T. Parry (2010). "*Fuel Consumption Due to Pavement Deflection Under Load*". In Proceedings of 2nd International Conference on Sustainable Construction Materials and Technologies, Ancona, Italy.

Sumitsawan, P., Ardenkani, S. A. and Romanoschi, S. (2009). "*Effect of Pavement Type on Fuel Consumption and Emissions*". In Proceedings of the 2009 Mid-Continent Transportation Research Symposium, Ames, IA.

Tabatabaie, A. M. and Barenberg, E. J. (1978). "*Finite-Element Analysis of Jointed or Cracked Concrete Pavements*". Transportation Research Record, No. 671, Transportation Research Board, Washington, D.C.

Taylor, G.W., Marsh, P. and Oxelgres, E. (2000). "*Effects of Pavement Structure on Vehicle Fuel Consumption – Phase II: Seasonal Tests*". Report No CSTT – HWV – CTR – 041 Portland Cement Association. Skokie, IL.

Taylor, G.W., Farrel, P. and Woodside, A. (2002). "*Additional analysis of the Effects of Pavement Structure on Truck Fuel Consumption*". National Research Council of Canada, Ottawa, Ontario.

Taylor, G.W. and Patten, J.D. (2006). "*Effects of Pavement Structure on Vehicle Fuel Consumption – Phase III"*. Report No CSTT – HVC – TR – 068 National Research Council of Canada, Ottawa, Ontario.

Toor, W. (2016). "*It's Time to Cut Greenhouse Gas Emissions from Transportation (Transportation Ranks 1st in Emissions that Cause Climate Change*)". In Southwest Energy Efficiency Project (SWEEP).

Zaabar, I., & Chatti, K. (2011). "*New Mechanistic–Empirical Approach for Estimating the Effect of Roughness on Vehicle Durability*". Journal of Transportation Research Board, Transportation Research Record No. 2227, pp.180-188.

Zaabar, I., Chatti, K., Lee, H.S., and Lajnef, N. (2014). "*Backcalculation of Asphalt Concrete Modulus Master Curve from Field Measured Falling Weight Deflectometer Data Using a New Time Domain Viscoelastic Dynamic Solution and Genetic Algorithm*". Journal of Transportation Research Board, Transportation Research Record No. 2457, pp. 80-92.

Zaabar I. and Chatti, K. (2014). "*Estimating Vehicle Operating Costs Due to Pavement Surface Conditions*". Journal of Transportation Research Board, Transportation Research Record No. 2455, pp. 63-76.

Zaabar, I., Chatti, K. (2014). "*A field investigation of the effect of pavement type on fuel consumption*". In Sustainability, Eco-Efficiency and Conservation in Transportation Infrastructure Asset Management Proceedings of the 3rd International Conference on Transportation Infrastructure, ICTI 2014 pp. 541-548.

Wary, B. R., DeJong, J. T., Schantz, T. (2012). "*Guidelines for Estimation of Shear Wave Velocity Profiles*". PEER Report Pacific Earthquake Engineering Research Center Headquarters at the University of California.